

# **ELECTRONIC PROPERTIES OF MOLYBDENUM DISULPHIDE CALCULATED FROM FIRST PRINCIPLES**

By

Farzad Hayati

A Thesis Submitted to  
**THE UNIVERSITY OF BIRMINGHAM**  
for the Degree of  
**DOCTOR OF PHILOSOPHY**

School of Electronic, Electrical  
and Systems Engineering  
College of Engineering  
and Physical Sciences  
University of Birmingham  
May 2015

**UNIVERSITY OF  
BIRMINGHAM**

**University of Birmingham Research Archive**

**e-theses repository**

This unpublished thesis/dissertation is copyright of the author and/or third parties. The intellectual property rights of the author or third parties in respect of this work are as defined by The Copyright Designs and Patents Act 1988 or as modified by any successor legislation.

Any use made of information contained in this thesis/dissertation must be in accordance with that legislation and must be properly acknowledged. Further distribution or reproduction in any format is prohibited without the permission of the copyright holder.

## Abstract

The electrical properties of bulk and single-layer molybdenum disulphide and the electrical and magnetic properties of molybdenum disulphide nanoribbons have been investigated using density functional theory within the first principles' calculation framework. Changes in energy band structure observed during the transition from bulk to single-layer MoS<sub>2</sub> are linked to atomic orbitals through the use of maximally-localised Wannier functions. Extensive structural optimisation studies have been used to explore the effects of stress and strain on the electronic properties of both bulk and single-layer MoS<sub>2</sub>. It has been found that the electronic structure and in particular, the energy band gap of MoS<sub>2</sub> nanoribbons are sensitive to the relaxation of the lattice; and consequently, measurements of the electronic properties will depend strongly on both the preparation of the sample and the substrate on which it is deposited. The spin polarised energy band structure and the charge density were used to determine the magnetic states of zigzag nanoribbons. It has been found that both ferromagnetic and anti-ferromagnetic states are equally probable in both passivated and non-passivated zigzag nanoribbons and the calculated result depends on the initial spin configuration prior to optimisation. A new hydrogen passivation structure on the edges of MoS<sub>2</sub> nanoribbons was suggested, which shows zigzag nanoribbons can also become semiconducting. Finally, the electrical and magnetic properties of a novel chiral MoS<sub>2</sub> nanoribbon were modelled, which showed that the chiral MoS<sub>2</sub> nanoribbons can exhibit both semiconducting and ferromagnetic behaviour simultaneously; this has never been previously reported.

Birmingham, United Kingdom

May 2015

Farzad Hayati

*This thesis is dedicated to my parents  
for their endless love, support  
and encouragement*

## Acknowledgements

First and foremost, I would like to express my special thanks and appreciation to my supervisor, Dr Tony Childs for guiding me not just in my PhD but also in the life issues that I faced during my studies. It was such an honour to work with him and he is a great supervisor and a trustworthy person to me.

I especially would like to thank Dr Timothy Jackson who helped me to finalise and submit my thesis due to the stressful and unexpected circumstances I have faced in the last year of my PhD.

I would also like to express my special thanks to Dr Phil Atkins my line manager who helped me with all my difficulties both academically and in life, and tolerated me during my PhD. He is a valuable mentor to me and I will never forget his continuous support.

This work was supported by the Birmingham Environment for Academic Research (BlueBEAR), the supercomputing cluster of the University of Birmingham; and the supercomputing cluster at the University of Warwick (Minerva) through MidPlus agreement; and without their support this project was not feasible; especially the support provided by Paul Hatton.

My Head of School, Professor Peter Gardner, was very encouraging during my PhD and made me feel well supported. Dr Timothy Jackson was a great mentor to me and made me feel welcome to discuss my problems with him whenever I needed. The staff of the School of Electronic, Electrical and Systems Engineering have been like my family over these years. I would like to thank Donna Johnson, Mary Winkles, Samantha McCauley, Andy Dunn, Alan Yates, David Checkley and Robert Davies for making me feel welcome and helping me when needed.

My mother, Fatemeh Makuie and my father, Naser Hayati have been very supportive not only during my PhD, but through my life, believing in me even when I did not believe in myself and they always been there for me whenever I needed them with their endless

love. They are my life.

I would also like to mention my friends Ahmad Astineh, Dr Zoualfaghari, and in particular my beloved Sanaz Roshanmanesh who stayed by my side through difficult times during my PhD and without her support and encouragement this thesis would not have been completed.

This thesis was copy edited for conventions of language, spelling and grammar by Janet's Proofreading Service.

# Contents

<b>1</b>	<b>Introduction</b>	<b>1</b>
1.1	Motivation and Objectives . . . . .	2
1.2	Thesis Overview . . . . .	4
<b>2</b>	<b>Fundamental Theory</b>	<b>6</b>
2.1	The History of Band Structure at a Glance . . . . .	6
2.1.1	Quantum Mechanics . . . . .	6
2.1.2	Band Theory . . . . .	8
2.2	Density Functional Theory (DFT) . . . . .	8
2.2.1	Schrödinger Equation . . . . .	9
2.2.2	Thomas-Fermi-Dirac Approximation . . . . .	12
2.2.3	Hohenberg-Kohn Theorems . . . . .	13
2.2.4	Kohn-Sham Ansatz . . . . .	16
2.2.5	Force Theorem . . . . .	20
2.3	Exchange-Correlation Functionals . . . . .	21
2.3.1	Local Density Approximation (LDA) . . . . .	24
2.3.2	Generalised Gradient Approximation (GGA) . . . . .	29
2.4	Pseudo-potentials . . . . .	35
2.5	Projector Augmented Waves (PAW) . . . . .	37
2.6	GW Approximation . . . . .	40
2.6.1	Brief History . . . . .	43

2.6.2	Concepts . . . . .	44
2.7	Bloch Functions and Wannier Functions . . . . .	47
2.8	Summary . . . . .	50
<b>3</b>	<b>MoS<sub>2</sub> Material</b>	<b>51</b>
3.1	MoS <sub>2</sub> Physical Properties . . . . .	51
3.1.1	Chemical Family . . . . .	51
3.1.2	Crystallography . . . . .	52
3.1.3	Atomic Unit Cell . . . . .	54
3.1.4	Stability . . . . .	56
3.1.5	Usage and Fabrication . . . . .	57
3.2	MoS <sub>2</sub> Simulation Tools . . . . .	58
3.3	MoS <sub>2</sub> as Bulk . . . . .	60
3.3.1	Convergence Study . . . . .	60
3.3.2	Band Structure . . . . .	64
3.3.3	GW Correction . . . . .	65
3.4	MoS <sub>2</sub> as a Single Layer . . . . .	71
3.4.1	Convergence and Band Structure . . . . .	71
3.4.2	GW Correction . . . . .	74
3.5	MoS <sub>2</sub> Orbital Decomposition . . . . .	74
3.6	MoS <sub>2</sub> Relaxation and Elastic Strain Effect . . . . .	83
3.7	Summary . . . . .	87
<b>4</b>	<b>MoS<sub>2</sub> Nanoribbons</b>	<b>90</b>
4.1	Armchair Nanoribbons . . . . .	92
4.2	Zigzag Nanoribbons . . . . .	96
4.2.1	Spin Polarisation and Magnetic Properties . . . . .	100
4.3	Summary . . . . .	106

<b>5 MoS<sub>2</sub> Nanoribbon edges</b>	<b>108</b>
5.1 Edge Passivation . . . . .	108
5.2 MoS <sub>2</sub> Zigzag Nanoribbons . . . . .	112
5.3 Extra H Absorption at Zigzag Nanoribbon Edges . . . . .	121
5.4 Chiral Nanoribbons . . . . .	125
5.5 Conclusion . . . . .	129
<b>6 Conclusion &amp; Future Work</b>	<b>133</b>
6.1 Summary . . . . .	133
6.2 Future Work . . . . .	135
<b>A Fundamental Physical Constants</b>	<b>137</b>
<b>B Atomisation Energy of Molecules</b>	<b>138</b>
<b>C Periodic Table of Elements</b>	<b>139</b>
<b>D Atomic Orbitals</b>	<b>141</b>
<b>E Numerical Results</b>	<b>143</b>
E.1 2 <i>H</i> -MoS <sub>2</sub> convergence . . . . .	143
E.2 2 <i>H</i> -MoS <sub>2</sub> Band Gap Energies . . . . .	144
<b>F Supplementary Results</b>	<b>148</b>
F.1 2 <i>H</i> -MoS <sub>2</sub> and 1 <i>H</i> -MoS <sub>2</sub> band structure . . . . .	148
F.2 Atomic Charge and Magnetization of Nanoribbons . . . . .	159
F.3 Projected Band Structure and Density of States . . . . .	175
<b>G Sample ABINIT Script</b>	<b>205</b>
<b>List of References</b>	<b>209</b>

# List of Figures

2.1	Solvay Conference 1933 . . . . .	7
2.2	Jacob's ladder of XC functional . . . . .	23
2.3	Comparison of various GGA functionals in short range . . . . .	33
2.4	Comparison of various GGA functionals in long range . . . . .	34
2.5	All-electron potential versus pseudo-potential . . . . .	38
2.6	Molybdenum all-electron wave functions . . . . .	41
2.7	Molybdenum 4s orbital PAW wave functions . . . . .	42
2.8	Band gap error between DFT and GWA . . . . .	43
2.9	Inverse photo-emission spectroscopy . . . . .	45
2.10	The DFT band gap error . . . . .	46
2.11	Bloch functions versus Wannier functions . . . . .	48
3.1	A large sample of MoS <sub>2</sub> . . . . .	52
3.2	MoS <sub>2</sub> Crystalline structure and stacking . . . . .	53
3.3	Bulk 2H-MoS <sub>2</sub> structure and unit cell . . . . .	54
3.4	Reciprocal lattice and Brillouin zone of MoS <sub>2</sub> . . . . .	55
3.5	Monkhorst-Pack method meshing . . . . .	61
3.6	2H-MoS <sub>2</sub> convergence curves . . . . .	62
3.7	2H-MoS <sub>2</sub> band gap . . . . .	66
3.8	2H-MoS <sub>2</sub> convergence curves . . . . .	67
3.9	MoS <sub>2</sub> 3D energy of conduction band . . . . .	68
3.10	MoS <sub>2</sub> 3D energy of valence band . . . . .	68

3.11	One-shot GW correction calculation steps . . . . .	69
3.12	$2H\text{-MoS}_2$ band gap corrected using GW . . . . .	70
3.13	Single layer $\text{MoS}_2$ unit cell . . . . .	71
3.14	Single layer $\text{MoS}_2$ band structure . . . . .	73
3.15	$2H\text{-MoS}_2$ $4d_{z^2}$ projected MLWF cross-section . . . . .	78
3.16	$1H\text{-MoS}_2$ $4d_{z^2}$ projected MLWF cross-section . . . . .	79
3.17	Projected band structure of $2H\text{-MoS}_2$ . . . . .	81
3.18	Projected band structure of $1H\text{-MoS}_2$ . . . . .	82
3.19	Strain effect on $2H\text{-MoS}_2$ band gap . . . . .	84
3.20	Strain effect on $1H\text{-MoS}_2$ band gap . . . . .	85
3.21	Strain effect on the band gap of $2H\text{-}$ and $1H\text{-MoS}_2$ . . . . .	86
4.1	$\text{MoS}_2$ nanoribbon edge patterns . . . . .	91
4.2	$\text{MoS}_2$ armchair nanoribbon super cell . . . . .	93
4.3	Band structure of bare edge $\text{MoS}_2$ armchair nanoribbon . . . . .	94
4.4	Band structure of $\text{MoS}_2$ armchair nanoribbon (2x unit cell) . . . . .	95
4.5	Band gap of $\text{MoS}_2$ armchair nanoribbons . . . . .	97
4.6	Charge density of bare $\text{MoS}_2$ armchair nanoribbons (iso=0.25) . . . . .	98
4.7	Charge density of bare $\text{MoS}_2$ armchair nanoribbons (iso=0.15) . . . . .	99
4.8	$\text{MoS}_2$ zigzag nanoribbon super cell . . . . .	101
4.9	Band structure of an $\text{MoS}_2$ zigzag nanoribbons . . . . .	102
4.10	Band structure of an $\text{MoS}_2$ zigzag nanoribbons . . . . .	103
4.11	Different magnetic moment in $\text{MoS}_2$ zigzag nanoribbon . . . . .	104
4.12	Atom resolved charge in $\text{MoS}_2$ zigzag nanoribbon . . . . .	105
5.1	Passivated armchair $\text{MoS}_2$ unit cell . . . . .	110
5.2	Passivated zigzag $\text{MoS}_2$ unit cell . . . . .	111
5.3	Band structure of passivated $\text{MoS}_2$ armchair nanoribbon . . . . .	113
5.4	Charge density of passivated $\text{MoS}_2$ armchair nanoribbons (iso=0.25) . . . . .	114

5.5	Charge density of passivated MoS <sub>2</sub> armchair nanoribbons (iso=0.15) . . . . .	115
5.6	Anti-ferromagnetic band structure of zigzag MoS <sub>2</sub> . . . . .	118
5.7	Zigzag MoS <sub>2</sub> nanoribbon (FM) partial charge density near $E_F$ . . . . .	119
5.8	Zigzag MoS <sub>2</sub> nanoribbon (AFM) partial charge density near $E_F$ . . . . .	120
5.9	MoS <sub>2</sub> 6 hydrogen absorbtion . . . . .	122
5.10	Ferromagnetic band structure of MoS <sub>2</sub> . . . . .	123
5.11	Band structure of MoS <sub>2</sub> passivated with 6 H . . . . .	124
5.12	MoS <sub>2</sub> nanoribbon possible edge patterns . . . . .	127
5.13	MoS <sub>2</sub> nanoribbon with chiral edges . . . . .	128
5.14	Band structure of MoS <sub>2</sub> nanoribbon with chiral edges . . . . .	130
5.15	Edge density in the MoS <sub>2</sub> chiral nanoribbon . . . . .	131
F.1	2H-MoS <sub>2</sub> band structure using GGA . . . . .	149
F.2	2H-MoS <sub>2</sub> band structure using GGA+PAW . . . . .	150
F.3	2H-MoS <sub>2</sub> band structure using LDA . . . . .	151
F.4	2H-MoS <sub>2</sub> band structure using LDA+PAW . . . . .	152
F.5	1H-MoS <sub>2</sub> band structure using GGA . . . . .	153
F.6	1H-MoS <sub>2</sub> band structure using GGA+PAW . . . . .	154
F.7	1H-MoS <sub>2</sub> band structure using LDA . . . . .	155
F.8	1H-MoS <sub>2</sub> band structure using LDA+PAW . . . . .	156
F.9	2H-MoS <sub>2</sub> band structure using APW . . . . .	157
F.10	MoS <sub>2</sub> zigzag nanoribbon atom index . . . . .	160
F.11	MoS <sub>2</sub> chiral nanoribbon atom index . . . . .	171
F.12	2H-MoS <sub>2</sub> projected band structure and DOS for Mo $4d_{z^2}$ orbital . . . . .	175
F.13	2H-MoS <sub>2</sub> projected band structure and DOS for Mo $4d_{xz}$ and $4d_{yz}$ . . . . .	176
F.14	2H-MoS <sub>2</sub> projected band structure and DOS for Mo $4d_{xy}$ and $4d_{x^2-y^2}$ . . . . .	177
F.15	2H-MoS <sub>2</sub> projected band structure and DOS for Mo $5s$ orbital . . . . .	178
F.16	2H-MoS <sub>2</sub> projected band structure and DOS for Mo $4p$ orbital . . . . .	179
F.17	2H-MoS <sub>2</sub> projected band structure and DOS for Mo $4d$ orbital . . . . .	180

F.18	$2H\text{-MoS}_2$ projected band structure and DOS for sulphur $3s$ orbital . . . . .	181
F.19	$2H\text{-MoS}_2$ projected band structure and DOS for sulphur $3p$ orbital . . . . .	182
F.20	$2H\text{-MoS}_2$ projected band structure and DOS for sulphur $3p_z$ orbital . . . . .	183
F.21	$2H\text{-MoS}_2$ projected DOS for molybdenum $4d$ orbital . . . . .	184
F.22	$2H\text{-MoS}_2$ projected DOS for molybdenum $5s$ , $4p$ and $4d$ orbital . . . . .	185
F.23	$2H\text{-MoS}_2$ projected DOS for sulphur $3s$ and $3p$ orbital . . . . .	186
F.24	$1H\text{-MoS}_2$ projected band structure and DOS for Mo $4d_{z^2}$ orbital . . . . .	187
F.25	$1H\text{-MoS}_2$ projected band structure and DOS for Mo $4d_{xz}$ and $4d_{yz}$ . . . . .	188
F.26	$1H\text{-MoS}_2$ projected band structure and DOS for Mo $4d_{xy}$ and $4d_{x^2-y^2}$ . . . . .	189
F.27	$1H\text{-MoS}_2$ projected band structure and DOS for Mo $5s$ orbital . . . . .	190
F.28	$1H\text{-MoS}_2$ projected band structure and DOS for Mo $4p$ orbital . . . . .	191
F.29	$1H\text{-MoS}_2$ projected band structure and DOS for Mo $4d$ orbital . . . . .	192
F.30	$1H\text{-MoS}_2$ projected band structure and DOS for sulphur $3s$ orbital . . . . .	193
F.31	$1H\text{-MoS}_2$ projected band structure and DOS for sulphur $3p$ orbital . . . . .	194
F.32	$1H\text{-MoS}_2$ projected band structure and DOS for sulphur $3p_z$ orbital . . . . .	195
F.33	$1H\text{-MoS}_2$ projected DOS for molybdenum $4d$ orbital . . . . .	196
F.34	$1H\text{-MoS}_2$ projected DOS for molybdenum $5s$ , $4p$ and $4d$ orbital . . . . .	197
F.35	$1H\text{-MoS}_2$ projected DOS for sulphur $3s$ and $3p$ orbital . . . . .	198
F.36	$1H\text{-MoS}_2$ $4d_{z^2}$ projected MLWF . . . . .	199
F.37	$1H\text{-MoS}_2$ $4d_{x^2-y^2}$ projected MLWF . . . . .	200
F.38	$1H\text{-MoS}_2$ $4d_{xy}$ projected MLWF . . . . .	201
F.39	$1H\text{-MoS}_2$ $4d_{xz}$ projected MLWF . . . . .	202
F.40	$1H\text{-MoS}_2$ $4d_{yz}$ projected MLWF . . . . .	203
F.41	$2H\text{-MoS}_2$ $4d_{z^2}$ projected MLWF . . . . .	204

# List of Tables

2.1	The parameters used by Vosko et al. formulations . . . . .	29
3.1	MoS <sub>2</sub> lattice parameters . . . . .	56
3.2	Comparison between DFT software accuracies . . . . .	59
3.3	2H-MoS <sub>2</sub> unit cell parameters . . . . .	61
3.4	calculated 2H-MoS <sub>2</sub> lattice parameters . . . . .	63
3.5	calculated 1H-MoS <sub>2</sub> lattice parameters . . . . .	72
3.6	2H-MoS <sub>2</sub> orbital projections . . . . .	76
3.7	1H-MoS <sub>2</sub> orbital projections . . . . .	77
3.8	MoS <sub>2</sub> band gap calculated using different XE functionals . . . . .	87
3.9	Reported parameters for 2H-MoS <sub>2</sub> and 1H-MoS <sub>2</sub> . . . . .	88
5.1	Atomic covalent radii . . . . .	109
5.2	H-bond parameters of passivated MoS <sub>2</sub> nanoribbins . . . . .	109
5.3	Comparison of reported MoS <sub>2</sub> nanoribbon types . . . . .	116
5.4	Reported magnetic properties of MoS <sub>2</sub> . . . . .	117
5.5	Variation of magnetic moment in zigzag MoS <sub>2</sub> . . . . .	125
B.1	Comparison between atomisation energies . . . . .	138
D.1	Orbital definitions: angular functions . . . . .	142
D.2	Orbital definitions: radial functions for $l = 0$ . . . . .	142
E.1	2H-MoS <sub>2</sub> energy during $k$ -mesh convergence . . . . .	143

E.2	$2H\text{-MoS}_2$ energy for different kinetic cut-off energies	144
E.3	$2H\text{-MoS}_2$ stress tensor relaxation	144
E.4	Calculated energy levels for strained $2H\text{-MoS}_2$	145
E.5	Calculated energy levels for strained $1H\text{-MoS}_2$	146
E.6	Calculated parameters for zigzag nanoribbon	147
F.1	$2H\text{-MoS}_2$ symmetry properties of Bloch sums	158
F.2	Bare edge zigzag $\text{MoS}_2$ atomic charges (ferromagnetic)	161
F.3	Bare edge zigzag $\text{MoS}_2$ atomic charges (anti-ferromagnetic)	162
F.4	$2H$ passivated (Mo edge) zigzag $\text{MoS}_2$ atomic charges (ferromagnetic)	163
F.5	$2H$ passivated (Mo edge) zigzag $\text{MoS}_2$ atomic charges (anti-ferromagnetic)	164
F.6	$2H$ passivated (S edge) zigzag $\text{MoS}_2$ atomic charges (ferromagnetic)	165
F.7	$2H$ passivated (S edge) zigzag $\text{MoS}_2$ atomic charges (anti-ferromagnetic)	166
F.8	$4H$ passivated edge zigzag $\text{MoS}_2$ atomic charges (ferromagnetic)	167
F.9	$4H$ passivated edge zigzag $\text{MoS}_2$ atomic charges (anti-ferromagnetic)	168
F.10	$5H$ type I passivated edge zigzag $\text{MoS}_2$ atomic charges	169
F.11	$5H$ type II passivated edge zigzag $\text{MoS}_2$ atomic charges	170
F.12	Chiral $\text{MoS}_2$ nanoribbon atomic charge (Mo)	172
F.13	Chiral $\text{MoS}_2$ nanoribbon atomic charge (lower S)	173
F.14	Chiral $\text{MoS}_2$ nanoribbon atomic charge (upper S)	174

# List of Abbreviations

**a.u.** atomic units (Hartree).

**BZ** Brillouin zone.

**DFT** Density Functional Theory.

**DOS** Density of States.

**GGA** Generalised Gradient Approximation.

**GW** Green's Function.

**LDA** Local Density Approximation.

**LSDA** Local Spin-Density Approximation.

**MLWF** Maximally Localised Wannier Function.

**MoS<sub>2</sub>** Molybdenum disulphide.

**OPW** Orthogonalised Plane Wave.

**PAW** Projector Augmented Wave.

**PW** Plane Waves.

*“If you can’t explain it simply, you don’t understand it well enough.”*

— Albert Einstein

# Chapter 1

## Introduction

Since the discovery of electrons in the 1890s by Lorentz, Zeeman and Thomson, scientists were faced with a big challenge to explain the properties of matter. It was only after the emerging of the laws of quantum physics in the 1920s that scientists started to explain the electrical behaviour of the electrons in matter and the first realistic models of the interacting electrons started to appear. Some of the early techniques, such as the Hartree-Fock method introduced in the 1920s and 1930s are still in use today. However, the calculation of the electrical properties and band structure was not significantly improved until the 1950s when scientists started to calculate more complicated band structures such as semiconductors.

In the 1960s the new density functional theory (DFT) was introduced by Hohenberg and Kohn; it claimed all the properties of matter can be derived through the electrons' charge density. However, this calculation was very limited until the 1990s when the computation power increased significantly and the modelling of realistic systems with hundreds of atoms became possible.

Nowadays, the DFT calculation is one of the most popular techniques to describe the properties of matter. This technique is also called, in the Latin term *ab initio*<sup>1</sup> that means from the beginning or referred to as the first principle. This is because the DFT technique relies on very few parameters and calculates all the properties from the basic parameters

of the system.

Although the density functional theory is exact in principle, some approximation has to be made for realistic calculation of matter. These approximations lead to situations where the DFT is not successful in describing matter and many different factors have to be taken into account in such situations. One of these situations is the prediction of the matter's build of atoms with partially filled *d* – orbital<sup>2</sup> such as metals, semi-metals and semiconductors.

Among the advances made in electronic devices, one good candidate to be used in semiconducting components is molybdenum disulphide, which has electrons in the *d* – orbital and the approximations used in DFT calculations can lead to a wrong description of this material if extra care is not taken in the calculation.

This research aims to provide more understanding on the electronic properties of molybdenum disulphide ( $\text{MoS}_2$ ) and answer the disagreement reported in the literature on the properties of this material using extensive simulations. The obtained electrical properties in this research are grouped in three categories: (i) bulk  $\text{MoS}_2$  or three-dimensional (3D) properties; (ii) single-layer  $\text{MoS}_2$  or two-dimensional (2D) properties; and (iii) nano dimensioned ribbons.

## 1.1 Motivation and Objectives

The realisation of stable two-dimensional structures such as graphene [2–4] has generated considerable interest in their properties and applications. This is primarily because of the easy fabrication of these materials and their extraordinary charge transport and optical and thermal properties [2, 3, 5–8]; as well as their diverse applications [8–14]. Many other inorganic materials analogous to graphene such as silicon carbide (SiC), gallium nitride (GaN) and manganese oxide ( $\text{MnO}_2$ ) have been studied and reported [15–22]. Among

---

<sup>1</sup>Oxford English Dictionary [1]: **ab ini · tio** /,ab ɪ'niʃɪə/ **adverb, adjective** (formal or Law) *adv.* from the beginning; *adj.(attrib.)* initial, primary, elementary. **ORIGIN** Latin.

<sup>2</sup>The orbital occupation and the shape of each orbit are provided in appendix C and D respectively.

these materials, the transition-metal dichalcogenide<sup>3</sup> semiconductors such as molybdenum disulphide ( $\text{MoS}_2$ ) and tungsten disulphide ( $\text{WS}_2$ ), which are compounds between a transition-metal and a chalcogen<sup>4</sup> are particularly of interest due to their layered structure and interesting electronic properties [23]. Over the past decade the number of research papers published on graphene has increased more than 120 times<sup>5</sup>; while not much attention has been paid to similar materials such as  $\text{MoS}_2$  or  $\text{WS}_2$ .

Although molybdenum disulphide has been discovered for many years now and is widely used as a dry lubricant, still not much research has been carried out on its electrical properties and its suitability to be used in electronic devices. Graphene is a zero band gap material and it requires band gap engineering which increases its fabrication complexity and either reduces its mobilities to the level of strained silicon films, or requires high voltages, which are not desirable [24]. Previously, the mobility of the electrons for molybdenum disulphide was reported to be between  $0.5$  and  $3 \text{ cm}^2 \text{ V}^{-1} \text{ s}^{-1}$  [25]. Recently a research study showed that single atomic layer molybdenum disulphide at room temperature, has a mobility of at least  $200 \text{ cm}^2 \text{ V}^{-1} \text{ s}^{-1}$ , similar to the mobility of graphene nanoribbons [24]. This is almost 2.5 times higher than the highest achieved mobility using conventional semiconductors; that high achievement belongs to indium antimonide ( $\text{InSb}$ ) with a mobility of  $78 \text{ cm}^2 \text{ V}^{-1} \text{ s}^{-1}$  [26,27]. However, in practice the actual mobility from band gap engineered graphene is lower at around  $10 \text{ cm}^2 \text{ V}^{-1} \text{ s}^{-1}$  [27]. Recently, several research studies have been reported on the use of  $\text{MoS}_2$  in various areas, such as photovoltaic cells, photo-catalysts and lithium-ion batteries [28–34]. It can be observed that single layer  $\text{MoS}_2$ , unlike its bulk form, has a direct band gap [35]. As a result, this material becomes a very good candidate to be used in electronic devices such as the gate material of field effect transistors or optical devices, because of its direct band gap; there is a great research opportunity in this area [36].

---

<sup>3</sup>The transition-metal dichalcogenides are further discussed and explained in § 3.

<sup>4</sup>The transition-metals are elements belonging to the groups 3–12 of the periodic table of elements and chalcogens are the elements belonging to the group 16 of the periodic table of elements. The periodic table of elements is presented in appendix C.

<sup>5</sup>The statistical data is obtained from ISI Web of Science™: The number of articles published under the topic of ‘Graphene’, in the year 2004 were 162, and in the year 2014 were 19,879.

In this research, the change in the electronic properties of molybdenum disulphide in transition from bulk to single-layer and the effect of the structural relaxation on the band gap and elastic strain that can occur, due to the presence of the substrate, were investigated. Also, the reason behind the disagreement in the reported results on the magnetic behaviour of molybdenum disulphide nanoribbons was examined and finally, a new edge pattern for molybdenum disulphide nanoribbons is suggested; which, to the best knowledge of the author, has not yet been studied up to the date of submitting this thesis.

## 1.2 Thesis Overview

This research is presented in six chapters which summarise this study on the electronic properties of MoS<sub>2</sub> as bulk, single-layer and nanoribbon.

Chapter 1 gives an overview of the objectives and the motivation for this research and discusses the layout and structure of this thesis.

Chapter 2 reviews the fundamental theory of the simulations which have been carried out in this research; this includes density functional theory calculation within the first principle framework as well as other techniques, such as Wannier functions atomic orbital decomposition.

Chapter 3 provides a general understanding about the electrical properties of MoS<sub>2</sub> by discussing the band structure and the structure and crystallography of the material in a well-known situation. Then the changes that will occur in the electrical properties of MoS<sub>2</sub> when it is presented as a single layer and certain forces i.e. van der Waals between layers, do not exist will be explored.

Chapter 4 discusses the behaviour and properties of the nanoribbons made from MoS<sub>2</sub>, the effect of the edges and the exposed atoms on each edge of the nanoribbon on its electrical properties; and furthermore, the induced magnetic effects due to the introduced unsymmetrical bonds at the edge are considered.

Chapter 5 presents the effect of the passivated edges of MoS<sub>2</sub> nanoribbons on magnetic

behaviour and on the band gap of the nanoribbon; various levels of absorption of hydrogen on the edges will be studied. Finally, the electrical properties of a new edge pattern on the nanoribbon will be investigated.

Chapter 6 summarises and highlights the achievements in this research and finalises this thesis by suggesting possible future works.

*“As far as the laws of mathematics refer to reality, they are not certain, and as far as they are certain, they do not refer to reality.”*

— Albert Einstein

# Chapter 2

## Fundamental Theory

### 2.1 The History of Band Structure at a Glance

The knowledge of electricity goes back to ancient times; although it was not known as electricity, but incidents like the ‘shock’ from electric fish are noticeable in the ancient Egyptian and Romans’ records [37]. It was not until the discovery of electrons in the late 1890s that people started to talk about electronic structure.

Nobel prizes in 1902 and 1906 were awarded to Pieter Zeeman and Sir Joseph John (J.J.) Thomson respectively for research, which led to a model of the atom as a sphere of a positively charged substance in which negatively charged electrons were situated.

A few years later in 1911, Ernest Rutherford invalidated J. J. Thomson’s model by his well-known gold foil experiment and proposed a model for atoms with a small positive charge in the middle [38]. This proposed model was not in-line with the rules defined by conventional physics and the stability of the matter was unexplainable.

#### 2.1.1 Quantum Mechanics

To solve the problem of explaining the stability of the matter, Niels Bohr joined Rutherford to work on this issue. In 1913, they produced a new model which was called the Rutherford–Bohr model and they explained the atom as a positively charged nucleus with



Figure 2.1: 7<sup>th</sup> Solvay Conference, Bruxelles (October 1933). *Standing (left to right):* Émile Henriot, Francis Perrin, Frédéric Joliot-Curie, **Werner Heisenberg**, Hendrik Anthony Kramers, Ernst Stahel, **Enrico Fermi**, Ernest Walton, **Paul Dirac**, Peter Debye, Nevill Francis Mott, Blas Cabrera y Felipe, George Gamow, Walther Bothe, Patrick Blackett, M.S. Rosenblum, Jacques Errera, Ed. Bauer, **Wolfgang Pauli**, Jules-Émile Verschaffelt, Max Cosyns, E. Herzen, John Douglas Cockcroft, Charles Drummond Ellis, Rudolf Peierls, Auguste Piccard, Ernest O. Lawrence, Léon Rosenfeld. *Seated (left to right):* **Erwin Schrödinger**, Irène Joliot-Curie, **Niels Henrik David Bohr**, Abram Ioffe, Marie Curie, Paul Langevin, Owen Willans Richardson, **Lord Ernest Rutherford**, Théophile de Donder, Maurice de Broglie, **Louis de Broglie**, Lise Meitner, James Chadwick [40].

electrons moving in orbit around the nucleus. In their model, Bohr explained the stability of the atoms with certain ‘energy levels’ that exist for electrons and this was the initial start of today’s quantum mechanics [39]. Bohr’s work was awarded with a Nobel prize in 1922.

Bohr’s idea inspired other scientists such as de Broglie, Heisenberg and Schrödinger and their work led to the emergence of the quantum mechanics’ laws in the 1920s.

### 2.1.2 Band Theory

In 1928 Felix Bloch proposed the theory of conduction in metals. This was a significant movement towards the understanding of electrons in a periodic potential. Bloch's theorem only considered the ground state of a single electron in a fixed periodic potential and it neglected the interaction between electrons [41]. Soon after, the remarkable work of researchers like Léon Nicolas Brillouin [41, 42] and Sir Alan Herries Wilson [41, 43] led to the definition of the Brillouin zone, the periodic energy–wave vector relation and the energy-band structure of solids.

In the 1930s the first realistic multi-electron band structure calculations started to appear. One of the most significant works on the calculation of the electronic structure of atoms in this period was carried out by Douglas Rayner Hartree [44]; this was the starting point of most of today's numerical atomic calculations [45]. Another important work in this decade was achieved by Vladimir Aleksandrovich Fock and that was the very first appearance of what is known as the Hartree–Fock method today [45].

## 2.2 Density Functional Theory (DFT)

The density functional theory in general and its applications are discussed in a tremendous amount of literature and it is necessary to have limits and be selective about the techniques and bibliography [46]. A few notable textbooks in this area are the books by Parr and Yang [47], Dreizler and Gross [48] and Martin [45], as well as the hand-book by Drake [46].

Unlike the Hartree–Fock technique that works directly with the many–body wave functions, the density functional theory only works with the electron density of the system. This theory is applicable to the correlated many–body systems and states: any property of a many body system can be presented as a functional of the density in the ground state of that system.

The initial equation is the total energy of a many–body system consisting of electrons

and nuclei which is the Hamiltonian of the system; that is [45]

$$\hat{\mathcal{H}} = - \sum_i \frac{\hbar^2}{2m_e} \nabla_i^2 - \sum_I \frac{\hbar^2}{2M_I} \nabla_I^2 + \frac{1}{2} \sum_{i \neq j} \frac{e^2}{|\mathbf{r}_i - \mathbf{r}_j|} + \frac{1}{2} \sum_{I \neq J} \frac{Z_I Z_J e^2}{|\mathbf{R}_I - \mathbf{R}_J|} + \sum_{i,I} \frac{Z_I e^2}{|\mathbf{r}_i - \mathbf{R}_I|}, \quad (2.1)$$

where the symbols corresponding to the nuclei are in capitals, and lower case letters are used to represent quantities related to electrons. The  $\nabla^2$  notation is referring to the Laplace operator (Laplacian) of the correspondent indices. The first two terms of the Hamiltonian above represent kinetic energy operators of the electrons and nuclei respectively and the next three terms are the potential energy of the Coulomb interaction between electron-electron, nucleus-nucleus and electron-nucleus respectively. Term  $M_I$  is the mass of nuclei and  $\mathbf{R}_{I|J}$  is the position of the nuclei; while  $\mathbf{r}_{i|j}$  is the position of the electron.

### 2.2.1 Schrödinger Equation

In 1926 Erwin Schrödinger introduced his theory of matter waves that was based on the wave relation described by Louis de Broglie [49]. This was a partial differential equation that described the system states using wave functions in relation to time [50]. The general form of the time-dependent non-relativistic Schrödinger equation is

$$i\hbar \frac{\partial}{\partial t} \Psi(\mathbf{r}, t) = \hat{\mathcal{H}} \Psi(\mathbf{r}, t), \quad (2.2)$$

where  $\hat{\mathcal{H}}$  and  $\Psi$  represent the Hamiltonian and the wave function of the system respectively.

However, it is very difficult to solve this equation without breaking down the wave function. In 1927 Max Born and Julius Robert Oppenheimer introduced the Born–Oppenheimer approximation [51] that takes advantage of the large difference between the mass of the nuclei and electrons in the system; which is more than 1800 times. This

means the nuclei movements are considerably slower than the electrons; which makes it possible to separate them and considering the speed of the electrons, we can assume that the nuclei are fixed. This will convert the nuclei to a static external potential acting on the electrons. Thus, we can write the Hamiltonian equation as

$$\hat{\mathcal{H}} = \hat{T} + \hat{U} + \hat{V} \stackrel{\text{def}}{=} -\sum_i \frac{-\hbar^2}{2m_e} \nabla_i^2 + \frac{1}{2} \sum_{i \neq j} \frac{e^2}{|\mathbf{r}_i - \mathbf{r}_j|} + \sum_{i,I} V_I (|\mathbf{r}_i - \mathbf{R}_I|), \quad (2.3)$$

where  $\hat{T}$  is the kinetic energy operator;  $\hat{U}$  is the electron-electron interaction; and  $\hat{V}$  is the external potential which is from the nuclei.

This is the simplified Hamiltonian of the system and does not include nuclei-nuclei interaction or other potentials such as an external electric field. However, these terms are not essential to describe the electrons and can be added to the equation for particular calculations if needed [45].

To predict the stationary states of the system or what is called orbital, we consider the special case of Equation 2.2 that is known as the time-independent Schrödinger equation

$$E\Psi(\mathbf{r}) = \hat{\mathcal{H}}\Psi(\mathbf{r}) \quad (2.4)$$

and simply means the total energy of the system is the sum of kinetic and potential energy of that system.

In the non-relativistic context<sup>1</sup>, the spin has been taken into account as an *ad hoc* procedure through defining two components' wave function [52, 53] as

$$\Psi(\mathbf{r}) = \begin{pmatrix} \Psi_\alpha(\mathbf{r}) \\ \Psi_\beta(\mathbf{r}) \end{pmatrix}. \quad (2.5)$$

The spin independent operators such as Hamiltonian  $\hat{\mathcal{H}}$  will act on both components of the constructed wave function proportional to the unit matrix  $I_2$ , whereas the operators

---

<sup>1</sup>For more details about spin in relativistic quantum mechanics and many-body systems, one could refer to Spin in density-functional theory by Jacob and Reiher [54].

such as electron spin operator  $\hat{s}$  that are expressed in terms of the Pauli matrices [54]

$$\sigma_x = \begin{pmatrix} 0 & 1 \\ 1 & 0 \end{pmatrix}, \quad \sigma_y = \begin{pmatrix} 0 & -i \\ i & 0 \end{pmatrix}, \quad \sigma_z = \begin{pmatrix} 1 & 0 \\ 0 & 1 \end{pmatrix}, \quad (2.6)$$

will distinguish the two components of the wave function. The electron spin operator  $\hat{s}$  is defined as

$$\hat{s} = \frac{\hbar}{2}\sigma = \frac{\hbar}{2}(\sigma_x, \sigma_y, \sigma_z)^T, \quad (2.7)$$

that is related to the intrinsic magnetic moment of the electron [52, 54–56] described as

$$\hat{\mu}_s = -\frac{2\mu_B}{\hbar}\hat{s} = -\mu_B\sigma, \quad (2.8)$$

where  $\mu_B$  is the Bohr magneton.

It is also possible to represent the spin implicitly using different notation that is more commonly used in quantum chemistry, as it is more convenient for handling many-body systems [54]. This is achieved by introducing orthogonal spin functions  $\alpha(s)$  and  $\beta(s)$ , which are dependent to the spin variable  $s$  [52, 55, 57]. The spin variable  $s$  only takes two values of  $\pm\frac{1}{2}$  and consequently, the spin functions are defined as

$$\alpha\left(+\frac{1}{2}\right) = 1 \text{ and } \alpha\left(-\frac{1}{2}\right) = 0, \quad (2.9a)$$

$$\beta\left(+\frac{1}{2}\right) = 1 \text{ and } \beta\left(-\frac{1}{2}\right) = 0. \quad (2.9b)$$

Thus, the wave function can be constructed as

$$\Psi(\mathbf{r}, s) = \Psi_\alpha(\mathbf{r})\alpha(s) + \Psi_\beta(\mathbf{r})\beta(s). \quad (2.10)$$

Consequently, each of the two components of the wave function can be given by

$$\Psi \left( \mathbf{r}, +\frac{1}{2} \right) = \Psi_\alpha(\mathbf{r}), \quad (2.11a)$$

and

$$\Psi \left( \mathbf{r}, -\frac{1}{2} \right) = \Psi_\beta(\mathbf{r}). \quad (2.11b)$$

It has to be noted that the spin functions  $\alpha$  and  $\beta$  are purely a way to define the two components of the wave function using the  $s$  variable, that in turn acts as a label for each wave function.

### 2.2.2 Thomas-Fermi-Dirac Approximation

The initial density functional model was proposed in 1927 by Thomas [58] and Fermi [59] and is known as the Thomas-Fermi theory. In their model, the electron density  $n(\mathbf{r})$ , that is defined as the probability of an electron being present at the location  $\mathbf{r}$ , was used as a variable instead of the system wave function and the kinetic energy of the electrons is a functional of the density. In the original Thomas-Fermi approximation the exchange and correlation were ignored among the electrons and the model represented the local density of non-interacting electrons in a homogeneous electron gas<sup>2</sup> as

$$E_{TF}[n] = C_k \int n(\mathbf{r})^{5/3} d^3\mathbf{r} + \int V_{ext}(\mathbf{r})n(\mathbf{r}) d^3\mathbf{r} + \frac{1}{2}e^2 \iint \frac{n(\mathbf{r})n(\mathbf{r}')}{|\mathbf{r} - \mathbf{r}'|} d^3\mathbf{r} d^3\mathbf{r}',^3 \quad (2.12)$$

where the constant term,  $C_k$ , is:

$$C_k = \frac{\hbar^2}{m_e} 2\pi^2 \frac{3}{5} \left( \frac{3}{8\pi} \right)^{2/3}. \quad (2.13)$$

Equation 2.12 consists of three terms; the first term indicates the kinetic energy of the non-interacting electrons in homogeneous electron gas confined in a three-dimensional

---

<sup>2</sup>For more details, one could refer to § 20.1 of handbook of atomic, molecular and optical physics [46].

<sup>3</sup>the  $d^3\mathbf{r}$  symbol is used to denote the volume element in coordinate space [60].

box. The second term is the nuclei–electron Coulomb interaction where the  $V_{ext}$  is the potential energy of the electron due to one or more nuclei and is defined as  $V_{ext}(\mathbf{r}) = -\sum_i Z_i/|\mathbf{r} - \mathbf{R}_i|$ . The final term is the Hartree potential or Coulomb repulsion between electrons in three-dimensional space. In 1930, the original Thomas-Fermi model was extended by Dirac [61] to include the local exchange term which is known as the Thomas-Fermi-Dirac approximation [62]

$$E_{TFD}[n] = C_k \int n(\mathbf{r})^{5/3} d^3\mathbf{r} + \int V_{ext}(\mathbf{r})n(\mathbf{r}) d^3\mathbf{r} + \frac{1}{2}e^2 \iint \frac{n(\mathbf{r})n(\mathbf{r}')}{|\mathbf{r} - \mathbf{r}'|} d^3\mathbf{r} d^3\mathbf{r}' + C_e \int n(\mathbf{r})^{4/3} d^3\mathbf{r} \quad (2.14)$$

where  $C_k$  is defined in Equation 2.13 and  $C_e$  is

$$C_e = \frac{1}{4\pi^3} \left(3\pi^2\right)^{4/3} e^2 = \frac{3}{4} \left(\frac{3}{\pi}\right)^{1/3} e^2. \quad (2.15)$$

Although this approximation was not very accurate, it demonstrates the basic idea of using the density functional. However, Dirac in his paper, suggested that his equation gives a meaningless result for the outside of the atom [61]. This suggests that this approximation needs modification for any area in which the density is small.

### 2.2.3 Hohenberg-Kohn Theorems

The Second World War (from 1939 to 1945) had a significant impact on theoretical studies and the focus moved to war work. However, the developments in technology during the war had a positive impact on research in the 1950s and 1960s [41]. Some, but not all of the developments included the invention of bipolar transistors, the development of electrical computers and improvement in experimental techniques.

In 1964, Pierre Hohenberg and Walter Kohn proved two theorems that made the density functional theory possible [63].

**The first theorem** states, *for an arbitrary number of electrons under influence of an*

external potential  $V_{ext}(\mathbf{r})$ , apart from a trivial additive constant, the potential  $V_{ext}(\mathbf{r})$  is a unique functional of density  $n(\mathbf{r})$  in its ground state [63].

To prove this theorem here, the simple case of ‘non-degenerate ground state’ is used; however, it is possible to prove the theorem for degenerate ground states as well [64]. This proof is shown by the “*Reductio ad absurdum*”<sup>4</sup> technique by assuming that there is another ground state and potential that leads to the same density. From the variational principle we know that there is no other wave function  $\Psi'$  that gives a ground state energy  $E'$  less than the energy of wave function  $\Psi$  for same Hamiltonian  $\hat{\mathcal{H}}$ ; hence, using Dirac’s bra-ket notation [65] we can write

$$E < E' \stackrel{\text{def}}{=} \langle \Psi | \hat{\mathcal{H}} | \Psi \rangle < \langle \Psi' | \hat{\mathcal{H}} | \Psi' \rangle \quad (2.16)$$

where

$$\langle \Psi' | \hat{\mathcal{H}} | \Psi' \rangle = \langle \Psi' | \hat{\mathcal{H}}' | \Psi' \rangle + \langle \Psi' | \hat{\mathcal{H}} - \hat{\mathcal{H}}' | \Psi' \rangle, \quad (2.17)$$

therefore

$$E < E' + \int (V_{ext}(\mathbf{r}) - V'_{ext}(\mathbf{r})) n(\mathbf{r}) d^3\mathbf{r}. \quad (2.18)$$

Similarly, due to the non-degenerate ground state the densities for the Hamiltonians are identical and Equation 2.16 can be written as

$$E' = \langle \Psi' | \hat{\mathcal{H}}' | \Psi' \rangle < \langle \Psi | \hat{\mathcal{H}}' | \Psi \rangle, \quad (2.19)$$

hence

$$\begin{aligned} E' &< \langle \Psi | \hat{\mathcal{H}} | \Psi \rangle + \langle \Psi | \hat{\mathcal{H}}' - \hat{\mathcal{H}} | \Psi \rangle \\ &< E + \int (V'_{ext}(\mathbf{r}) - V_{ext}(\mathbf{r})) n(\mathbf{r}) d^3\mathbf{r}. \end{aligned} \quad (2.20)$$

---

<sup>4</sup>This is a Latin phrase meaning reduction to absurdity that is a technique in mathematics.

Adding Equation 2.18 and 2.20 results in an inconsistency

$$E + E' < E' + E. \quad (2.21)$$

Therefore, the potential  $V_{ext}(\mathbf{r})$  is a unique functional of density  $n(\mathbf{r})$ . However, there is no procedure to calculate this function which is extremely complicated if it even can be written down at all [46].

**The second theorem** states that, *there can be written a universal functional for energy  $E[n(\mathbf{r})]$ , in terms of density  $n(\mathbf{r})$ , valid for any external potential  $V_{ext}(\mathbf{r})$ , such that, for any given  $V_{ext}(\mathbf{r})$  the global minimum value of the functional is the exact ground state energy of the system, and the value of density which minimises this functional is the exact density of the system ground state* [45, 63].

The proof of this theorem is similar to the first theorem. As all the system properties such as kinetic and interaction energy are solely determinable by density  $n(\mathbf{r})$ , therefore they can be written as a functional of density and evidently the total energy of the system:

$$\begin{aligned} E[n(\mathbf{r})] &\stackrel{\text{def}}{=} \hat{T}[n(\mathbf{r})] + \hat{U}[n(\mathbf{r})] + \hat{V}[n(\mathbf{r})] \\ &= F[n(\mathbf{r})] + \int V_{ext}(\mathbf{r}) n(\mathbf{r}) d^3\mathbf{r} \end{aligned} \quad (2.22)$$

where  $\hat{T}[n(\mathbf{r})]$  and  $\hat{U}[n(\mathbf{r})]$  are the kinetic and the electron-electron interaction energy respectively. The functional  $F[n(\mathbf{r})]$  is a universal functional valid for any number of particles and any external potential  $V_{ext}(\mathbf{r})$  [63] that is defined as

$$F[n(\mathbf{r})] \stackrel{\text{def}}{=} \hat{T}[n(\mathbf{r})] + \hat{U}[n(\mathbf{r})]. \quad (2.23)$$

For a system with ground state density  $n(\mathbf{r})$  related to a specific external potential

$V_{ext}(\mathbf{r})$  we can write:

$$\begin{aligned} E[\Psi] &\stackrel{\text{def}}{=} \langle \Psi | \hat{T} + \hat{U} + \hat{V} | \Psi \rangle \\ &= \langle \Psi | \hat{\mathcal{H}} | \Psi \rangle \\ &= E[n(\mathbf{r})] \end{aligned} \quad (2.24)$$

which has the Hamiltonian  $\hat{\mathcal{H}}$  for the unique ground state of the system with a wave function  $\Psi$ . Similarly, for another system with a different density  $n'(\mathbf{r})$  and inevitably a different wave function  $\Psi'$  we can show:

$$E[\Psi'] = \langle \Psi' | \hat{\mathcal{H}} | \Psi' \rangle. \quad (2.25)$$

By the variational principle we know that the new density  $n'(\mathbf{r})$  inevitably gives a higher energy than  $n(\mathbf{r})$ ; hence we can write:

$$E[\Psi] = \langle \Psi | \hat{\mathcal{H}} | \Psi \rangle < \langle \Psi' | \hat{\mathcal{H}} | \Psi' \rangle = E[\Psi']. \quad (2.26)$$

Therefore, the energy functional calculated for the ground state density is lower than the energy functional calculated for any other density. Thus, if the functional  $F[n(\mathbf{r})]$  in Equation 2.23 was known, the ground state energy and density could be found by minimizing the energy functional with respect to the density. Similar to the first theorem, this is only valid for a non-degenerate ground state of the system and if there is more than one wave function for the ground state energy of the system i.e. degenerate ground state, an alternative definition of the theorem is required. This was established by Mel Levy [64] and developed more mathematically by Elliot Lieb [66].

## 2.2.4 Kohn-Sham Ansatz<sup>5</sup>

The Hohenberg-Kohn theorems only prove the concept of density functional theory and showed that it is possible to calculate the ground state energy from the density. How-

ever, there was not any possible mathematical solution to obtain the density  $n(\mathbf{r})$  or the functional defined in Equation 2.23.

In 1965, the approach presented by Walter Kohn and Lu Jeu Sham, made the density functional theory mathematically possible [68]. Their approach was to replace the Hamiltonian many-body problem with another auxiliary non-interacting system that is easy to solve using mathematical techniques, by assuming that these two systems have an identical ground state density; and then they proved that these two systems indeed have identical ground state density. Considering the fact that there is no rule for defining this simpler auxiliary system in exchange for the actual problem, this is an *ansatz* which only paraphrases the problem [45].

This approach converts the non-solvable many-body problem to an independent particle system that can be solved with an exact mathematical solution. The defined N particle non-interacting system by Kohn-Sham has a Hamiltonian as:

$$\hat{\mathcal{H}}_{KS} \stackrel{\text{def}}{=} \sum_{i=1}^N \left[ -\frac{\hbar^2}{2m_e} \nabla_i^2 + V_{eff}(\mathbf{r}_i) \right], \quad (2.27)$$

where  $V_{eff}$  is the effective potential on a single particle at  $\mathbf{r}_i$  due to the remaining  $(N - 1)$  particles. To solve this Hamiltonian and calculate the ground state for an independent particle system with N electrons, we can solve the one-electron Schrödinger-like equation

$$\left( -\frac{\hbar^2}{2m_e} \nabla^2 + V_{eff}(\mathbf{r}) \right) \psi_i(\mathbf{r}) = \varepsilon_i \psi_i(\mathbf{r}), \quad (2.28)$$

for each of the available N molecular orbitals  $\psi_i(\mathbf{r})$ . The  $\varepsilon_i$  above is the orbital energy of the corresponding orbital  $\psi_i(\mathbf{r})$ . The density of the auxiliary system  $n(\mathbf{r})$  can be obtained by [68]

$$n(\mathbf{r}) = \sum_{i=1}^N |\psi_i(\mathbf{r})|^2. \quad (2.29)$$

---

<sup>5</sup>Oxford English Dictionary [67]: **an · satz** /'ænsæts/ **noun** (Mathematics) an assumption about the form of an unknown function which is made in order to facilitate solution of an equation or other problem.  
**ORIGIN** 1940s: from German Ansatz ‘approach, attempt’.

The kinetic energy  $T_S$  of the non-interacting particles is calculated by:

$$T_S[n(\mathbf{r})] \stackrel{\text{def}}{=} \sum_{i=1}^N \int \psi_i^* \left( -\frac{\hbar^2}{2m_e} \nabla^2 \right) \psi_i d^3\mathbf{r}, \quad (2.30)$$

and the Coulomb interaction or the Hartree energy is defined as:

$$E_{Hartree}[n(\mathbf{r})] \stackrel{\text{def}}{=} \frac{1}{2} \tilde{e}^2 \iint \frac{n(\mathbf{r})n(\mathbf{r}')}{|\mathbf{r} - \mathbf{r}'|} d^3\mathbf{r} d^3\mathbf{r}', \quad (2.31)$$

where

$$\tilde{e}^2 \stackrel{\text{def}}{=} \frac{e^2}{4\pi\epsilon_0}. \quad (2.32)$$

Ignoring the nuclei-nuclei interaction, the Kohn-Sham equation is the re-written form of the Hohenberg-Kohn theorem defined in Equation 2.22 as:

$$E_{KS} \stackrel{\text{def}}{=} T_s[n(\mathbf{r})] + E_{Hartree}[n(\mathbf{r})] + E_{xc}[n(\mathbf{r})] + \int V_{ext}(\mathbf{r})n(\mathbf{r}) d^3\mathbf{r}, \quad (2.33)$$

where the  $V_{ext}(\mathbf{r})$  is the external potential acting on the electrons due to the nuclei. By comparing Equations 2.22 and 2.33, the universal functional  $F[n(\mathbf{r})]$  defined in Equation 2.23 becomes:

$$F[n(\mathbf{r})] = T_s[n(\mathbf{r})] + E_{Hartree}[n(\mathbf{r})] + E_{xc}[n(\mathbf{r})]. \quad (2.34)$$

Comparing Equation 2.23 with 2.34, the  $E_{xc}$  is the difference between both the internal interaction and kinetic energies of the assumed non-interacting system and the actual interacting system; it can be written as:

$$E_{xc}[n(\mathbf{r})] = (\langle \hat{T}[n(\mathbf{r})] \rangle - T_s[n(\mathbf{r})]) + (\langle \hat{U}[n(\mathbf{r})] \rangle - E_{Hartree}[n(\mathbf{r})]). \quad (2.35)$$

Using the variational theorem and Equation 2.22, subject to the conservation of the

number of electrons  $N$ , we can write:

$$\delta \left\{ F[n(\mathbf{r})] + \int V_{ext}(\mathbf{r})n(\mathbf{r}) d^3\mathbf{r} - \mu \left( \int n(\mathbf{r}) d\mathbf{r} - N \right) \right\} = 0, \quad (2.36)$$

where  $\mu$  is the Lagrangian multiplier [60] which represents the Fermi energy at absolute zero and is known as the chemical potential. Solving for  $\mu$ , leads to:

$$\mu = \frac{\delta F[n(\mathbf{r})]}{\delta n(\mathbf{r})} + V_{ext}(\mathbf{r}). \quad (2.37)$$

Substituting Equation 2.34 into 2.37 yields:

$$\begin{aligned} \mu &= \frac{\delta T_s[n(\mathbf{r})]}{\delta n(\mathbf{r})} + \frac{\delta E_H[n(\mathbf{r})]}{\delta n(\mathbf{r})} + \frac{\delta E_{XC}[n(\mathbf{r})]}{\delta n(\mathbf{r})} + V_{ext}(\mathbf{r}) \\ &= \frac{\delta T_s[n(\mathbf{r})]}{\delta n(\mathbf{r})} + V_{Hartree}(\mathbf{r}) + V_{XC}(\mathbf{r}) + V_{ext}(\mathbf{r}). \end{aligned} \quad (2.38)$$

The last three terms on the right-hand side of Equation 2.38 are the effective potential  $V_{eff}(\mathbf{r})$  in Equation 2.28. This is known as the Kohn–Sham potential and is defined as:

$$V_{eff}(\mathbf{r}) \stackrel{\text{def}}{=} V_{Hartree}(\mathbf{r}) + V_{XC}(\mathbf{r}) + V_{ext}(\mathbf{r}). \quad (2.39)$$

It is possible to calculate the exact ground state energy and density of the interacting system using Equations 2.29 and 2.33, if the exact correlation and exchange functional,  $E_{XC}$  were known. This is because all the terms in the equations are the exact and explicit functional of density. However, in practice, some approximations have to be made to calculate the  $V_{XC}$  and  $E_{XC}$ .

Unlike the Schrödinger equation (2.4), the Kohn–Sham eigenvalues of energy for Equation 2.28 have no physical meaning and are not representing energies. However, there is one exception [66] which is the occupied orbitals with the highest eigenvalue,  $\varepsilon_{max}^{KS}$ . This eigenvalue represents the chemical potential  $\mu$  and equals to the inverted ionisation energy [45]. The mathematical meaning of the eigenvalues is known as the Slater–Janak

theorem [69] within the Kohn–Sham formalism. This theorem states that the eigenvalue  $\varepsilon_i$  is the derivative of the total energy of the system with respect to the occupation of a state  $n_i$  [45]:

$$\varepsilon_i = \frac{\partial E}{\partial n_i} = \int \frac{\delta E}{\delta n(\mathbf{r})} \frac{\partial n(\mathbf{r})}{\partial n_i} d^3\mathbf{r}. \quad (2.40)$$

One of the limitations of Kohn–Sham density functional theory is the spin-restriction problem. Since the single electron Hamiltonian does not consider the spin of the electron, each energy eigenvalue is two-fold degenerate. This means each orbital can be combined with an  $\alpha$  or  $\beta$  spin function [54]. Notably, the orbitals are identical for both  $\alpha$  and  $\beta$  electrons and consequently the exact wave function will be spin restricted.

In this situation, each orbital  $\varphi_i$  can either be occupied by both  $\alpha$  and  $\beta$  electrons (doubly occupied) or either an  $\alpha$  or  $\beta$  electron (singly occupied). Consequently, for the ground state, the singly occupied orbitals can only occur once at the highest occupied molecular orbital. Thus, the singly occupied orbitals can only be occurring more than once if the highest occupied molecular orbital is degenerate [54, 70, 71].

### 2.2.5 Force Theorem

Once the ground state energy was calculated using the density functional theory, it is possible to calculate other properties of the system such as forces and stresses from the total energy. This can be carried out using force theorem that is commonly known as Hellmann–Feynman theorem. This theorem has been formulated separately by Güttinger [72], Pauli [73] and Hellmann [74]. However, in 1939, Feynman [75] explicitly pointed out that the force on a nucleus is given solely in terms of charge density and it is independent of the kinetic energy, exchange and correlation [45].

Consider a system with Hamiltonian  $\hat{H}(\lambda)$  that is depending on parameter  $\lambda$ , if  $|\psi(\lambda)\rangle$  is an eigenvector of  $\hat{H}(\lambda)$  with corresponding eigenvalue of  $E(\lambda)$ , then

$$\hat{H}(\lambda) |\psi(\lambda)\rangle = E(\lambda) |\psi(\lambda)\rangle; \quad (2.41)$$

with further assumption that  $|\psi(\lambda)\rangle$  is normalised such that

$$\langle\psi(\lambda)|\psi(\lambda)\rangle = 1, \quad (2.42)$$

the Hellman–Feynman theorem states that

$$\frac{\partial E}{\partial \lambda} = \left\langle \psi(\lambda) \left| \frac{\partial \hat{H}}{\partial \lambda} \right| \psi(\lambda) \right\rangle. \quad (2.43)$$

In other words the derivative of the total energy with respect to  $\lambda$  is equal to the derivative of the Hamiltonian with respect to  $\lambda$ . By associating the  $\lambda$  with the nuclear coordinates  $\mathbf{R}_I$ , the forces acting on the atom can be calculated as

$$\mathbf{F}_I = \frac{\partial E}{\partial \mathbf{R}_I} = \nabla_I \varepsilon(\mathbf{R}_I) = \left\langle \psi_0 \left| \nabla_I \hat{H}(\mathbf{R}_I) \right| \psi_0 \right\rangle. \quad (2.44)$$

Using this theorem one could show [45]

$$\mathbf{F}_I = \frac{\partial E}{\partial \mathbf{R}_I} = - \int n(\mathbf{r}) \frac{\partial V_{ext}(\mathbf{r})}{\partial \mathbf{R}_I} d^3\mathbf{r}' - \frac{\partial E_{II}}{\partial \mathbf{R}_I}, \quad (2.45)$$

which is known as the electrostatic theorem for the forces due to Feynman [45, 75, 76].

## 2.3 Exchange-Correlation Functionals

The key point of the Kohn-Sham ansatz was the separation that they made between the exchange–correlation energies ( $E_{xc}$ ) and the rest of the kinetic and internal energies. However, to use the Kohn–Sham practically, we must know the exchange and correlation which is yet to be found and may never be found in the form of a mathematical functional.

For a system with a sufficiently slowly varying density  $n(\mathbf{r})$  it can be shown that  $E_{xc}$  can be approximated as a nearly local functional of the density [45, 63, 68]:

$$E_{xc}[n] = \int n(\mathbf{r}) \epsilon_{xc}(n(\mathbf{r})) d^3\mathbf{r}, \quad (2.46)$$

where  $\epsilon_{xc}$  is the exchange and the correlation energy per electron of a uniform electron gas having a density of  $n$  [68]. This is the very basic and simple approximation that was originally proposed by Kohn and Sham in their paper and is known as the local density approximation (LDA). Consequently, the exchange–correlation potential  $V_{XC}$ , which is the functional derivative of  $E_{XC}$  can be written as [45]:

$$V_{xc}(\mathbf{r}) = \epsilon_{xc}(n(\mathbf{r})) + n(\mathbf{r}) \frac{\delta \epsilon_{xc}(n(\mathbf{r}))}{\delta n(\mathbf{r})}. \quad (2.47)$$

To date, there are hundreds of approximations for the exchange–correlation functional and the list is still growing; although they can be categorised into a few categories, based on the complexity and the technique. This classification was proposed by Perdew [77] as ‘Jacob’s ladder’ and is illustrated in Figure 2.2. The ladder starts from the Hartree approximation and goes to the dreaming destination of an exact exchange–correlation functional. Going up each rung of the ladder, the complexity of the functional technique increases and the assurance of the answer decreases. Based on the required accuracy and the specific needs or calculations, different functionals might be used to fulfil requirements with consideration of computational resources. However, at the present time, only the first two techniques are guaranteed as safe approximations [77]. These two techniques will be discussed in sections 2.3.1 and 2.3.2 in detail.

The generalised gradient approximation (GGA) technique, similar to LDA, is a local approximation but it also considers the gradient of the density  $\nabla n(\mathbf{r})$  at each point. Moving forward on the ladder, the meta-GGA group is very similar to the GGA category but it considers the second derivative of the electron density  $\nabla^2 n(\mathbf{r})$  as well. Moving further up, the hybrid-GGA and hybrid-meta-GGA techniques are mainly a combination of the previous techniques. For example PBE0 approximation is simply a mixture of the original PBE<sup>6</sup> approximation mixed with Hartree Fock exchange energy:

$$E_{XC}^{PBE0} = \frac{1}{4} E_X^{HF} + \frac{3}{4} E_X^{PBE} + E_C^{PBE}, \quad (2.48)$$

## Chemical Accuracy

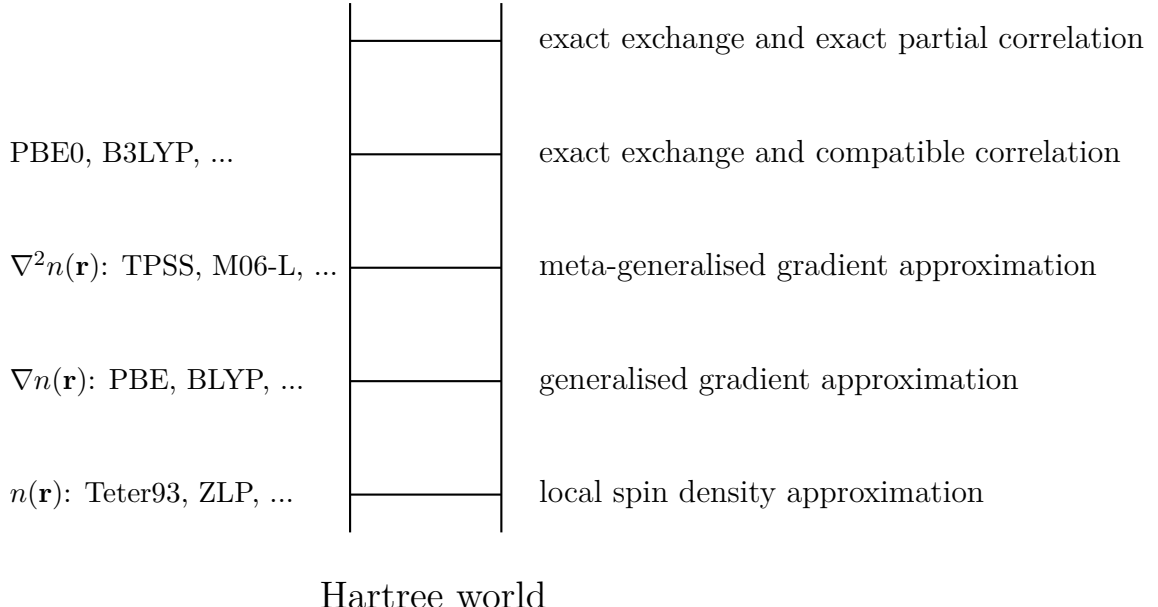


Figure 2.2: Jacob’s ladder of exchange–correlation functional approximations proposed by Perdew [77]. The types of approximation are listed on the right-hand side of the ladder and a few examples of each method are named on the left-hand side of the ladder.

where the  $E^{PBE}$  is the original PBE exchange–correlation functional [78]; and subscript  $X$  and  $C$  denote the exchange and correlation energies respectively. The  $E_X^{HF}$  is the Hartree-Fock exchange functional [79–81] that is defined as:

$$E_X^{HF} = -\frac{1}{2} \sum_i^{\text{occ.}} \sum_j^{\text{occ.}} \iint \psi_i^*(\mathbf{r}) \psi_j^*(\mathbf{r}') \frac{\tilde{e}^2}{|\mathbf{r} - \mathbf{r}'|} \psi_i(\mathbf{r}) \psi_j(\mathbf{r}') d^3\mathbf{r} d^3\mathbf{r}'. \quad (2.49)$$

Similarly, the very popular B3LYP<sup>7</sup> approximation is again a weighted mixture of the first two techniques [82–85]:

$$\begin{aligned} E_{XC}^{B3LYP} = & E_X^{LDA} + a_0 (E_X^{HF} - E_X^{LDA}) + a_x (E_X^{GGA} - E_X^{LDA}) + \\ & E_C^{LDA} + a_c (E_C^{GGA} - E_C^{LDA}) \end{aligned} \quad (2.50)$$

<sup>6</sup>PBE stands for Perdew, Burke and Ernzerhof approximation. See § 2.3.2 for details.

<sup>7</sup>B3LYP stands for Becke’s three-parameter, Lee-Yang-Parr approximation.

where  $a_0$ ,  $a_x$  and  $a_c$  are semi-empirical coefficients determined by curve fitting on experimental data with optimal values of 0.20, 0.72 and 0.81 respectively.

### 2.3.1 Local Density Approximation (LDA)

The local density approximation (LDA) or more generally, the local spin density approximation (LSDA) is the first, simplest, yet reasonably accurate, exchange–correlation functional that is still in use today. Kohn and Sham in their paper derived this approximation for homogeneous electron gas, but it is also applicable to solids; as in this context, solids can be considered as locally similar to homogeneous electron gas [68].

Starting from Equation 2.46, the  $\epsilon_{XC}$  functional can be divided into exchange and correlation components:

$$\begin{aligned} E_{xc}^{LDA}[n] &= \int n(\mathbf{r}) \epsilon_{xc}^{\text{hom}}(n(\mathbf{r})) d^3\mathbf{r} \\ &= \int n(\mathbf{r}) \epsilon_x^{\text{hom}}(n(\mathbf{r})) + \epsilon_c^{\text{hom}}(n(\mathbf{r})) d^3\mathbf{r}, \end{aligned} \quad (2.51)$$

where  $\epsilon_x^{\text{hom}}$  and  $\epsilon_c^{\text{hom}}$  correspond to exchange and correlation energies respectively. Now the exact value of the exchange part of the functional can be estimated using the Dirac formulation:

$$\epsilon_x[n] = -C_e n(\mathbf{r})^{1/3}, \quad (2.52)$$

where

$$C_e = \frac{3}{4} \left( \frac{3}{\pi} \right)^{1/3} \tilde{e}^2. \quad (2.53)$$

Consequently, the exchange energy  $E_x^{LDA}$  becomes [86]:

$$E_x^{LDA}[n] = -\frac{3}{4} \left( \frac{3}{\pi} \right)^{1/3} \tilde{e}^2 \int n(\mathbf{r})^{4/3} d^3\mathbf{r} \quad (2.54)$$

and the effective potential will be:

$$V_x^{LDA}(\mathbf{r}) = - \left( \frac{3}{\pi} n(\mathbf{r}) \right)^{1/3} \tilde{e}^2. \quad (2.55)$$

This is the same equation as the  $X\alpha$  formulation proposed by Slater in 1951 [80] with  $\alpha$  being set to 2/3 [47]:

$$v_{x\alpha}(\mathbf{r}) = -\frac{3}{2}\alpha \left(\frac{3}{\pi}n(\mathbf{r})\right)^{1/3} \tilde{e}^2. \quad (2.56)$$

In the original equation by Slater, the value of  $\alpha$  was set to 1; however, after more experiments it is now proven that for atoms and molecules, the optimum value for  $\alpha$  is about  $\sim 0.75$  [47, 87].

A similar principle applies to local spin density approximation. Equation 2.51 can be expanded to take into account the spin with the assumption of having the same density of opposite spins at all points in the space:

$$\begin{aligned} E_{xc}^{LSDA}[n^\uparrow, n^\downarrow] &= \int n(\mathbf{r}) \epsilon_{xc}^{\text{hom}}(n^\uparrow(\mathbf{r}), n^\downarrow(\mathbf{r})) d^3\mathbf{r} \\ &= \int n(\mathbf{r}) \epsilon_x^{\text{hom}}(n^\uparrow(\mathbf{r}), n^\downarrow(\mathbf{r})) + \epsilon_c^{\text{hom}}(n^\uparrow(\mathbf{r}), n^\downarrow(\mathbf{r})) d^3\mathbf{r}, \end{aligned} \quad (2.57)$$

where  $n^\uparrow(\mathbf{r})$  and  $n^\downarrow(\mathbf{r})$  are the collinear opposite spins namely known as spin-up and spin-down and the difference between these two spins is known as fractional spin polarisation of the system with  $n_e$  defined as total density:

$$\zeta(\mathbf{r}) = \frac{n^\uparrow(\mathbf{r}) - n^\downarrow(\mathbf{r})}{n_e(\mathbf{r})}. \quad (2.58)$$

In the case of the unpolarised homogeneous electron gas, there will be no exchange energy between the particles having opposite spin; therefore the total exchange energy will be:

$$E_x[n^\uparrow, n^\downarrow] = \frac{1}{2} (E_x[2n^\uparrow] + E_x[2n^\downarrow]). \quad (2.59)$$

Hence, by knowing the exchange energy of unpolarised homogeneous gas, we can write the total energy as:

$$E_x^{LSDA}[n^\uparrow, n^\downarrow] = -2^{1/3} \frac{3}{4} \left(\frac{3}{\pi}\right)^{1/3} \tilde{e}^2 \int n_\uparrow^{4/3}(\mathbf{r}) + n_\downarrow^{4/3}(\mathbf{r}) d^3\mathbf{r}. \quad (2.60)$$

In the case of relative polarisation ( $\zeta \neq 0$ ) Equation 2.60 will become [86]:

$$E_x^{LSDA}[n_e, \zeta] = \int \epsilon_x[n(\mathbf{r}), \zeta(\mathbf{r})] n_e(\mathbf{r}) d^3\mathbf{r} \quad (2.61)$$

where the exchange energy is given by:

$$\epsilon_x[n_e, \zeta] = -\frac{1}{2} \frac{3}{4} \left(\frac{3}{\pi}\right)^{1/3} \tilde{e}^2 n_e^{1/3}(\mathbf{r}) \left([1 + \zeta(\mathbf{r})]^{4/3} + [1 - \zeta(\mathbf{r})]^{4/3}\right). \quad (2.62)$$

Now replacing the total density  $n_e$  with  $r_s$ , which is defined as the radius of a sphere enclosing a single electron on average (i.e. the average distance between electrons) and is known as the Wigner–Seitz radius<sup>8</sup>, yields:

$$\epsilon_x^{LSDA}(r_s, \zeta) = \epsilon_x(r_s, \zeta = 0) + [\epsilon_x(r_s, \zeta = 1) - \epsilon_x(r_s, \zeta = 0)] f(\zeta), \quad (2.63)$$

where

$$\epsilon_x(r_s, \zeta = 0) = -\frac{3}{4\pi} \left(\frac{9\pi}{4}\right)^{1/3} \frac{1}{r_s} \frac{\tilde{e}^2}{a_0}, \quad (2.64)$$

$$\epsilon_x(r_s, \zeta = 1) = 2^{1/3} \epsilon_x(r_s, \zeta = 0), \quad (2.65)$$

and

$$f(\zeta) = \frac{(1 + \zeta)^{4/3} + (1 - \zeta)^{4/3} - 2}{2(2^{1/3} - 1)}. \quad (2.66)$$

Equation 2.63 to 2.66 provide exact analytical solutions for the exchange energy of the system. There is still no exact analytical solution available for the correlation energy. For many years no accurate approximate solution was available for the correlation energy, until Gell-Mann and Breuckner introduced their correction [88] in the parametrisation of the

---

<sup>8</sup>in the three-dimensional space, for a homogeneous system having  $N$  particles enclosed in a finite volume  $\Omega$ , with the particle density defined as  $n = \frac{N}{\Omega}$ , the Wigner–Seitz radius is defined as  $\frac{3}{4\pi} r_s^3 = \frac{N}{\Omega}$

or  $r_s = \left(\frac{3}{4\pi n}\right)^{1/3}$

<sup>9</sup> $a_0$  is the notation for Bohr radius (See Appendix A)

correlation energy previously carried out by Wigner [89], Macke [90] and Pines [91]. However, Gell-Mann's and Breuckner's work was only valid for very high density unpolarised systems. Their expression (in atomic units<sup>10</sup>) was defined as:

$$\begin{aligned}\epsilon_c &= \frac{2}{\pi^2} (1 - \ln 2) \ln r_s + C + \text{terms that vanish as } r_s \rightarrow 0 \\ &= A \ln r_s + C + \mathcal{O}(r_s),^{11}\end{aligned}\quad (2.67)$$

where  $C$  is a constant estimated approximately with a value of 0.158. The Gell-Mann and Breuckner formulation for  $A$  confirmed previous works, but they defined  $C$  as:

$$C = \frac{2}{\pi^2} (1 - \ln 2) \left\{ \ln \left[ \frac{4}{\pi} \left( \frac{4}{9\pi} \right)^{1/3} \right] - \frac{1}{2} + \langle \ln R \rangle_{Av} \right\} + \delta \quad (2.68)$$

where  $\delta = -0.0508$  and numerical integration results to a value of  $-0.551$  for  $\langle \ln R \rangle_{Av}$ . This yields to a considerably smaller  $C$  with the value of  $-0.096 \pm 0.002$ . For a partially polarised system, similar to the exchange energy defined in Equation 2.63, one could use:

$$\epsilon_c(r_s, \zeta) = \epsilon_c(r_s, \zeta = 0) + [(r_s, \zeta = 1) - (r_s, \zeta = 0)] f(\zeta). \quad (2.69)$$

Over the past years, different parametrisation for LSDA were proposed by various researchers and this led to several LSDA functionals. Perdew and Zunger [93] suggested four different sets of equations for Equation 2.69, for both high and low density systems. In their parametrisation the correlation energy of a high density ( $0 \leq r_s \leq 1$ ) unpolarised electron gas is described as:

$$\epsilon_c^{PZ}(r_s, \zeta = 0) = (0.0311 \ln r_s - 0.048 + 0.0020 r_s \ln r_s - 0.0116 r_s) \frac{\tilde{e}^2}{a_0}. \quad (2.70)$$

This is in a similar form to Equation 2.67. For fully polarised high density electron gas,

---

<sup>10</sup>The atomic units notation used hereafter refers to the Hartree atomic unit ( $\hbar = e = m_e = 1$ ) unless otherwise indicated.

<sup>11</sup>This is the Big O mathematical notation ( $\mathcal{O}(f^n)$ ) to denote the order of accuracy of a numerical method. For more details refer to § 20.1 of Advanced Engineering Mathematics (10<sup>th</sup> ed.) by Erwin Kreyszig [92].

they introduced different parameters into the same equation resulting in:

$$\epsilon_c^{PZ}(r_s, \zeta = 1) = (0.01555 \ln r_s - 0.0269 + 0.0007r_s \ln r_s - 0.0048r_s) \frac{\tilde{e}^2}{a_0}. \quad (2.71)$$

The two equations presented by Perdew and Zunger for low density ( $r_s \geq 1$ ) are different from high density, but these equations meet agreeably at  $r_s = 1$ . Their proposed equation for low density unpolarised electron gas was:

$$\epsilon_c^{PZ}(r_s, \zeta = 0) = \frac{0.1423}{1 + 1.0525\sqrt{r_s} + 0.3334r_s} \frac{\tilde{e}^2}{a_0}. \quad (2.72)$$

Similarly, for a fully polarised low density electron gas, a similar equation with different coefficients was proposed:

$$\epsilon_c^{PZ}(r_s, \zeta = 1) = \frac{0.0843}{1 + 1.3981\sqrt{r_s} + 0.2611r_s} \frac{\tilde{e}^2}{a_0}. \quad (2.73)$$

Vosko, Wilk and Nusair proposed rather a different approach [84] to Equation 2.69 which was:

$$\begin{aligned} \epsilon_c(r_s, \zeta) = & \epsilon_c(r_s, \zeta = 0) + \alpha_c(r_s) \frac{f(\zeta)}{f''(0)} (1 - \zeta^4) + \\ & [\epsilon_c(r_s, \zeta = 1) - \epsilon_c(r_s, \zeta = 0)] f(\zeta) \zeta^4. \end{aligned} \quad (2.74)$$

The  $\alpha_c$  and  $\epsilon_c$  are each calculated using:

$$\begin{aligned} & A \left\{ \ln \left( \frac{r_s}{r_s + B\sqrt{r_s} + C} \right) + D \arctan \left( \frac{E}{2\sqrt{r_s} + B} \right) \right. \\ & \left. + F \ln \left[ \frac{(\sqrt{r_s} + G)^2}{r_s + B\sqrt{r_s} + C} \right] \right\} \frac{\tilde{e}^2}{a_0}, \end{aligned} \quad (2.75)$$

with the dimensionless parameters listed in Table 2.1; note that  $(\tilde{e}^2/a_0)$  gives the units of energy density. Similar approaches to Equation 2.74 were also suggested by Perdew and Wang [94]; one of the accurate and popular LDA approaches today. Most of the analytical

solutions to correlation energy to date are mathematical interpolations of values calculated using the quantum Monte Carlo simulation. However, to the author's knowledge, there is still no 'exact' analytical solution for correlation energy in LDA functionals.

Despite the simplicity of the LDA approximation, it often estimates the exchange-correlation energy surprisingly well. Likewise, it usually gives very good results for systems with slowly varying charge densities [95]. However there are well-known drawbacks in LDA calculation; such as under-estimation of the energy gap in semiconductor materials or over-estimation of binding and atomisation energy [77, 95]. Furthermore, the LDA technique does not account for strong correlation energies due to the electrons in  $d$  orbitals in some transition metals. Many papers have pointed out the weakness in exchange-correlation energy calculation due to the large error in approximation of exchange energy [47] and the need for alternative solutions. These weaknesses in LDA calculations led to the development of more reliable and complex XC functionals, such as generalised gradient approximations that also take into account the gradient corrections.

### 2.3.2 Generalised Gradient Approximation (GGA)

As discussed in § 2.3.1, the LDA approximation assumes that the system is homogeneous, which in most cases is not a realistic assumption. The use of the gradient of density

Table 2.1: The parameters used in Equation 2.75 to calculate exchange energy using the method proposed by Vosko, Wilk and Nusair. Each column of the table provides the parameters required to calculate that particular equation. These parameters are dimensionless constants.

Parameter	$\alpha_c(r_s)$	$\epsilon_c(r_s, \zeta = 0)$	$\epsilon_c(r_s, \zeta = 1)$
$A$	-0.0169	0.0311	0.01555
$B$	1.1311	3.7274	7.0604
$C$	13.0045	12.9352	18.0578
$D$	0.3177	1.2474	3.3767
$E$	7.1231	6.1520	4.7309
$F$	0.0004	0.0312	0.1446
$G$	0.0048	0.1050	0.3250

$|\nabla n|^2$  was originally suggested by Kohn and Sham in their paper [68] and later on was implemented by Herman et al. [96]. The technique was known as gradient expansion approximation (GEA); it was not very successful in improving the LDA technique and in some cases, it was even worse than LDA. This was mainly due to the large value of the gradient in reality, which causes the expansion to break down [45]. To overcome this issue, Perdew introduced a real-space cut-off to the gradient expansion technique [97] that led to a new accurate density functional for the exchange energy. However, the level of the complexity added to the functional was too much and made it very difficult to use the technique for practical applications [98]. One year later, Perdew and Wang modified and simplified the original complicated functional so that it was possible to use it more practically in the self-consistent density functional calculations [98]. They named their simplified functional as ‘Generalised’ gradient approximation (GGA) and it was generally defined as [98]:

$$\begin{aligned} E_{\text{xc}}^{\text{GGA}}[n^\uparrow, n^\downarrow] &= \int n(\mathbf{r}) \epsilon_{\text{xc}}(n^\uparrow, n^\downarrow, \nabla_{n^\uparrow}, \nabla_{n^\downarrow}) d^3\mathbf{r} \\ &= \int n(\mathbf{r}) \epsilon_{\text{x}}^{\text{hom}}[n(\mathbf{r})] f_{\text{xc}}^{\text{GGA}}(n^\uparrow, n^\downarrow, \nabla_{n^\uparrow}, \nabla_{n^\downarrow}) d^3\mathbf{r}, \end{aligned} \quad (2.76)$$

where the  $f^{\text{GGA}}$  is a dimensionless enhancement factor.

Similar to the LDA approximation, we can separate the exchange and the correlation parts of the GGA approximation. For the exchange part of the energy we only have to consider the spin unpolarised case as we can use the spin scaling relation (Equation 2.59) [45]. Hence we can write:

$$E_{\text{x}}^{\text{GGA}}[n] = -C_e \int n(\mathbf{r})^{4/3} f_{\text{x}}(s) d^3\mathbf{r}, \quad (2.77)$$

where  $C_e$  is defined in Equation 2.53;  $s$  is the dimensionless  $i$ th order reduced density gradient defined as:

$$s_i = \frac{|\nabla^i n|}{(2k_F)^i n}, \quad (2.78)$$

and  $k_F$  is the radius of the Fermi sphere

$$k_F = \left(3\pi^2 n\right)^{1/3} = \left(\frac{9\pi}{4}\right)^{1/3} \frac{1}{r_s}. \quad (2.79)$$

The original enhancement factor proposed by Perdew and Wang in 1986 was defined as:

$$f_x(s) = \left( \frac{1 + 0.0864s_1^2}{m} + bs_1^4 + cs_1^6 \right)^m, \quad (2.80)$$

where  $m = 1/15$ ;  $b = 14$ ; and  $c = 0.2$ . However, several other formulations have been suggested for the  $f_x$  enhancement factor over the years. One of the first formulations that is still in use in the Hybrid XC functions is Becke's formulation published in 1988 [99]; it was an enhancement to the  $X\alpha\beta$  technique proposed by Herman et al. [96, 100] and is known as B88 [101]:

$$f_x^{\text{GGA-B88}} \stackrel{\text{def}}{=} \frac{1 + s \cdot a_2 \cdot \sinh^{-1}(s \cdot a_1) + a^3 \cdot s^2}{1 + s \cdot a_2 \cdot \sinh^{-1}(s \cdot a_1)}, \quad (2.81)$$

where  $a_1 = (48\pi^2)^{1/3}$ ;  $a_2 = 6 \cdot a_1$  and

$$a_3 = \frac{a_1^2 \cdot \beta}{2^{1/3} \cdot C_e}. \quad (2.82)$$

The  $C_e$  is defined in Equation 2.53 and  $\beta$  is a parameter obtained using the least-squares fitting on the empirical data. Becke found this parameter to be 0.0042 in atomic units (a.u.) [99].

Another popular enhancement factor is the proposed formulation by Perdew and Wang in 1991 [102, 103] that is identical to Becke's 88 functional with two extra Gaussian and  $s^4$  terms [104, 105]:

$$f_x^{\text{GGA-PW91}} \stackrel{\text{def}}{=} \frac{1 + s \cdot a_2 \cdot \sinh^{-1}(s \cdot a_1) + (a_3 + a_4 \cdot e^{-100 \cdot s^2})}{1 + s \cdot a_2 \cdot \sinh^{-1}(s \cdot a_1) + a_5 \cdot s^4}, \quad (2.83)$$

where  $a_4 = \frac{10}{81} - a_3$  and

$$a_5 = \frac{a_1^4 \times 10^{-6}}{2^{1/3} \cdot C_e}. \quad (2.84)$$

However, for small values of  $s$ , the functional can be simplified [104] to:

$$f_x^{\text{GGA-PW91}} \stackrel{\text{def}}{=} 1 + \frac{10 \cdot s^2}{81} + \mathcal{O}(s^4). \quad (2.85)$$

The Perdew and Wang formulation was again refined [106] in 1996 by Perdew, Burke and Ernzerhof [78, 107]; which yielded one of the most popular formulations in recent studies. This XC functional is known as PBE and is defined as:

$$f_x^{\text{GGA-PBE}} \stackrel{\text{def}}{=} 1 + \kappa - \frac{\kappa}{1 + \frac{\mu}{\kappa} \cdot s^2}, \quad (2.86)$$

where  $\kappa = 0.804$  and  $\mu = 0.21951$ . The value of  $\kappa$  is chosen in such a manner to allow the maximum local Lieb-Oxford bound [78, 107, 108] and the value of  $\mu$  is set to recover the linear response of uniform density; hence the effective gradient coefficient for exchange cancels that for correlation [106, 107].

All these proposed formulations produce very similar values for the small range of  $s$  (see Figure 2.3). Indeed, most of the real systems fall in a range between zero and three [45]. Even so, the big difference at long range values, caused by different formulations, produce dissimilar XC-energies for van der Waals interactions and dispersion forces [109, 110]; which require significant work and improvement in the future. Figure 2.4 illustrates this difference in the long range. The majority of the other formulations suggested for  $f_x^{\text{GGA}}$  fall between PBE and B88 approximations [45].

The calculation of the correlation energy  $f_c^{\text{GGA}}(s)$  is not as simple as the exchange energy to write it as a functional. However, the correlation has much less contribution to the total energy than the exchange contributes. The magnitude of the correlation energy is inversely proportional to the density gradient and it will tend to zero as the  $s$  increases [45].

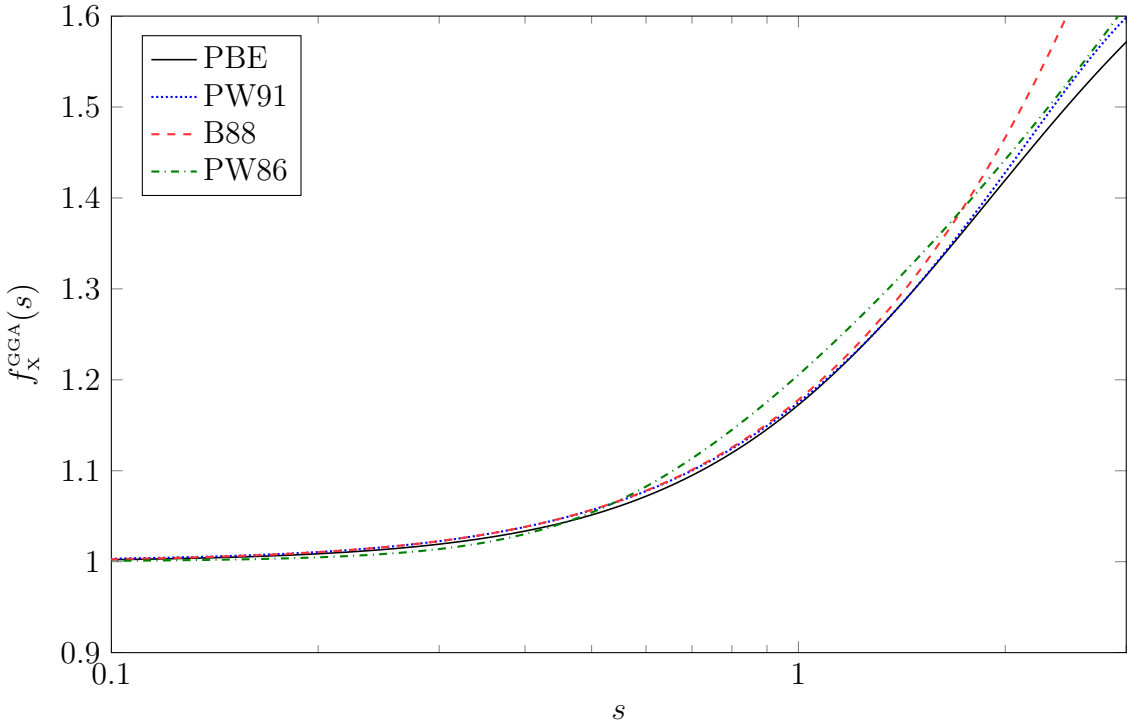


Figure 2.3: Comparison of the three most popular generalised gradient approximation (GGA) functional values in the short range with the original Perdew and Wang 1986 formulation. The extended responses of these functions ( $s > 3$ ) are illustrated in Figure 2.4.

One of the simplest and yet accurate explicit correlation functionals that is in use today is the PBE correlation functional; which is defined [78, 104] as:

$$E_C^{\text{GGA-PBE}} \left[ n^\uparrow, n^\downarrow \right] \stackrel{\text{def}}{=} \int n \left[ \epsilon_C^{\text{hom}}(r_s, \zeta) + H(r_s, \zeta, t) \right] d^3\mathbf{r}, \quad (2.87)$$

where  $t$  is a dimensionless density gradient:

$$t \stackrel{\text{def}}{=} \frac{|\nabla n|}{2\phi k_s n}. \quad (2.88)$$

Here,  $\phi$  is the spin scaling factor:

$$\phi = \phi(\zeta) = \frac{[(1 + \zeta)^{2/3} + (1 - \zeta)^{2/3}]}{2}, \quad (2.89)$$

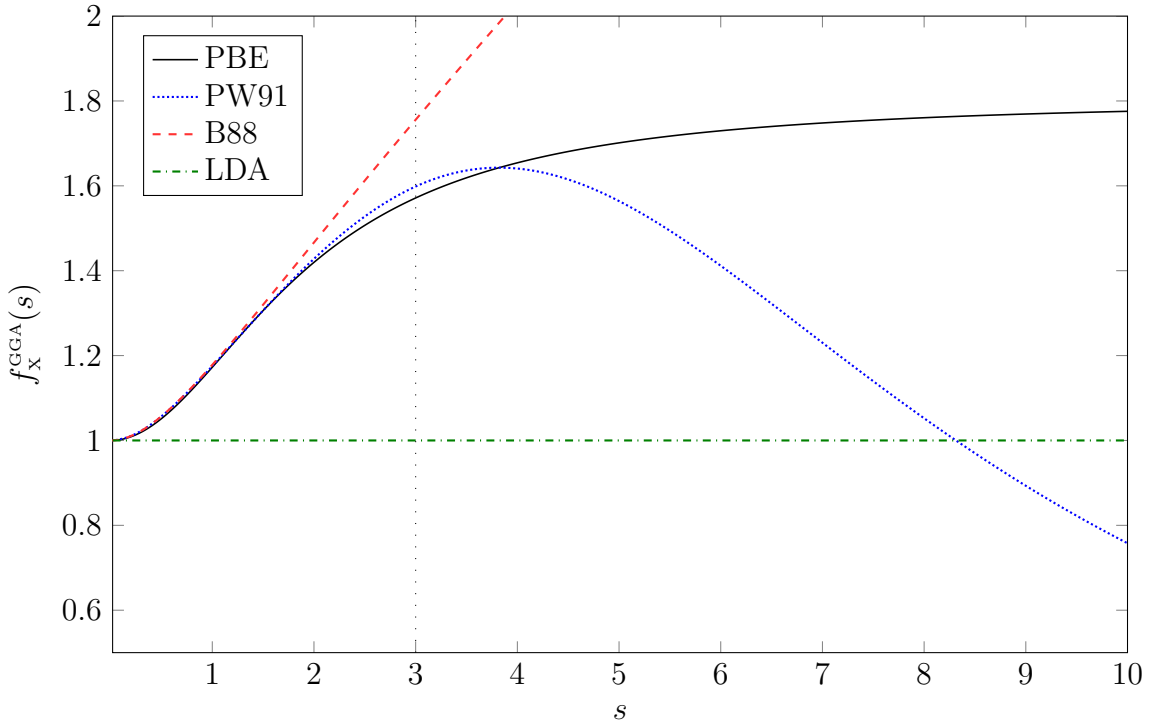


Figure 2.4: Comparison of the three most popular generalised gradient approximation (GGA) functional values in the long range. Please refer to Figure 2.3 for the short range comparison up to the loosely dotted line ( $s = 3$ ).

and  $k_s$  is the Thomas–Fermi screening wave number:

$$k_s = \sqrt{\frac{4k_F}{\pi a_0}}. \quad (2.90)$$

The  $H$  function is the gradient contribution and is defined as:

$$H \stackrel{\text{def}}{=} \left(\frac{\tilde{e}^2}{a_0}\right) \gamma \phi^3 \times \ln \left[ 1 + \frac{\beta}{\gamma} t^2 \left( \frac{1 + At^2}{1 + At^2 + A^2 t^4} \right) \right], \quad (2.91)$$

where  $\beta \simeq 0.066725$ ;  $\gamma$  is a weak function of relative spin polarisation  $\zeta$  and can be replaced by its value when  $\zeta = 0$  which yields:

$$\gamma = \frac{(1 - \ln 2)}{\pi^2}, \quad (2.92)$$

and

$$A = \frac{\beta}{\gamma} \times \left[ \exp \left( \frac{-\epsilon_c^{\text{hom}} a_0}{\gamma \phi^3 e^2} \right) - 1 \right]^{-1}. \quad (2.93)$$

Many other quantitative derivations exist for the correlation functional, but they all rely on experimental data and the parameters are chosen to fit molecular data [45]. The fact that different XC functionals produce dissimilar results shows a lack of knowledge to explain the exchange and correlation energies using a universal functional. Although a functional might produce a correct result for certain materials and molecules it might fail to describe other materials. The choice of the correct XC functional is very important based on the type of material and it has to be evaluated in well-known situations before being used to predict unknown situations.

In general, the GGA technique has advantages over the LDA due to the consideration of the density gradient. For example, the atomisation energy calculated using the GGA is on average about four times more accurate than the same calculation made using the LDA (see appendix B for details). However, neither of these techniques is accurate and universal. As shown in Figure 2.4, even different descriptions within the same technique produce various results and can lead to a wrong result if they are chosen without thought and investigation for their suitability in a particular calculation.

## 2.4 Pseudo-potentials

Another approximation that is usually done in the DFT calculations is based on the effects of the other existing atoms on the core electrons, which is negligible. In the context of condensed matter physics, to solve the Schrödinger equation for a given space aggregated with atoms, the space can be divided into two distinct regions with considerably different properties. The first area is the “core region” in the vicinity of the nuclei of the atom which is occupied with tightly bonded core electrons that do not respond very much to the presence of any other atom. The remaining area is mainly occupied with the bonding or valence electrons that are less attracted to the core potential (compared to the core

electrons) and are more responsive to the neighbouring atoms [111].

The idea of pseudo-potentials was initially introduced by Fermi in 1934 [59]; however, the pseudo-potential approach, as it is known today, is based on the idea from Phillips and Kleinman cancellation theorem in 1959 [112]. The main idea of pseudo-potentials comes from the orthogonalised plane wave (OPW) technique for crystals, introduced by Conyers Herring in 1940 [113]; which replaces the core electrons with an effective repulsive potential that acts on the valence electrons. This will significantly decrease the number of electrons in the system and leads to a faster and less expensive computation. Herring suggested that wave functions and energy values of an electron in a crystalline structure can be calculated by solving a characteristic polynomial (secular equation) with valence wave functions simply be a set of Plane Waves (PW) orthogonal to all of the core wave functions  $|\psi_c\rangle$  [111]:

$$|\text{OPW}(\mathbf{k})\rangle = N \left[ |\text{PW}(\mathbf{k})\rangle - \sum_c^{\text{core}} |\psi_c\rangle \langle \psi_c| \text{PW}(\mathbf{k}) \right], \quad (2.94)$$

where  $\mathbf{k}$  is the Bloch wave-vector and  $N$  is the Gram–Schmidt normalisation constant given by [114]:

$$N = \left[ 1 - \sum_c \langle \psi_c | \text{PW} \rangle \langle \text{PW} | \psi_c \rangle \right]^{-1/2}. \quad (2.95)$$

However, as the size of the region over which the PW's are normalised increases, the overlap  $\langle \psi_c | \text{PW} \rangle$  decreases. This yields to a unity  $N$  as the normalisation size becomes infinity.

To smooth out the valence states in the core region, first the orthogonal ripples of the core wave functions are subtracted from the valence states, which leads to the creation of the smooth pseudo-states  $|\phi_v\rangle$  as:

$$|\psi_v\rangle = |\phi_v\rangle + \sum_c |\psi_c\rangle \alpha_c. \quad (2.96)$$

Then if the inner product of Equation 2.96 is taken with only one of the core states  $|\psi_i\rangle$ ,

this yields:

$$\langle \psi_i | \psi_v \rangle = \langle \psi_i | \phi_v \rangle + \sum_c \alpha_c \langle \psi_i | \psi_c \rangle = 0, \quad (2.97)$$

owing to the orthogonality of the core and valence wave functions (i.e.  $\forall c : \langle \psi_c | \psi_v \rangle = 0$ ). Equation 2.96 can then be rewritten using the terms on the right-hand side of Equation 2.97 as:

$$|\psi_v\rangle = |\phi_v\rangle - \sum_c |\psi_c\rangle \langle \psi_c | \phi_v \rangle. \quad (2.98)$$

By substituting the obtained equation into the time-independent Schrödinger equation (2.4):

$$\hat{\mathcal{H}} |\phi_v\rangle - \sum_c E_c |\psi_c\rangle \langle \psi_c | \phi_v \rangle = E |\phi_v\rangle - E \sum_c |\psi_c\rangle \langle \psi_c | \phi_v \rangle, \quad (2.99)$$

or

$$\hat{\mathcal{H}} |\phi_v\rangle + \sum_c (E - E_c) |\psi_c\rangle \langle \psi_c | \phi_v \rangle = E |\phi_v\rangle. \quad (2.100)$$

The obtained result in Equation 2.100 is satisfying the Schrödinger equation with an additional non-local energy-dependent potential  $\hat{V}_{nl}$  defined as:

$$\hat{V}_{nl} = \sum_c^{\text{core}} (E - E_c) |\phi_c\rangle \langle \phi_c|. \quad (2.101)$$

## 2.5 Projector Augmented Waves (PAW)

Due to the requirement of orthogonality, in the nuclei region that contains non-zero states, the wave functions contain very sharp features; while further away from nuclei, the only non-zero states are the valence states and this leads to much smoother wave functions. To be able to correctly describe the high feature oscillatory behaviour in the core region, a very dense grid or a large set of plane waves is required. Figure 2.6 illustrates the all electron wave function for the molybdenum atom.

As described earlier in § 2.4, one solution is use of pseudo-potentials to replace the nuclei and core states with an effective smooth potential and solve the Kohn-Sham equation

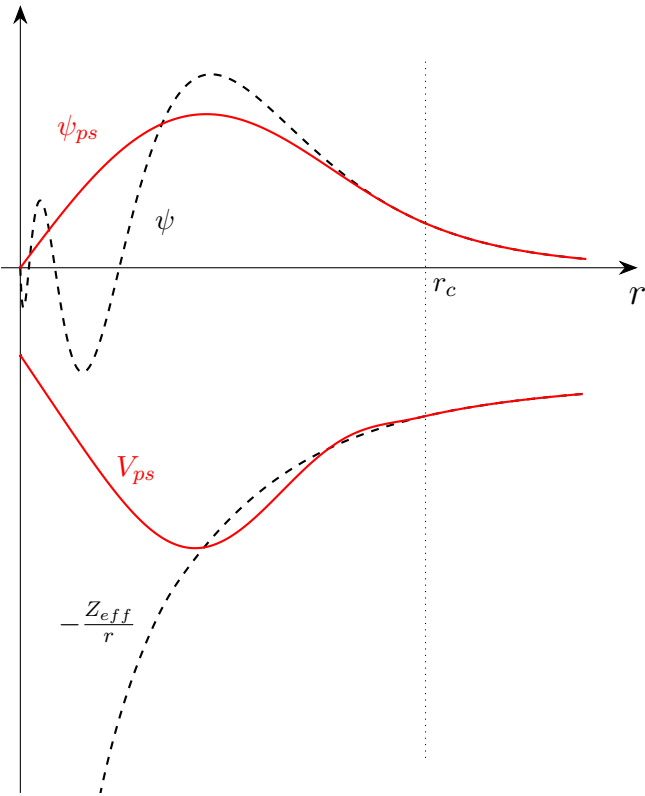


Figure 2.5: The comparison between all-electron calculation of the potential and the equivalent pseudo-potential. The  $r_c$  denotes the core radius where the value of the pseudo-potential matches the all-electron potential. Here, the pseudo-potential and the wave function are showing the 4s orbital of a molybdenum atom with arbitrary unit. The potential waveforms have been shifted down with respect to the x-axis for better illustration.

solely for the valence electrons. One drawback for this technique is the loss of information on complete wave functions near the nuclei. In addition, this approximation has to be tested for reliable results with known realistic systems.

Another approach to this problem is using the augmented plane wave (APW) method. In this technique, the space around the atom is divided by an augmented sphere centred at the atom. Inside the sphere the wave functions are treated as atom-like partial waves and some envelop functions are defined outside the sphere that is known as the bonding region [115]. A more general approach is the projector augmented wave method (PAW) [116] that was introduced in 1994 by Peter E. Blöchl as a generalised approach that reformulates orthogonalised plane waves (OPW).

In this technique that generalises both the augmented plane wave method and pseudo-

potential method, to address the problem of describing oscillatory behaviour of wave functions near the nuclei, an auxiliary smooth wave function  $|\tilde{\psi}_n\rangle$  with a linear transformation  $\mathcal{T}$  transforms to all electron Kohn-Sham single particle wave function  $|\psi_n\rangle$  such that

$$|\psi_n\rangle = \mathcal{T}|\tilde{\psi}_n\rangle. \quad (2.102)$$

This linear transformation is expected to be unity except inside the augmented sphere that is atom-centred. Now, expanding each smooth function  $|\tilde{\psi}_n\rangle$  in partial waves  $m$  within a defined atom-centred sphere, yields<sup>12</sup>

$$|\tilde{\psi}\rangle = \sum_m c_m |\tilde{\psi}_m\rangle, \quad (2.103)$$

with the corresponding all-electron function

$$|\psi\rangle = \mathcal{T}|\tilde{\psi}_n\rangle = \sum_m c_m |\psi_m\rangle. \quad (2.104)$$

Using Equation 2.103 and 2.104 the complete wave function can be written as

$$|\psi\rangle = |\tilde{\psi}_n\rangle + \sum_m c_m (|\psi_m\rangle - |\tilde{\psi}_m\rangle). \quad (2.105)$$

To satisfy the linearity requirements of the transformation  $\mathcal{T}$ , the coefficients  $c_m$  have to be given by a projection in the sphere

$$c_m = \langle \tilde{p}_m | \tilde{\psi} \rangle, \quad (2.106)$$

for some sets of projection operators  $\tilde{p}$  [45]. Thus, if the projection operators satisfy the bi-orthogonality condition  $\langle \tilde{p}_m | \tilde{\psi}_{m'} \rangle = \delta_{mm'}$ , then the expansion  $\sum_m |\tilde{\psi}_m\rangle \langle \tilde{p}_m | \tilde{\psi} \rangle$  of the smooth function  $\tilde{\psi}$  will be equal to itself. Figure 2.7 illustrates molybdenum 4s wave function  $\psi$  and the correspondent smooth wave function  $\tilde{\psi}$  and projection  $\tilde{p}$ . Similar

---

<sup>12</sup>The subscript  $n$  has been omitted for better readability.

to the pseudo-potentials, there are many possible projectors of  $\tilde{\psi}$  for  $\tilde{p}$  being related to pseudo-potential projection operators, but unlike pseudo-potentials the transformation  $\mathcal{T}$  uses the complete all-electron wave function

$$\mathcal{T} = 1 + \sum_m \left( |\psi_m\rangle - |\tilde{\psi}_m\rangle \right) |\tilde{p}_m\rangle. \quad (2.107)$$

For any operator  $\hat{A}$  in the all electron problem, the transformed operator  $\tilde{A}$  can be introduced to operate on the smooth part of the wave function such that

$$\tilde{A} = \mathcal{T}^\dagger \hat{A} \mathcal{T} = \hat{A} + \sum_{mm'} |\tilde{p}_m\rangle \left( \langle \psi_m | \hat{A} | \psi_{m'} \rangle - \langle \tilde{\psi}_m | \hat{A} | \tilde{\psi}_{m'} \rangle \right) \langle \tilde{p}_{m'}|. \quad (2.108)$$

Furthermore, any operator if form of

$$\hat{B} - \sum_{mm'} |\tilde{p}_m\rangle \langle \tilde{\psi}_m | \hat{B} | \tilde{\psi}_{m'} \rangle \langle \tilde{p}_{m'}| \quad (2.109)$$

can be added to the right-hand side of Equation 2.108 without changing the expectation values<sup>13</sup>.

## 2.6 GW Approximation

As mentioned previously in § 2.2.4, the eigenvalues of the KS equation have no physical meaning apart from the highest occupied energy which corresponds to the ionisation energy [118]. Nevertheless, these values are usually interpreted as one-particle excitation energy, but there is no theoretical justification for this interpretation [119]. Although these energies are usually in good agreement with experimental results, there are exceptions where these values do not match. An example of this disagreement is the underestimation of the band gap in insulators and semiconductors by 30–100%; this is well-known as the “band-gap” problem [119]. Thus, an appropriate technique has to be used to calculate

---

<sup>13</sup>For further readings one could refer to [116], [45] and [115].

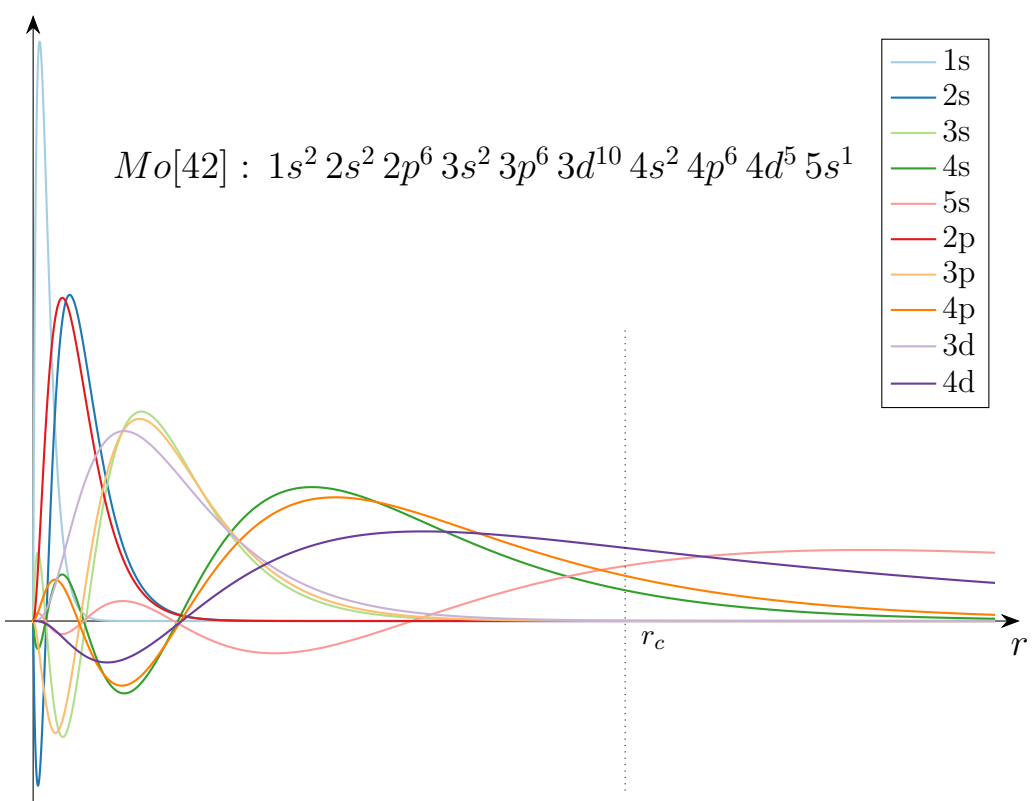


Figure 2.6: All electron wave functions of molybdenum atom calculated using Atom-Paw [117]. The  $r_c$  indicates the cut-off region which separates the core region from the valence region.

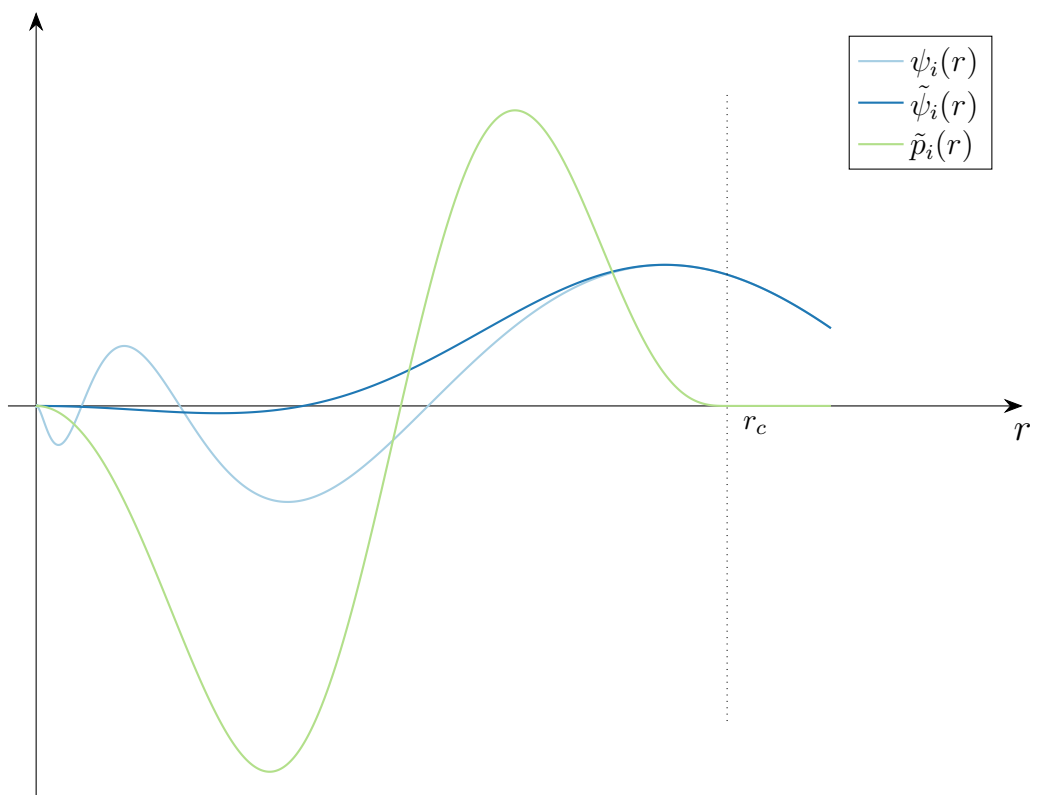


Figure 2.7: All electron wave function, the soft PAW wave function and the PAW projection for 4s orbital of molybdenum atom calculated using AtomPaw [117]. The  $r_c$  indicates the cut-off region which separates the core region from the valence region.

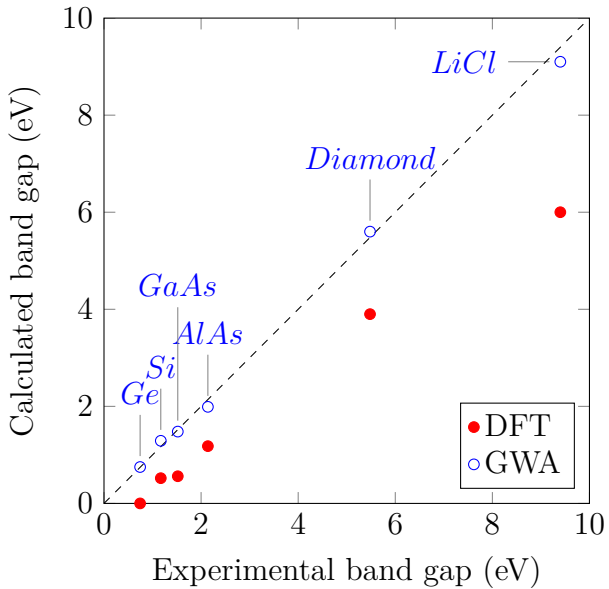


Figure 2.8: The band gap calculated using local density approximation within density functional theory [119] and Green’s function approximation [124, 125] compared to an experimentally measured band gap [126].

the excitation energies.

One alternative approach to calculate the one-particle excitation or quasi-particle energies [120, 121] is using Green’s function theory [122, 123], also known as the GW approximation. This name comes from the equation itself that is a product of the Green function,  $G$  and the screened Coulomb interaction,  $W$ . Figure 2.8 illustrates the corrected band gap error using the GW approximation compared to the density functional theory.

### 2.6.1 Brief History

In fact, the GW approximation is older than the DFT and is primarily based on the Hartree-Fock approximation, but it also takes screened Coulomb interaction energy into account. The very first attempts on GW calculation for homogeneous electron gas were done by Quinn and Ferrell in 1958 [127], followed by DuBois in 1959 [128, 129]. However their techniques were only applicable to the energy states near the Fermi level and small Wigner–Seitz radius. Yet, the first complete calculation of self-energy was done several years later by Hedin in 1965 [130]; where in his paper he stated that “*there is not much*

*new in principle in this paper”* [130].

After Hedin’s work, several extensive calculations were made on self-energy of the electron gas by Rice [131] and Lundqvist [132–134]. However, because of the expensive computation required by the technique, it was not applied to any real material until the mid-eighties when Hybertsen and Louie presented their calculations using the GW approximation on semiconductors [119, 124, 135, 136]. Similar results were also published by Godby, Sham and Schlüter on the same calculations [125, 137–139], with their results confirming those published by Hybertsen and Louie. These reported results and the good agreement with the experimental data on the silicon attracted the attention of scientists who used the GW technique on more complicated systems such as transition metals and their compounds [140]. In particular, the various GW approximations performed by Mahan, Sernelius and Frota in the late eighties [141] and early nineties [142] are notable. This group accomplished an extensive study on electron gas self energy using different forms of GW approximations and the importance of vertex corrections [143]. Their results showed a very small difference between the analytical and numerical values [144].

### 2.6.2 Concepts

The proof and theory behind GW calculation is significantly long and one can find more details from many quantum theory textbooks such as [145] by Abrikosov et al., [146] by Mahan or [86] by Sólyom; however, here, the basic idea behind this theory is briefly described.

Firstly, a solid is considered and an electron is injected into it as illustrated in Figure 2.9. This procedure can be done by a technique such as inverse photoemission. After this injection, the solid takes up a state that is not an eigenstate of the system; however, if it is projected into the quantum numbers, the spectral distribution of the power will usually show peaks at recognised energies [119]. These induced quasi-particle excitation energies in the solid can be described by a Schrödinger-like equation with an extra term,

$\Sigma$ , as [119, 130]

$$\left( -\frac{\hbar^2}{2m_e} \nabla^2 + V_{Hartree}(\mathbf{r}) \right) \psi_i(\mathbf{r}) + \int \Sigma(\mathbf{r}, \mathbf{r}'; \varepsilon_i) \psi_i(\mathbf{r}') d^3 \mathbf{r}' = \varepsilon_i \psi_i(\mathbf{r}), \quad (2.110)$$

where  $\Sigma$  is an energy dependent non-local potential also known as self-energy.

Calculation of  $\Sigma$  however, is very difficult and it is not straight forward even for homogeneous electron gas, as it contains the effect of exchange and correlation energies between the quasi-particles.

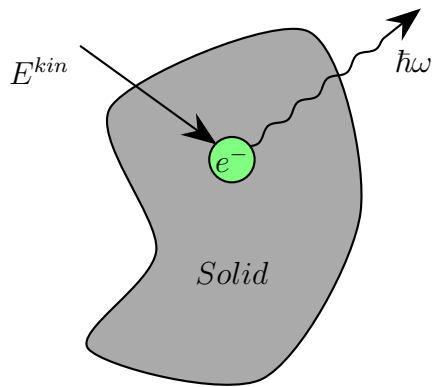


Figure 2.9: Inverse photo-emission spectroscopy by injecting an electron to the solid

Using Hedin's approach [130], the self-energy can be expanded as screened Coulomb interaction and keeping the lowest term only, yields the approximation that is known as GW [119, 147]:

$$\Sigma^{GW}(\mathbf{r}, \mathbf{r}'; \omega) = \frac{i}{2\pi} \int e^{-i\delta\omega'} G(\mathbf{r}, \mathbf{r}'; \omega + \omega') W(\mathbf{r}, \mathbf{r}'; \omega') d\omega', \quad (2.111)$$

where  $\delta$  is an infinitesimal positive time;  $G$  is the one-particle Green's function<sup>14</sup> that in Lehmann representation is

$$G(\mathbf{r}, \mathbf{r}', \omega) = \sum_i \frac{f_i(\mathbf{r}) f_i^*(\mathbf{r}')}{\omega - E_i}, \quad (2.112)$$

---

<sup>14</sup>For further details and derivations refer to §3 of [148].

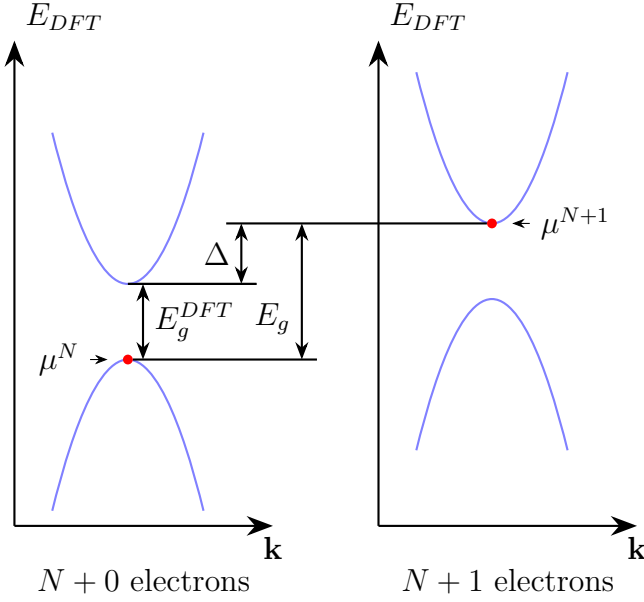


Figure 2.10: Illustration of the error in band gap calculated using the DFT and the actual quasi-particle band gap calculated by adding an electron to the solid [139]. This error can be as big as 100% of the band gap.

with  $f_i(\mathbf{r})$  or Lehmann amplitudes<sup>15</sup> defined as

$$f_i(\mathbf{r}) \stackrel{\text{def}}{=} \begin{cases} \langle N0|\psi(\mathbf{r}\mathbf{0})|N+1i\rangle, & \text{when } E_i > \mu \\ \langle N-1i|\psi(\mathbf{r}\mathbf{0})|N0\rangle, & \text{when } E_i < \mu, \end{cases} \quad (2.113a)$$

and  $E_i$  or the quasi-particle energies defined as

$$E_i(\mathbf{r}) \stackrel{\text{def}}{=} \begin{cases} E_{N+1i} - E_{N0} - i\eta^{16}, & \text{when } E_i > \mu \\ E_{N0} - E_{N-1i} + i\eta, & \text{when } E_i < \mu. \end{cases} \quad (2.113b)$$

The  $W$  is the screened Coulomb interaction defined as:

$$W(\mathbf{r}, \mathbf{r}'; \omega) = \int \epsilon^{-1}(\mathbf{r}, \mathbf{r}''; \omega) v(\mathbf{r}' - \mathbf{r}''; \omega) d^3\mathbf{r}''. \quad (2.114)$$

Here,  $v$  is the bare Coulomb interaction and  $\epsilon^{-1}$  is the inverse dielectric matrix that can

---

<sup>15</sup>Lehmann amplitudes are also known as Dyson orbital or quasiparticle wave functions.

<sup>16</sup> $\eta$  is an infinitesimally positive number ( $\eta = 0^+$ ).

be estimated by a suitable technique such as random phase approximation (RPA) [147, 149–151]. Ideally, the one-particle Green’s function has to be estimated self-consistently through the Dyson equation [152–154]; however, during 1990s, in nearly all cases, the non-interaction Green’s function at LDA level was only considered [147].

## 2.7 Bloch Functions and Wannier Functions

In the previous sections, it was shown that the ground state of a many-body system can be determined using wave functions of a non-interacting auxiliary system. In the solids with a crystalline structure however, the electrons will face a periodic potential due to the nature of crystalline structures that are built of a periodic pattern. The wave functions in these systems are mainly described in terms of Bloch wave functions or orbitals [155]. The Bloch theorem [156] states that the solution to the Schrödinger equation applied to a periodic system is in a special form of:

$$\psi_{n,\mathbf{k}}(\mathbf{r}) = u_{n,\mathbf{k}}(\mathbf{r}) \cdot \exp(i\mathbf{k} \cdot \mathbf{r}), \quad (2.115)$$

where  $u_{\mathbf{k}}(\mathbf{r})$  is a periodic function with a periodicity of the crystal translation distance; and  $\exp(i\mathbf{k} \cdot \mathbf{r})$  is a plane wave that is also known as an envelope function. Here, the  $\mathbf{k}$  denotes the crystal wave vector that has a direct relation with crystal momentum with a factor of reduced Planck’s constant; and  $n$  subscription refers to the energy band index. Although this technique is the main choice for calculating the electronic structure and ground state in solids, other representations of wave function such as Wannier functions [157,158] (WF) are also possible and may be considered [155].

The Wannier functions are simply the localised linear combination or superposition of all the Bloch functions of a given band in the Brillouin zone [159]. This means unlike Bloch functions that are the eigenstates of the Hamiltonian and localised in energy, the Wannier functions are not the solutions to the Hamiltonian and are localised in space [155]. These functions are generally obtained by a set of unitary transformations of the Bloch functions

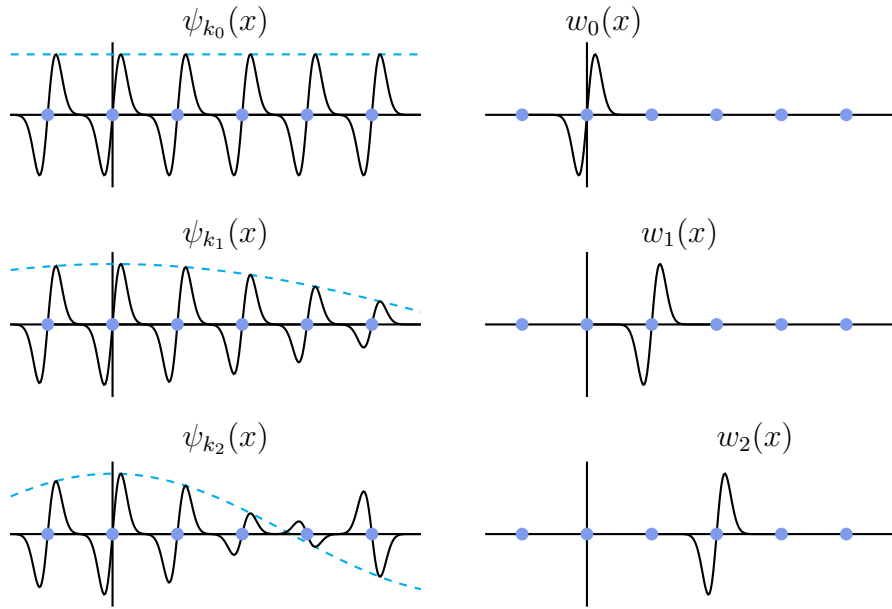


Figure 2.11: A set of Bloch functions in real space (the real part only) for an arbitrary one-dimensional system with  $p$ -like orbitals on the left and transformed Wannier functions of that system on the right. The filled circles are representing the atoms and the dashed line is the Bloch envelope function of  $e^{ikr}$ . The x and y units are arbitrary [155].

introduced by Gregory Wannier in 1937 [157, 158].

Originally, the Wannier functions were introduced in solid state theory for post processing and further characterisation of solids, such as calculation of the effective mass of electrons. However, the complete calculation of the Wannier functions was not carried out often [155]. Nonetheless, moving across to computational chemistry, a field with many overlapping interests, this was totally different and knowledge of localised molecular orbitals (LMOs) [160–164] in molecules, which are akin to Wannier functions, was greatly emphasised to provide an insight into the nature of bondings in the material.

To construct the Wannier functions, we start with superimposing all the Bloch functions for a specific band in the Brillouin zone. Thus, we can write:

$$w_0(\mathbf{r}) = \frac{\Omega_{cell}}{(2\pi)^3} \int_{BZ} \psi_{n,\mathbf{k}}(\mathbf{r}) d^3\mathbf{k}, \quad (2.116)$$

where  $\Omega_{cell}$  is the volume of the primitive cell in real space; and  $BZ$  denotes the Brillouin zone. The multiplicand before integration normalises the integral over the Brillouin

zone [155, 165]. Equation 2.116 has no phase and can be interpreted as the Wannier function localised in the home unit cell, as illustrated in the top right section of Figure 2.11. To make Equation 2.116 more general, it can be modified to contain a phase factor ‘ $\exp(-i\mathbf{k} \cdot \mathbf{R})$ ’ within, as:

$$|\mathbf{R}n\rangle = \frac{\Omega_{cell}}{(2\pi)^3} \int_{BZ} \exp(-i\mathbf{k} \cdot \mathbf{R}) |\psi_{n,\mathbf{k}}\rangle d^3\mathbf{k}, \quad (2.117)$$

so other Wannier functions can be constructed [155, 157]. Here,  $\mathbf{R}$  is a lattice vector in real space; and  $|\mathbf{R}n\rangle$  is the bra-ket notation of the Wannier function  $w_{n\mathbf{R}}$  which corresponds to the energy band  $n$  and cell  $\mathbf{R}$ . With the phase factor included in the equation, it becomes like a Fourier transform and it is possible to translate the  $|\mathbf{R}n\rangle$  to  $|\mathbf{R}'n\rangle$  by the lattice vector  $\mathbf{R}' \stackrel{\text{def}}{=} \mathbf{R} - \mathbf{R}'$  in real space [166]. Consequently, the inverse transform can be written as:

$$|\psi_{n,\mathbf{k}}\rangle = \sum_{\mathbf{R}} \exp(-i\mathbf{k} \cdot \mathbf{R}) |\mathbf{R}n\rangle. \quad (2.118)$$

This simply means that the same information provided by the Bloch functions also comes from Wannier functions and the Wannier functions are localised. Therefore, it is possible to construct any Bloch wave function on the left-hand side of Figure 2.11 by superimposing the Wannier functions on the right, if the correct phase is chosen.

The main challenge to construct Wannier functions in realistic calculations is their non-uniqueness and dealing with degeneracies among the Bloch states, which is very difficult [167]. These obstacles have been overcome by Marzari, Vanderbilt and Souza [165, 167] by the development of a practical technique for extracting “maximally localized” Wannier functions from both ‘isolated’<sup>17</sup> group of bands [165] and ‘entangled’<sup>18</sup> bands [167].

---

<sup>17</sup>Isolated means group of bands that may become degenerate with one another at certain points in the Brillouin zone, but separated from all other bands by finite gaps throughout the entire Brillouin zone. A good example of these bands can be the set of valence bands of an insulator [167].

<sup>18</sup>An example of entangled bands is the  $d$  bands of a transition-metal that are hybridized with  $s$  band which consecutively is attached to higher bands [167].

## 2.8 Summary

In this chapter, the common technique to calculate the band structure of many-body systems was discussed and the weakness of this technique was highlighted; this was followed by a possible solution to resolve this weakness. Density functional theory is the most common technique used in solid state physics and has been improved significantly over the past years. In principle this is an exact calculation; however, the solution to exchange and correlation energies between particles is yet to be found and up to now, still approximation through various techniques is being used to estimate this value. Although the results calculated using the DFT are in-line with experimental measurements, this technique suffers from under-estimation of the minimum band gap in semiconductors and insulators. One solution to this problem is to use a more appropriate technique such as GW approximation, to correct this under-estimation of the band gap by expecting very expensive computation.

Wannier functions are another expansion to the density functional approximation; to get an insight into the nature of energy bands and can be utilised as informative tools in band gap engineering to understand the significance of semiconductor atomic bonding structure in the band gap. However, the proper selection of the Wannier functions is a big challenge and can be very difficult in the context of solid state physics and crystalline structures.

In the next chapter the basic electronic properties and band structure of the material that we have used in this research, which is known as molybdenum disulphide, will be explored using the techniques covered in this chapter.

*“You can never solve a problem on the level  
on which it was created.”*

— Albert Einstein

# Chapter 3

## Molybdenum Disulphide Material

### 3.1 MoS<sub>2</sub> Physical Properties

#### 3.1.1 Chemical Family

Molybdenum disulphide is an inorganic mineral known as molybdenite. It is a grey and silvery crystalline material as shown in Figure 3.1, which belongs to a well-known chemical group called ‘transition-metal dichalcogenides’. There are about 60 known compounds in this group with an MX<sub>2</sub> empirical formula [168, 169], where M is a transition metal such as molybdenum or tungsten and X is a chalcogen such as sulphur or selenium.

Molybdenum disulphide, being very similar to other layered materials such as graphite, consists of strong covalent bounded S–Mo–S layers stacked on top of each other with weak Van-der-Waals forces between the layers. The electrical band gap in this material is indirect and therefore is not a good candidate for photo-luminescence applications [170]; however, it also has a direct band gap. The indirect band gap is from the highest point of the valence band positioned at the  $\Gamma$  point in high symmetry, to the lowest point of the conductance band placed half way between the  $\Gamma$  and the K points of high symmetry [169]. The indirect and direct band gap have been experimentally measured to be about 1.29 eV and 1.9 eV respectively [170].



Figure 3.1: A large sample of MoS<sub>2</sub> with an approximate size of  $15 \times 20\text{ mm}$  [36].

### 3.1.2 Crystallography

Each ‘S–Mo–S’ layer of molybdenum disulphide is formed of three sub-layers. These sub-layers make a sandwich with molybdenum atoms in the middle and sulphur atoms on the top and bottom. Figure 3.2 (a) illustrates this layered structure. Molybdenum disulphide has polymorphism ability and is a poly-type structured material. Molybdenum disulphide is known to have three different crystalline structures consisting of 2-hexagonal symmetry ( $2H$ ) with 2 sandwich layers in the unit cell, 3-rhombohedral symmetry ( $3R$ ) with three sandwich layers in the unit cell and 1-tetragonal symmetry ( $1T$ ) with only one sandwich layer in the unit cell. The bulk form of MoS<sub>2</sub> can also have a mixture of both  $2H$  and  $3R$  combined. The sandwich of S–Mo–S itself can take two different phases; either as a trigonal prism or octahedral symmetry, as it is shown in Figure 3.2 (b).

The  $2H$  and  $3R$  variation of the MoS<sub>2</sub> are usually made of a trigonal prism; while the  $1T$  variation can be created by having only one layer of an octahedral phase in a unit cell. Figure 3.2 (c) illustrates the unit cell for the  $2H$  and  $3R$  variation of MoS<sub>2</sub>.

The  $1T$ -MoS<sub>2</sub> has a very similar structure to tantalum sulphide ( $1T$ -TaS<sub>2</sub>) and it is known as cadmium iodide ( $CdI_2$ ) structure which belongs to the crystallography symmetry group  $P\bar{3}m1$  ( $D_{3d}^3$ ) [171]. Although the  $D_{3d}^3$  symmetry group is a trigonal group, the Bravais lattice is hexagonal [171]. However,  $1T$ -MoS<sub>2</sub> is observed to have certain irregularities that have to be accounted for and one could use a symmetry space group such as  $C2/m$  ( $C_{2h}^3$ ) to model the  $1T$ -MoS<sub>2</sub> structure. The  $2H$ -MoS<sub>2</sub> belongs to  $P6_3/mmc$  ( $D_{6h}^4$ )

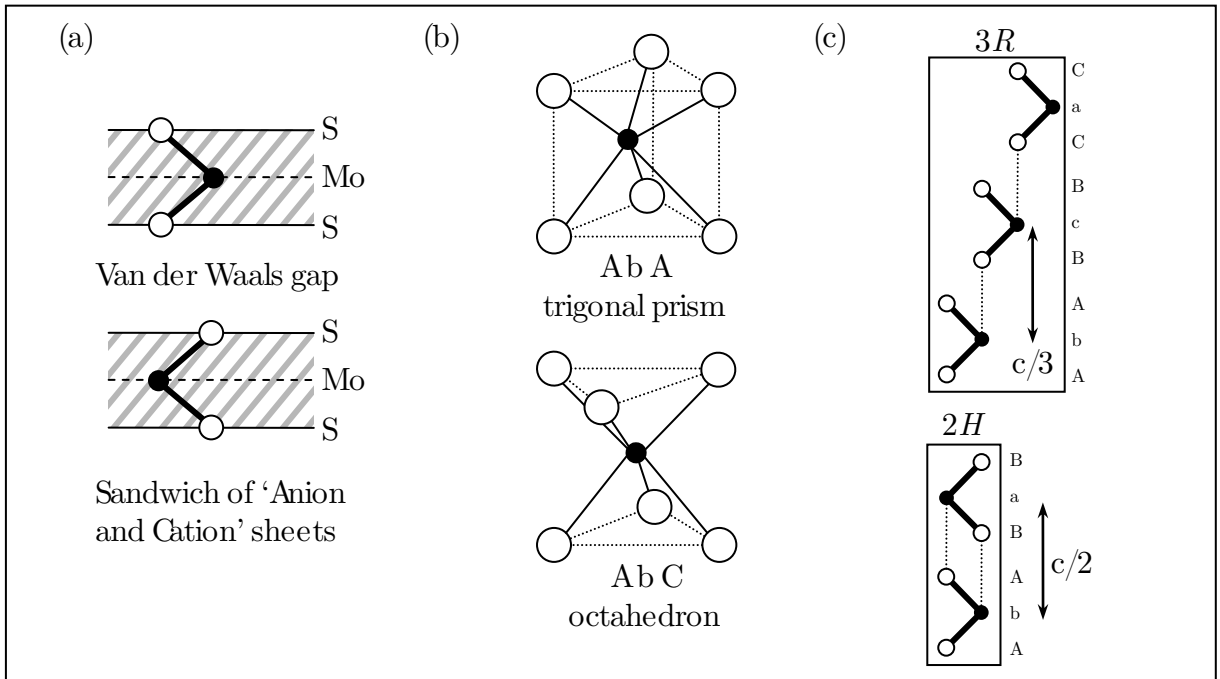


Figure 3.2: Crystalline structure of molybdenum disulphide: (a) the  $[11\bar{2}0]$  section of stacked MoS<sub>2</sub> sandwich layers; (b) two possible atomic structures of MoS<sub>2</sub> in three-dimensions and (c) the  $[11\bar{2}0]$  section of the 2H and 3R stacking unit cell. The small filled circles are representing the molybdenum atoms and medium white circles are sulphur atoms.

space and 3R-MoS<sub>2</sub> belongs to the  $R3m$  ( $C_{3v}^5$ ) space group [172, 173]. However, the two variations of 1T-MoS<sub>2</sub> and 3R-MoS<sub>2</sub> are known to have metastable structures [174, 175] and may change their phase to the more stable 2H-MoS<sub>2</sub> structure [175, 176]. The  $11\bar{2}0$  sections<sup>1</sup> of these two structures are visualised in Figure 3.2 (c).

On average, about 80% of molybdenum disulphide occurrences are of the 2H-MoS<sub>2</sub> type; while only 3% are 3R-MoS<sub>2</sub> and the rest are mainly a mixture of these two types [168, 177]. This makes the 2H-MoS<sub>2</sub> dominant among other types of MoS<sub>2</sub> crystals due to the stability of this structure. Moreover, the 1T variant of MoS<sub>2</sub> has metallic properties [171, 176] and is not semiconducting; hence the 2H-MoS<sub>2</sub> atomic structure was chosen for studying and modelling of the MoS<sub>2</sub> structure.

<sup>1</sup> $11\bar{2}0$  is a plane in Miller-Bravais (4 axis) notation which is based on Miller indices [178] but as  $[h k i l]$  where  $i \stackrel{\text{def}}{=} -(h + k)$  that is particularly useful for hexagonal and rhombohedral structures. More details are available in chapter 3 of ref [179].

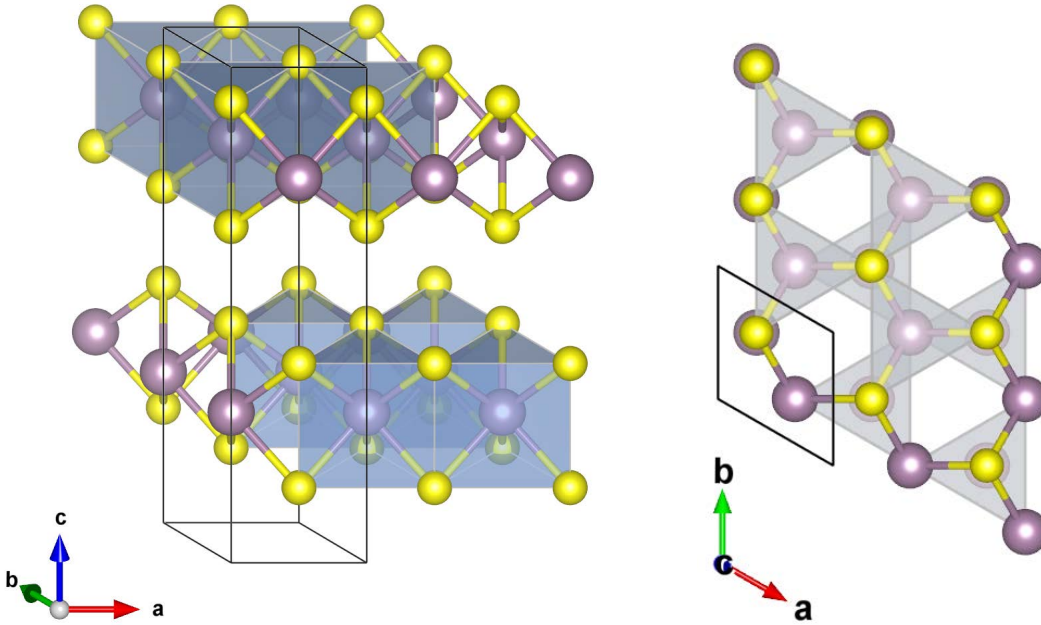


Figure 3.3: The unit cell of bulk 2H-MoS<sub>2</sub> shown with black lines and the compasses on the side of the illustrations show the direction of the translation vectors  $\vec{a}$ ,  $\vec{b}$  and  $\vec{c}$ . The large purple atoms are molybdenum and the smaller yellow atoms are the sulphur atoms.

### 3.1.3 Atomic Unit Cell

Molybdenum disulphide has a hexagonal lattice structure with three, six or nine atoms in the unit cell. This is similar to graphene's structure; however, MoS<sub>2</sub> layers are quasi-two-dimensional as the atoms do not lie on the same plane. Figure 3.3 shows the unit cell for 2H-MoS<sub>2</sub>. For the purpose of illustration and visualisation of the atomic data and the calculated results, a 3D-visualisation software called “Visualisation for Electronic and STructural Analysis (VESTA)” published by JP-Minerals has been used [180].

The unit cell is defined using six parameters consisting of three translation vectors  $\vec{a}$ ,  $\vec{b}$  and  $\vec{c}$ , which are analogous to x, y and z directions in Cartesian and three angles between these three vectors. The angles are defined as alpha ( $\alpha$ ) between the  $\vec{b}$  and  $\vec{c}$  vectors; beta ( $\beta$ ) between the  $\vec{a}$  and  $\vec{c}$  vectors; and gamma ( $\gamma$ ) between the  $\vec{a}$  and  $\vec{b}$  vectors. For both  $R3m$  and  $P6_3/mmc$  structures, the alpha, beta and gamma angles are 90, 90 and 120 degrees respectively. The gamma angle being 120 degrees makes the coordination more suitable for hexagonal structures. To translate the real space primitive cell into the

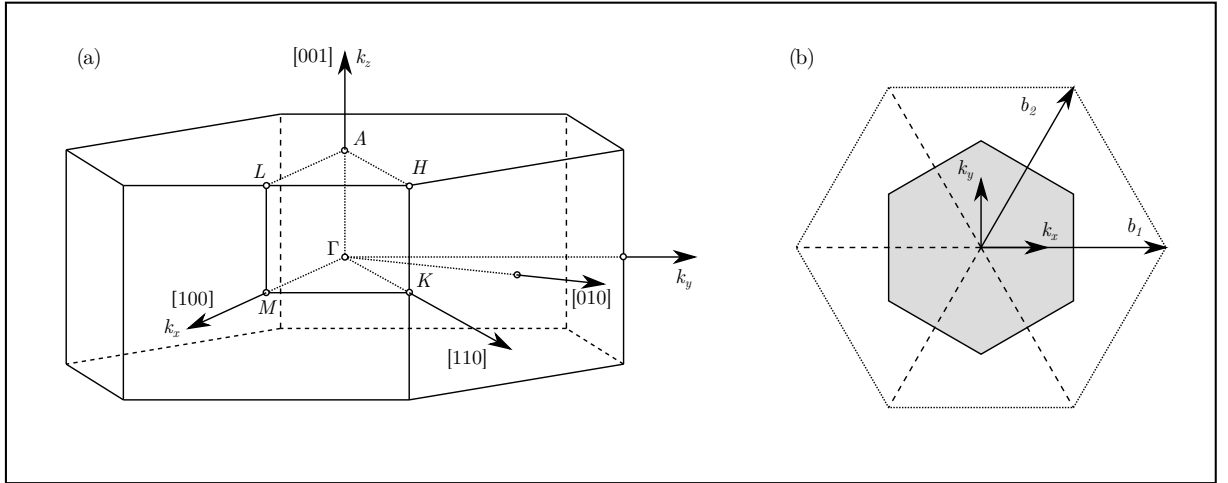


Figure 3.4: The symmetry points of the irreducible wedge of Brillouin zone (a) and the first Brillouin zone (b) of MoS<sub>2</sub> [181]

Cartesian coordinates, the transformation matrix

$$R = \begin{pmatrix} 1 & 0 & 0 \\ -1/2 & \sqrt{3}/2 & 0 \\ 0 & 0 & 1 \end{pmatrix}, \quad (3.1)$$

can be used. Similarly, to transfer the coordinates into the reciprocal space the coordinates will be multiplied by

$$G = R^{-T} = \begin{pmatrix} 1 & \frac{\sqrt{3}}{3} & 0 \\ 0 & \frac{2\sqrt{3}}{3} & 0 \\ 0 & 0 & 1 \end{pmatrix}. \quad (3.2)$$

In the case of *R*3*m* the lattice parameters have been measured to be 3.163 angstroms (Å) and 18.37 Å for vectors  $\vec{a}$  and  $\vec{c}$  respectively. Similarly for *P*6<sub>3</sub>/*mmc*, these parameters are  $\vec{a} = 3.161$  Å and  $\vec{c} = 12.295$  Å [172]. In both cases, the length of vector  $\vec{b}$  is the same as vector  $\vec{a}$ . A more-recently published work suggested another set of numbers which are ( $\vec{a}=3.166$  Å,  $\vec{c}=18.41$  Å) and ( $\vec{a}=3.1602$  Å,  $\vec{c}=12.294$  Å) for *R*3*m* and *P*6<sub>3</sub>/*mmc* respectively [168].

The correct *P*6<sub>3</sub>/*mmc* structure contains 4 twofold and 2 fourfold positions into which

Table 3.1: Special symmetry points of the irreducible wedge of the first Brillouin zone of MoS<sub>2</sub> quoted in reduced coordinates.

Point	$\vec{a}$	$\vec{b}$	$\vec{c}$	Point	$\vec{a}$	$\vec{b}$	$\vec{c}$
$\Gamma$	0	0	0	A	0	0	1/2
M	1/2	0	0	L	1/2	0	1/2
K	1/3	1/3	0	H	1/3	1/3	1/2

Mo and S atoms can be translated and arranged; but in the literature, several known crystallography reference books such as [182–185] contain a wrong translation that will cause incorrect inter-atomic distances [168] and extra care has to be taken in the creation of the unit cell and translation of the atoms. With the correct translation, the unit cell can be made by one of each of the Mo and S atoms positioned at (1/3, 2/3, 1/4) and (1/3, 2/3, 5/8) respectively [186]. These coordinates are presented as reduced-coordinates which are relative to the translation vectors of the unit cell in each direction and more convenient to use.

The first Brillouin zone [156] of the 2H-MoS<sub>2</sub> is hexagonal and is illustrated in Figure 3.4 [181] along with the irreducible wedge of the Brillouin zone and its symmetry points. These symmetry points are named conventionally and the reduced coordinates of these points are tabulated in Table 3.1 [187].

### 3.1.4 Stability

Molybdenum disulphide compound is chemically inactive and in the absence of other elements i.e. in the vacuum, remains stable up to 1100 degrees Celsius (°C) [24] and can endure a temperature of 1203 °C before breaking into molybdenum sulphide (Mo<sub>2</sub>S<sub>3</sub>) [188]. However, with the presence of oxygen, MoS<sub>2</sub> is thermally stable only up to 315 °C before oxidisation [189]; it will then break into molybdenum trioxide (MoO<sub>3</sub>). Most solvents are unable to dissolve the MoS<sub>2</sub> apart from very strong oxidising reagents such as nitrohydrochloric acid<sup>2</sup> that can oxidise and dissolve the MoS<sub>2</sub> crystals [190, 191].

---

<sup>2</sup>nitrohydrochloric acid is also known as Aqua Regina (Latin, =royal water) and is obtained by 1:3 mixture of nitric acid and hydrochloric acid (HNO<sub>3</sub>+3HCl).

Most of the layered materials that can be used as a lubricant are required to absorb vapour molecules to weaken the Van-der-Waals force between their layers [192, 193]; while MoS<sub>2</sub> does not require this absorption. Molybdenum disulphide has a very small friction coefficient of 0.1 [194] and has a unique interlayer interaction compared to other layered materials, as the Van-der-Waals force between the layers is exceptionally small [195–198].

### 3.1.5 Usage and Fabrication

Molybdenum disulphide is widely used as a ‘dry’ lubricant and in particular in the anode of lithium-ion batteries [199]. The lubrication property of MoS<sub>2</sub> is unique and it has always been considered for extreme conditions like vacuum environments and spacecraft applications [196, 198].

Molybdenum disulphide is also a strong candidate for photovoltaic and photo-catalytic applications due to the strong absorption in the solar spectrum region [200]. Recent studies show that molybdenum disulphide nano-films (single planar atomic layer) have a different electronic band structure and luminescence properties compared to bulk MoS<sub>2</sub> [35, 200]. Depending on the size and the type of atoms on the edge of the produced film, this material can shows magnetic behaviours and a different energy band gap [200, 201].

The MoS<sub>2</sub> crystals can be either extracted from molybdenite ore deposit or be synthesised artificially. One method to grow MoS<sub>2</sub> crystals is using chemical vapour transport technique where a mixture of molybdenum, sulphur and a halogen is annealed at a high temperature for several days [202–204]. Different halogens such as iodine and chlorine can be used to create 2*H* and 3*R* crystals of MoS<sub>2</sub> respectively [191]. Other synthesis techniques used are direct sulphidisation of molybdenum atoms [190, 205], or using an intermediate step by creating a metastable molybdenum compound and transforming of the created compound into MoS<sub>2</sub> crystals under high pressure and high temperature [206–209].

The weakly coupled layers of molybdenum disulphide can be separated to create a thin film on single layered MoS<sub>2</sub> by micro-exfoliation on a quartz, silicon or silicon dioxide SiO<sub>2</sub> substrate [35]. Using chemical and electrochemical techniques [210], it is possible

to produce a variety of nano structured MoS<sub>2</sub> which have very interesting properties and potential applications in electronic devices.

## 3.2 MoS<sub>2</sub> Simulation Tools

Up to now, there are more than 80 implementations of the first principle calculations available under various terms of use and licences. Among these implementations,a few of them have become more popular due to the ease of use or the implemented features. Vienna Ab-initio Simulation Package (VASP) [211–214], Spanish Initiative for Electronic Simulations with Thousands of Atoms (SIESTA) [215], Spartan by Wavefunction Inc. [216], Quantum ESPRESSO [217] and CASTEP [218] are a few of these implementations. However, many of these software packages are available commercially and the details of the implementation and techniques may not be accessible. A list of these software packages with their features and abilities is available in [219]. Table 3.2 provides the accuracy of some of these codes compared to all-electron calculations.

The presented results in this research have been obtained through the code name ABINIT [220–223], a common project of the Université Catholique de Louvain, Corning Incorporated, and other contributors<sup>3</sup>, developed under the terms of the GNU General Public License (GPL) Version 3 of Free Software Foundation, Incorporation. This code is mainly implemented using FORTRAN90 language and is provided as a source code.

Apart from being open source and having access to the source code, one of the advantages of ABINIT compared to the other available codes, is the modular format of the application<sup>4</sup>, with each module being developed and tested separately [227–241].

The ABINIT code used in this research was the released version 6.6 (7<sup>th</sup> February 2011) and was compiled using Intel Fortran Compiler (ifort) version 13.0 using Intel Mathematics

---

<sup>3</sup>Four other institutions have significantly contributed to the ABINIT effort: the Université de Liège, the Commissariat à l’Energie Atomique, Mitsubishi Chemical Corp. and the Ecole Polytechnique Palaiseau.

<sup>4</sup>Code name CASTEP is also modular and is available under a free of charge license to all UK academic research group [218].

Table 3.2: The accuracy of some of the popular DFT codes compared to all-electron calculation. Here, the  $\Delta_{err}$  is the average error with respect to all-electron methods expressed in mili-electron volts per atom. This calculation was carried out by Lejaeghere et al. [224] and for a breakdown of these values one could refer to their original publication [224].

Code Name	Method	Year	$\Delta_{err}$
ABINIT	JTH01	2013	1.1
ABINIT	JTH02	2014	0.6
CASTEP	Vdb	1998	6.5
CASTEP	OTFG7	2013	2.5
CASTEP	OTFG9	2015	0.7
GPAW [225, 226]	GPAW06	2010	3.6
GPAW	GPAW09	2012	1.6
Quantum ESPRESSO	PSlib031	2013	1.7
Quantum ESPRESSO	PSlib100	2013	1.0
VASP	VASP2007	2007	2.0
VASP	VASP2012	2012	0.8
VASP	VASPGW2015	2015	0.6

Kernel Library (MKL) version 11.0 on an Intel Xeon processor cluster (HPC) running Red Hat Enterprise Linux (RHEL6). The reliability of the compiled code was evaluated using more than 500 benchmarked tests in well-known situations.

The norm-conserving pseudo-potentials used in the calculations were Troullier-Martins [242] types and are generated using fhi98PP [231, 243] code as well as semi-core Hartwigsen-Goedecker-Hutter (HGH) [244] and ONCV pseudo-potentials [245]. In the case of PAW pseudo-potentials generated using AtomPaw [117] were used and the results have been tested [246] using a Murnaghan equation of state [247] and Morse potential [248].

For the calculation of the Wannier functions, the maximally-localised Wannier functions (MLWFs) technique proposed by Marzari and Vanderbilt [155, 165, 167, 249] implemented as Wannier90 [250] code has been used.

For the visualisation of the atomic structures, calculation results and volumetric three-dimensional data, the Visualisation for Electronic and STructural Analysis (VESTA) [180] application by JP-Minerals has been used. Other post processing techniques such as the

calculation of the effective mass or projected density of states (DOS) was implemented by the author using C++, Python and MATLAB.

### 3.3 MoS<sub>2</sub> as Bulk

Although many DFT implementations are available to use and the number of people using these modelling tools is considerably increasing, it has to be kept in mind that these implementations do not necessarily produce correct answers and many factors have to be taken into account to perform a realistic simulation. Using these tools without considering all the factors that are usually set as “default” can cause the computer to behave as “Garbage in, Garbage out” [251] and the model does not explain the system properly.

#### 3.3.1 Convergence Study

The unit cell of the bulk 2H-MoS<sub>2</sub> was initially defined using parameters obtained from [172] which are listed in Table 3.3. After creation of the unit cell, two important parameters have to be studied; the number of sampling  $k$  points in the reciprocal space and the kinetic energy cut-off value that controls the number of plane waves at a given point.

The reciprocal  $k$ -meshing was done using the Monkhorst-Pack method [252] as illustrated in Figure 3.5, with an initial value of  $1 \times 1 \times 1$  (i.e. single  $k$  point) located at  $\Gamma$  and increased to reach the convergence. The used convergence criterion was the variation in total energy of the unit cell between each iteration; while the other parameters were kept constant. The total energy of 2H-MoS<sub>2</sub> is calculated using Teter Pade parametrization [253] of the local density approximation with Hartwigsen-Goedecker-Hutter (HGH) pseudo-potentials [244] and tabulated in Table E.1 of Appendix E. The calculation of total energy was considered as converged after having an energy variation smaller than 1  $\mu$ Hartree for two consequence iterations. The converged  $k$ -mesh was  $20 \times 20 \times 3$  with an error of about 0.5  $\mu$ Hartree (15  $\mu$ eV).

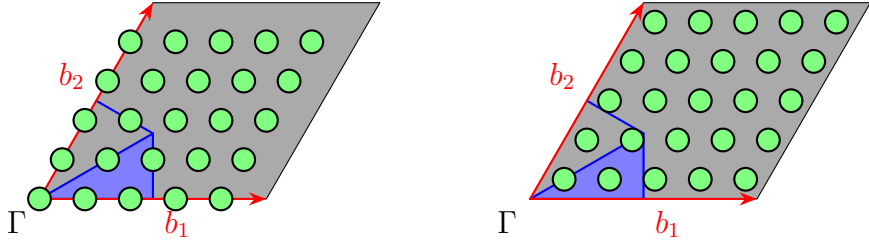


Figure 3.5: Meshing the reciprocal lattice using the Monkhorst-Pack method with the mesh starting from origin (left) and shifted mesh along  $b_1$  and  $b_2$  by  $1/2$  (right). The irreducible wedge of the Brillouin zone is shown in blue and the grid points are marked with green circles.

Subsequently, using the obtained meshing parameters, the value of the kinetic energy cut-off had to be converged. Similar to the  $k$ -mesh analysis, using the same convergence criteria, the value of the kinetic energy cut-off is increased while the other parameters are kept constant. The results obtained from this analysis are tabulated in Table E.2 in Appendix E. The suitable cut-off energy, obtained from the convergence study, was chosen to be 50 Hartree which provides an accuracy in the order of 1 mHartree ( $\sim 25$  meV). The  $k$ -mesh and kinetic energy cut-off convergence curves are illustrated in Figure 3.6.

Using the obtained values, the original unit cell which was created from the experimental measurements was then relaxed to minimise the tension on the atoms and obtain a more realistic and natural structure. This was done by: (1) modifying the unit cell

Table 3.3: The parameter required to create the initial unit cell of 2H-MoS<sub>2</sub> taken from experimental measurements [172].

Parameter	Type	Value
$\vec{a}$	length	3.161 Å
$\vec{b}$	length	3.161 Å
$\vec{c}$	length	12.295 Å
$\alpha$	angle	90 °
$\beta$	angle	90 °
$\gamma$	angle	120 °
Space group	symmetry	$P6_3/mmc$
Mo atom	coordinate	(1/3, 2/3, 1/4)
S atom	coordinate	(1/3, 2/3, 5/8)

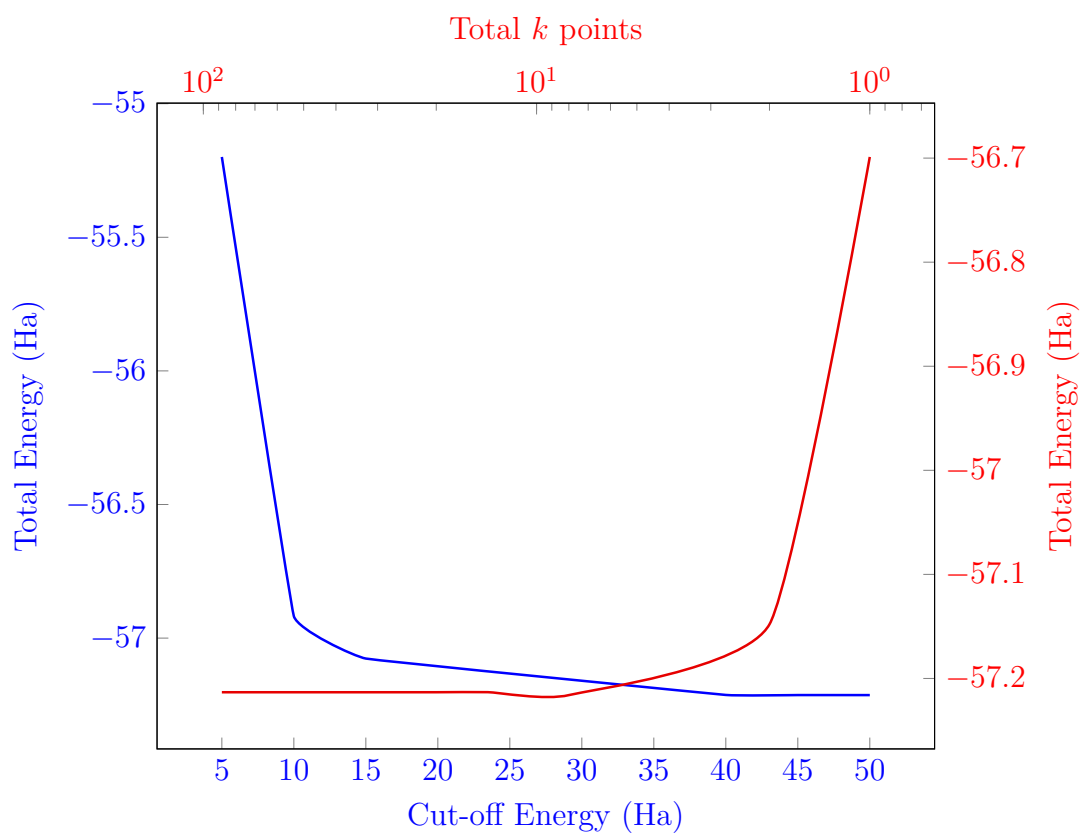


Figure 3.6: The convergence curves for the number of  $k$  sampling points in reciprocal space (blue) and the kinetic energy cut-off (red).

lattice vector lengths to optimise the unit cell while taking into account the symmetry of the system; and (2) moving the ions (atoms) to reduce the effective forces acting on them i.e. reducing the stress. This was carried out using a very popular minimisation technique [254] invented by Broyden, Fletcher, Goldfarb and Shanno which is known as the BFGS technique, named after these inventors. The technique used has been modified to take into account both the total energy and the energy gradients [255]. The relaxation result obtained from this technique was compared with another popular molecular dynamics algorithm known as the Verlet algorithm [256]; however, the convergence speed and efficiency of the result obtained using the modified BFGS technique outperformed the same results obtained using the Verlet technique.

The residual stress after optimisation of the unit cell was reduced 15 times compared to the initial stress tensor (See Table E.3 in Appendix E). Both the Teter Pade parametrization [253] of the local density approximation (LDA) and the Perdew-Burke-Ernzerh (PBE) generalised gradient approximation (GGA) [78] of the exchange and correlation functional were employed in the calculations and the optimised unit cell parameters are tabulated in Table 3.4. These values are obtained using semi-core pseudo-potential to obtain an accurate physical description of the material [257]. The optimal structure was defined as having a maximum force smaller than  $10^{-7}$  Hartree/Bohr ( $\sim 5 \times 10^{-6}$  eV/Å) on each atom.

The optimised 2H-MoS<sub>2</sub> structures obtained from both the LDA and GGA were in

Table 3.4: Comparison between parameters obtained using theoretical calculation with semi-core pseudo-potential and experimentally measured values of lattice parameters of bulk MoS<sub>2</sub> (2H-MoS<sub>2</sub>).

Measure	LDA	GGA	Experiment
$\vec{a}$ (Å)	3.19	3.21	3.16 [169, 258, 259], 3.20 [260]
$\vec{c}$ (Å)	12.42	12.48	12.29 [258], 12.58 [259]
$\theta_{S-Mo-S}$ (°)	82.3	80.3	81.3 [169]
$d_{Mo-S}$ (Å)	2.45	2.42	2.41 [169]
$d_{S-S}$ (Å)	3.22	3.13	3.19 [169]

good agreement with the experimentally measured values, but as the LDA result was describing the material more accurately, this was used in subsequent calculations.

Using the optimised unit cell obtained from the relaxation study in the previous stage, the ground state energies and the excited states (band structure) were calculated using both the TP-LDA and PBE-GGA exchange and correlation functional. Likewise, both plane wave and projector augmented wave (PAW) methods were employed in the calculations.

A convergence study similar to the plane wave has been carried out for the cases where the PAW technique was used to obtain the optimal kinetic energy cut-off value. The obtained value that was used in the calculations was 20 Hartree. However, for the fine FFT grid the cut-off energy was set to 70 Hartree.

The convergence of the calculation was defined as the residual of potential  $V(\mathbf{r})$  being smaller than  $1 \times 10^{-12}$ . The residual of potential was calculated on each iteration of the self-consistent field (SCF) calculation by subtracting the calculated potential from the input potential. The calculated potential is obtained from the charge density that itself is calculated using eigenfunctions of the input potential. The final value of the residual of potential is calculated by summing the square values of residual over all the FFT points.

### 3.3.2 Band Structure

Lattice parameters  $\vec{a}$  ( $= \vec{b}$ ) and  $\vec{c}$  were initially set to 3.17 Å and 12.32 Å, [186] respectively and these subsequently relaxed to 3.19 Å and 12.42 Å with LDA and 3.21 Å and 12.48 Å with GGA. The energy band structure calculated using LDA is shown in Figure 3.7 with the corresponding density of states. An indirect energy band gap of 0.93 eV is observed between the  $K$ -point and the  $\Gamma$  points; although a second conduction band minimum (CBM) occurs at half way between  $\Gamma$  and  $K$  points at an energy level only  $\sim 0.05$  eV above that at the K point. This can be seen in Figure 3.8. Likewise, the lowest conduction band and highest valence band are illustrated in Figure 3.9 and 3.10 respectively. The LDA+PAW calculation gives a similar result but with a band gap of 0.88 eV between

the minima located half way between the  $\Gamma$  and the  $K$  points and the maxima at the  $\Gamma$  point. These results are in-line with those reported in the literature [261, 262]. Both these methods result in an optical band gap of 1.55 eV. The band structures calculated using different methods are presented in section F.1 of Appendix F. The band structure calculated using the augmented plain wave (APW) by Mattheiss [263] is also provided in Figure F.9 in Appendix F for comparison purposes.

The electron effective mass is important from the point of view of charge transport and this was found to be  $0.66 m_0$  and  $0.49 m_0$  for the conduction band minima located halfway between the  $\Gamma$  and the  $K$  points ( $\rightarrow \Gamma$ ), and the  $K$  point ( $\rightarrow \Gamma$ ) respectively, where  $m_0$  is the free electron mass.

From the relaxation study, it was found that the very small structural change due to the relaxation has a noticeable effect on the band gap, particularly on the conduction band minima located at the  $K$  point. This will be discussed in more depth in § 3.6.

It was also observed that the bulk MoS<sub>2</sub> does not have a net magnetic moment and does not show any magnetic behaviour.

### 3.3.3 GW Correction

It is well known that the DFT calculation underestimates the band gap and a more accurate calculation, such as Heyd-Scuseria-Ernzerhof (HSE) [264] or GW is required to obtain a more realistic result. Recently Ataca and Ciraci [262] reported a band gap of 0.72 eV using LDA and 0.85 eV using GGA, both corrected using GW to be 1.44 and 1.28 eV for bulk MoS<sub>2</sub> respectively. The experimentally measured band gap for bulk MoS<sub>2</sub> is found to be 1.23 and 1.29 eV using two different methods. [258, 265]

To obtain an accurate energy band gap the GW correction [130] technique used. This was done using ‘one-shot’ GW correction that is also known as  $G_0W_0$  which means calculating both the screening Coulomb potential,  $W$ , and the Green’s function,  $G$ , only once with no iteration. This is shown schematically in Figure 3.11.

The GW calculation technique used was based on a self-consistent quasi-particle

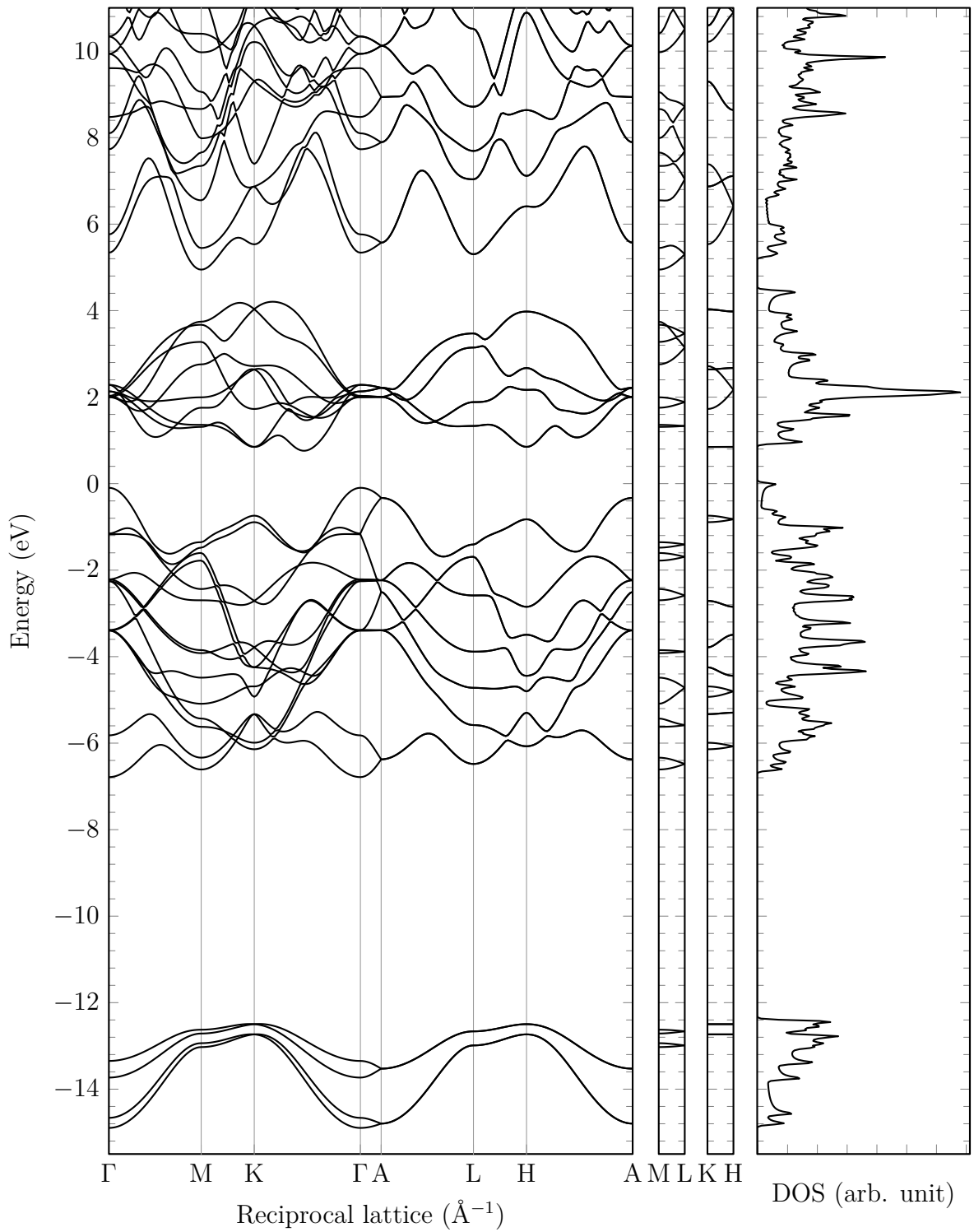


Figure 3.7: The calculated band gap of 2H-MoS<sub>2</sub> along the symmetry points of the irreducible wedge of the first Brillouin zone using LDA technique. The second  $\Gamma$  point is located in the next Brillouin zone with the reduced coordinates of (1,0,0). The corresponding Density of States (DOS) is on the right with arbitrary unit. The energy axis is set to zero at the Fermi energy.

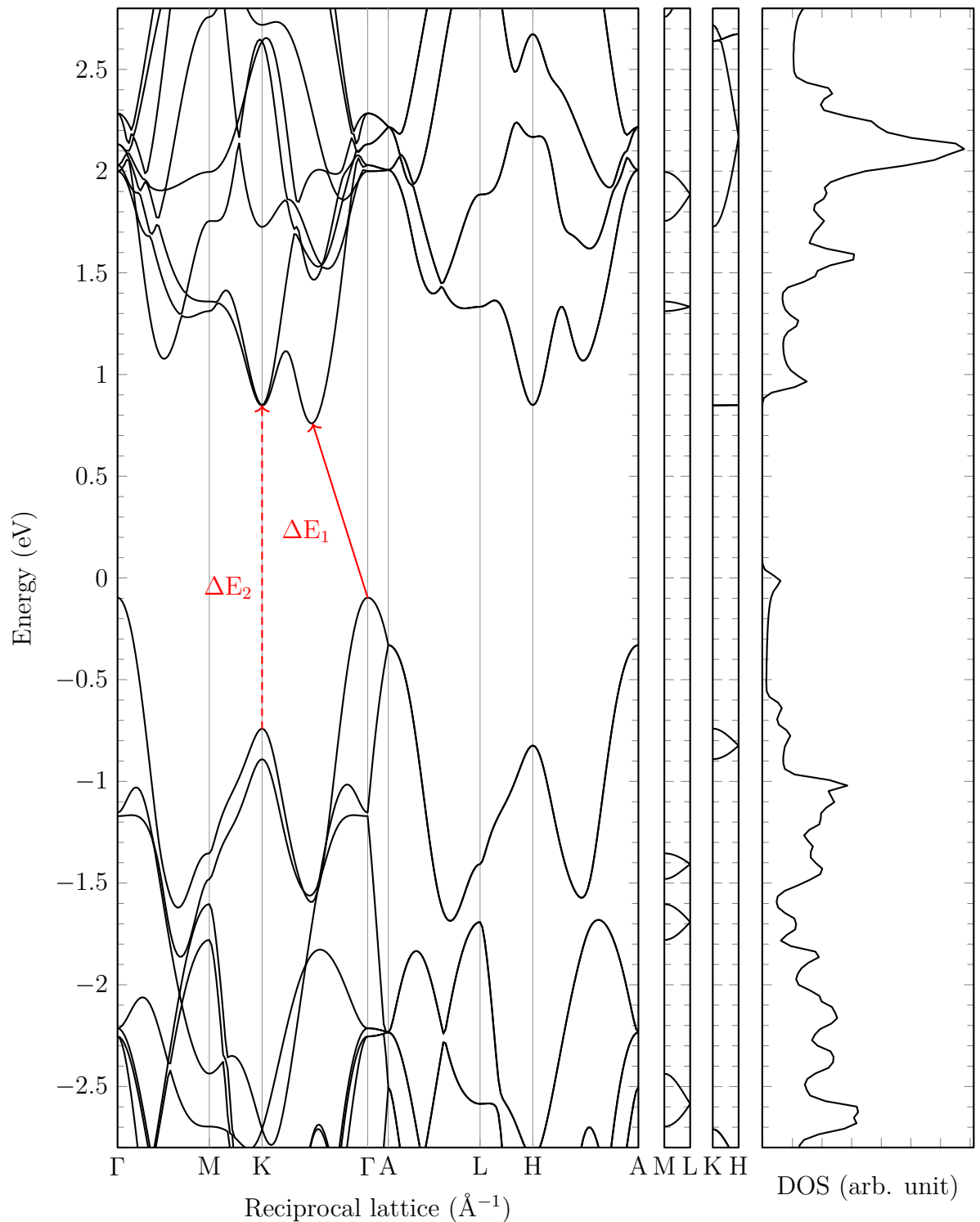


Figure 3.8: The calculated band gap of 2H-MoS<sub>2</sub> along the symmetry points of the irreducible wedge of the first Brillouin zone using LDA technique showing the indirect energy band gap ( $\Delta E_1$ ) and the direct band gap ( $\Delta E_2$ ). The second  $\Gamma$  point is located in the next Brillouin zone with the reduced coordinates of (1,0,0). The corresponding Density of States (DOS) is on the right with arbitrary unit. The energy axis is set to zero at the Fermi energy.

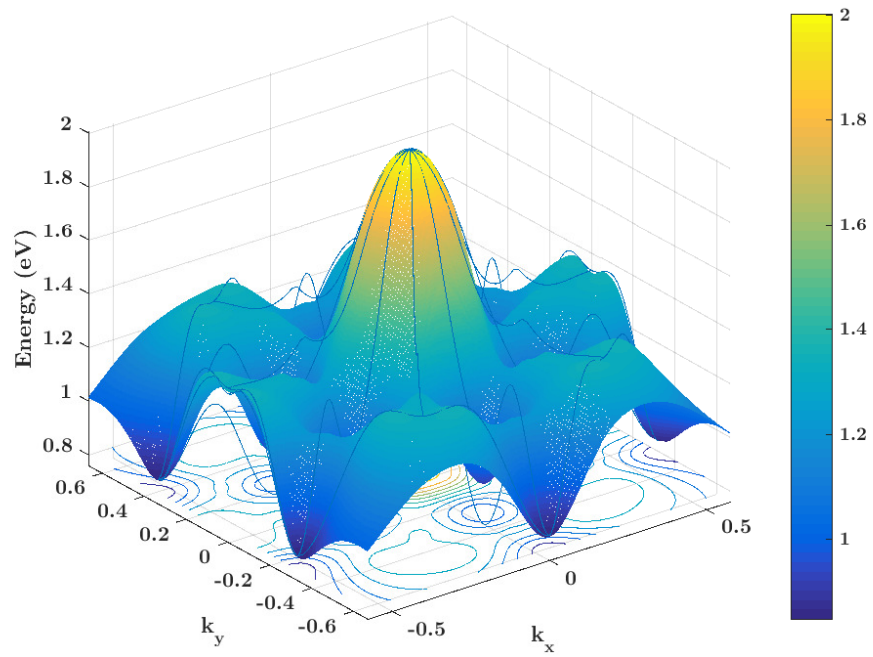


Figure 3.9: The three-dimensional visualisation of the energy band corresponding to the lowest conduction band of 2H-MoS<sub>2</sub> in the first Brillouin zone.

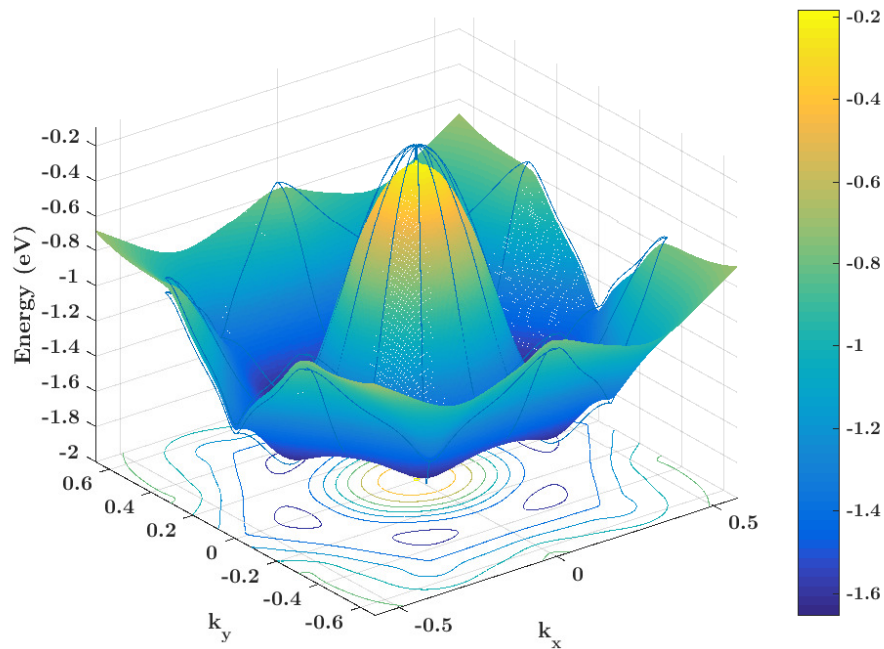


Figure 3.10: The three-dimensional visualisation of the energy band corresponding to the highest valence band of 2H-MoS<sub>2</sub> in the first Brillouin zone.

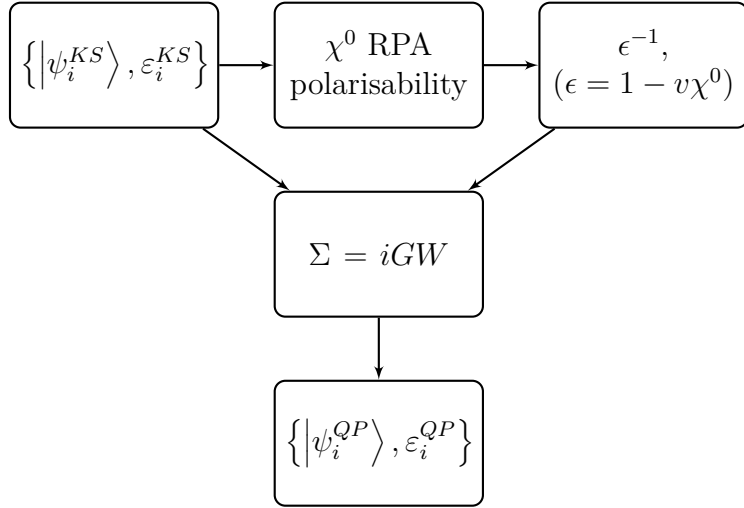


Figure 3.11: One-shot GW correction calculation steps, starting from Kohn-Sham states on the top left-hand side to calculate the independent-particle susceptibility ( $\chi^0$ ) through random phase approximation (RPA) and consequently inverse dielectric matrix ( $\epsilon^{-1}$ ) and then the self-energy ( $\Sigma$ ) matrix at the given  $k$ -points.

method proposed by Faleev et al. [266] using a plasmon-pole model proposed by Godby-Needs [267] for the frequency dependence of the dielectric matrix.

Two frequencies,  $\omega=0$  and a purely imaginary frequency from the peak in the electron energy-loss spectroscopy (EELS) spectrum of 2H-MoS<sub>2</sub> obtained from [268] were used for the plasmon-pole model. The latter had a corresponding energy of 23 eV<sup>5</sup>.

After the convergence study on the number of  $k$ -points, number of energy bands and the cut-off energy, a  $12 \times 12 \times 1$   $k$ -mesh with 1/2 shift in the  $c$  direction was chosen. This means there were 38  $k$ -points in the irreducible wedge of the Brillouin Zone, together with 12 symmetry operations and time-reversal symmetry yielding 288 points in the full Brillouin Zone, with 250 energy bands and an energy cut-off of 20 Hartree ( $\sim 544$  eV).

The corrected band gap of 2H-MoS<sub>2</sub> was found to be 1.18 eV using LDA eigenfunctions (LDA+G<sub>0</sub>W<sub>0</sub>) and 1.29 eV using GGA eigenfunctions, (GGA+G<sub>0</sub>W<sub>0</sub>), both in excellent agreement with the experimentally measured band gap of 2H-MoS<sub>2</sub>. Figure 3.12 shows the corrected band gap of 2H-MoS<sub>2</sub> using G<sub>0</sub>W<sub>0</sub>.

---

<sup>5</sup>Energy can be converted to the frequency using  $f = E/h$  where  $f$  is the frequency;  $E$  is the energy in Joules and  $h$  is the plank's constant.

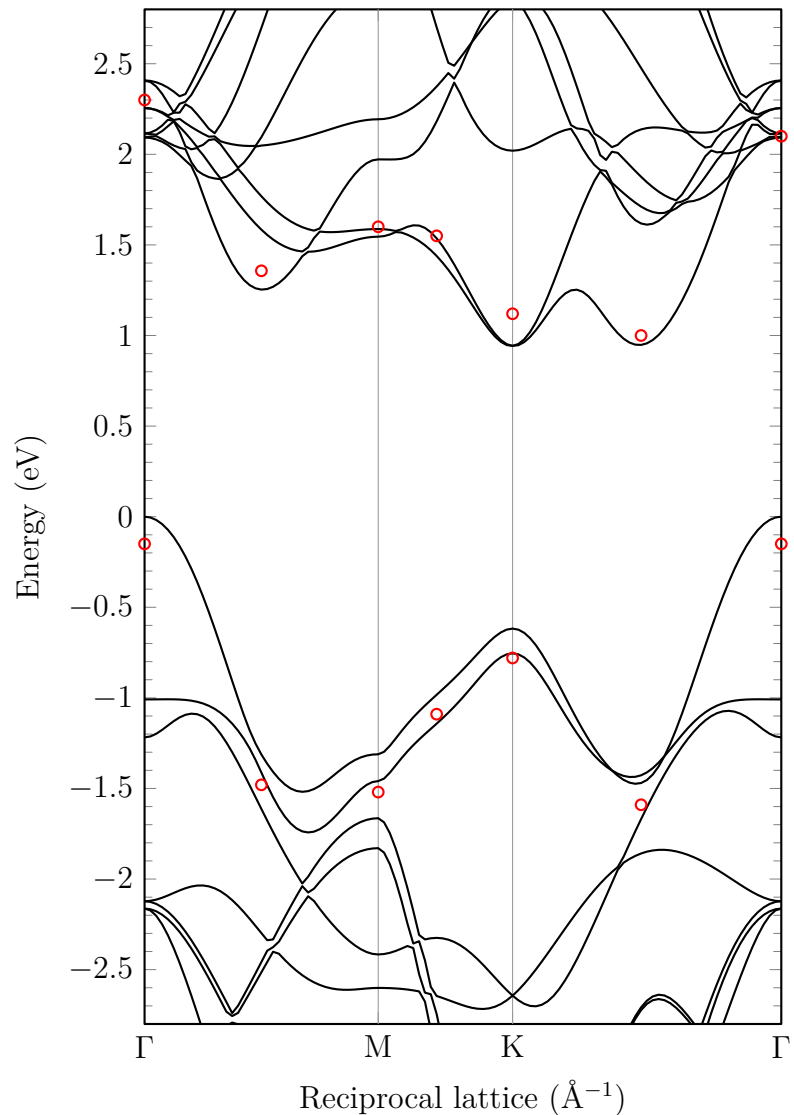


Figure 3.12: The corrected band gap of 2H-MoS<sub>2</sub> using PBE-GGA and one-shot GW approximation technique. The actual calculated points are marked with red dots.

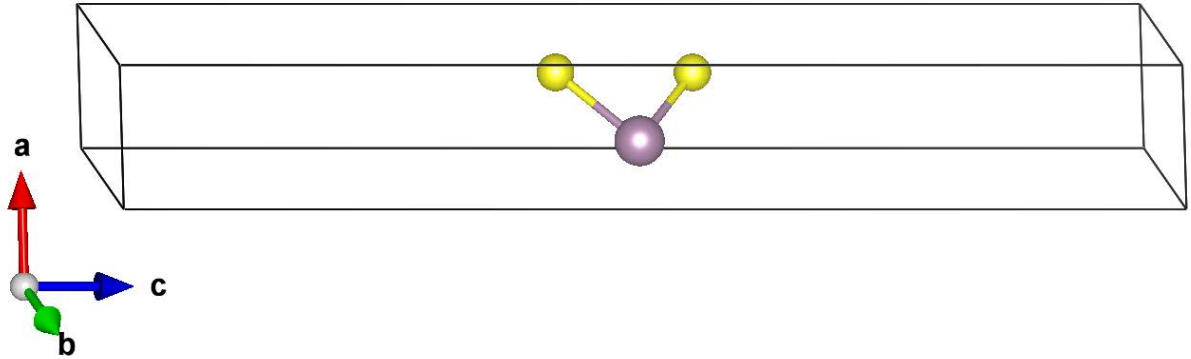


Figure 3.13: The unit cell of single layer molybdenum disulphide

### 3.4 MoS<sub>2</sub> as a Single Layer

Single-layer MoS<sub>2</sub>, unlike its bulk form, has a direct band gap located at the *K*-point in the Brillouin zone [35]. This suggests that in addition to the intra-layer interactions, the interlayer interactions also contribute to the band gap of MoS<sub>2</sub>. In this section, the energy band structure and the properties of single-layer MoS<sub>2</sub> will be investigated.

To construct the single-layer MoS<sub>2</sub>, the same unit cell as the bulk MoS<sub>2</sub> has been used and it was modified to contain only one MoS<sub>2</sub> molecule inside i.e. 3 atoms. Furthermore, the length of the *c* vector was increased to produce at least 20 Å distance between the layers. This is shown in Figure 3.13.

The new unit cell has only one set of MoS<sub>2</sub> atoms inside and therefore only one hexagonal symmetry which is referred to as single-layer MoS<sub>2</sub> or 1H-MoS<sub>2</sub>. The symmetry class and the crystallography space group of the new unit cell has to be changed to account for the discontinuity introduced along the *c* axis. The crystallography group used to describe the unit cell symmetry was *P* $\bar{6}m2$  ( $D_{3h}^1$ ) space group.

#### 3.4.1 Convergence and Band Structure

A similar analysis to that described above in § 3.3.1 for bulk MoS<sub>2</sub> was undertaken on 1H-MoS<sub>2</sub>. The obtained kinetic energy cut-off value was similar to the 2H-MoS<sub>2</sub> with a

value of 50 Hartree for LDA and GGA while 20 Hartree was chosen for the LDA+PAW and GGA+PAW cases. The energy cut-off value for the fine FFT grid was again set to 70 Hartree. However, the number of  $k$ -points used was a Monkhorst-Pack grid of  $20 \times 20 \times 1$  with a  $1/2$  shift along the  $c$  axis.

Starting with structural optimisation the lattice vector  $\vec{a}$  was relaxed to  $3.20 \text{ \AA}$  with LDA and  $3.19 \text{ \AA}$  with GGA. This was done with semi-core pseudo-potentials similar to the bulk MoS<sub>2</sub> as described in § 3.3.1. Other calculated parameters are tabulated in Table 3.5. Again, the band structure was calculated with four different methods: LDA, LDA+PAW, GGA, GGA+PAW and was corrected using GW approximation. Figure 3.14 visualises the band structure of 1H-MoS<sub>2</sub> calculated using the LDA technique. The band structures calculated using different methods are presented in section F.1 of Appendix F.

By comparison with the experiment, the band gap for 1H-MoS<sub>2</sub> is underestimated by all methods. The closest calculated band gap to the experimentally measured band gap was obtained by LDA calculation without using the PAW technique. This was 1.73 eV which is underestimating the band gap by 0.17 eV compared to the experimentally measured band gap of 1.9 eV. The GGA resulted in a very similar band gap with a value of 1.71 eV. Using the PAW technique caused both the LDA and GGA techniques to predict a smaller band gap with values of 1.69 eV and 1.68 eV respectively.

The calculated effective mass ( $K \rightarrow \Gamma$ ) of electrons and holes in 1H-MoS<sub>2</sub> at the conduction band minima and at the valence band maxima, are found to be  $0.55 m_0$  and

Table 3.5: Comparison between parameters obtained using theoretical calculation using semi-core pseudo-potentials and experimentally measured values of lattice parameters of 1H-MoS<sub>2</sub>.

Measure	LDA	GGA	Experiment
$\vec{a} (\text{\AA})$	3.20	3.19	3.20 [260]
$\vec{c} (\text{\AA})$	24.89	24.80	
$\theta_{S-Mo-S} (\text{^\circ})$	82.0	81.1	
$d_{Mo-S} (\text{\AA})$	2.45	2.42	
$d_{S-S} (\text{\AA})$	3.21	3.15	

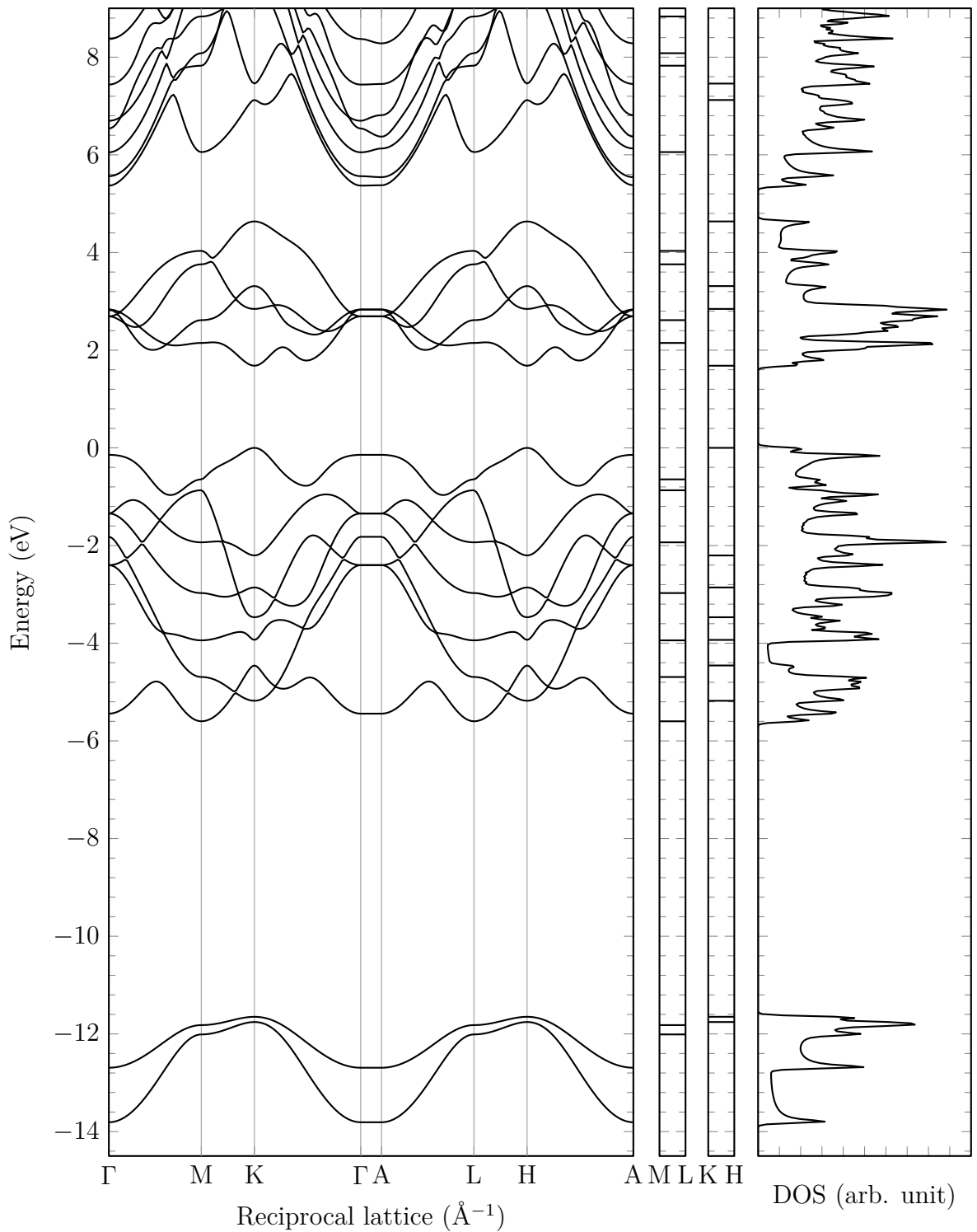


Figure 3.14: The band structure of 1H-MoS<sub>2</sub> calculated using LDA technique along the irreducible wedge of the Brillouin zone with the corresponding electron density of states (DOS) on the right-hand side.

0.63 m<sub>0</sub>, respectively; both values are lower than in bulk MoS<sub>2</sub>.

### 3.4.2 GW Correction

The same parameters as with the bulk MoS<sub>2</sub> were used to calculate the band gap correction using GW approximation. The GW correction was applied on the band gap calculated using both LDA+PAW and PBE-GGA+PAW.

Apart from GW calculation, hybridisation of DFT calculation with Hartree-Fock (e.g. techniques such as B3LYP method [269] as explained in § 2.3) is expected to provide a better band gap prediction compared to DFT on its own; although it was reported by Heda et al. [261] that B3LYP overestimates the band gap of 1H-MoS<sub>2</sub> by about 0.5 eV.

After correcting the band gap using G<sub>0</sub>W<sub>0</sub> it is found that the band gap of 1H-MoS<sub>2</sub> is overestimated by almost  $\sim$ 1 eV. Therefore, other GW correction techniques such as GW<sub>0</sub> were explored; which iterates G while W is kept fixed from the initial calculation; and GW, which similar to GW<sub>0</sub> iterates G, while W is calculated iteratively as well.

Using these techniques, after three iterations, the band gap was reduced to the value of 2.57 eV, which is about 0.6 eV more than the experimentally measured band gap. Ataca and Ciraci [262] also reported that GW overestimates the band gap.

The discrepancy between the experimental and theoretical results for the case of single layer MoS<sub>2</sub> may be due to the nature of the material studied. The measurement of the energy band gap was made by Mak et. al. [170] on MoS<sub>2</sub> layers deposited on oxide-covered silicon substrates prepared with arrays of 1.0 and 1.5  $\mu$ m circular holes (wells); whereas this theoretical analysis here assumes the structure is optimally relaxed. However, this may only account for some of the difference in the band gap.

## 3.5 MoS<sub>2</sub> Orbital Decomposition

Calculation of maximally-localised Wannier functions (MLWFs) and disentanglement of hybridised bands was performed using Wannier90 code [250]. This software requires ho-

mogeneous  $k$ -point grid so a homogeneous Monkhorst-pack  $k$ -point grid of  $12 \times 12 \times 3$  for bulk MoS<sub>2</sub> and  $12 \times 12 \times 2$  for the single-layer MoS<sub>2</sub> has been used. In total 32 MLWFs were calculated for bulk MoS<sub>2</sub> and 17 MLWFs for the single-layer MoS<sub>2</sub>. The initial knowledge about the orbitals used to calculate the MLWFs are based on tight binding and LCAO interpretation of the MoS<sub>2</sub> band structure by Mattheiss [263] and the MoS<sub>2</sub> orbital scheme by Fleischauer et al. [270].

The Wannier90 is able to project onto functions with  $s$ ,  $p$ ,  $d$  (see Table D.1 and D.2 in Appendix D) and  $f$  symmetry, plus the hybrids  $sp$ ,  $sp^2$ ,  $sp^3$ ,  $sp^3d$ ,  $sp^3d^2$  localised functions associated with a site and an angular momentum state [250]<sup>6</sup>. The band projections used for the bulk and single-layer MoS<sub>2</sub> are tabulated in Tables 3.6 and 3.7 respectively.

The MLWFs analysis of 1H-MoS<sub>2</sub> indicates that the molybdenum  $4d_{z^2}$ ,  $4d_{xy}$  and  $4d_{x^2-y^2}$  orbitals are associated with the energy bands in the region of the band gap as observed with 2H-MoS<sub>2</sub>. The energy bands in the vicinity of the Fermi energy for both 2H and 1H-MoS<sub>2</sub> are mainly due to the  $4d$  orbital of molybdenum atoms with a smaller contribution (less than 20%) from the  $3p$  orbitals of sulphur atoms.

It has been found that in addition to the intra-layer hybridisation, the interlayer interaction affects the  $d_{z^2}$  orbital and causes a significant change, moving from 2H-MoS<sub>2</sub> to 1H-MoS<sub>2</sub>. This leads to the change of band gap from indirect to direct. This can be seen visually by comparing the contour lines in Figures 3.15 and 3.16. Forming a single layer of MoS<sub>2</sub> removes interlayer coupling and leads to a dramatic loss of energy in the valence band maxima located at the  $\Gamma$  point which results in a direct band gap at the  $K$  point.

Projected density of states (PDOS), obtained from MLWFs (Figure 3.17), show that the lower energy bands (-15 to -12 eV) are mainly associated with the  $s$  orbital of sulphur atoms. The energy region immediately below the Fermi energy (-7 to 0 eV) is associated with the hybridised molybdenum  $d$  and sulphur  $p$  states [261, 271]. Once more, the group

---

<sup>6</sup>For further details on projection and disentanglement done using Wannier90 refer to maximally-localised Wannier functions projection technique by Marzari and Vanderbilt [165] and MLWFs for entangled energy bands by Marzari, Vanderbilt and Souza [167] and the wannier90 implementation [250].

Table 3.6: The orbital projections used for 2H-MoS<sub>2</sub>. The  $l$ ,  $m_r$  and  $r$  represent the azimuthal quantum number, magnetic quantum number and radial nodes respectively.

Reduced Coordinates	$l$	$m_r$	$r$	Description
(2/3, 1/3, 0.1247257)	0	1	2	S1 3s (2 radial nodes)
(2/3, 1/3, 0.3752743)	0	1	2	S2 3s (2 radial nodes)
(2/3, 1/3, 0.6247257)	0	1	2	S3 3s (2 radial nodes)
(2/3, 1/3, 0.8752743)	0	1	2	S4 3s (2 radial nodes)
(2/3, 1/3, 0.1247257)	1	1	1	S1 3pz (1 radial nodes)
(2/3, 1/3, 0.1247257)	1	2	1	S1 3px (1 radial nodes)
(2/3, 1/3, 0.1247257)	1	3	1	S1 3py (1 radial nodes)
(2/3, 1/3, 0.3752743)	1	1	1	S2 3pz (1 radial nodes)
(2/3, 1/3, 0.3752743)	1	2	1	S2 3px (1 radial nodes)
(2/3, 1/3, 0.3752743)	1	3	1	S2 3py (1 radial nodes)
(2/3, 1/3, 0.6247257)	1	1	1	S3 3pz (1 radial nodes)
(2/3, 1/3, 0.6247257)	1	2	1	S3 3px (1 radial nodes)
(2/3, 1/3, 0.6247257)	1	3	1	S3 3py (1 radial nodes)
(2/3, 1/3, 0.8752743)	1	1	1	S4 3pz (1 radial nodes)
(2/3, 1/3, 0.8752743)	1	2	1	S4 3px (1 radial nodes)
(2/3, 1/3, 0.8752743)	1	3	1	S4 3py (1 radial nodes)
(1/3, 2/3, 1/4)	0	1	4	Mo1 5s (4 radial nodes)
(2/3, 1/3, 3/4)	0	1	4	Mo2 5s (4 radial nodes)
(1/3, 2/3, 1/4)	1	1	2	Mo1 4pz (2 radial nodes)
(1/3, 2/3, 1/4)	1	2	2	Mo1 4px (2 radial nodes)
(1/3, 2/3, 1/4)	1	3	2	Mo1 4py (2 radial nodes)
(2/3, 1/3, 3/4)	1	1	2	Mo2 4pz (2 radial nodes)
(2/3, 1/3, 3/4)	1	2	2	Mo2 4px (2 radial nodes)
(2/3, 1/3, 3/4)	1	3	2	Mo2 4py (2 radial nodes)
(1/3, 2/3, 1/4)	2	1	4	Mo1 4d <sub>z<sup>2</sup></sub> (4 radial nodes)
(1/3, 2/3, 1/4)	2	2	4	Mo1 4d <sub>xz</sub> (4 radial nodes)
(1/3, 2/3, 1/4)	2	3	4	Mo1 4d <sub>yz</sub> (4 radial nodes)
(1/3, 2/3, 1/4)	2	4	4	Mo1 4d <sub>x<sup>2</sup>-y<sup>2</sup></sub> (4 radial nodes)
(1/3, 2/3, 1/4)	2	5	4	Mo1 4d <sub>xy</sub> (4 radial nodes)
(2/3, 1/3, 3/4)	2	1	1	Mo2 4d <sub>z<sup>2</sup></sub> (1 radial nodes)
(2/3, 1/3, 3/4)	2	2	1	Mo2 4d <sub>xz</sub> (1 radial nodes)
(2/3, 1/3, 3/4)	2	3	1	Mo2 4d <sub>yz</sub> (1 radial nodes)
(2/3, 1/3, 3/4)	2	4	1	Mo2 4d <sub>x<sup>2</sup>-y<sup>2</sup></sub> (1 radial nodes)
(2/3, 1/3, 3/4)	2	5	1	Mo2 4d <sub>xy</sub> (1 radial nodes)

Table 3.7: The orbital projections used for 1H-MoS<sub>2</sub>. The  $l$ ,  $m_r$  and  $r$  represent the azimuthal quantum number, magnetic quantum number and radial nodes respectively. The  $l$ ,  $m_r$  and  $r$  specify the angular part ( $\Theta_{lm_r}(\theta, \varphi)$ ) and the radial part ( $R_r(r)$ ) of the projection functions (see Table D.1 and D.2 in Appendix D)

Reduced Coordinates	$l$	$m_r$	$r$	Description
(2/3, 1/3, 0.4355438)	0	1	2	S1 3s (2 radial nodes)
(2/3, 1/3, 0.5644562)	0	1	2	S2 3s (2 radial nodes)
(2/3, 1/3, 0.4355438)	1	1	1	S1 3p <sub>z</sub> (1 radial nodes)
(2/3, 1/3, 0.4355438)	1	2	1	S1 3p <sub>x</sub> (1 radial nodes)
(2/3, 1/3, 0.4355438)	1	3	1	S1 3p <sub>y</sub> (1 radial nodes)
(2/3, 1/3, 0.5644562)	1	1	1	S1 3p <sub>z</sub> (1 radial nodes)
(2/3, 1/3, 0.5644562)	1	2	1	S1 3p <sub>x</sub> (1 radial nodes)
(2/3, 1/3, 0.5644562)	1	3	1	S1 3p <sub>y</sub> (1 radial nodes)
(1/3, 2/3, 1/2)	0	1	4	Mo1 5s (4 radial nodes)
(1/3, 2/3, 1/2)	1	1	2	Mo1 4p <sub>z</sub> (2 radial nodes)
(1/3, 2/3, 1/2)	1	2	2	Mo1 4p <sub>x</sub> (2 radial nodes)
(1/3, 2/3, 1/2)	1	3	2	Mo1 4p <sub>y</sub> (2 radial nodes)
(1/3, 2/3, 1/2)	2	1	1	Mo1 4d <sub>z<sup>2</sup></sub> (1 radial nodes)
(1/3, 2/3, 1/2)	2	2	1	Mo1 4d <sub>xz</sub> (1 radial nodes)
(1/3, 2/3, 1/2)	2	3	1	Mo1 4d <sub>yz</sub> (1 radial nodes)
(1/3, 2/3, 1/2)	2	4	1	Mo1 4d <sub>x<sup>2</sup>-y<sup>2</sup></sub> (1 radial nodes)
(1/3, 2/3, 1/2)	2	5	1	Mo1 4d <sub>xy</sub> (1 radial nodes)

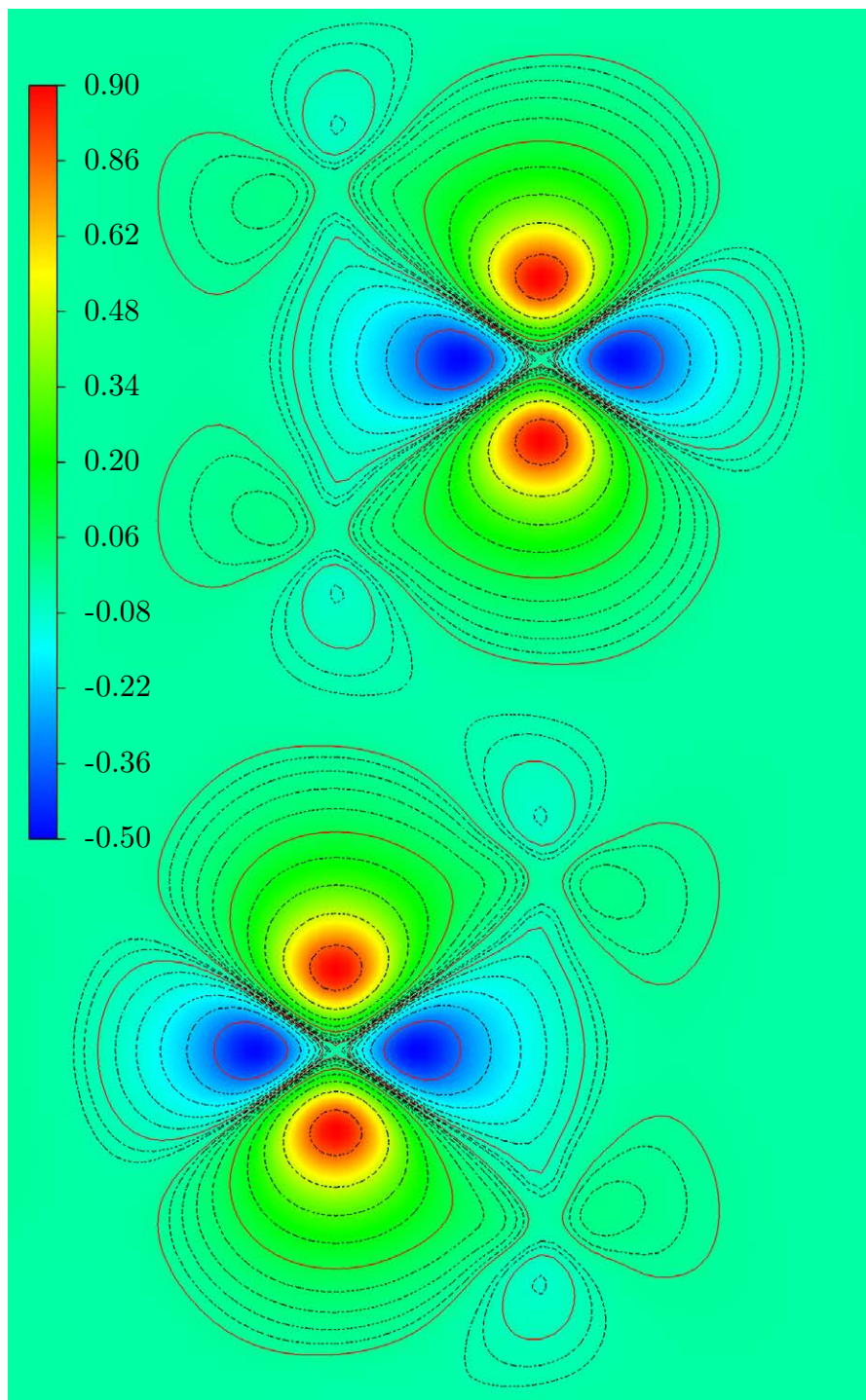


Figure 3.15: Molybdenum  $4d_{z^2}$  projected MLWF cross-section and contour lines along  $(1,1,0)$  lattice plane for bulk MoS<sub>2</sub> (2H-MoS<sub>2</sub>).

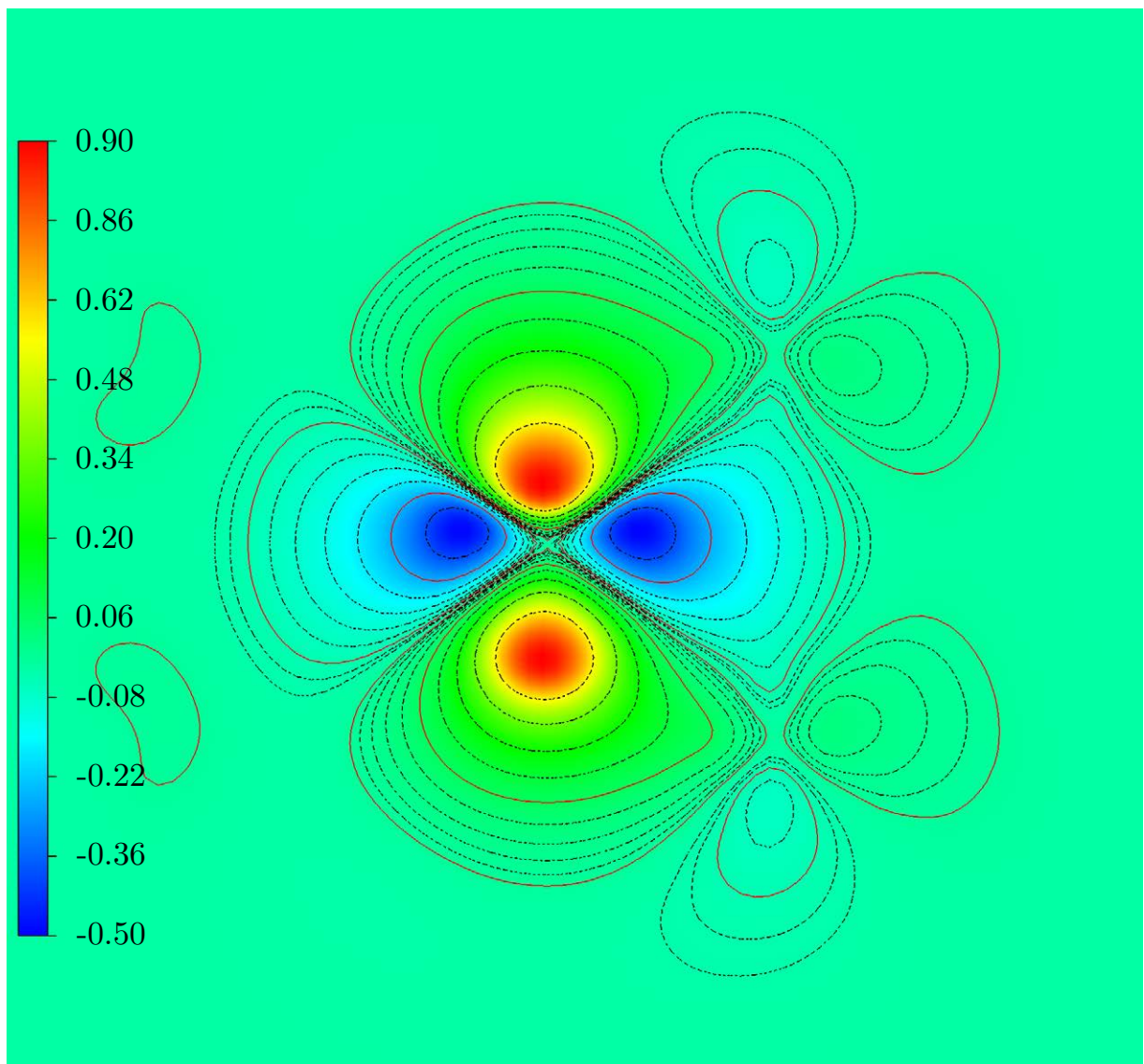


Figure 3.16: Molybdenum  $4d_{z^2}$  projected MLWF cross-section and contour lines along  $(1,1,0)$  lattice plane for single-layer MoS<sub>2</sub> (1H-MoS<sub>2</sub>).

of bands above the Fermi energy (up to about 11 eV) is associated with the molybdenum  $d$  and sulphur  $p$  orbitals with a small contribution of molybdenum  $s$  and  $p$  orbitals and the sulphur  $s$  orbital. Around the Fermi energy and the band gap, in the region -0.5 to 0 eV and 1 to 1.5 eV, the band gap is due to molybdenum  $4d_{xy}$  and  $4d_{x^2-y^2}$  orbitals bonding with sulphur  $3p_x$  and  $3p_y$  orbitals and anti-bonding molybdenum  $4d_{z^2}$  and sulphur  $3p_x$  and  $3p_y$  orbitals [272]. More detailed graphs are presented in section F.3 of Appendix F.

The results of the MLWFs imply that the band gap occurring in  $2H\text{-MoS}_2$  results mainly from intra-layer hybridisation between  $d_{z^2}$  and  $d_{xy}$ ,  $d_{x^2-y^2}$  sub-bands, as suggested by Mattheiss [263].

The valence band maxima located at  $K$  is associated with the molybdenum  $4d_{xy}$  and  $4d_{x^2-y^2}$  orbitals and the sulphur  $3p_x$  and  $3p_y$  orbitals and these are not greatly influenced by the intra-layer interactions; while the molybdenum  $4d_{z^2}$  and sulphur  $3p_z$  orbitals are more affected by inter-layer coupling. As a result, the band gap at the  $K$  point differs only by 0.1-0.2 eV between  $2H\text{-MoS}_2$  and  $1H\text{-MoS}_2$ . The valence band maxima, located at the  $\Gamma$  point, is associated with the  $4d_{z^2}$  orbital and its energy in  $1H\text{-MoS}_2$  is 1 eV lower than in  $2H\text{-MoS}_2$ . An alternative perspective of this change in band structure has been provided by Mak et al. [170]. They attribute the indirect-direct-gap crossover to the relatively strong effects of quantum confinement on the indirect gap conduction and valence band edge, as the out of plane effective mass of electrons and holes is light compared to the corresponding mass for the direct band gap at the  $K$  point.

The projected density of states (PDOS) for  $1H\text{-MoS}_2$  yields similar results to  $2H\text{-MoS}_2$ . The largest contribution naturally comes from the molybdenum  $4d_{z^2}$ ,  $4d_{xy}$  and  $4d_{x^2-y^2}$  orbitals and sulphur  $p$  orbitals; while the molybdenum  $4d_{yz}$  and  $4d_{xz}$  orbitals are found to make only a small contribution (Figure 3.18). More detailed graphs are presented in section F.3 of Appendix F.

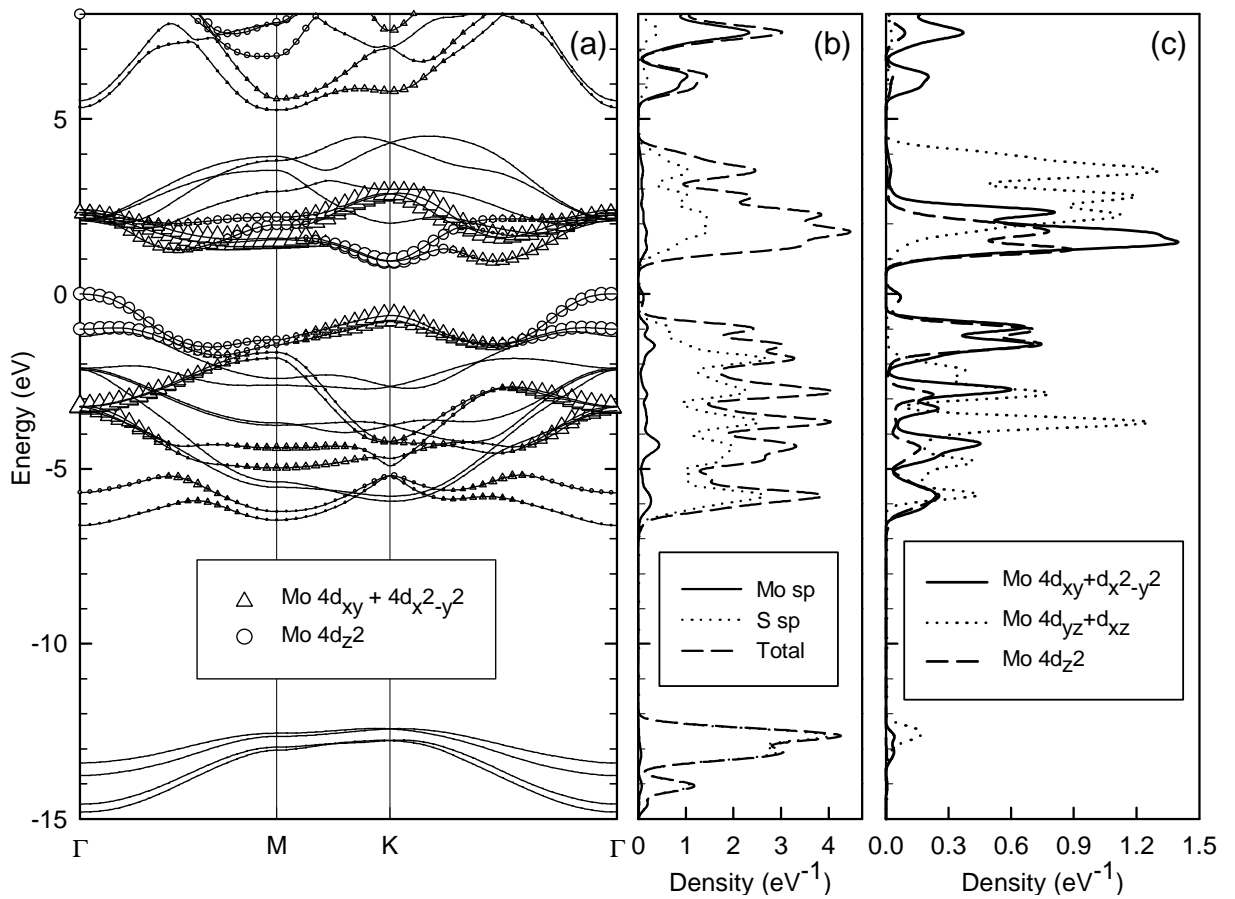


Figure 3.17: (a) Projected band structure of 2H-MoS<sub>2</sub> obtained using MLWFs. The size of markers reflects the relative contribution of the projection on the energy bands. (b) and (c) are the corresponding projected density of states also computed using MLWFs.

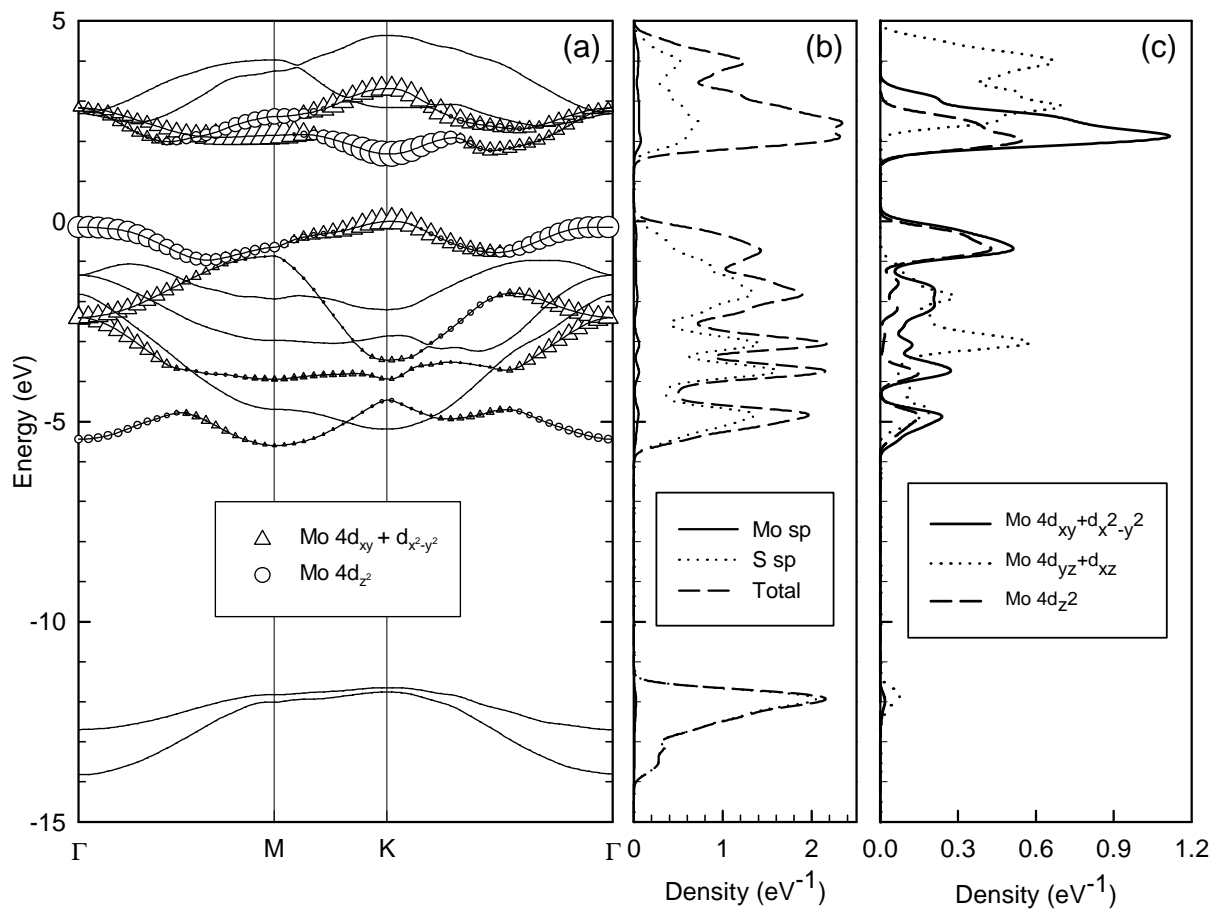


Figure 3.18: (a) Projected band structure of  $1H$ -MoS<sub>2</sub> obtained using MLWFs. The size of markers reflects the relative contribution of the projection on the energy bands. (b) and (c) are the corresponding projected density of states also computed using MLWFs.

### 3.6 MoS<sub>2</sub> Relaxation and Elastic Strain Effect

The 2H-MoS<sub>2</sub> and 1H-MoS<sub>2</sub> respond similarly to biaxial compressive and tensile strain. However, due to the difference in their band structure, their properties change differently. In Figure 3.19 the band structure is calculated for both relaxed and strained 2H-MoS<sub>2</sub> obtained using GGA+PAW with a limited degree of freedom and restricted BFGS relaxation to preserve the induced strain. The tensile and compressive strain is usually studied for a wide range (i.e. 15-20%) while the effect of small strain is neglected.

Even a small strain significantly affects the energy of the conduction band minima at  $K$  and can lead to a change in minimum from halfway between  $\Gamma$  and  $K$  to  $K$ . The MoS<sub>2</sub> structure is capable of enduring 20% strain before starting to deform [273]. However, here, the calculated strain is in a range of  $\pm 2\%$  which can be imposed to the MoS<sub>2</sub> when deposited on a substrate. As found with 2H-MoS<sub>2</sub>, a significant change in the energy band gap of 1H-MoS<sub>2</sub> was observed when strained, as shown in Figure 3.20. Only a small strain on 1H-MoS<sub>2</sub> is required to change the band gap from direct to indirect.

Figure 3.21 summarises the effect of strain on the band gap of 2H-MoS<sub>2</sub> and 1H-MoS<sub>2</sub>. As it can be seen in the figure, the direct band gap of 1H-MoS<sub>2</sub> can change to indirect when the amount of strain exceeds 3.20 Å. These results are in-line with the strain study on MoS<sub>2</sub> published by Scalise et al. [274]; however, their work reports on large induced compressive and tensile strain (2–15%), while this work is looking into small strain (0–2%) that can be imposed on MoS<sub>2</sub> during fabrication.

The energy levels at the symmetry points of the Brillouin zone for the highest valence band and the lowest conduction band is tabulated in Table E.4 (2H-MoS<sub>2</sub>) and Table E.5 (1H-MoS<sub>2</sub>) of Appendix E.

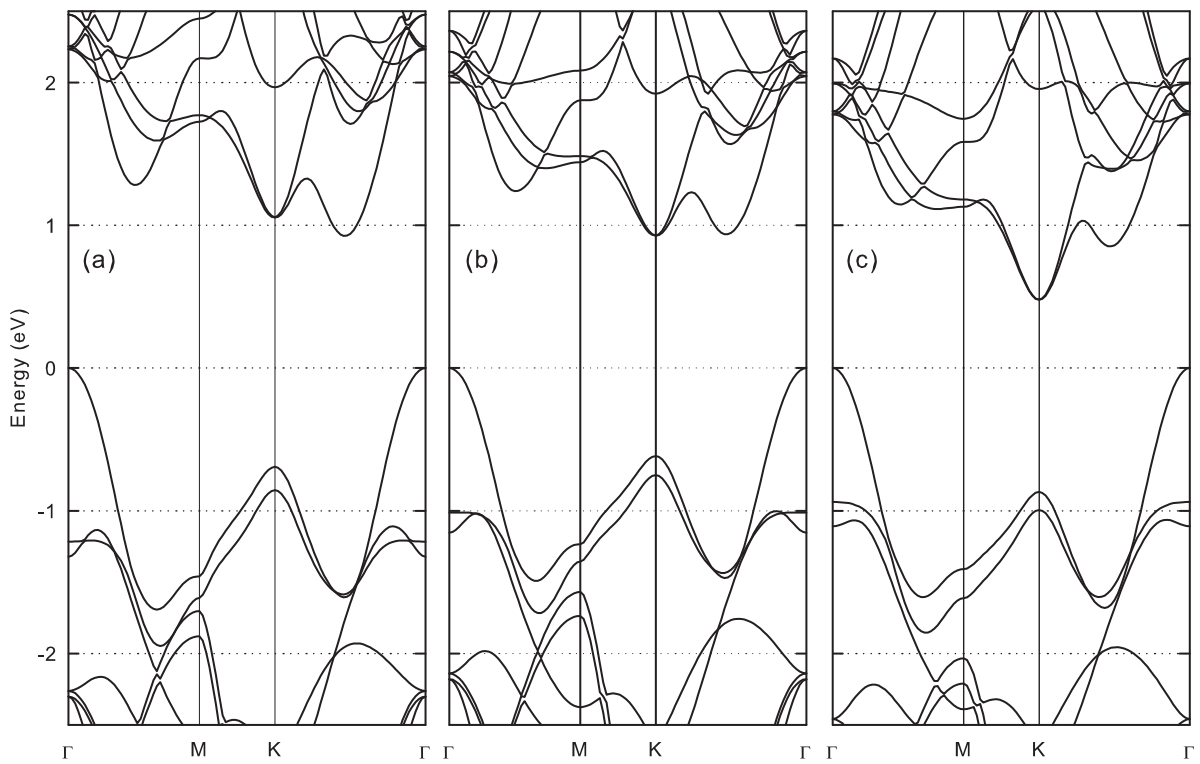


Figure 3.19: Band structure of 2H-MoS<sub>2</sub> showing the effect of biaxial elastic strain on the band gap of bulk MoS<sub>2</sub> calculated using GGA+PAW; (a) calculated with a lattice vector of  $\vec{a}=3.13$  Å (compressive strain); (b) calculated with  $\vec{a}=3.21$  Å (relaxed); and (c) calculated with  $\vec{a}=3.27$  Å (tensile strained).

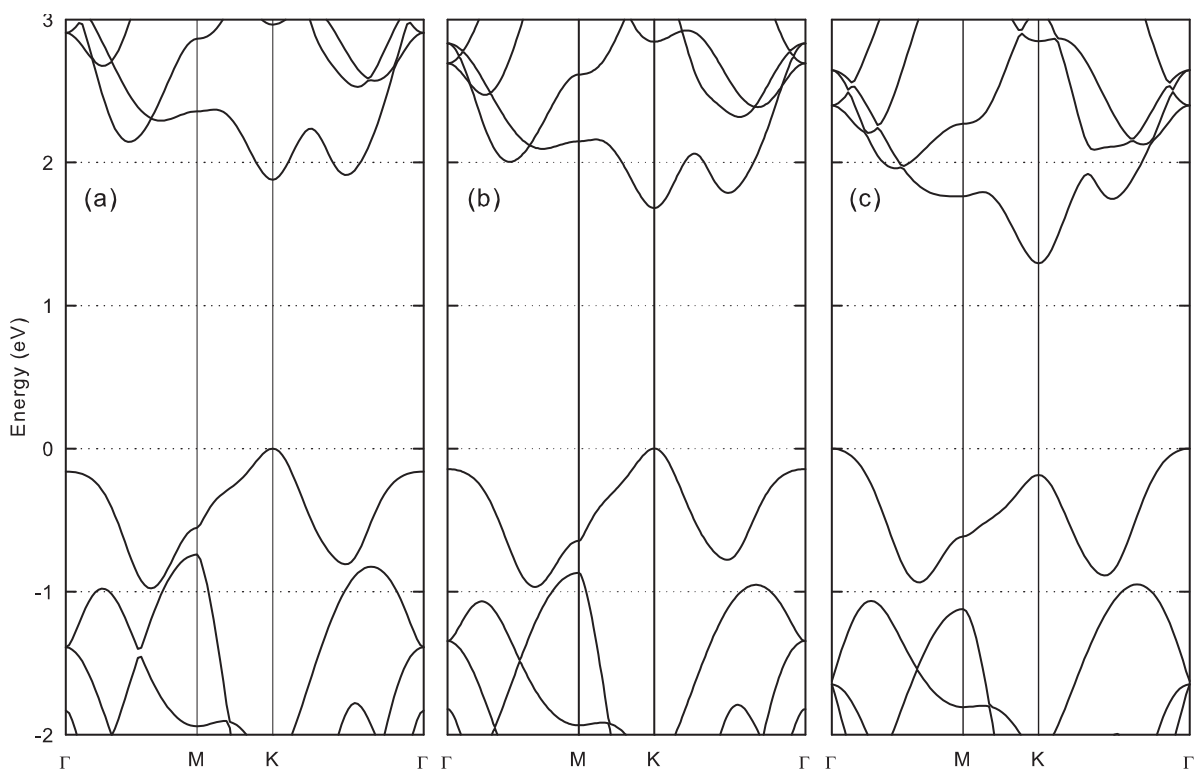


Figure 3.20: Band structure of 1H-MoS<sub>2</sub> showing the effect of biaxial elastic strain on the band gap of single layer MoS<sub>2</sub> calculated using GGA+PAW; (a) calculated with a lattice vector of  $\vec{a}=3.13 \text{ \AA}$  (compressive strain); (b) calculated with  $\vec{a}=3.19 \text{ \AA}$  (relaxed); and (c) calculated with  $\vec{a}=3.27 \text{ \AA}$  (tensile strained).

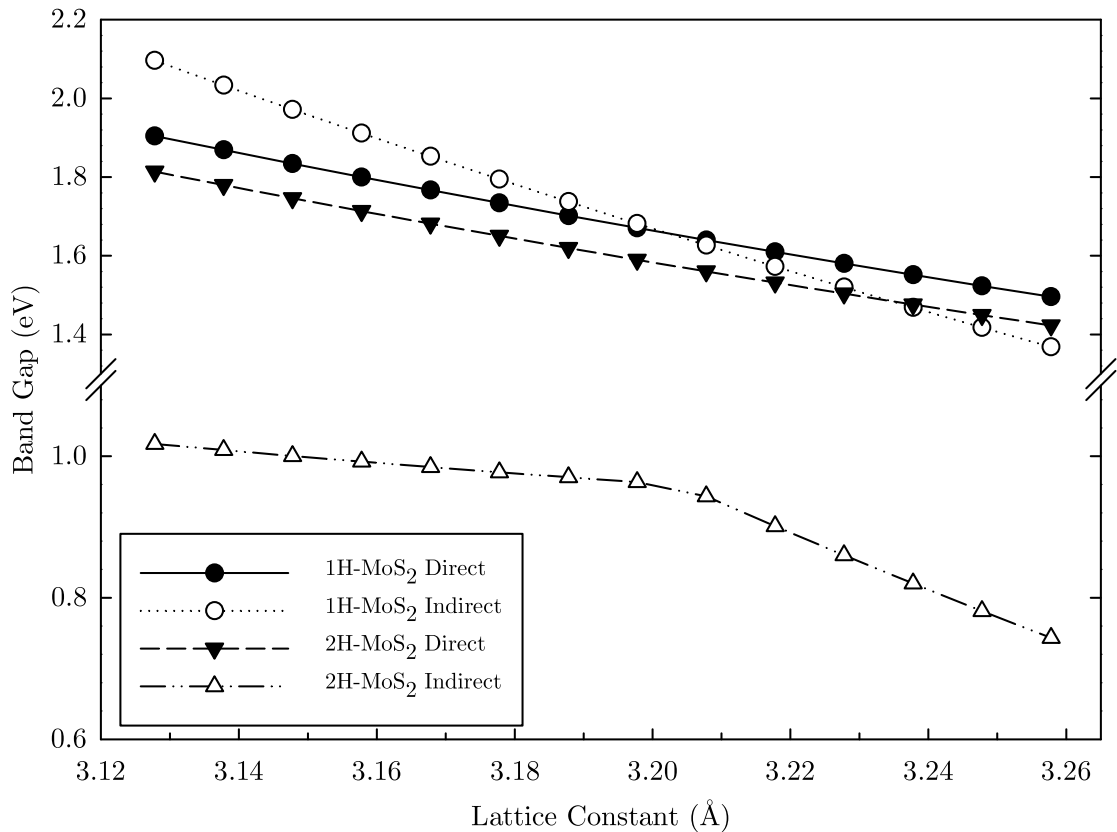


Figure 3.21: Variation of band gap calculated using DFT-GGA in bulk (2H) and single-layer (1H) MoS<sub>2</sub> due to biaxial elastic strain. More details are available in Table E.4 (2H-MoS<sub>2</sub>) and Table E.5 (1H-MoS<sub>2</sub>) of Appendix E.

Table 3.8: Band gap calculated for bulk and single layer MoS<sub>2</sub> using different correlation functions compared with previously published experimentally measured results.

Material	LDA			GGA			Experiment
	PW	PAW	GW	PW	PAW	GW	
2H-MoS <sub>2</sub>	0.87	0.88	1.18	0.94	0.93	1.29	1.2 [265], 1.3 [258]
1H-MoS <sub>2</sub>	1.73	1.69	2.57	1.71	1.68	2.59	1.9 [170]

## 3.7 Summary

In this chapter, the energy band structure of 1H-MoS<sub>2</sub> (single-layer) and 2H-MoS<sub>2</sub> (bulk) has been calculated using density functional theory and the results obtained with different methodologies were compared. The obtained results were in-line with published results from experimentally measured values in the literature; which confirms the reliability of the model and the techniques that were used. Table 3.8 summarises these values. Using similar techniques (LDA and GGA), the reported values in the literature, have more errors (compared to experimental values) than the values reported in this research. For the purpose of comparison with the other values reported in the literature, Table 3.9 provides some of the reported values.

The relationship between the atomic orbitals, energy band structure and band gap has been investigated using maximally-localised Wannier functions and the change in the band gap occurring when moving from bulk to 2-dimensional was studied. This change is mainly due to the decrease in energy of molybdenum 4d<sub>z<sup>2</sup></sub> orbital when the coupling between the layers of MoS<sub>2</sub> is not present.

Extensive structural optimisation calculations have been used to show the effects of stress and strain on the energy band gap in both bulk and single-layer MoS<sub>2</sub>. It was observed that the very small variations in the structural properties that can be imposed by external factors such as a substrate lattice can significantly affect the band structure of MoS<sub>2</sub>.

In the next chapter, using the established model from this chapter, discontinuity on

Table 3.9: Some of the reported parameters for bulk MoS<sub>2</sub> (2H-MoS<sub>2</sub>) and single-layer MoS<sub>2</sub> (1H-MoS<sub>2</sub>) in the literature calculated using various techniques.

Author	Bulk MoS <sub>2</sub> (2H-MoS <sub>2</sub> )			single-layer MoS <sub>2</sub> (1H-MoS <sub>2</sub> )			Software	
	Gap (eV)	$\vec{a}$ (Å)	$\vec{c}$ (Å)	$d_{Mo-S}$ (Å)	Gap (eV)	$\vec{a}$ (Å)	$d_{Mo-S}$ (Å)	
Yue [272]	—	—	—	—	1.65 <sup>d</sup> , 2.12 <sup>b</sup>	3.19	2.43	VASP <sup>a</sup>
Ataca [262]	0.72 <sup>e</sup> , 0.85 <sup>f</sup>	—	—	—	2.23 <sup>b</sup> , 2.50 <sup>f+g</sup> , 1.87 <sup>c</sup>	3.11 <sup>e</sup>	2.42 <sup>e</sup>	VASP
Ataca [262]	1.28 <sup>e+g</sup> , 1.44 <sup>f+g</sup>	—	—	—	2.78 <sup>h</sup> , 2.57 <sup>e+g</sup> , 1.58 <sup>d</sup>	3.20 <sup>f</sup>	2.42 <sup>f</sup>	VASP
Kumar [275]	0.75 <sup>c+j</sup> , 1.05 <sup>d+j</sup>	3.13 <sup>c</sup> , 3.23 <sup>d</sup>	12.02 <sup>c</sup> , 12.95 <sup>d</sup>	2.39 <sup>c</sup> , 2.45 <sup>d</sup>	1.89 <sup>c+j</sup> , 1.55 <sup>d+j</sup>	3.13 <sup>c</sup> , 3.23 <sup>d</sup>	2.39 <sup>c</sup> , 2.45 <sup>d</sup>	Siesta <sup>k</sup>
Ataca [276]	—	3.22 <sup>d,m</sup>	15.54 <sup>d</sup> , 12.41 <sup>m</sup>	2.44 <sup>m</sup>	—	3.22 <sup>d,m</sup>	2.44 <sup>m</sup>	QE <sup>p</sup>
Ataca [276]	—	3.26 <sup>m</sup> , 3.13 <sup>l</sup>	13.15 <sup>n</sup> , 12.14 <sup>l</sup>	—	—	3.25 <sup>n</sup> , 3.12 <sup>l</sup>	—	QE <sup>p</sup>

<sup>a</sup> PW91, E<sub>cut-off</sub>: 400 eV, 9 × 9 × 1  $k$ -points, Convergence: E<sub>step</sub><10<sup>-5</sup> eV, F<sub>max</sub><0.02 eV/Å

<sup>b</sup> Heya–Scuseria–Ernzerhof (HSE) hybrid functional [264]

<sup>c</sup> Local Density Approximation (LDA)

<sup>d</sup> Generalised Gradient Approximation (GGA)

<sup>e</sup> Local Density Approximation with Projector Augmented Wave (LDA+PAW)

<sup>f</sup> Generalised Gradient Approximation with Projector Augmented Wave (GGA+PAW)

<sup>g</sup> Iterative Green's Function (GW) or (GW<sub>0</sub>)  
<sup>h</sup> One-shot Green's Function (G<sub>0</sub>W<sub>0</sub>)

<sup>i</sup> PW91, E<sub>cut-off</sub>: 600 eV, 35 × 35 × 1  $k$ -points, Convergence: E<sub>step</sub><10<sup>-5</sup> eV, F<sub>max</sub><0.02 eV/Å

<sup>j</sup> Localised Orbital (LO)

<sup>k</sup> NOA, E<sub>cut-off</sub>: 200 Ry (=2721 eV), 30 × 30 × 30  $k$ -points, Convergence: E<sub>step</sub><10<sup>-5</sup> eV, F<sub>max</sub><0.01 eV/Å, Conjugate-Gradients

<sup>l</sup> Ultra-soft pseudo-potential

<sup>m</sup> GGA+D [277]

<sup>n</sup> GGA+DF [278]

<sup>p</sup> Quantum-ESPRESSO/PW91, E<sub>cut-off</sub>: 952 eV, 15 × 15 × 7/25 × 25 × 1  $k$ -points, Convergence: E<sub>step</sub><10<sup>-7</sup> eV, F<sub>max</sub><10<sup>-5</sup> eV/Å

the edges will be introduced to the model and the effect of loose atoms on the edges will be studied.

*“A theory can be proved by experiment; but no path leads from experiment to the birth of a theory.”*

— Albert Einstein

# Chapter 4

## Molybdenum Disulphide Nanoribbons

In the previous chapter the properties of both bulk and single-layer MoS<sub>2</sub> were calculated with periodic boundaries and no unsymmetrical atomic bond condition. However, in reality, there will be some asymmetric bonds on the edge of the sample and the free electrons and holes which are not participating in the atomic bonds on the edges will alter the electronic properties of the material. This is particularly important from a device and transport point of view, when nanoribbons are produced from the bulk form of MoS<sub>2</sub> material.

It is well established that the electronic properties and the band gap of two-dimensional materials can be altered and controlled by the edge pattern and the width of the produced nanoribbon from the two-dimensional materials [279–285].

The pattern of the atoms on the edge of the nanoribbon can be classified into two main categories of armchair and zigzag, as illustrated in Figure 4.1. However, it is also possible to cut the edges with any angle between these two categories which will lead to the creation of a nanoribbon known as having a chiral edge.

It is possible to obtain the MoS<sub>2</sub> nanoribbons directly by cutting through single layer MoS<sub>2</sub> [286]. In the case of the armchair nanoribbon, it can have two types of edges based

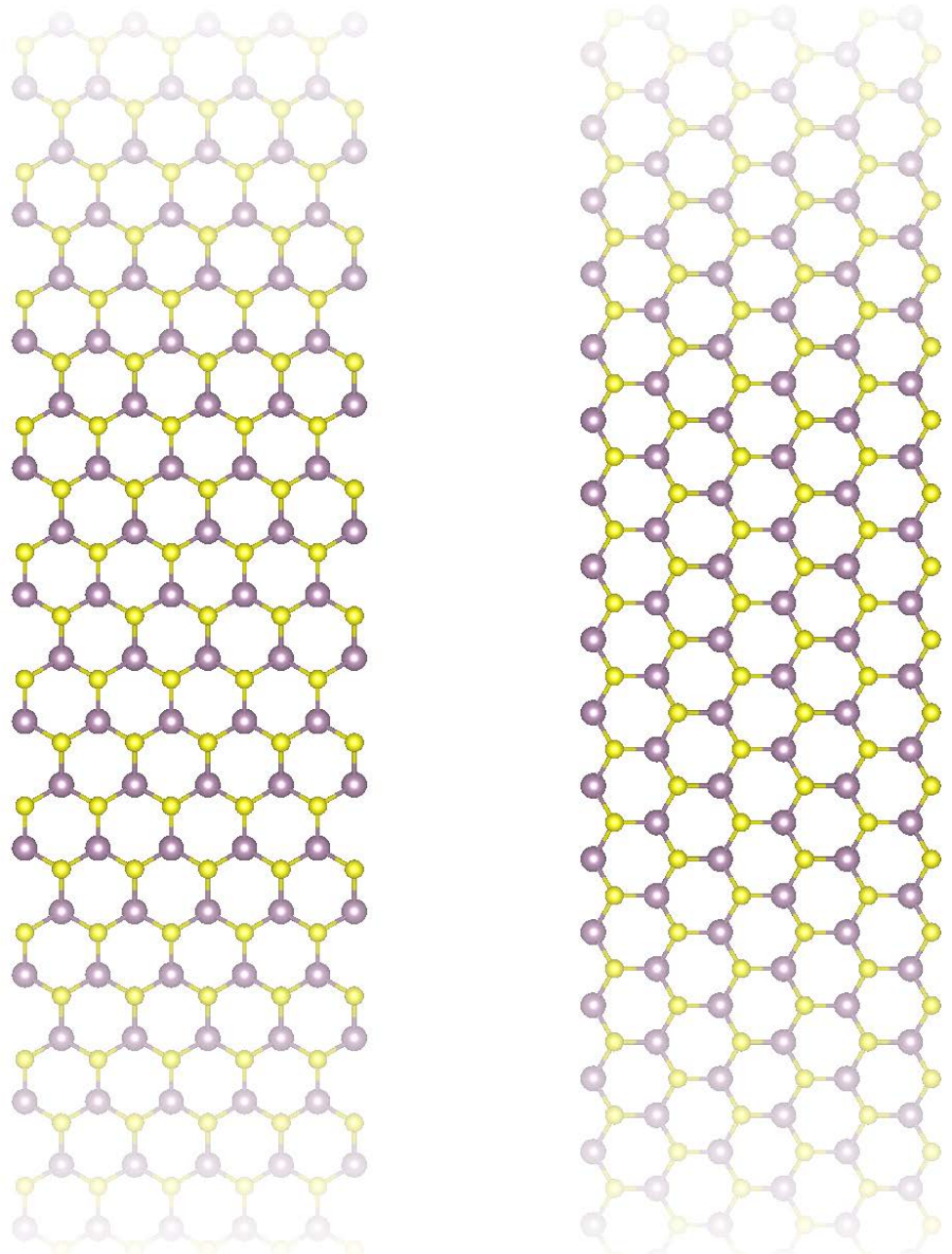


Figure 4.1: The armchair (left) and zigzag (right) edge patterns of MoS<sub>2</sub> nanoribbons.

on the number of atoms along the width of the produced nanoribbon. If the number of atoms along the width is even, the nanoribbon will have the same number of honeycomb cells along its length. However, an odd number of atoms along the width will result in an uneven number of honeycomb cells along the length of the nanoribbon. In both cases, the edge will have an equal number of sulphur and molybdenum atoms. The zigzag nanoribbon however, will always have one edge terminated by sulphur atoms and the other edge with molybdenum atoms.

## 4.1 Armchair Nanoribbons

To produce the MoS<sub>2</sub> armchair nanoribbon, a super cell was created from the modelled 1*H*-MoS<sub>2</sub> in the previous chapter, by translation of the coordinates to the Cartesian coordinates using Equation 3.1. Then a cubic cell was created with a 15 Å space along the *y* and *z* axes to emulate the vacuum. This means the unit cell's alpha, beta and gamma angles were all set to 90 degrees.

The crystallography space group that was used for the symmetry was the simple *P*1 space group. Figure 4.2 shows the unit cell used to model the MoS<sub>2</sub> armchair nanoribbon. By comparing the various techniques that were used in the previous chapter, it can be seen that the GGA+PAW technique produced the most realistic results compared to the experimental results; therefore, it was chosen for the modelling of the armchair nanoribbon.

After the convergence study, the one-dimensional Brillouin zone was sampled using  $16 \times 1 \times 1$  *k*-points. The energy cut-off value was chosen to be 25 Hartree with a 70 Hartree cut-off for the fine FFT grid.

The band diagram of the relaxed structure was modelled under both spin un-polarised and spin polarised conditions. It was observed that the armchair nanoribbon, regardless of the nanoribbon width, is semiconducting and does not show any magnetic behaviour and the net magnetic charge of the nanoribbon is always zero. Figure 4.3 shows the band

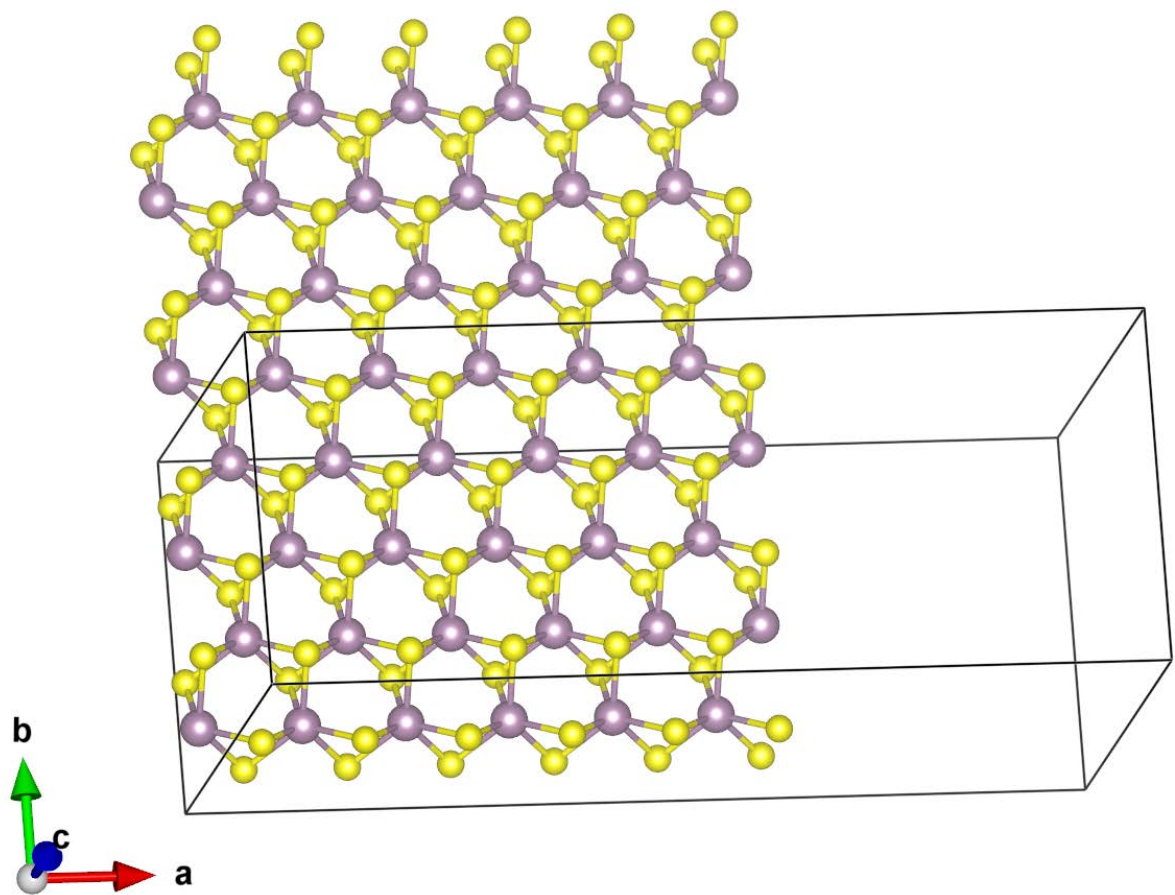


Figure 4.2: The super cell used to model MoS<sub>2</sub> armchair nanoribbons. Here a nanoribbon with eight atoms on the width is shown. The large purple atoms represent the molybdenum atoms and the smaller yellow atoms are sulphur atoms. The super cell is periodic along the *b* axis and discontinued along the *a* and *c* axes.

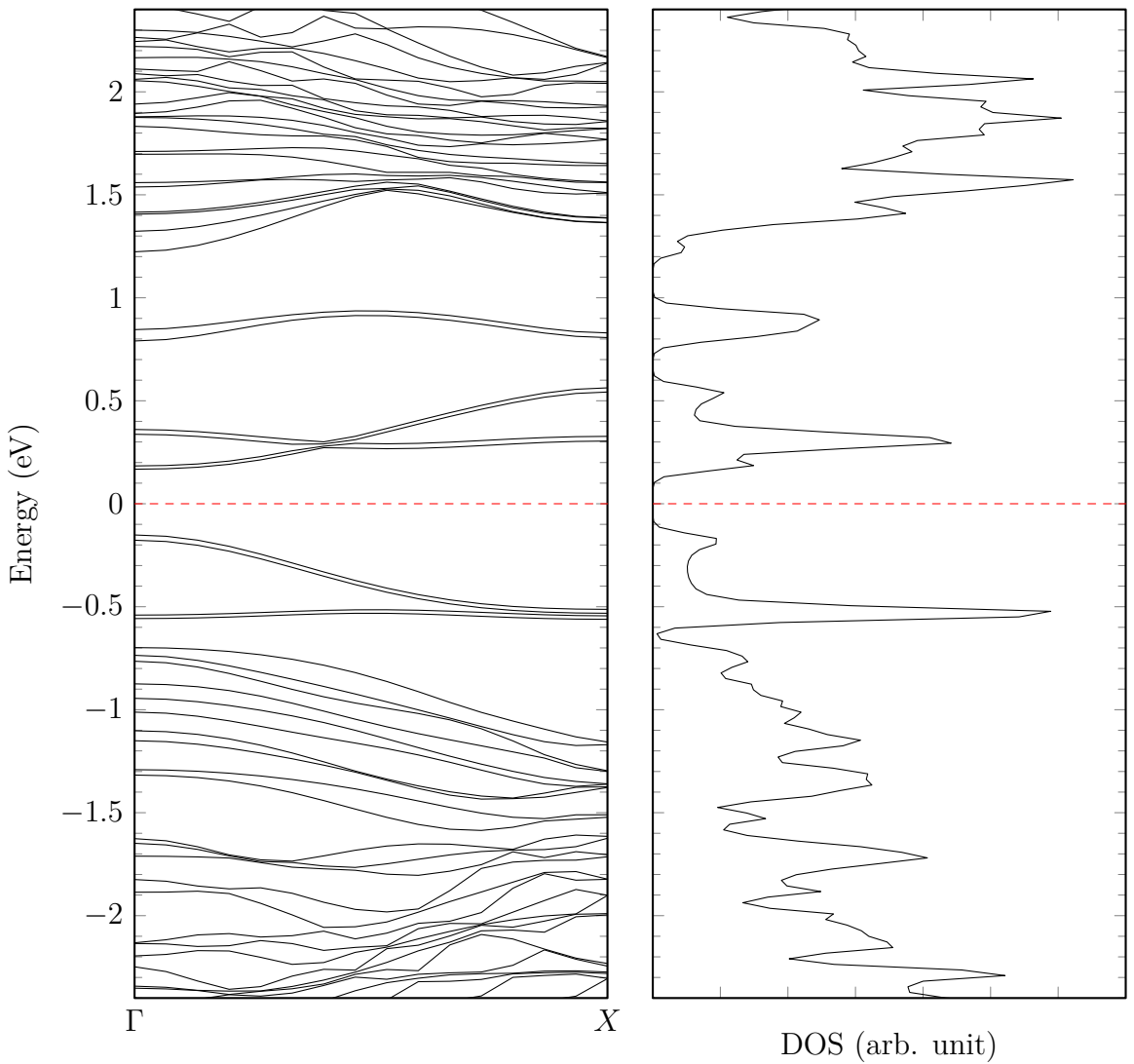


Figure 4.3: The band structure and density of states of a bare edge MoS<sub>2</sub> armchair nanoribbon with twelve atoms on the width of the nanoribbon.

gap of an armchair nanoribbon with twelve atoms along the width of the nanoribbon. Similarly Figure 4.4 shows the band structure of the same nanoribbon calculated over a unit cell twice as big (along the length of the nanoribbon) compared to the one used to calculate Figure 4.3. No edge reconstruction was observed during the relaxation and molecular dynamics performed on the 1x or 2x unit-cell.

The band gap of the MoS<sub>2</sub> armchair nanoribbon is direct and located at  $\Gamma$  point. The study of the variation of the band gap in relation to the width of the nanoribbon has revealed that the band gap in the MoS<sub>2</sub> armchair nanoribbon is more affected by the

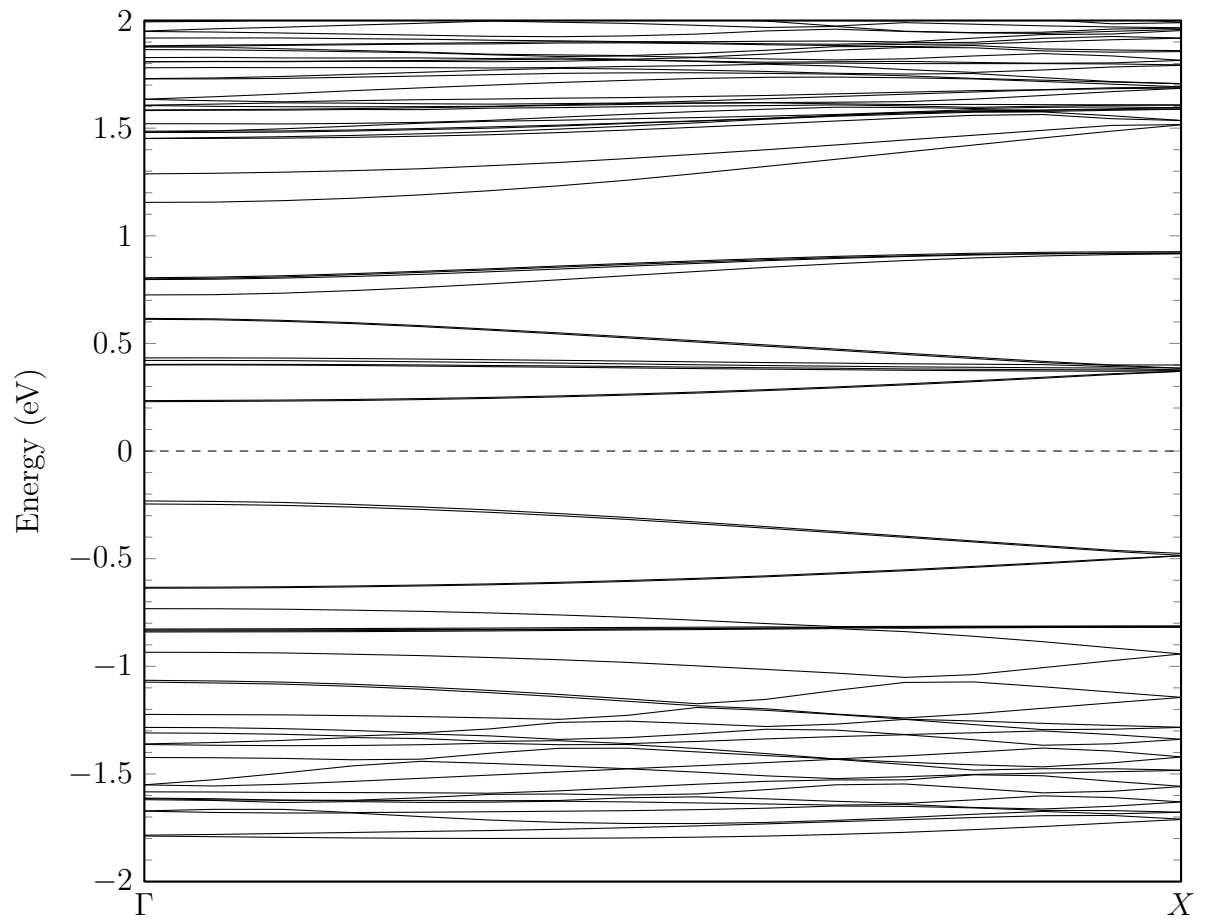


Figure 4.4: The band structure of an MoS<sub>2</sub> armchair nanoribbon with twelve atoms on the width of the nanoribbon calculated using two unit cells along the length of the nanoribbon.

edge symmetry, based on having an even or odd number of atoms along the width of the nanoribbon, rather than the width of the nanoribbon itself. However, by increasing the width of the nanoribbon this behaviour starts to vanish. This behaviour is displayed in Figure 4.5 for different nanoribbon widths. A similar result has also been reported by Ataca et al. [200], Li et al. [287] and Wang et al. [288].

As seen in Figure 4.5, the value of the band gap in a MoS<sub>2</sub> nanoribbon is considerably smaller than the single-layer MoS<sub>2</sub> and the trend in the band gap towards a single-layer band gap is insignificant. One explanation for this difference could be based on Ataca and Ciraci's [262] work on defects (vacancy) in single-layer MoS<sub>2</sub>. They have shown that a vacancy in single-layer MoS<sub>2</sub> will lead to the change of band gap and electrical properties of single-layer MoS<sub>2</sub> due to the dangling (unsymmetrical) bonds around the induced vacancy. This is very similar to the unsymmetrical bonds at the edges of the nanoribbon. Similar work to Ataca and Ciraci's [262] work was also carried out by Hong et al. [289].

The investigation of wave functions and the density revealed that most of the contribution towards the band gap and the energy bands near the band gap are from the atoms on the edge of the nanoribbon. Figure 4.6 shows the charge of a nanoribbon with twelve atoms along the width of the nanoribbon with the iso-surface level set to 0.25. Similarly, Figure 4.7 shows the same results but with a different iso-surface level (0.15) for better visualization of density near the sulphur atom. A dipole like potential at the molybdenum atoms on the edges is visible in Figure 4.6 that is mainly due to the unsymmetrical bound on the edges.

## 4.2 Zigzag Nanoribbons

The procedure to create the MoS<sub>2</sub> zigzag nanoribbon super cell was very similar to the steps that were taken in the previous section to model the MoS<sub>2</sub> armchair nanoribbon. However, the super cell is periodic along the *x* axis, as shown in Figure 4.8. After the

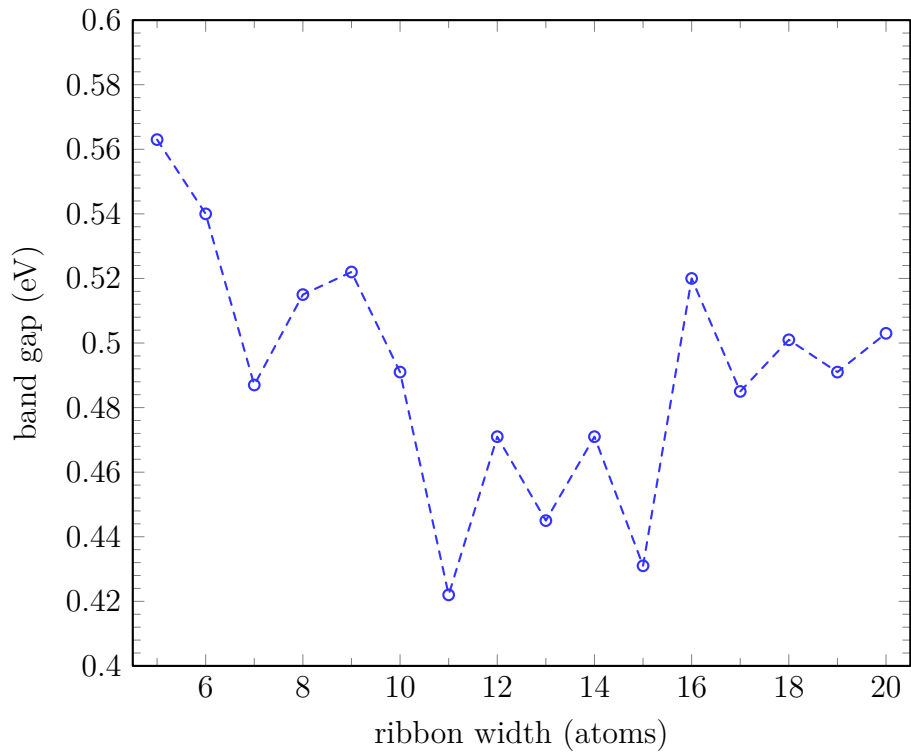


Figure 4.5: The band gap of an  $\text{MoS}_2$  armchair nanoribbon calculated using the GGA+PAW technique for different widths of nanoribbons. The effect of change in the edge symmetry between even and odd number of atoms along the width of the nanoribbon is clearly visible on the graph.

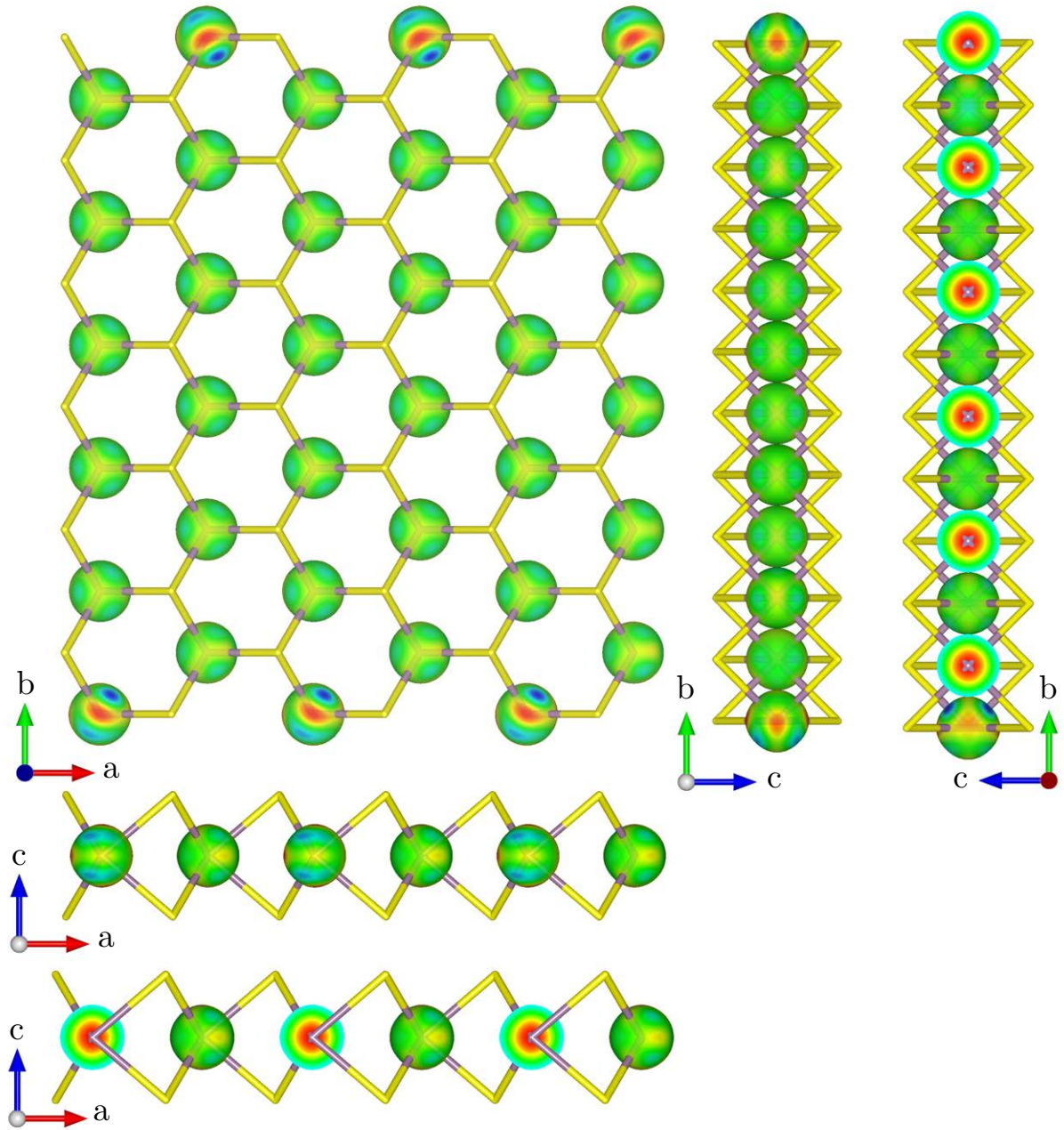


Figure 4.6: The density of electrons on the bare edge MoS<sub>2</sub> armchair nanoribbon. The iso-surface level is set to 0.25 and the colouring of the iso-surface is based on the total Kohn-Sham potential. The super cell is periodic along the *b* axis and discontinued along the *a* and *c* axes.

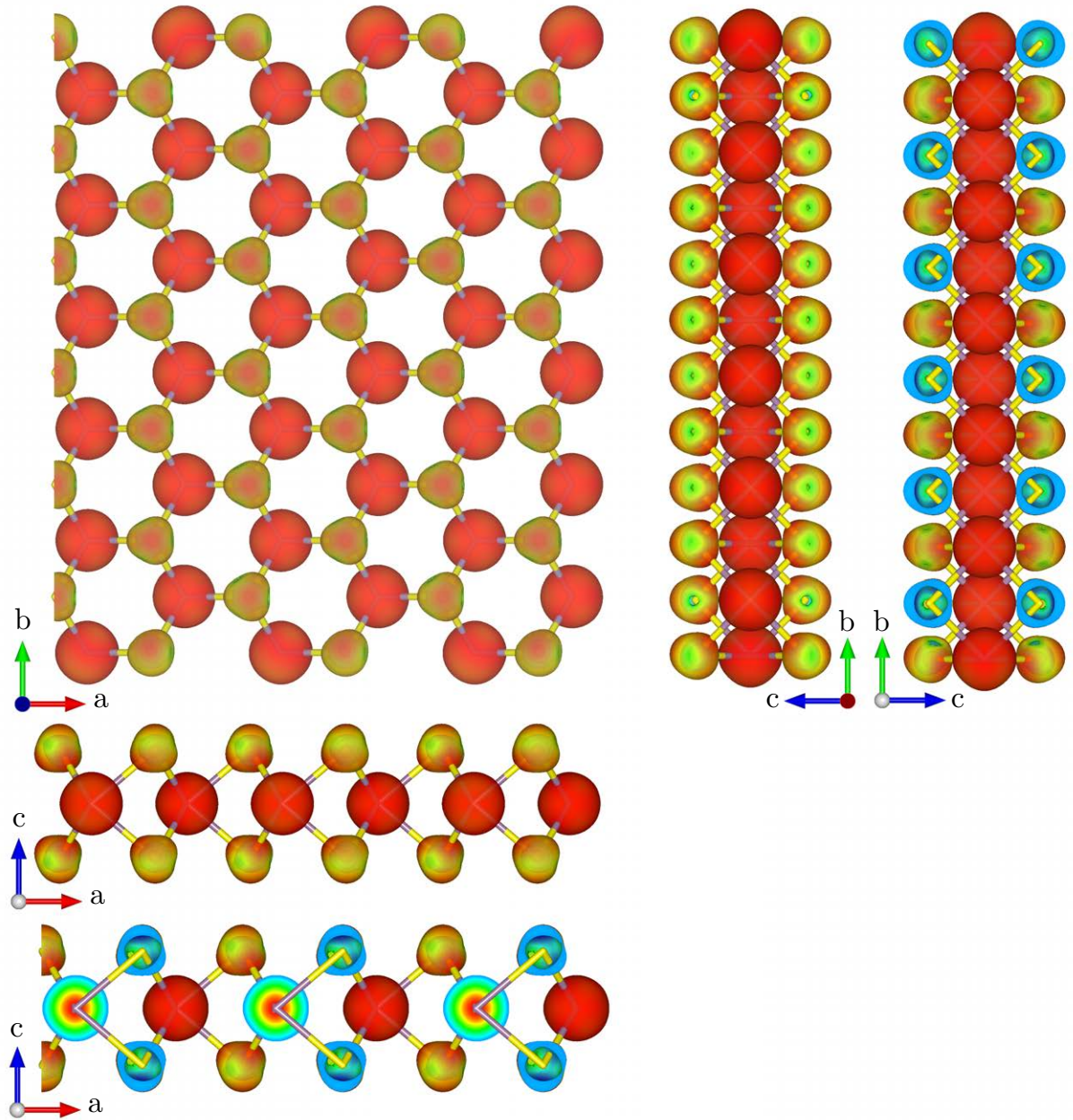


Figure 4.7: The density of electrons on the bare edge MoS<sub>2</sub> armchair nanoribbon. The iso-surface level is set to 0.15 and the colouring of the iso-surface is based on the total Kohn-Sham potential. The super cell is periodic along the *b* axis and discontinued along the *a* and *c* axes.

convergence study, the same number of  $k$  sampling points ( $16 \times 1 \times 1$ ) and cut off energy (25 and 70 Hartree) have been used for the MoS<sub>2</sub> zigzag nanoribbon. Figure 4.9 shows the band structure and density of states (DOS) of a zigzag nanoribbon with ten atoms along the width of the nanoribbon in a ferromagnetic state and Figure 4.10 is showing the same nanoribbon in an anti-ferromagnetic state. In both cases the ground state energy of the nanoribbon was -1862.697675 Hartree (-50686.5814 eV).

Recent calculations of the electrical and magnetic properties of MoS<sub>2</sub> nanoribbons have shown considerable disparities. As it has been reported in the literature, MoS<sub>2</sub> zigzag nanoribbons, regardless of the width or edge state (bare edges or passivated edges using hydrogen atoms) are metallic and magnetic. However, the reported magnetic and metallic types are inconsistent [200, 201, 287].

#### 4.2.1 Spin Polarisation and Magnetic Properties

Unlike MoS<sub>2</sub> armchair nanoribbons, the MoS<sub>2</sub> zigzag nanoribbons have collinear magnetic properties and exhibit both ferromagnetic and anti-ferromagnetic behaviour. This behaviour is mainly due to dangling and unsymmetrical bonds on the edges of the nanoribbon, with loose electrons and holes which do not participate in the bonding.

The results obtained based on the used model, suggests that in MoS<sub>2</sub> zigzag nanoribbons, the spin polarised ground state is energetically more favourable than the spin unpolarised ground state with an energy difference of at least 43meV (1.59mHa) per supercell. Table E.6 in Appendix E provides the ground state energy of each nanoribbon for comparisons. Surprisingly, both the ferromagnetic and anti-ferromagnetic ground states of zigzag nanoribbons have identical energy and are equally probable.

The molybdenum edge of zigzag nanoribbons is always ferromagnetic, having either spin up or down. However, the magnetic alignment on the sulphur edge of the nanoribbon is anti-ferromagnetic. Depending on the initial spin direction on the molybdenum atoms on the sulphur side of the nanoribbon, whether it is aligned-parallel to the other edge or opposite-parallel, the net magnetic dipole moment of the nanoribbon can become either

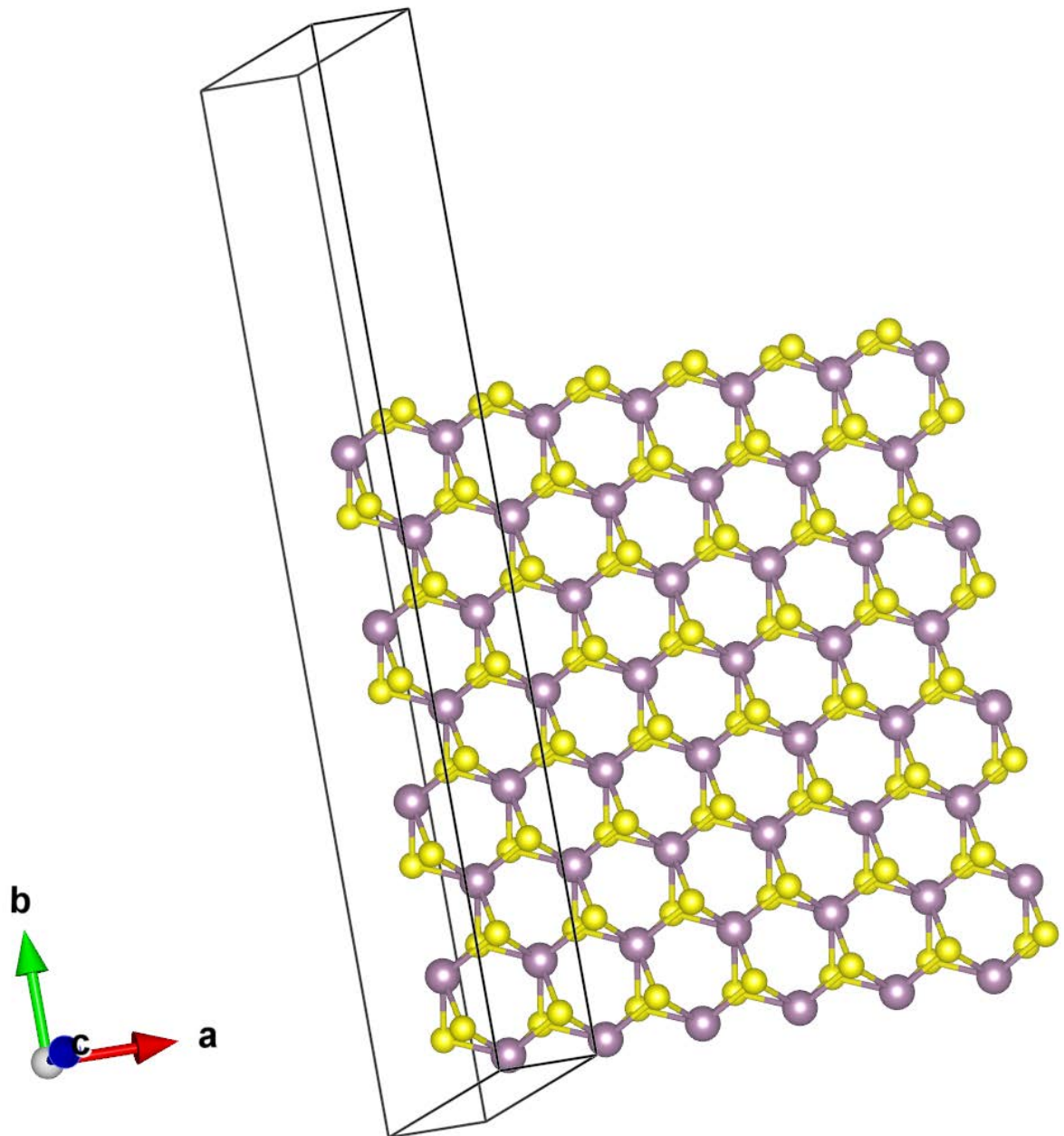


Figure 4.8: The super cell used to model MoS<sub>2</sub> zigzag nanoribbons. Here a nanoribbon with sixteen atoms on the width is shown. The large purple atoms represent the molybdenum atoms and the smaller yellow atoms are sulphur atoms. The super cell is periodic along the *a* axis and discontinued along the *b* and *c* axes.

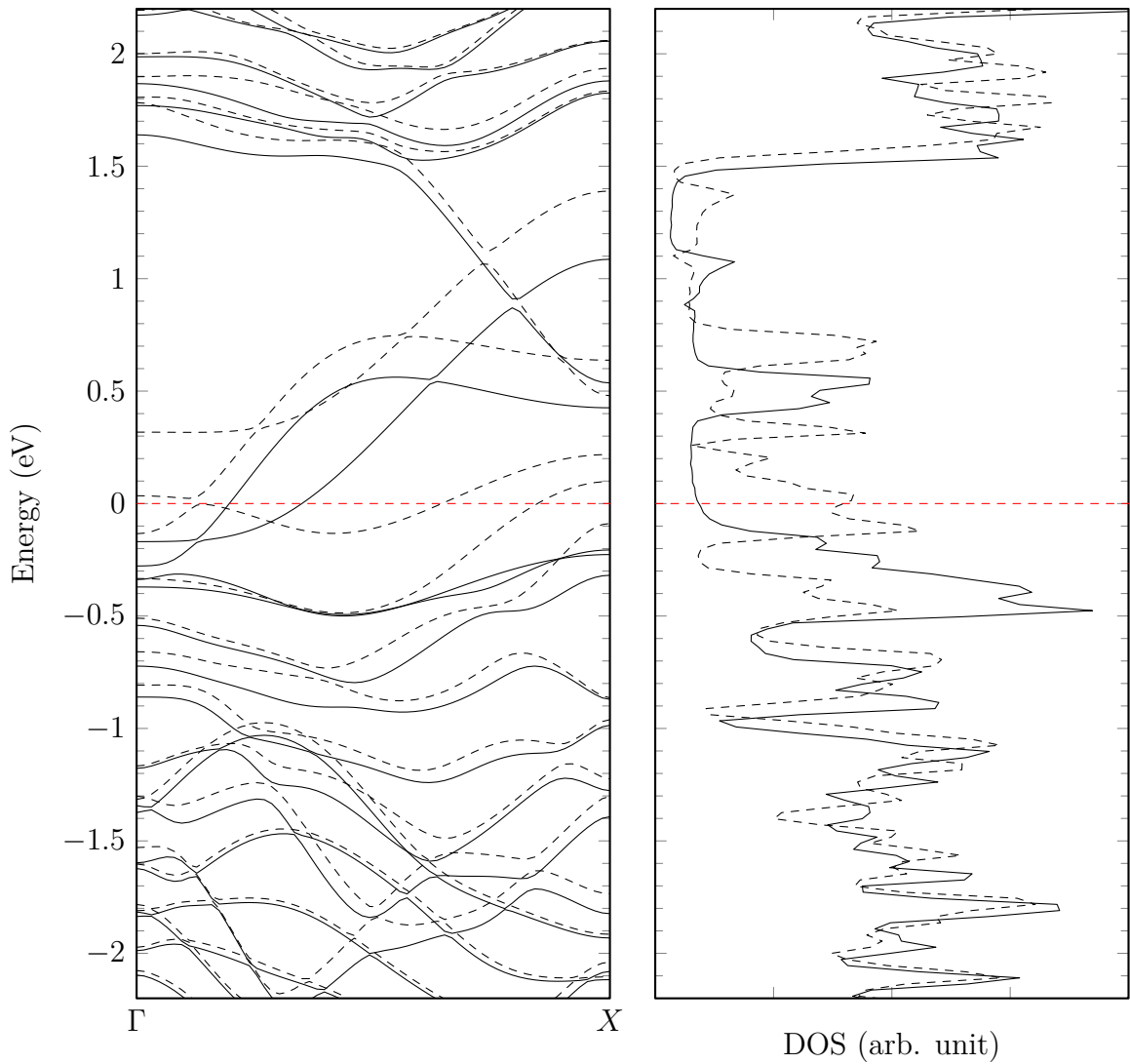


Figure 4.9: The spin polarised band structure and density of states (DOS) of  $\text{MoS}_2$  zigzag nanoribbon with ten atoms along the width of the nanoribbon in a ferromagnetic state with a total magnetization of  $0.932\mu_B$  per super-cell. The solid lines represent the spin up and the dashed lines are the spin down energy bands.

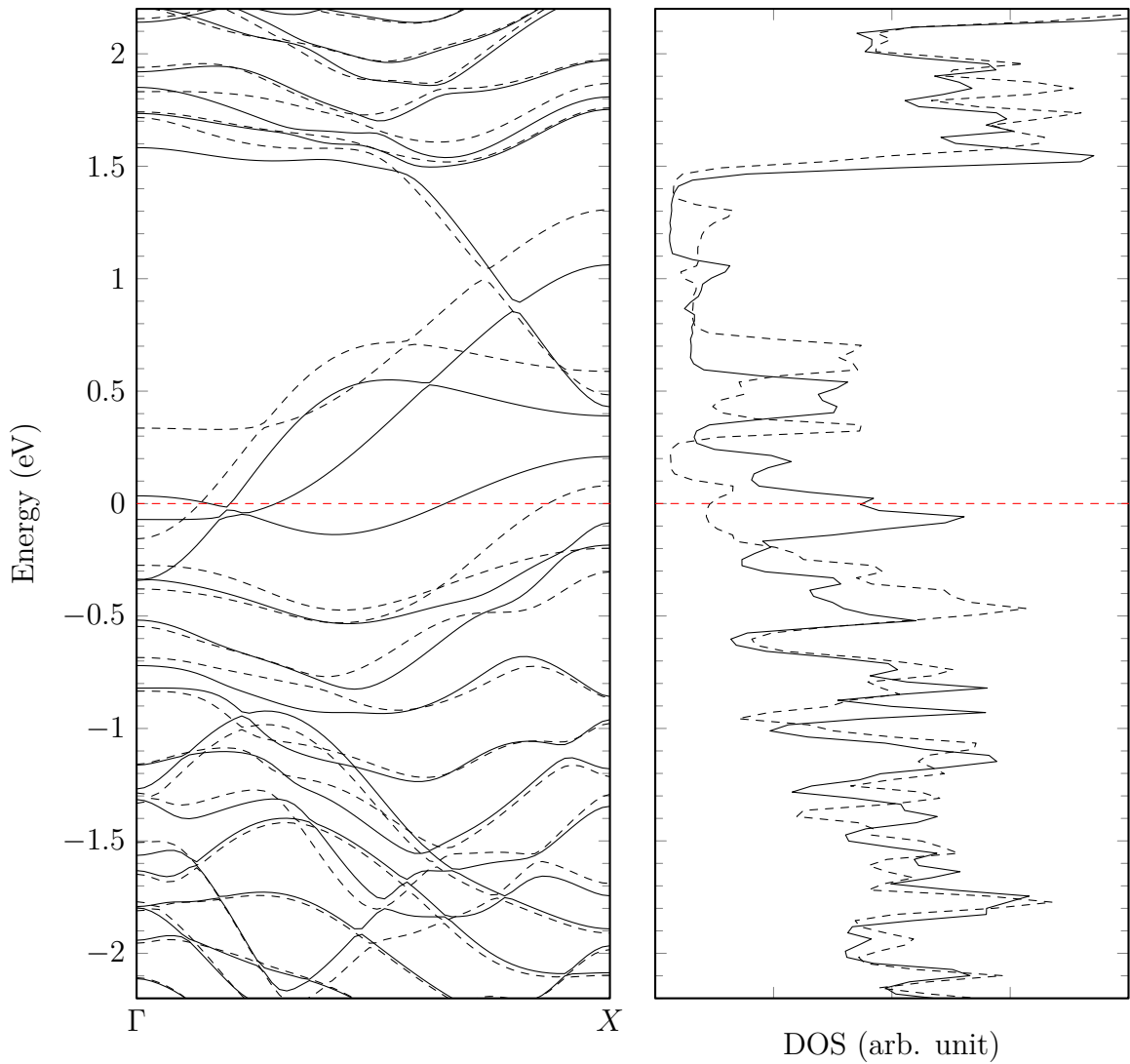


Figure 4.10: The spin polarised band structure and density of states (DOS) of  $\text{MoS}_2$  zigzag nanoribbon with ten atoms along the width of the nanoribbon in an anti-ferromagnetic state with a total magnetization of  $0.002\mu_B$  per super-cell. The solid lines represent the spin up and the dashed lines are the spin down energy bands.

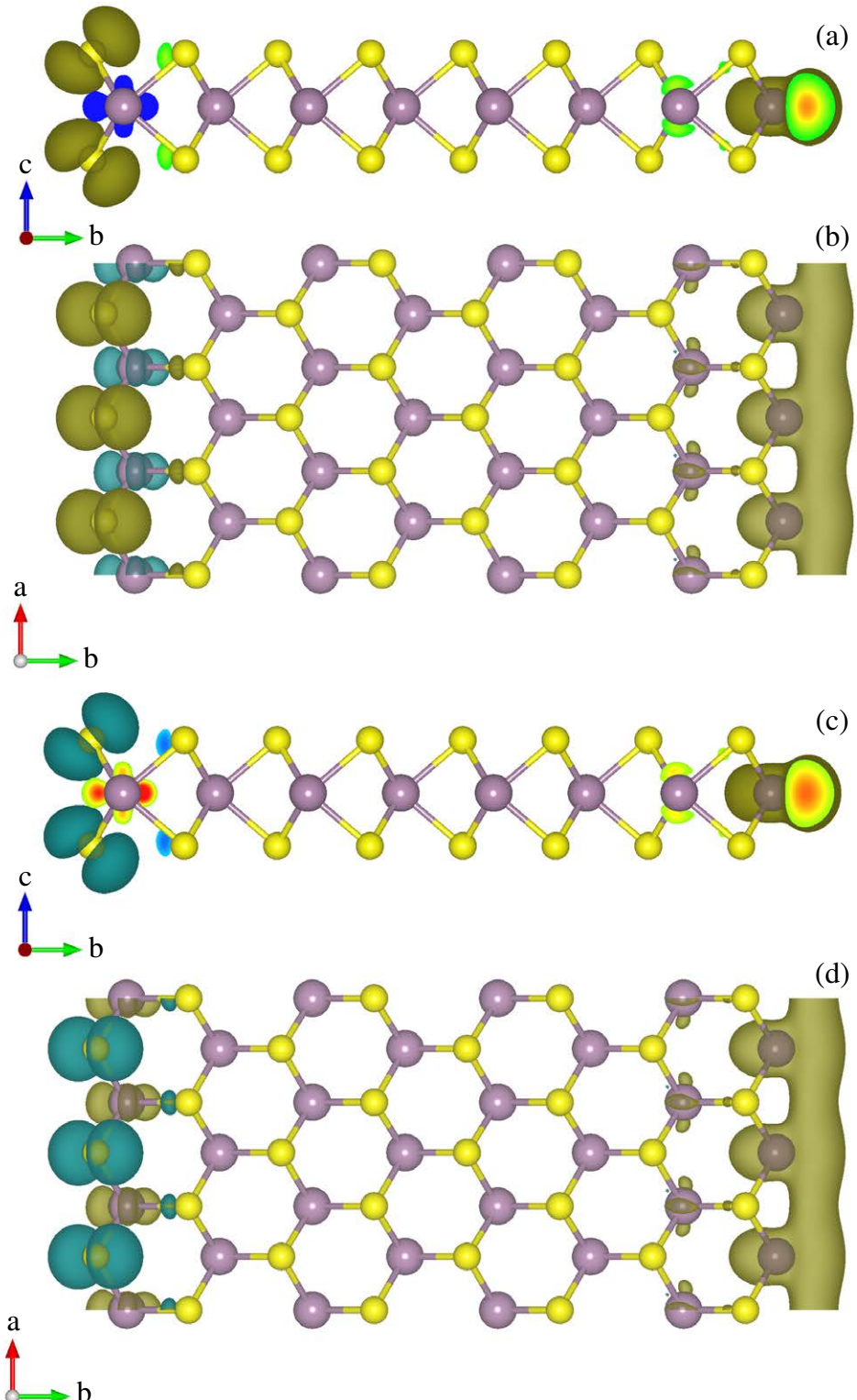


Figure 4.11: The different magnetic moments on the edge of an  $\text{MoS}_2$  zigzag nanoribbon with 16 atoms along the width of the nanoribbon. The top two (a and b) illustrations show the nanoribbon in a ferromagnetic state and the bottom two (c and d) illustrations are the same nanoribbon in an anti-ferromagnetic state.

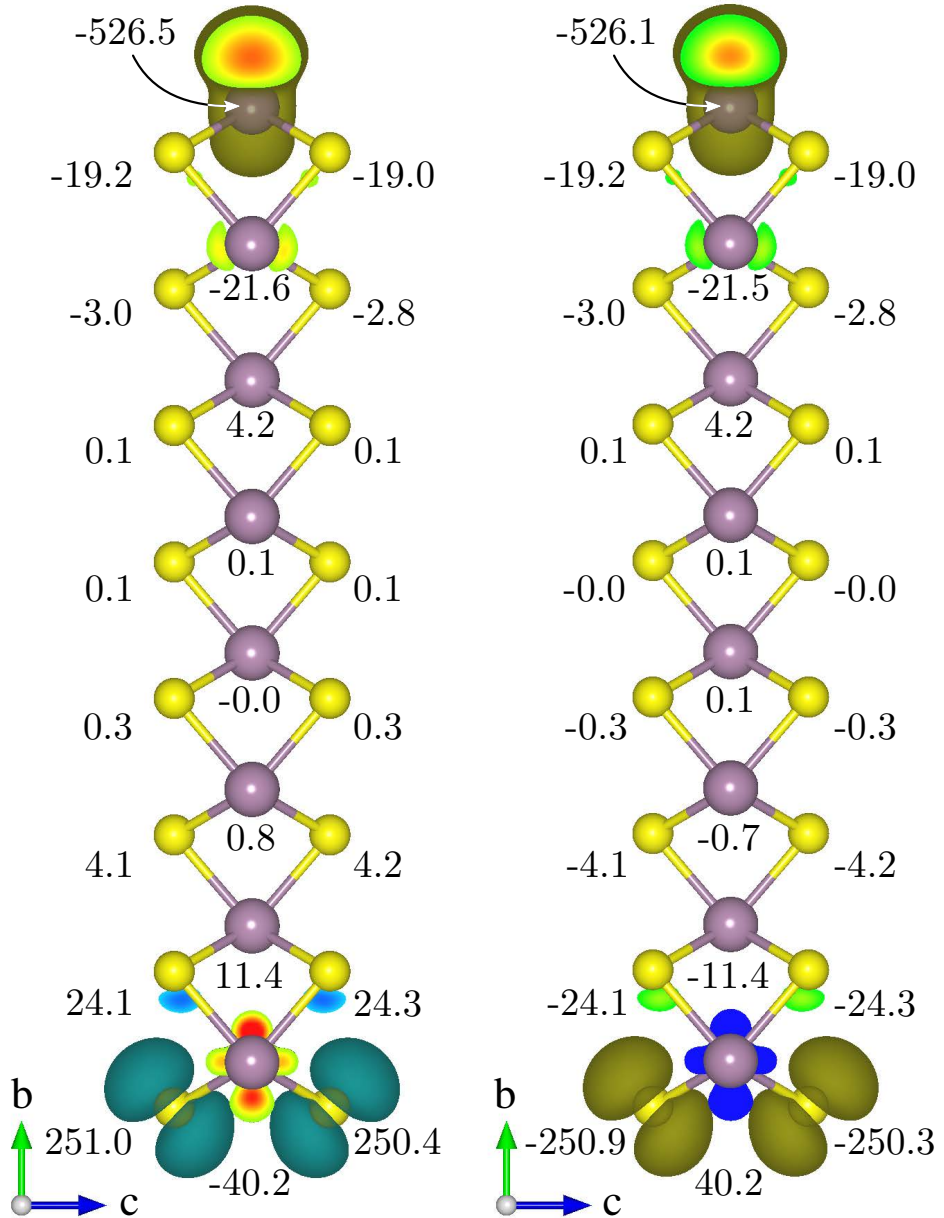


Figure 4.12: The atom resolved Hirshfeld charge calculated for an  $\text{MoS}_2$  zigzag nanoribbon with 16 atoms along the width. On the left the nanoribbon is in the anti-ferromagnetic state and the same nanoribbon in a ferromagnetic state is presented on the right. The partial charges quoted on the figure are scaled up by a factor of  $10^3$  for better readability. The quoted negative zeros mean a very small negative charge.

ferromagnetic or anti-ferromagnetic. If the induced magnetic moments on the sulphur atoms, due to the neighbouring molybdenum atoms at the sulphur edge and molybdenum atoms on the other edge, show the same aligned-parallel spin, the nanoribbon will become ferromagnetic; while the sulphur atoms can have the opposite spin relative to the molybdenum atoms on the other side. Having opposite spin will cause the nanoribbon to become quasi anti-ferromagnetic with a very small magnetic dipole moment of less than 0.05 Bohr magneton ( $\mu_B$ ) across the super-cell. Figure 4.11 illustrates this behaviour of zigzag MoS<sub>2</sub> nanoribbons. For a better illustration of this effect, the Hirshfeld charge [290] of each atom is presented next to the atoms in Figure 4.12. The complete list of Hirshfeld charges of each atom for various types of zigzag nanoribbons are tabulated in section F.2 of Appendix F.

The calculation on the magnetic moment of a MoS<sub>2</sub> zigzag nanoribbon was done several times with a complete set of random initial spin states on each occasion and in all cases the total energy converged to the same value; while the nanoribbon had two different magnetic moments (anti-ferro- and ferromagnetic). This result strongly suggests that the significant variety of magnetic moments reported in zigzag nanoribbons [200, 201, 287] is due to this spin initialisation.

### 4.3 Summary

In this chapter, the electrical properties of the nanoribbons built from 1H-MoS<sub>2</sub> with either armchair or zigzag edges were investigated using PBE GGA+PAW approximation of the DFT calculation. It was shown that unlike graphene, the band gap in MoS<sub>2</sub> armchair nanoribbons is not significantly affected by the width of the nanoribbon. It was also noted that the MoS<sub>2</sub> armchair nanoribbons are always semiconducting; while the MoS<sub>2</sub> zigzag nanoribbons are always metallic and magnetic. During the atomic force relaxation and molecular dynamics studies, no obvious edge reconstruction was observed in 1x or 2x super-cell and reconstruction in the edges of zigzag and armchair nanoribbons

is not reported in the literature. However, during the preparation of this thesis, Cui et al. [291] reported on the possibility of the edge reconstruction in sulphur edges of zigzag nanoribbon using 2x super-cell.

The intensive modelling and spin simulation on the MoS<sub>2</sub> zigzag nanoribbons suggested that this material can take both ferromagnetic and anti-ferromagnetic states with equal probability and this can be the reason behind the various magnetic behaviours reported on the MoS<sub>2</sub> zigzag nanoribbons in the literature.

In the next chapter, various types of absorption of the atoms on the edges of both MoS<sub>2</sub> zigzag and armchair nanoribbons will be investigated and the effect of passivated edges on the electronic properties of this material will be explored.

*“No amount of experimentation can ever prove me right; a single experiment can prove me wrong.”*

— Albert Einstein

# Chapter 5

## Molybdenum Disulphide Nanoribbon Edges

In the previous chapters it was shown that after introducing edges on the MoS<sub>2</sub> material, the appearance of the loose atoms on these edges will alter the electrical properties of the material. It is a common practice to add extra atoms on the edges of material to create bonds with loose atoms and ‘passivate’ the active states on the edges.

### 5.1 Edge Passivation

The passivation of the edges is usually carried out using hydrogen atoms [201, 292–294]; however, the usage of other atoms is also possible [295, 296]. This technique is expected to increase the stability of the material and naturalise the edges [286].

To passivate the edges on MoS<sub>2</sub> armchair nanoribbons using hydrogen atoms, the super cell was modified to contain one and two hydrogen atoms per sulphur and molybdenum atom inside the super cell respectively. The hydrogen atoms were initially located at a distance equal to the summation of the covalent radii of each edge atom and the hydrogen from Table 5.1 with an angle of 128 ° relative to other participating atoms in that bond [296]. However, in the case of molybdenum atoms, the two hydrogen atoms added to the molybdenum were placed with an angle of 59 ° [296] (H-Mo-H bond angle).

Table 5.1: The covalent radii values of used atoms to create passivated nanoribbon obtained from [297].

Atomic number	Atom (symbol)	Covalent radii (Å)
1	hydrogen (H)	0.31
16	sulphur (S)	1.05
42	molybdenum (Mo)	1.54

Table 5.2: The obtained parameters for hydrogen bonds on the edges of MoS<sub>2</sub> zigzag and armchair nanoribbons after moving the ions and relaxing the structures.

Measure	Armchair		Zigzag	
	left side	right side	sulphur side	molybdenum side
$d_{Mo-H}$ (Å)	1.718	1.718	—	1.749
$d_{S-H}$ (Å)	1.358	1.358	1.393	—
$\theta_{H-Mo-S}$ (°)	89±1, 136±1	89±1, 136±1	—	85±3, 132±2
$\theta_{H-S-Mo}$ (°)	97.0±0.3	97.0±0.3	101.0±1	—
$\theta_{H-Mo-H}$ (°)	69.60	69.61	—	70.56

The new super cell for the passivated armchair nanoribbon was created with four hydrogen atoms on each edge (two on the molybdenum atom and one on each sulphur atom) leading to a total of eight hydrogen atoms per super cell; while in the case of the zigzag nanoribbon, each edge was naturalised using two hydrogen atoms with a total of four hydrogen atoms per super cell. This procedure is the same regardless of the width of the nanoribbon. For both armchair and zigzag nanoribbons, the distance between the hydrogen and molybdenum atoms was set to 1.85 Å and a value of 1.36 Å was used for the distance between the hydrogen and sulphur atoms.

After moving the ions and optimising the forces and energies, in the case of the MoS<sub>2</sub> armchair nanoribbon, the distance between the hydrogen atoms and molybdenum atoms was reduced to 1.71 Å; while the distance between the hydrogen atoms and sulphur atoms converged to a value of 1.35 Å. Similarly, for the zigzag nanoribbon the bond lengths of Mo-H and S-H were changed to 1.75 Å and 1.39 Å respectively. Table 5.2 summarises the hydrogen bonding details after convergence and the converged super cell for armchair and zigzag nanoribbons are illustrated in Figures 5.1 and 5.2 respectively.

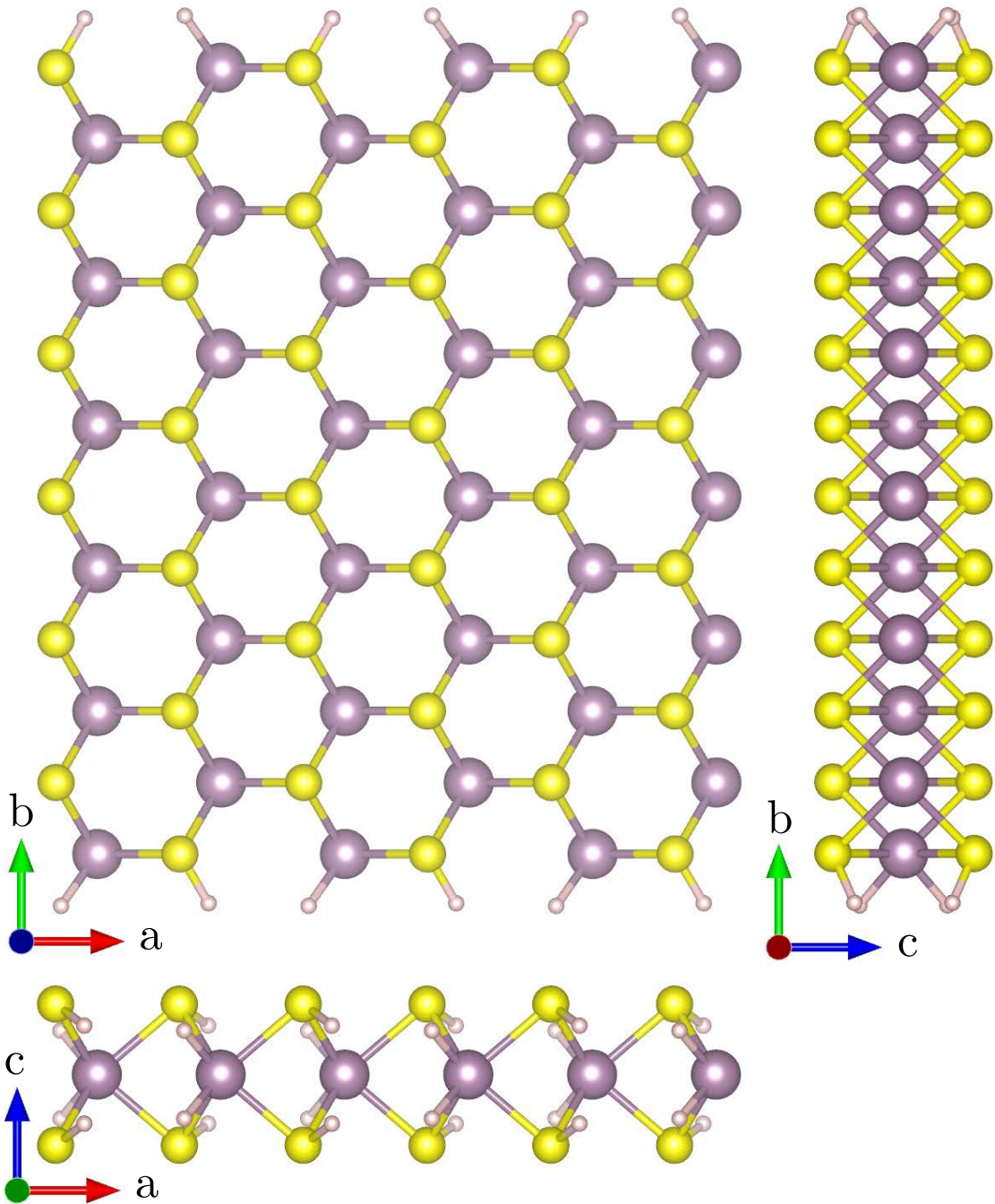


Figure 5.1: The super cell of the molybdenum disulphide armchair nanoribbon with passivated edges using hydrogen atoms (repeated 3 times along *a* axis).

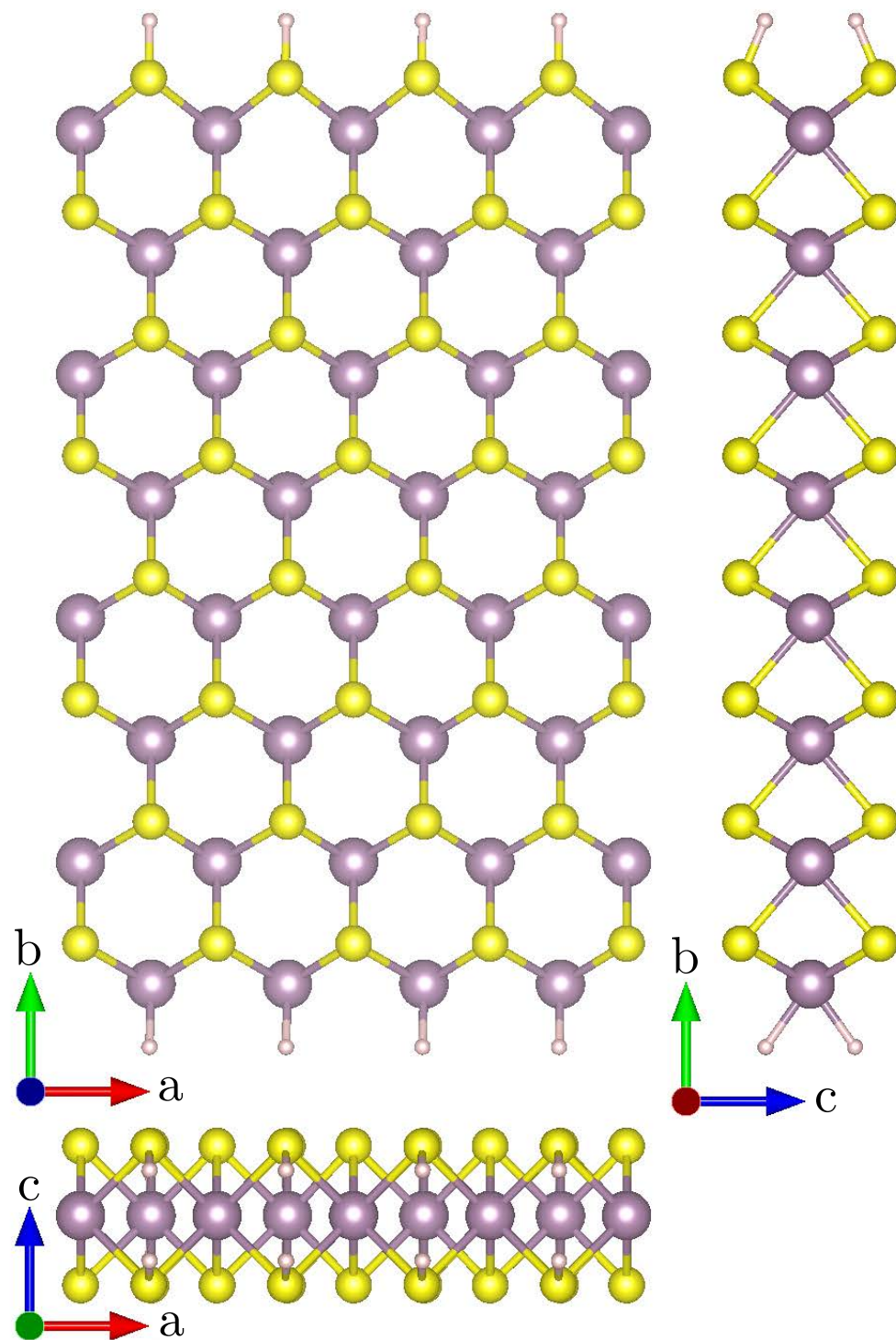


Figure 5.2: The super cell of the molybdenum disulphide zigzag nanoribbon with passivated edges using hydrogen atoms (repeated 4.5 times along  $a$  axis).

Previously, the calculation of Botello-Mendez et al. [201] showed that the MoS<sub>2</sub> armchair nanoribbons are only semiconducting if the edges are passivated with hydrogen atoms; while the results reported by Ataca et al. [200] disagree. However to the best of the author's knowledge, Botello-Mendez's work [201] is the only reported magnetic behaviour for armchair nanoribbons. One difference in Botello-Mendez's work compared to other published works is the use of a rhombohedral super cell instead of the usual cubic super cell. However, using a similar rhombohedral unit cell did not produce the same result and it was similar to the cubic unit cell. Additionally, they only considered 6 valence electrons for the molybdenum, while other works including this research considered semi-core pseudo-potential for molybdenum. Ataca et al. [200] showed that the passivation of the edges on armchair nanoribbons increases the band gap; the result from the calculation carried out in this work favours the results of Ataca et al. However, the results obtained for the MoS<sub>2</sub> zigzag nanoribbons are in-line with the results of Botello-Mendez et al. [201] and differ from those of Ataca et al. [200]. Table 5.3 and 5.4 summarize some of the reported types and magnetic values for armchair and zigzag nanoribbons. Figure 5.3 shows the band structure of an edge passivated MoS<sub>2</sub> armchair nanoribbon with twelve atoms on the width of the nanoribbon; and Figures 5.4 and 5.5 show the corresponding charge density with two different iso-surfaces.

## 5.2 MoS<sub>2</sub> Zigzag Nanoribbons

The magnetic behaviour of the zigzag nanoribbons was further explored by modelling possible partial passivation of the edges of the nanoribbon for a better insight into their behaviour. The simulations' results showed that passivating the edges with two (on either molybdenum or sulphur side) or four hydrogen atoms does not change the state of the nanoribbon from metallic to semiconducting. However, in the case of two and four hydrogen passivated edges, when the zigzag nanoribbon is showing anti-ferromagnetic behaviour, it will become semi-metallic with only energy bands corresponding to one of the

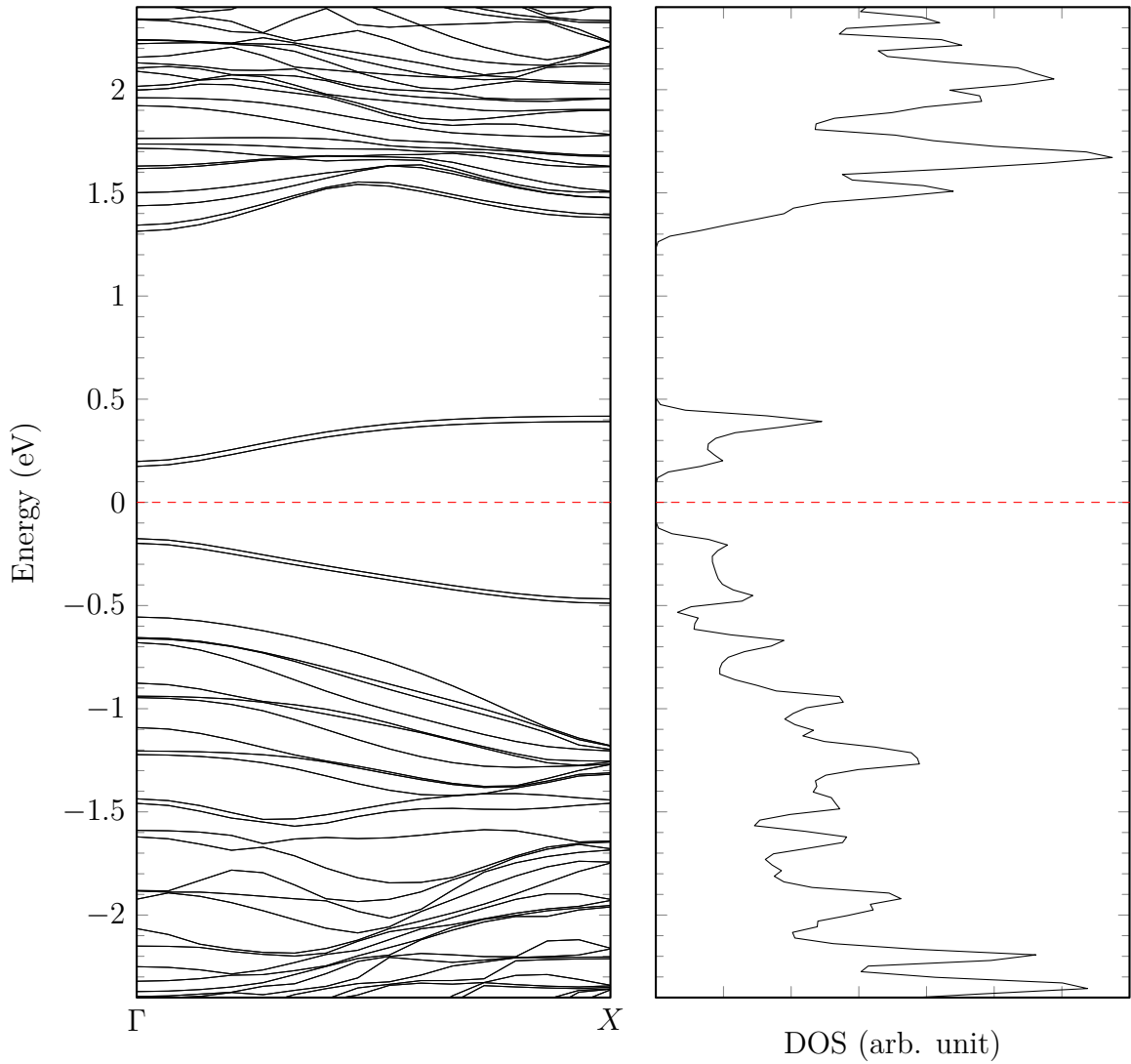


Figure 5.3: The band structure of an edge passivated  $\text{MoS}_2$  armchair nanoribbon with twelve atoms on the width of the nanoribbon and eight hydrogen atoms on the edges (four on each side).

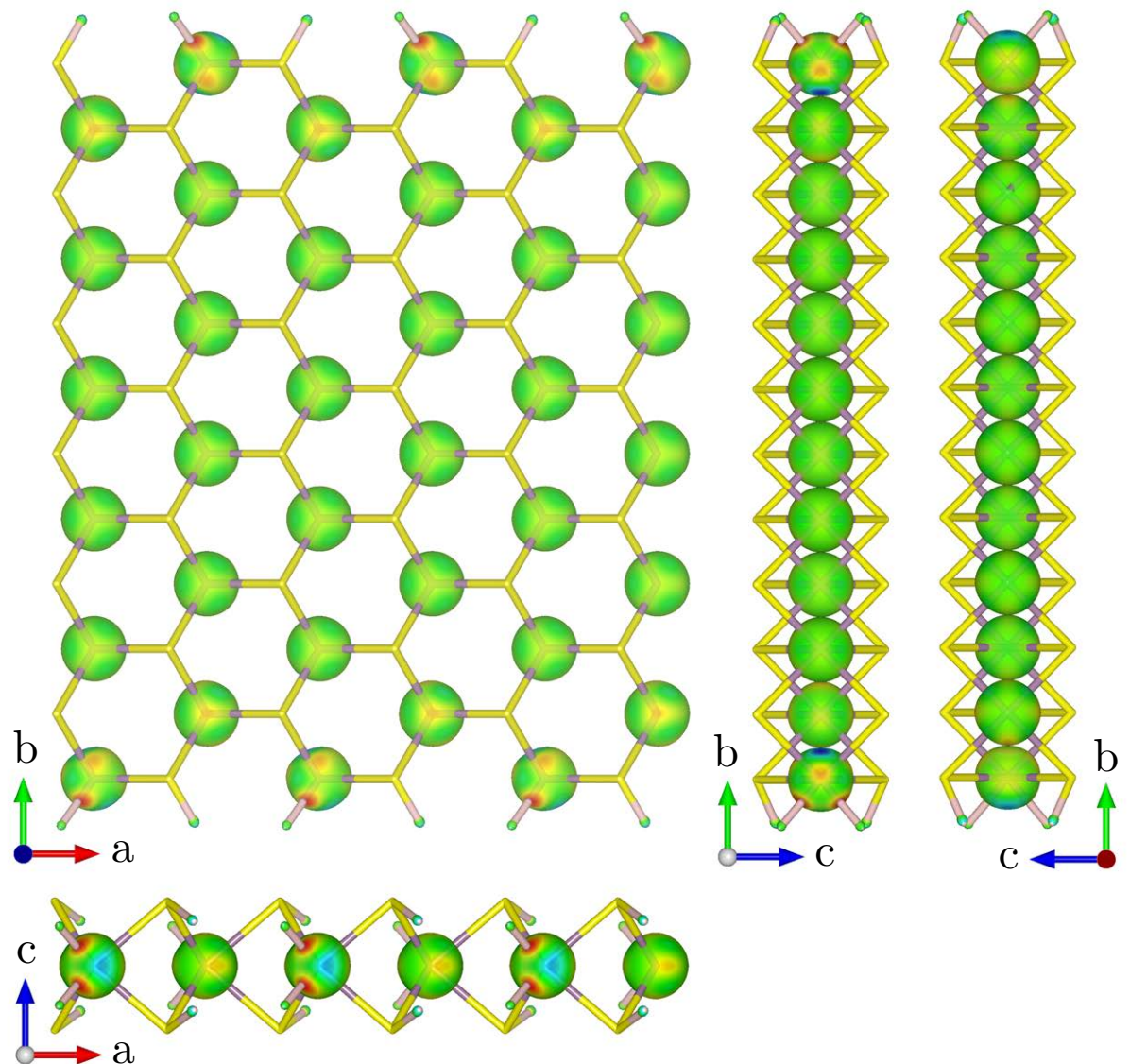


Figure 5.4: The density of electrons on the hydrogen passivated edge MoS<sub>2</sub> armchair nanoribbon. The iso-surface level is set to 0.25 and the colouring of the iso-surface is based on the total Kohn-Sham potential.

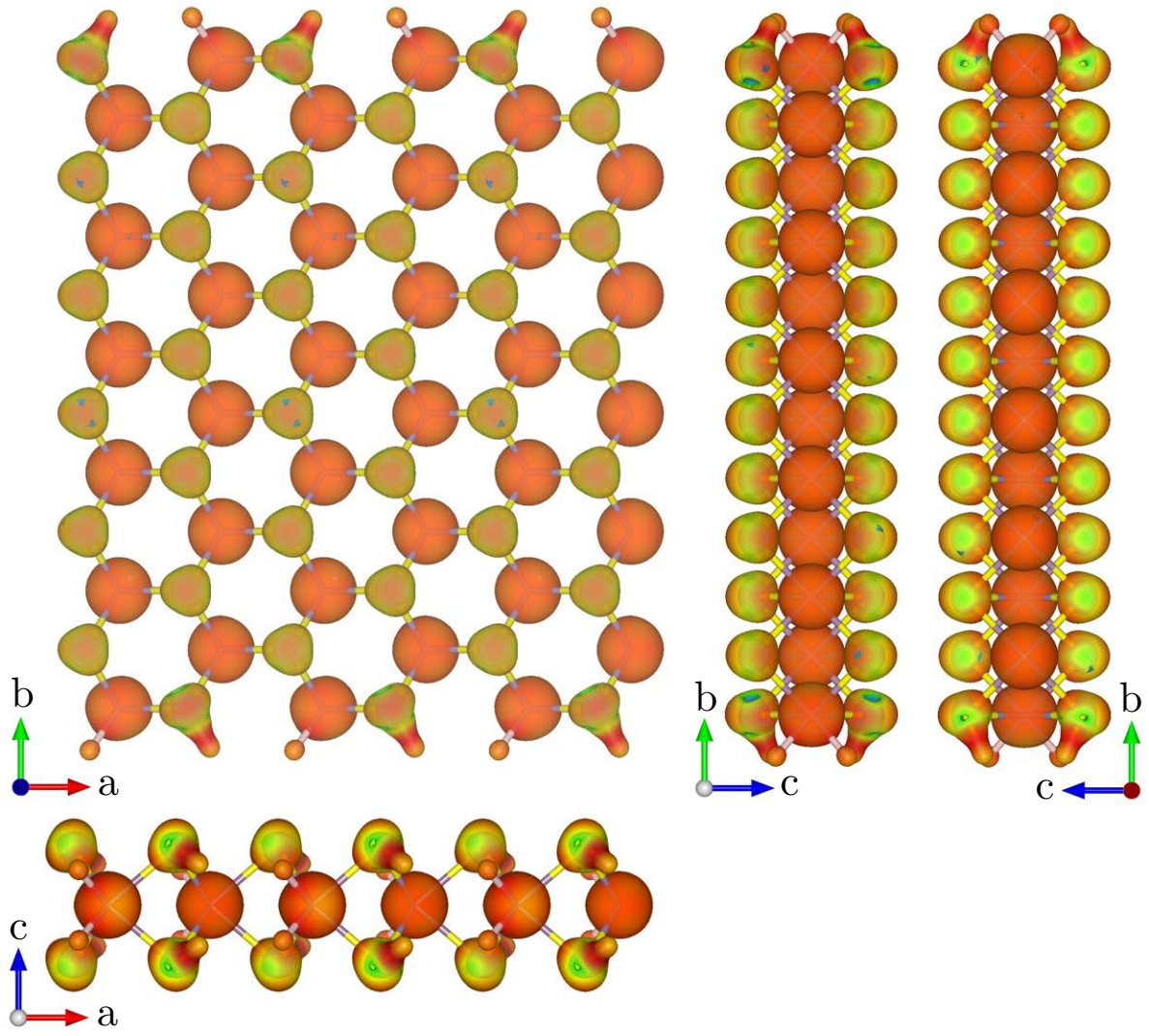


Figure 5.5: The density of electrons on the hydrogen passivated edge MoS<sub>2</sub> armchair nanoribbon. The iso-surface level is set to 0.15 and the colouring of the iso-surface is based on the total Kohn-Sham potential.

Table 5.3: A few of the reported MoS<sub>2</sub> nanoribbon types in the literature compared to this work. Here M, SM, S and MG stands for metallic, semi-metallic, semiconducting and magnetic respectively.

Work	Bare edge armchair				Passivated armchair				Software	Technique
	M	SM	S	MG	M	SM	S	MG		
Botello-Mendez [201]	✓			✓			✓		NAO	TM <sup>b</sup>
Li [287]		✓					✓		VASP	GGA+PAW
Ataca [200]		✓					✓		VASP	GGA+PAW
Pan [286]		✓					✓		VASP	GGA+PAW
This work		✓					✓		ABINIT	Various <sup>c</sup>

Work	Bare edge zigzag				Passivated zigzag				Software	Technique
	M	SM	S	MG	M	SM	S	MG		
Botello-Mendez [201]	✓			✓	✓				✓ <sup>a</sup>	NAO
Li [287]		✓			✓				VASP	TM <sup>b</sup>
Ataca [200]			✓		✓				VASP	GGA+PAW
Pan [286]		✓			✓				VASP	GGA+PAW
This work		✓		✓ <sup>d</sup>	✓	✓	✓ <sup>e</sup>	✓	ABINIT	Various <sup>c</sup>

<sup>a</sup> anti-ferromagnetic

<sup>b</sup> Troullier-Martins

<sup>c</sup> LDA, GGA, LDA+PAW and GGA+PAW

<sup>d</sup> both anti-ferromagnetic and ferromagnetic

<sup>e</sup> depending on the type of passivation

Table 5.4: Some of the reported magnetic values for zigzag nanoribbon in the literature. Here,  $\Delta E$  is the energy difference between spin polarised and spin unpolarised ground state.

Author	Parameters			Width
	$\Delta E$ (meV)	M ( $\mu_B$ )	$d_{Mo-S}$ (Å)	
Botello-Mendez [201]	-200	0.400	2.40–2.47	n=5
Li [287]	-29.88	0.733	2.39–2.41	n=5
Li [287]	-32.30	0.751	2.39–2.41	n=6
Li [287]	-35.62	0.769	2.39–2.41	n=8
Ataca [200]	—	2.000	2.42–2.56 <sup>a</sup>	n=6
Pan [286]	—	0.25/0.76 <sup>b</sup>	2.39	—

<sup>a</sup> only the armchair nanoribbon bond lengths were reported.

<sup>b</sup> per edge. Edge 1: S:0.38, Mo:-0.13; edge 2: S:0, Mo:0.76

spins (spin down) passing through the Fermi level and the energy bands corresponding to the other spin (spin up), result in a band gap of about 0.5 eV. This behaviour makes the MoS<sub>2</sub> nanoribbon a potential candidate for spintronics. Figure 5.6 shows the anti-ferromagnetic band structure of different hydrogen passivated zigzag nanoribbons. The bands passing through the Fermi energy are mainly from the edge atoms as shown in Figure 5.7 and 5.8.

The results reported by Li et al. [287] suggested that hydrogen saturated MoS<sub>2</sub> zigzag nanoribbons have a smaller magnetic moment compared to a bare nanoribbon; while the simulation in this thesis shows that hydrogen saturation of the edges will increase the magnetic moment by hydrogen atoms taking aligned-parallel spin with respect to the edge atoms (i.e. spin in the same direction of the other edge atoms).

For example, as shown in Table 5.5, a zigzag nanoribbon with n=8 has a magnetic moment of  $1.117\mu_B$  while passivating the edges with two or four hydrogen atoms will increase the magnetic moment to  $1.298\mu_B$  and  $1.433\mu_B$  respectively.

Similar to this work, Ataca et al. [200] also showed that 4-H absorption (2H on each side) will increase the total magnetic moment. However, they have proposed few different hydrogen absorptions on the edges that are different from the suggestions in this work.

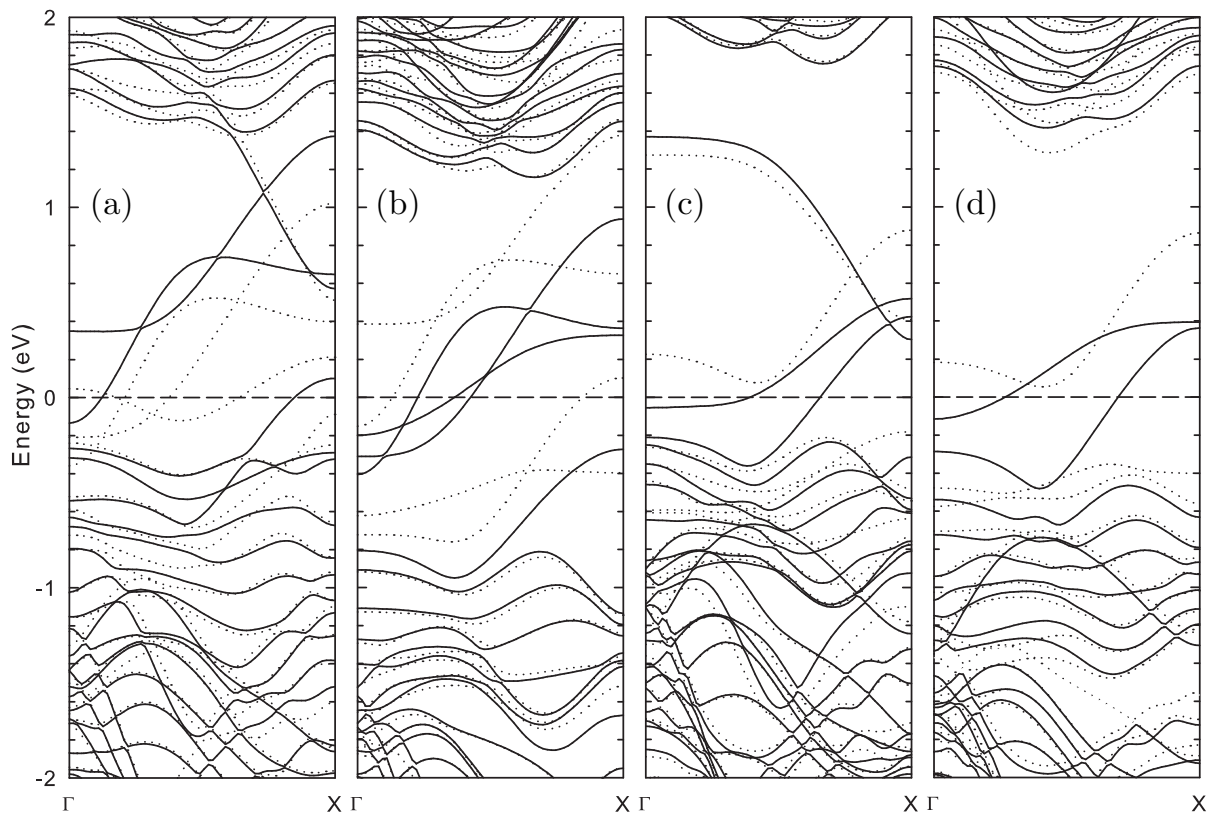


Figure 5.6: Anti-ferromagnetic band structure of zigzag nanoribbon ( $n=8$ ) with: (a) bare edges; (b) 2H on sulphur edge; (c) 2H on molybdenum edge; and (d) 4H on both edges (2 on each side) of the nanoribbon. The spin down and the spin up are represented by solid and dotted lines respectively; and the Fermi energy is set to 0 eV.

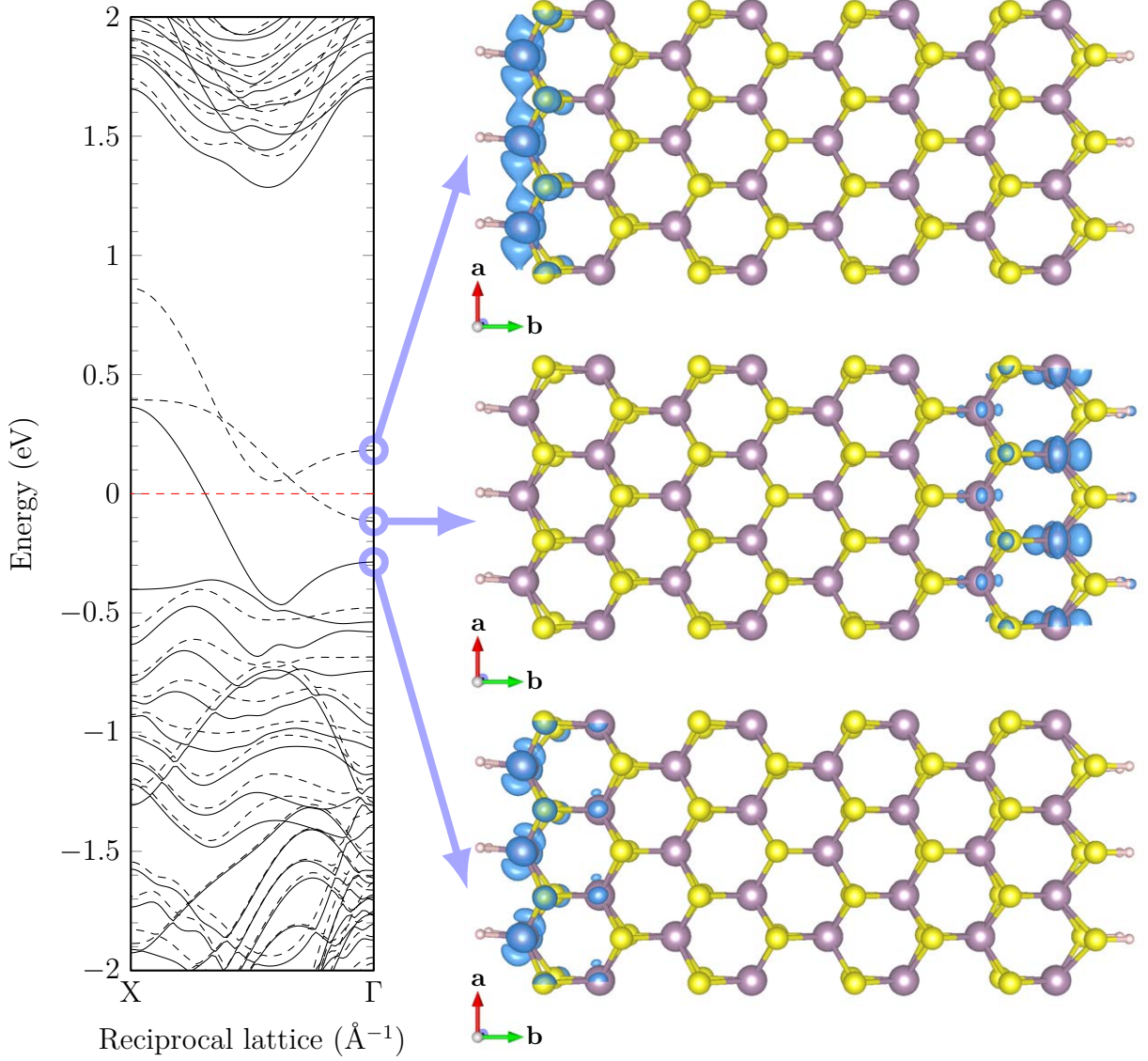


Figure 5.7: The band structure of zigzag MoS<sub>2</sub> nanoribbon ( $n=8$ ) with four hydrogen passivation (two on each edge) in ferromagnetic state on the left with the corresponding charge density iso-surfaces of states near the Fermi energy on the right. The spin down and the spin up are represented by solid and dotted lines respectively; and the Fermi energy is set to 0 eV. The nanoribbon is periodic along  $a$  axis.

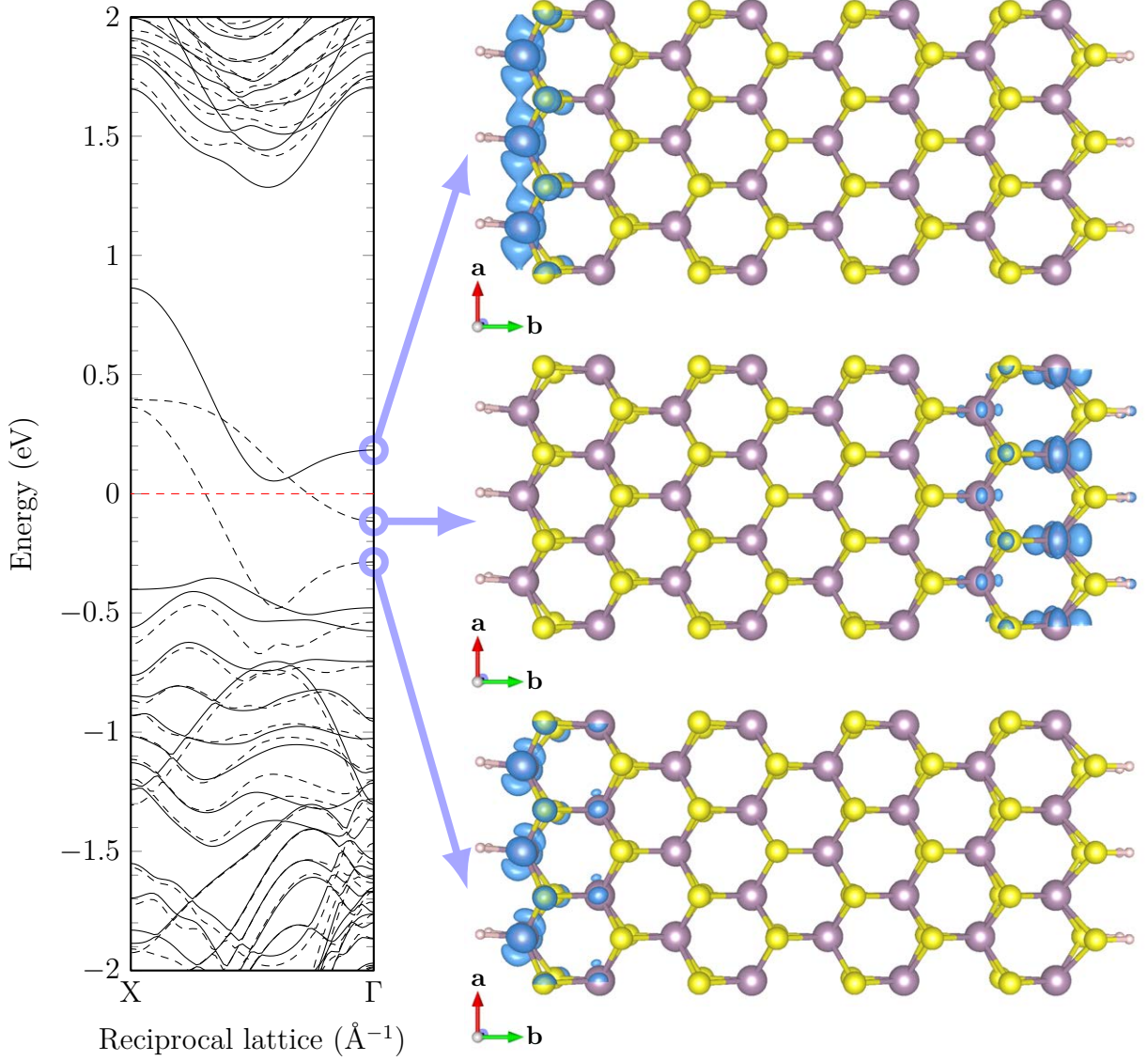


Figure 5.8: The band structure of zigzag  $\text{MoS}_2$  nanoribbon ( $n=8$ ) with four hydrogen passivation (two on each edge) in anti-ferromagnetic state on the left with the corresponding charge density iso-surfaces of states near the Fermi energy on the right. The spin down and the spin up are represented by solid and dotted lines respectively; and the Fermi energy is set to 0 eV. The nanoribbon is periodic along  $a$  axis.

### 5.3 Extra H Absorption at Zigzag Nanoribbon Edges

An exhaustive literature search on previous published works about the MoS<sub>2</sub> and other zigzag nanoribbon edge passivations shows that the passivations are mainly done using the conventional one hydrogen per each free valence electron [200, 201, 286, 294, 298–300]. However, the results of Cristol et al. [301, 302] on the hydrogen absorption on the edge of MoS<sub>2</sub> suggested several different possible absorptions. Several other types of MoS<sub>2</sub> passivation using sulphur [286, 295, 303], oxygen [303, 304], amidogen NH<sub>2</sub> [288] or hydroxyl OH [288] have also been reported in the literature. It has also been reported that the transition metals (i.e. molybdenum) at the edges have the ability to change their vacancy from 4+ to 5+ [303].

Using the suggested structures by Cristol et al. [301, 302] and molecular dynamics force relaxation by moving ions, three new types of edge saturations were created by adding five and six hydrogen atoms on the edges of MoS<sub>2</sub> zigzag nanoribbons, as illustrated in Figure 5.9.

The 5-hydrogen saturation occurs when the molybdenum atom absorbs one extra hydrogen atom on either edge of the nanoribbon, when the nanoribbon is already saturated with four hydrogen atoms. These extra absorptions were named as type I and II corresponding to the absorption on the sulphur and molybdenum edges of the nanoribbon respectively. The 6-hydrogen saturation happens when molybdenum atoms on both edges of the nanoribbon absorb one extra hydrogen atom, compared to the 4-hydrogen saturated structure. These extra absorptions occur with an increment to the super cell pressure, which increases the total pressure to about 1 Giga-Pascal (GPa), equal to  $6.24 \times 10^{-3}$  eV/Å<sup>3</sup>. However, after moving the ions and relaxing the structure, this pressure drops below 0.3 GPa ( $1.87 \times 10^{-3}$  eV/Å<sup>3</sup>) with x, y and z components of stress tensor equal to  $-4.72 \times 10^{-5}$ ,  $2.33 \times 10^{-5}$  and  $-9.32 \times 10^{-6}$  Hartree/Bohr<sup>-3</sup> respectively. The formation energies of these nanoribbons suggest that they will be stable (Table 5.5), however in practice the partial pressure required to produce these highly hydrogenated edge

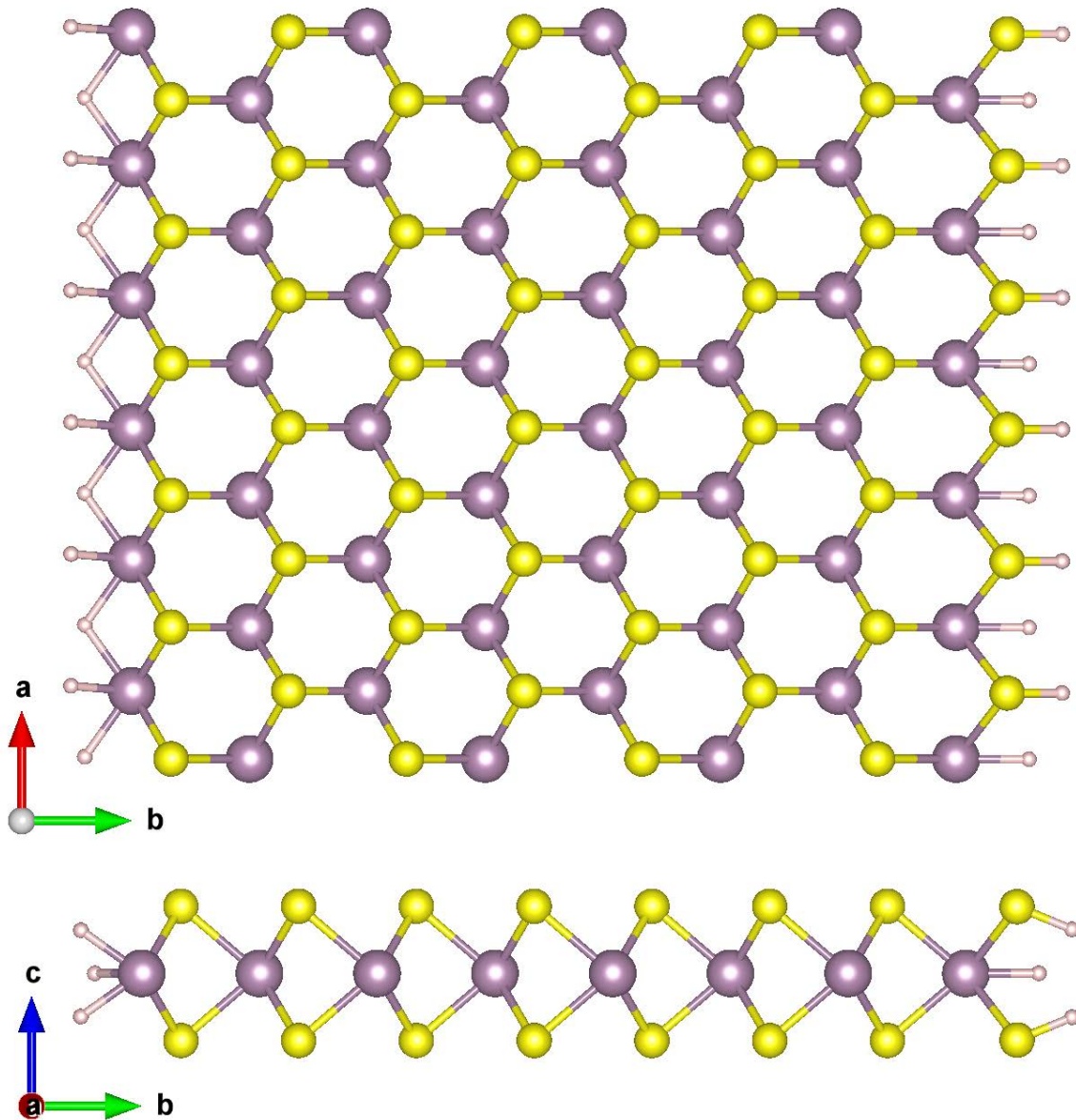


Figure 5.9: Absorption of five and six hydrogen atoms on the edge of MoS<sub>2</sub> zigzag nanoribbons.

would be very high<sup>1</sup>.

After calculation of the spin polarised band structure of both type I and II 5H saturation with different spin initialisation on the edge atoms, both types were found to be semi-metallic with only energy bands corresponding to one spin passing through the Fermi energy (Figure 5.10 (e) and 5.10 (f)). However, 6H saturation results in a non-

---

<sup>1</sup>Cristol, Paul and Payen have done extensive research on hydrogen and sulphur absorption on the edges of MoS<sub>2</sub> and the required hydrogen partial pressure. Refer to [301] and [302] for more details.

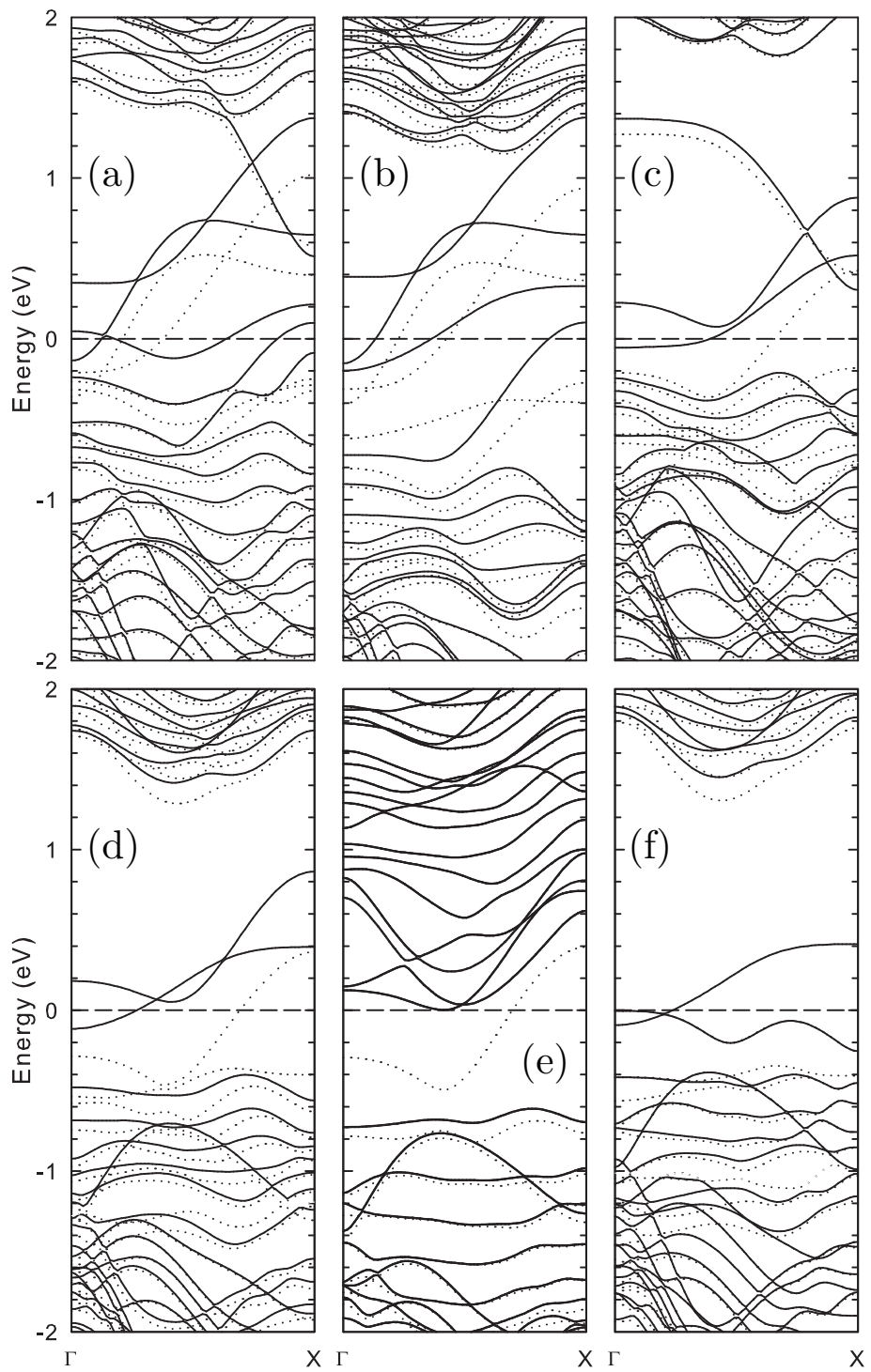


Figure 5.10: Ferromagnetic band structure of  $\text{MoS}_2$  zigzag nanoribbon ( $n=8$ ) with: (a) bare edge; (b) 2H on sulphur edge; (c) 2H on molybdenum edge; (d) 4H on edges (2 on each side); (e) 5H type I and (f) 5H type II saturation. The spin down and the spin up are represented by solid and dotted lines respectively; and the Fermi energy is set to 0 eV.

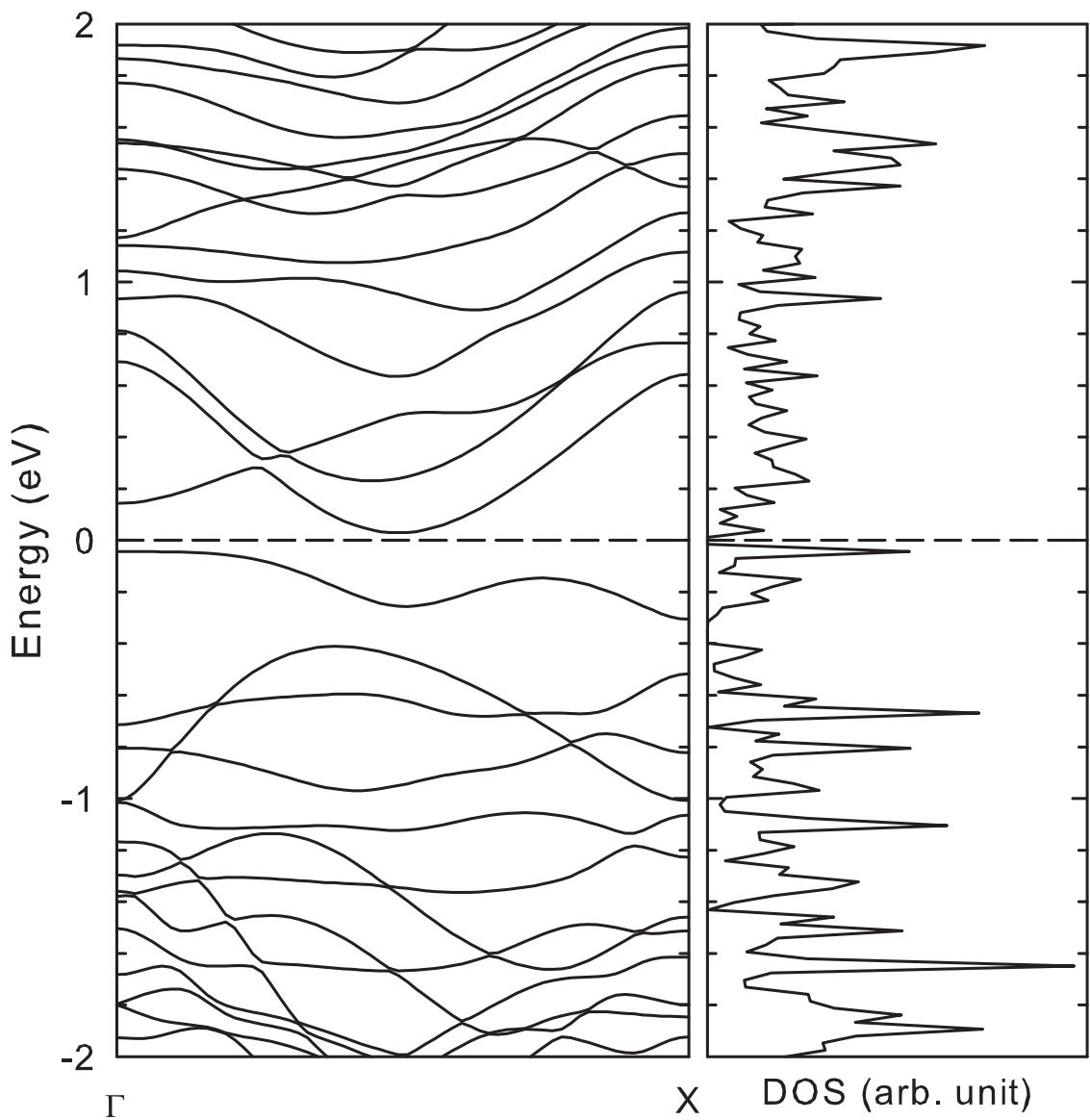


Figure 5.11: The band structure and the density of the states of MoS<sub>2</sub> zigzag nanoribbon passivated with six hydrogen atoms on its edges.

Table 5.5: Variation in magnetic moment and energy of a zigzag nanoribbon per unit cell ( $n=8$ );  $\Delta E_{sp}$  represents the difference between spin polarised and spin non-polarised nanoribbons; and  $\Delta E_{bare}$  represents the bond energy calculated using spin polarised bare edge nanoribbons and each passivated nanoribbon using  $E_{system} - (E_{bare} + (1/2E_{H_2} \times n_H))$ . The value in the parenthesis is calculated using the previous stable system instead of bare system. e.g.  $E_{4H} - (E_{2H} + 1/2E_{H_2} \times 2)$ , where  $E_{H_2} = -31.92342$  eV calculated using same parameters as the nanoribbon.

Edge type	$\Delta E_{sp}$ (meV)	M ( $\mu_B$ )		$\Delta E_{bare}$ (meV)
		FM	AFM	
Bare	-52.4	1.1177	0.0569	—
2H (S edge)	-97.2	1.2980	0.0734	-92.2
2H (Mo edge)	-43.2	1.2898	0.0166	-54.0
4H	-101.3	1.4332	0.0391	-328.7 (-236.4)
5H (type I)	-14.1	0.5858	—	-329.7 (-1.0)
5H (type II)	-76.9	0.7732	—	-367.2 (-38.5)
6H	—	—	—	-385.8 (-18.6)

magnetic and semiconducting nanoribbon with a fundamental indirect band gap of about 0.1 eV and optical (direct) band gap of 0.2 eV located at the gamma ( $\Gamma$ ) point. Figure 5.11 shows the energy band diagram corresponding to this structure. This suggests that different types of saturation on the edges of zigzag nanoribbons can possibly lead to the transformation of zigzag nanoribbons from metallic to semiconducting.

## 5.4 Chiral Nanoribbons

As mentioned in the previous chapter, if the nanoribbon edges are cut along any angle other than zigzag or armchair, the edge will be called chiral, which is usually a combination of partial zigzag and armchair patterns. As it can be seen in Figure 5.12, cutting along the  $a$  axis or any multiple of 60 degrees from this axis (0, 60, 120, ...) will result in a zigzag edge; whereas cutting at 30 degrees angle to the  $a$  axis or any multiple of 60 degrees from it (30, 90, 150, ...) will result in an armchair edge. However, if the nanoribbon is cut at any other angle apart from these angles it will produce a hybrid edge. This is illustrated in Figure 5.12 with a green arrow. The angle of this arrow is about 11 degrees

with respect to  $a$  and cutting along this angle will result in a combination of zigzag and armchair.

In theory, this hybrid edge is expected to have an electrical property consisting of both zigzag nanoribbons and armchair nanoribbons. The zigzag nanoribbon is metallic and magnetic, while the armchair nanoribbon is semiconducting and non-magnetic. Thus, the resultant nanoribbon has to be semiconducting due to the discontinuity of the zigzag edges and presence of armchair pattern and magnetic as well due to existence of zigzag pattern on the edges.

Although the electrical properties of nanoribbons with chiral edges have been studied for other two-dimensional materials such as graphene nanoribbons [7, 8, 305], to the author's knowledge there have been no such studies reported on the MoS<sub>2</sub> nanoribbons with chiral edges.

Due to the nature of the MoS<sub>2</sub> nanoribbons and the very high contribution of the edges to the band gap, it is expected that MoS<sub>2</sub> chiral nanoribbons will have different magnetic and electronic properties compared to zigzag and armchair nanoribbons. For this reason, a chiral MoS<sub>2</sub> nanoribbon with a deviation vector of (3,2) atoms was chosen, which will produce a chiral nanoribbon with 23.41 ° deviation from being zigzag or equivalently 6.59 ° deviation from being armchair, as illustrated in Figure 5.13.

A similar convergence procedure to the previous chapters was carried out on the supercell using PBE-GGA with PAW and a kinetic cut-off energy of 30 Hartree was chosen with 80 Hartree cut-off energy for the fine FFT grid. The one-dimensional Brillouin zone was sampled using  $18 \times 1 \times 1$   $k$ -points. The edge atoms were initialised with random spins and the calculation of the ground state was repeated several times.

The result obtained on the modelled chiral nanoribbon was very interesting as it showed both magnetic and semiconducting behaviour. This behaviour classifies the nanoribbon into the magnetic semiconductors group which is of interest in the field of spintronics. Having both magnetic and semiconducting properties provides the possibility of controlling the band gap of the material by changing the spin polarisation of that material.

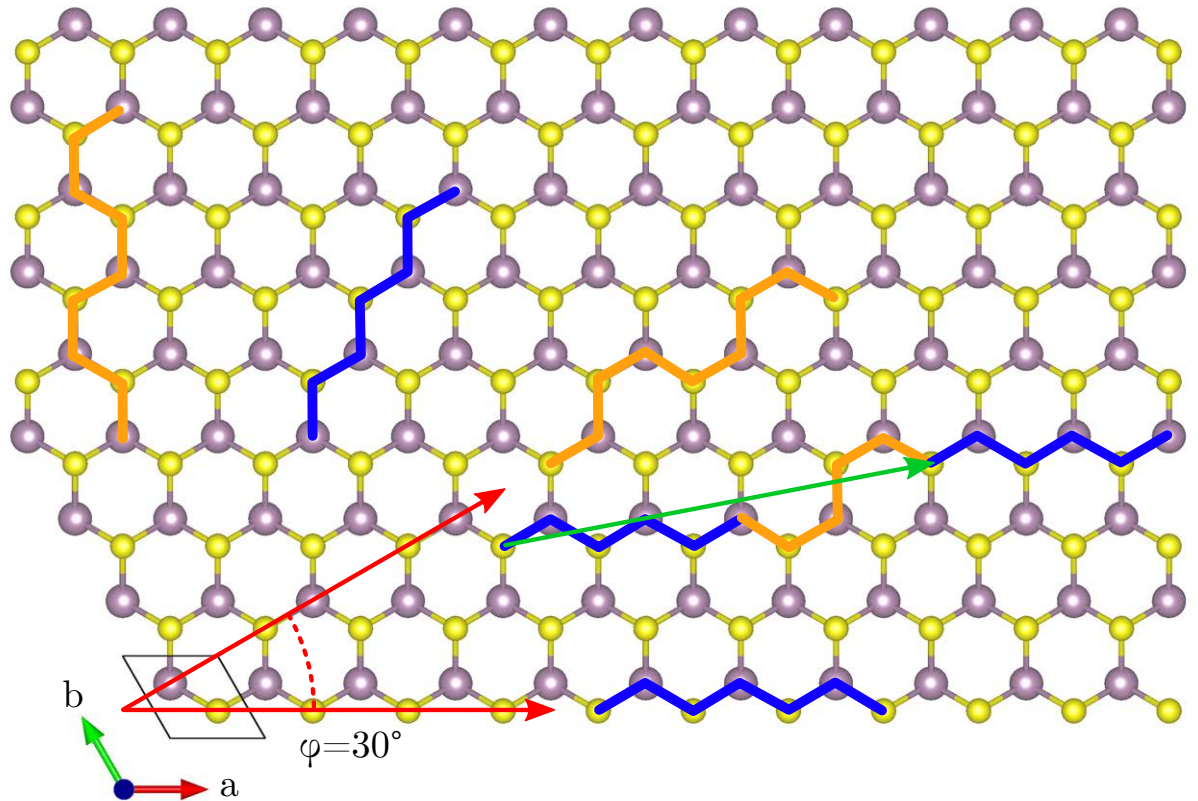


Figure 5.12: Possible edge patterns in  $\text{MoS}_2$ . The black rhombus is the unit cell and the red vectors with 30-degree separation show the directions to cut zigzag and armchair edges. The blue lines show the zigzag pattern and the orange lines show the armchair patterns. The green vector is 10.89 degrees deviated with respect to the  $a$  axis. Cutting along the green vector will result in a combination of zigzag and armchair that is called the chiral edge.

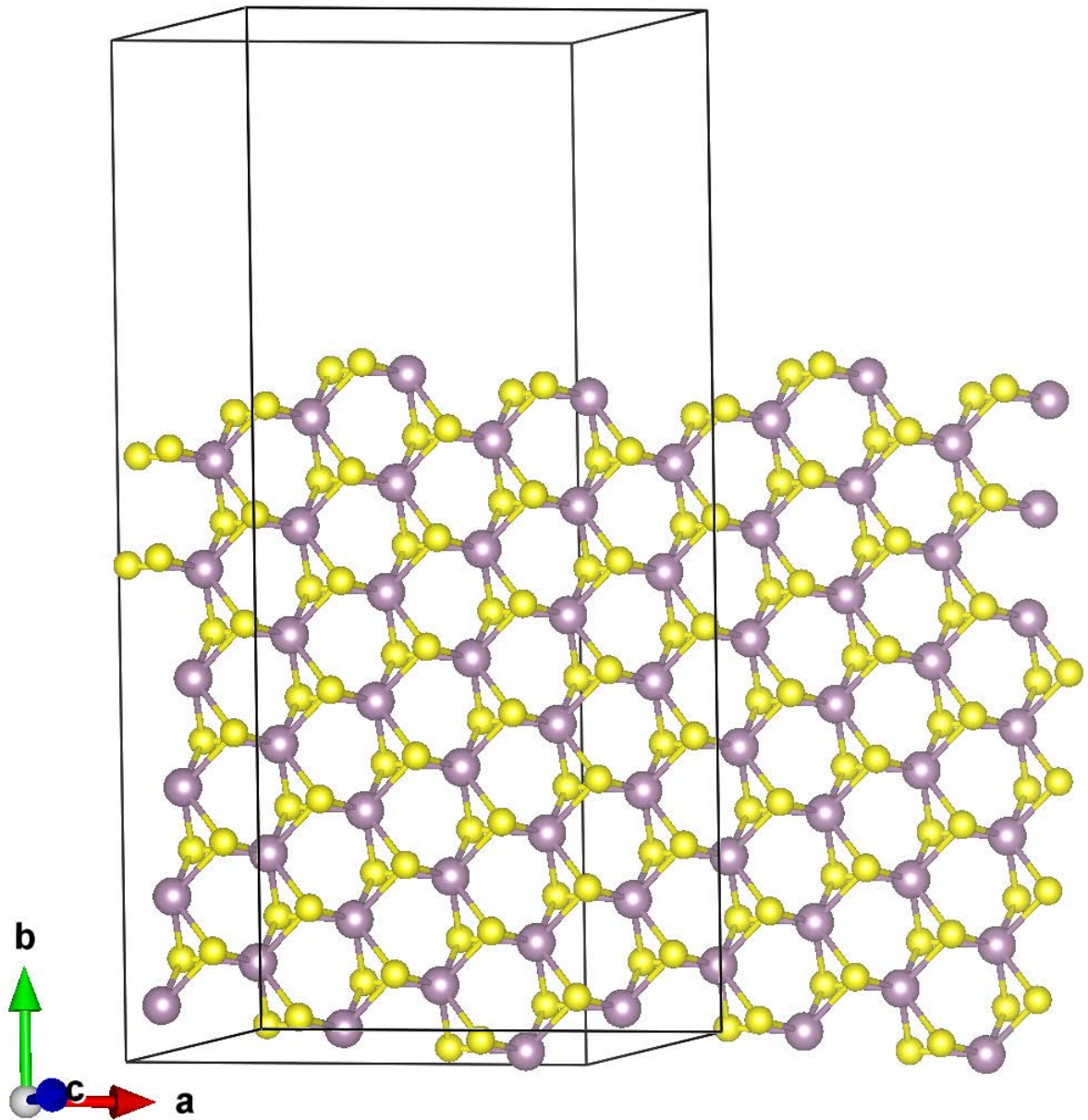


Figure 5.13: The super cell used to model the chiral nanoribbon with 96 atoms in the cell ( $\text{Mo}_{32}\text{S}_{64}$ ). The cell is periodic along the *a* the axis and discontinuous along the *b* and *c* axes.

This behaviour can be explained by having a combination of both zigzag and armchair patterns along the edge of the nanoribbon. The armchair section of the nanoribbon contributes to the band gap of the nanoribbon; while the existence of the zigzag pattern in the vicinity causes the nanoribbon to have magnetic behaviours. Figure 5.14 shows the calculated spin polarised band gap of this MoS<sub>2</sub> chiral nanoribbon. The calculated band structure of the modelled MoS<sub>2</sub> chiral nanoribbon was showing an indirect band gap of 0.1 eV, similar to the zigzag nanoribbon passivated with six hydrogen atoms and a total magnetic moment of 0.036 Bohr magneton ( $\mu_B$ ) was calculated for the nanoribbon. The calculated spin polarised charge density of the nanoribbon is visualised in Figure 5.15. The molybdenum atoms on the lower edge of the nanoribbon have a significant positive charge of about 0.574 and on the upper edge of the nanoribbon the molybdenum charge is reaching -0.310. However, the charge on any of the sulphur atoms on the edge does not exceed -0.032. The complete list of atom-resolved spin density and Hirshfeld charge is tabulated in Tables F.12 to F.14 in Appendix F.

## 5.5 Conclusion

In this chapter, the effect of passivation of the edges of MoS<sub>2</sub> nanoribbons has been investigated and possible hydrogen passivations of the edges have been modelled. The magnetic properties of zigzag nanoribbons have also been studied and the relationship between the initial spin condition and net magnetic moment of the nanoribbon has been investigated; this leads to zigzag nanoribbons becoming both ferromagnetic and anti-ferromagnetic.

An intensive study on the hydrogen passivation of the edges of zigzag nanoribbons has been carried out; which suggests that zigzag nanoribbons can become semiconducting as well. It was also shown that the zigzag edges of the MoS<sub>2</sub> nanoribbon are capable of absorbing up to three hydrogen atoms on each side. However, the conditions for which such a highly hydrogenated edge would be stable are difficult to obtain experimentally,

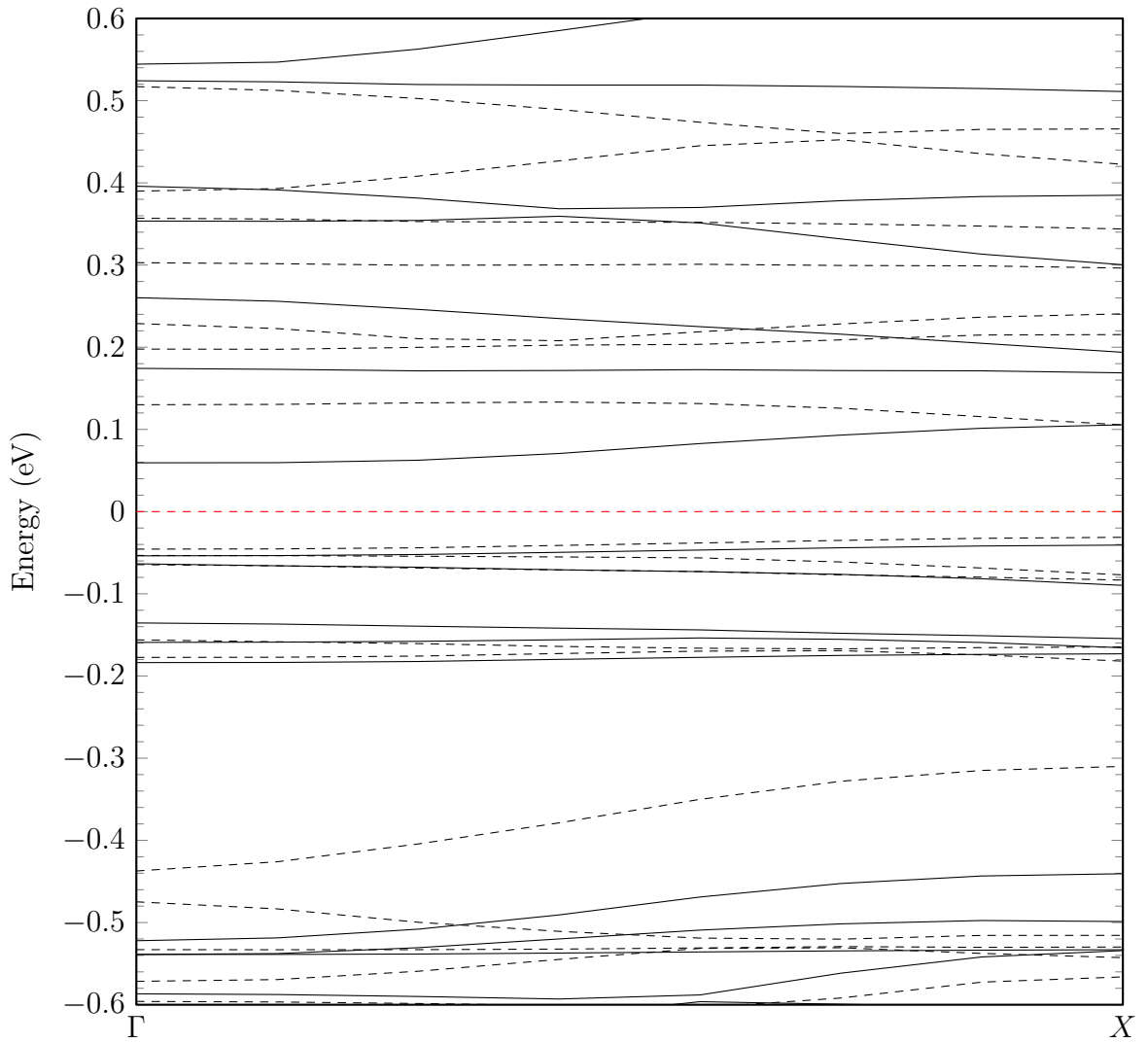


Figure 5.14: The band structure of the MoS<sub>2</sub> nanoribbon with chiral edges showing both magnetic properties and a semiconducting band gap.

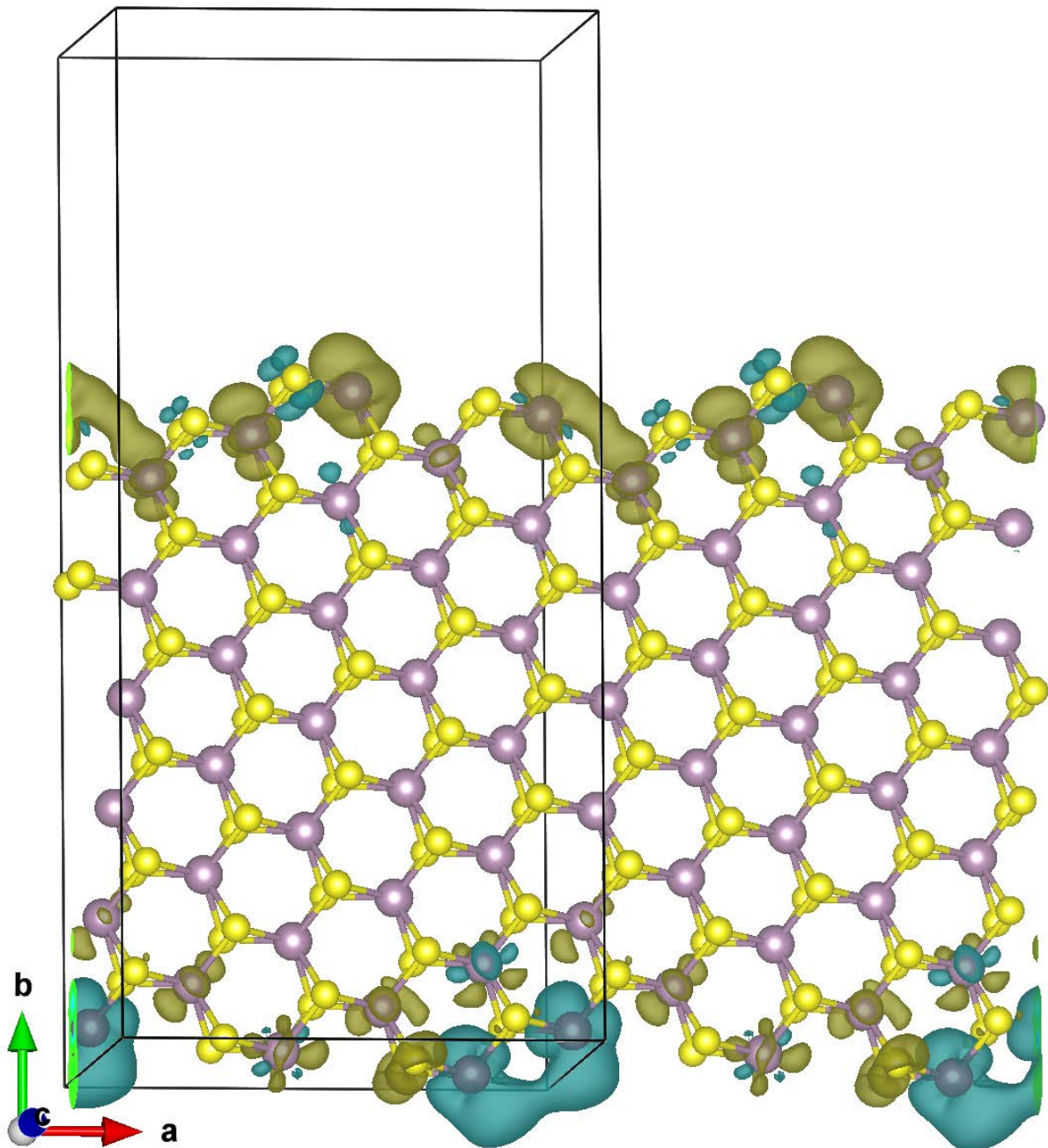


Figure 5.15: The band structure of MoS<sub>2</sub> nanoribbon with chiral edges showing zigzag and semiconducting type densities on the edges. The iso-surface value was calculated at 0.001 which was obtained using  $d(iso) = \langle |\rho| \rangle + n \times \sigma(|\rho|)$ ; where  $\langle |\rho| \rangle$  is the average of density;  $\sigma(|\rho|)$  is standard deviation of density; and  $n$  is an arbitrary scaling factor [306]. The teal colour represents positive density and the olive green colour is used for negative density.

and involve a large hydrogen partial pressure.

Finally, the electrical and magnetic properties of a novel chiral MoS<sub>2</sub> nanoribbon were modelled, which has shown that the chiral MoS<sub>2</sub> nanoribbons can exhibit both semiconducting and magnetic moment simultaneously; this has never been reported before and is of interest to the field of spintronics.

*“Success is not final, failure is not fatal: it is the courage to continue that counts.”*

— Winston Churchill

# Chapter 6

## Conclusion and Future Work

### 6.1 Summary

In this thesis the electrical properties of molybdenum disulphide materials were investigated from the first principles' calculations. Initially the basic properties of the material such as the crystalline structure and the stability and fabrication techniques to produce this material, were explored and were followed by the calculation of the basic electrical properties of the bulk form of this material.

Although the first principles' calculation relies on a very few basic parameters of the material, the calculation itself requires a significant amount of adjustments. Extra care has to be taken to model materials such as molybdenum disulphide with partially filled  $d$  orbitals. In this research, the calculation parameters were fully considered using various convergence studies and the produced results were evaluated in well-known situations. The obtained results in these known situations were fully in-line with published results from experimentally measured values in the literature, which confirms the reliability of the model and the techniques that were used.

Following the calculation of basic electrical properties of the material, the transition from the bulk form into a two-dimensional nano-structure was studied and the electrical band structure of the material was investigated. The change in the electrical behaviour

of the material moving from three-dimensions into two-dimensions was fully examined with the aid of localised Wannier functions. It was shown that this change is mainly due to the molybdenum  $4d_{z^2}$  orbital losing its energy when the coupling between the layers of molybdenum disulphide is not present. The relationship between the atomic orbitals, energy band structure and band gap has also been investigated.

Extensive structural optimisation calculations have been used to show the effects of stress and strain on the energy band gap in both bulk and single-layer MoS<sub>2</sub>; which suggested the very small variations in the structural properties that can be imposed by external factors, such as substrate lattice, can significantly affect the band structure of MoS<sub>2</sub>. This finding can potentially explain the difference between the experimentally-measured band gap of the two-dimensional material and the values obtained using accurate modelling techniques.

Using the established model for the molybdenum disulphide, the discontinuity on the edges of this material was investigated and the effect of loose atoms on the edges has been studied. It was shown that unlike graphene, the bandgap in MoS<sub>2</sub> armchair nanoribbons is not significantly affected by the width of the nanoribbon. It was also noted that the MoS<sub>2</sub> armchair nanoribbons are always semiconducting; while the MoS<sub>2</sub> zigzag nanoribbons are always metallic and magnetic.

The magnetic behaviours of the zigzag nanoribbons were intensively investigated and spin simulation on the MoS<sub>2</sub> zigzag nanoribbons suggested that this material can take both ferromagnetic and anti-ferromagnetic states with equal probability; this could be the reason behind the various magnetic behaviours of the MoS<sub>2</sub> zigzag nanoribbons reported in the literature.

The study of the band structure of the zigzag nanoribbons suggested that their metallic and magnetic behaviour is purely due to the edge atoms. With inspiration from a study on the absorption of hydrogen on the edges of molybdenum disulphide, a new hydrogen structure on the edges of MoS<sub>2</sub> nanoribbons was suggested, which showed that zigzag nanoribbons can become semiconducting as well. It was also demonstrated that the zigzag

edges of the MoS<sub>2</sub> nanoribbons are capable of absorbing up to three hydrogen atoms per super cell on each side.

Finally, the electrical and magnetic properties of a novel chiral MoS<sub>2</sub> nanoribbon were modelled, which showed that the chiral MoS<sub>2</sub> nanoribbons can exhibit both semiconducting and magnetic behaviours simultaneously; this has never been reported before and is of interest to the field of spintronics.

## 6.2 Future Work

Transition metal dichalcogenides such as molybdenum disulphide and tungsten disulphide, are analogous to graphene with comparable electrical properties. However, not much attention has been given to these materials compared to graphene. Many techniques applied to graphene material, such as uniaxial and biaxial strain, or band gap tuning using an external electric field can be investigated in these materials.

Since the original work presented in this thesis was completed in 2013, publications from other research groups have investigated several aspects of molybdenum disulphide material such as carrier mobility [307], electronic transport [308], surface defect passivation [309] and material fabrication [310]. Nearly all of these papers cite the earlier DFT studies [200, 201, 286, 287, 311, 312] and have used the previously established properties [308], apart from Cui et al [291] reporting on the possibility of edge reconstruction in zigzag nanoribbons at the sulphur edge. Significantly, none of the recent papers have reported on the magnetic behaviour and chiral electrical properties as derived from the research presented here.

The findings in this research concerning the possible new edge passivation of zigzag nanoribbons and the chiral edged nanoribbons can be further investigated and utilised in device structures. Obtaining a magnetic semiconductor purely from MoS<sub>2</sub> nanoribbons without any chemical alteration or doping, can lead to a simpler fabrication process and a possibly improved performance which has to be investigated.

The innovative discoveries in this research may light a new path to a wide range of potential applications and research on the undiscovered properties of this unique material in the future.

# Appendix A

## Fundamental Physical Constants

Name	Symbol	Definition	Value
Bohr magneton	$\mu_B$	$e\hbar/2m_e$	$9.274\,009 \times 10^{-24} \text{ J T}^{-1}$
Bohr radius	$a_0$	$4\pi\epsilon_0\hbar/m_e e^2$	$0.529\,177 \times 10^{-10} \text{ m}$
Electron magnetic moment	$\mu_e$		$-9.284\,764 \times 10^{-24} \text{ J T}^{-1}$ $-1.001\,160 \mu_B$
Electron mass	$m_e$		$9.109\,328 \times 10^{-31} \text{ kg}$
Permittivity of free space	$\epsilon_0$	$1/\mu_0 c^2$	$8.854\,188 \times 10^{-12} \text{ F m}^{-1}$
Elementary charge	$e$		$1.602\,176 \times 10^{-19} \text{ C}$
Hartree energy	$E_h$	$e^2/4\pi\epsilon_0 a_0$	$4.359\,744 \times 10^{-18} \text{ J}$ $27.211\,383 \text{ eV}$
Permeability of free space	$\mu_0$		$4\pi \times 10^{-7} \text{ N A}^{-2}$
Planck constant	$h$		$6.626\,069 \times 10^{-34} \text{ J s}$ $4.135\,667 \times 10^{-15} \text{ eV s}$
Reduced Planck constant	$\hbar$	$h/2\pi$	$1.054\,572 \times 10^{-34} \text{ J s}$ $6.582\,119 \times 10^{-16} \text{ eV s}$
Rydberg constant	$R_\infty$	$\alpha^2 m_e c / 2h$	$10\,973\,731.569 \text{ m}^{-1}$
Rydberg energy	Ry	$R_\infty h c$	$2.179\,872 \times 10^{-18} \text{ J}$ $13.605\,692 \text{ eV}$
Speed of light	c		$299\,792\,458 \text{ ms}^{-1}$

## Appendix B

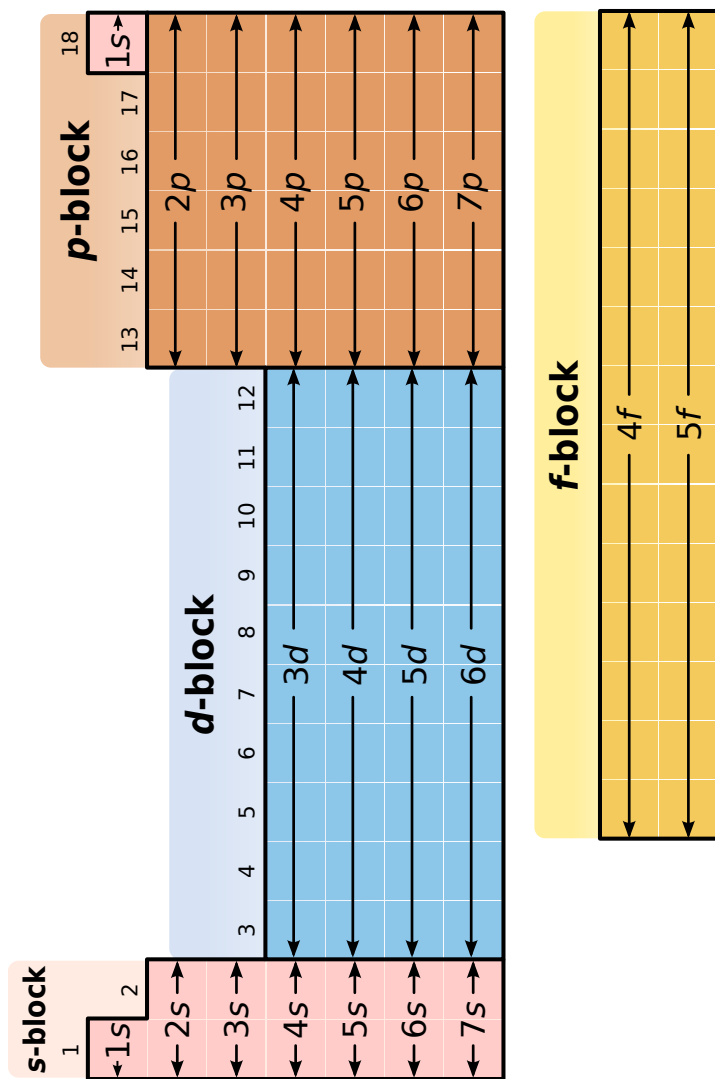
# Atomisation Energy of Molecules

Table B.1: Atomization energies of several small molecules for comparison in kcal/mol. Here, UHF denotes unrestricted Hartree-Fock method. This table is reproduced from [78].

Molecule	$\Delta E^{UHF}$	$\Delta E^{LSDA}$	$\Delta E^{PW91}$	$\Delta E^{PBE}$	$\Delta E^{Exp.}$
H <sub>2</sub>	84	113	105	105	109
LiH	33	60	53	52	58
CH <sub>4</sub>	328	462	421	420	419
NH <sub>3</sub>	201	337	303	302	297
OH	68	124	110	110	107
H <sub>2</sub> O	155	267	235	234	232
HF	97	162	143	142	141
Li <sub>2</sub>	3	23	20	19	24
LiF	89	153	137	136	139
Be <sub>2</sub>	-7	13	10	10	3
C <sub>2</sub> H <sub>2</sub>	294	460	415	415	405
C <sub>2</sub> H <sub>4</sub>	428	633	573	571	563
HCN	199	361	326	326	312
CO	174	299	269	269	259
N <sub>2</sub>	115	267	242	243	229
NO	53	199	171	172	153
O <sub>2</sub>	33	175	143	144	121
F <sub>2</sub>	-37	78	54	53	39
P <sub>2</sub>	36	142	120	120	117
Cl <sub>2</sub>	17	81	64	63	58
mean abs. error	71.2	31.4	8.0	7.9	—

# Appendix C

## Periodic Table of Elements



**IA**

1	1.008*	<b>H</b>	2
idrogeno			IA
3	6,94*	4	9,012

**Li** litio

**Be** berillio

11 22,99 12 24,31\*

**Na** magnesio

19 39,10 20 40,08

**Mg** calcio

19 44,96 22 47,87

23 50,94 24 52,00

25 54,94 26 55,85

27 58,93 28 58,69

29 63,55 30 65,38\*

31 69,72 32 72,63

33 74,92 34 78,96\*

35 79,90\* 36 83,80

**K** potassio

37 85,47 38 87,62

**Ca** scandio

39 88,91 40 91,22

**Sc** titanio

42 92,91 43 95,96

**Ti** vanadio

43 98,44 101,1

**V** cromo

25 50,94 26 55,85

27 58,93 28 58,69

29 63,55 30 65,38\*

31 69,72 32 72,63

33 74,92 34 78,96\*

35 79,90\* 36 83,80

**Mn** manganese

19 44,96 22 47,87

**Fe** ferro

23 50,94 24 52,00

**Cr** cobalto

25 54,94 26 55,85

**Co** nichel

27 58,93 28 58,69

**Ni** rame

29 63,55 30 65,38\*

**Zn** zinco

31 69,72 32 72,63

**Ga** gallio

33 74,92 34 78,96\*

**Ge** germanio

35 79,90\* 36 83,80

**Rb** rubidio

55 132,9 56 137,3

**Sr** stronzio

57 138,9 58 140,1

**Y** zirconio

59 140,9 60 144,2

**Tc** tecnecio

61 145] 62 150,4

**Ru** ruteno

63 152,0 64 157,3

**Rh** rodio

65 158,9 66 162,5

**Pd** palladio

67 164,9 68 167,3

**Ag** argento

69 170,4 70 173,1

**Cd** cadmio

71 175,0

**In** stagno

73 178,5 74 183,8

**Os** osmio

75 186,2 76 190,2

**Ir** iridio

77 192,2 78 195,1

**Hg** mercurio

79 197,0 80 200,6

**Pt** platino

81 204,4\* 82 207,2

**Au** oro

83 209,0 84 210,6

**Tl** talio

85 209,0 86 222]

**Pb** piombo

**Bi** bismuto

**Po** polonio

**At** astato

**Rn** radon

**Cs** cesio

104 [267] 105 [268]

**Ba** bario

106 [269] 107 [270]

**Hf** afnio

108 [269] 109 [278]

**Ta** tantalio

110 [281] 111 [281]

**W** tungsteno

112 [285] 113 [286]

**Re** renio

114 [289] 115 [288]

**Os** osmio

116 [293] 117 [294]

**Rf** rutherfordio

109 [226] 110 [227]

**Ds** dubnio

111 [227] 112 [228]

**Sg** seaborgio

113 [228] 114 [229]

**Bh** bohrio

115 [229] 116 [230]

**Hs** hassio

117 [230] 118 [231]

**Mt** meitnerio

118 [231] 119 [232]

**Rg** darmstadtio

119 [232] 120 [233]

**Cn** copernicio

121 [233] 122 [234]

**Uut** roentgenio

123 [234] 124 [235]

**F** ununtrio

125 [235] 126 [236]

**Fl** flerovio

126 [236] 127 [237]

**Uup** ununpentio

127 [237] 128 [238]

**Lv** livermorio

129 [238] 130 [239]

**Uus** ununseptio

131 [239] 132 [240]

**Uuo** ununoctio

133 [240] 134 [241]

\*H: [1,00784, 1,00811]

Li: [6,938, 6,997]

B: [10,806, 10,821]

C: [12,0096, 12,0116]

N: [14,00643, 14,00728]

O: [15,99903, 15,99977]

Mo: [24,304, 24,307]

Si: [26,084, 26,086]

S: [32,059, 32,061]

Cl: [35,446, 35,457]

Br: [79,901, 79,907]

Tl: [204,382, 204,385]

Zn: 65,38(2)

Se: 78,96(3)

Mo: 95,96(2)

\*Li: [1,00784, 1,00811]

Be: [10,806, 10,821]

Ca: [12,0096, 12,0116]

Mg: [14,00643, 14,00728]

Al: [15,99903, 15,99977]

Si: [26,084, 26,086]

Cl: [32,059, 32,061]

Br: [79,901, 79,907]

Tl: [204,382, 204,385]

Zn: 65,38(2)

Se: 78,96(3)

Mo: 95,96(2)

\*B: [10,806, 10,821]

C: [12,0096, 12,0116]

N: [14,00643, 14,00728]

O: [15,99903, 15,99977]

Mo: [24,304, 24,307]

Si: [26,084, 26,086]

Cl: [32,059, 32,061]

Br: [79,901, 79,907]

Tl: [204,382, 204,385]

Zn: 65,38(2)

Se: 78,96(3)

Mo: 95,96(2)

\*Cl: [32,059, 32,061]

Br: [79,901, 79,907]

Tl: [204,382, 204,385]

Zn: 65,38(2)

Se: 78,96(3)

Mo: 95,96(2)

\*Ar: [18,99903, 19,00077]

Ca: [20,99903, 21,00077]

Sc: [22,99903, 23,00077]

Cr: [24,99903, 25,00077]

Mn: [26,99903, 27,00077]

Fe: [28,99903, 29,00077]

Co: [30,99903, 31,00077]

Ni: [32,99903, 33,00077]

Cu: [34,99903, 35,00077]

Fe: [36,99903, 37,00077]

Ge: [38,99903, 39,00077]

As: [40,99903, 41,00077]

Se: [42,99903, 43,00077]

Pb: [44,99903, 45,00077]

Bi: [46,99903, 47,00077]

Po: [48,99903, 49,00077]

At: [50,99903, 51,00077]

Rn: [52,99903, 53,00077]

Fr: [54,99903, 55,00077]

Ra: [56,99903, 57,00077]

Fr: [58,99903, 59,00077]

Fr: [60,99903, 61,00077]

Fr: [62,99903, 63,00077]

Fr: [64,99903, 65,00077]

Fr: [66,99903, 67,00077]

Fr: [68,99903, 69,00077]

Fr: [70,99903, 71,00077]

Fr: [72,99903, 73,00077]

Fr: [74,99903, 75,00077]

Fr: [76,99903, 77,00077]

Fr: [78,99903, 79,00077]

Fr: [80,99903, 81,00077]

Fr: [82,99903, 83,00077]

Fr: [84,99903, 85,00077]

Fr: [86,99903, 87,00077]

Fr: [88,99903, 89,00077]

Fr: [90,99903, 91,00077]

Fr: [92,99903, 93,00077]

Fr: [94,99903, 95,00077]

Fr: [96,99903, 97,00077]

Fr: [98,99903, 99,00077]

\*He: [1,00784, 1,00811]

Be: [10,806, 10,821]

Ne: [12,00963, 12,0116]

Ar: [14,00643, 14,00728]

Cl: [15,99903, 15,99977]

Ar: [17,99903, 17,00077]

Ar: [19,99903, 19,00077]

Ar: [21,99903, 21,00077]

Ar: [23,9

## Appendix D

### Atomic Orbital

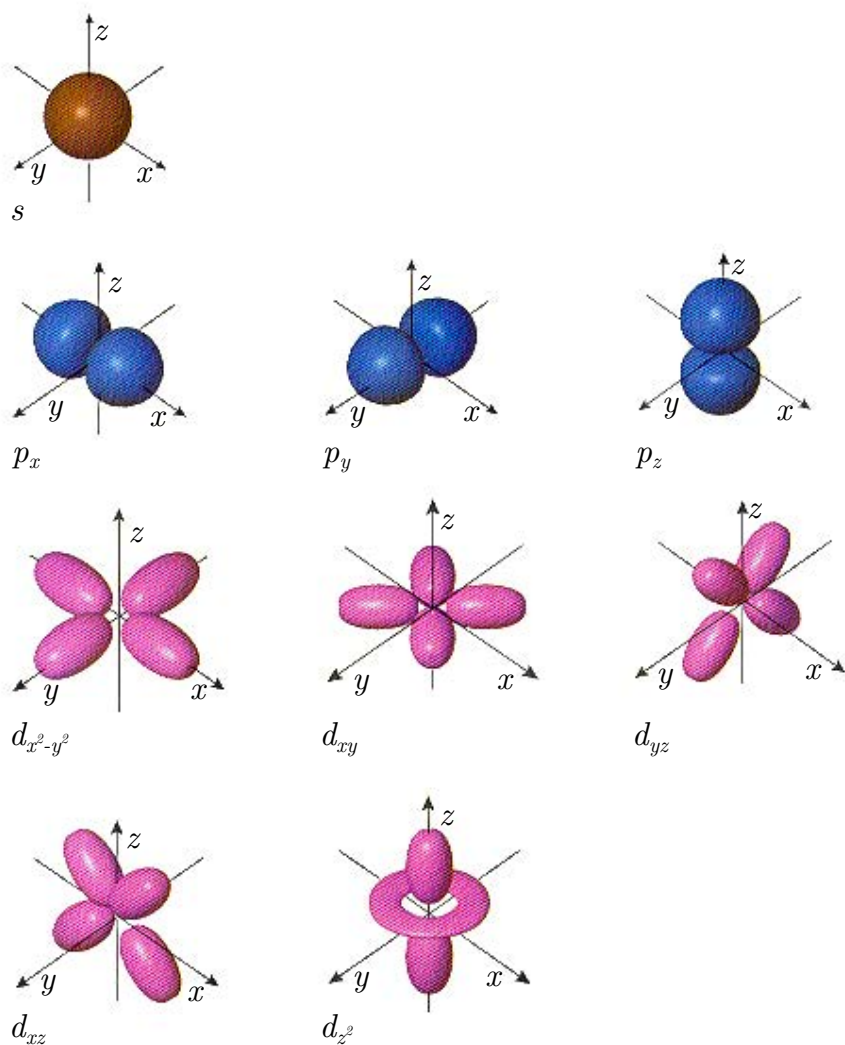


Table D.1: The definition of the angular functions  $\Theta_{lm_r}(\theta, \varphi)$ , where  $l$  and  $m_r$  represent the azimuthal quantum number and magnetic quantum number respectively. For further reading, one could refer to § 6 of Concepts of Modern Physics by Arthur Beiser [313].

$l$	$m_r$	Name	$\Theta_{lm_r}(\theta, \varphi)$
0	1	s	$\frac{1}{\sqrt{4\pi}}$
1	1	$p_z$	$\sqrt{\frac{3}{4\pi}} \cos \theta$
1	2	$p_x$	$\sqrt{\frac{3}{4\pi}} \sin \theta \cos \varphi$
1	3	$p_y$	$\sqrt{\frac{3}{4\pi}} \sin \theta \sin \varphi$
2	1	$d_{z^2}$	$\sqrt{\frac{5}{16\pi}} (3 \cos^2 \theta - 1)$
2	2	$d_{xz}$	$\sqrt{\frac{15}{16\pi}} \sin \theta \cos \theta \cos \varphi$
2	3	$d_{yz}$	$\sqrt{\frac{15}{16\pi}} \sin \theta \cos \theta \sin \varphi$
2	4	$d_{x^2-y^2}$	$\sqrt{\frac{15}{16\pi}} \sin^2 \theta \cos 2\varphi$
2	5	$d_{xy}$	$\sqrt{\frac{15}{16\pi}} \sin^2 \theta \sin 2\varphi$

Table D.2: A possible choice of the radial functions  $R_r(r)$  for  $l = 0$ . The  $\alpha$  is defined as  $Z/a_0$ . For further reading, one could refer to § 6 of Concepts of Modern Physics by Arthur Beiser [313].

$r$	$R_r(r)$
1	$2\alpha^{3/2} \exp(-\alpha r)$
2	$\frac{1}{2\sqrt{2}}\alpha^{3/2}(2 - \alpha r) \exp(-\alpha r/2)$
3	$\sqrt{\frac{4}{27}}\alpha^{3/2}(1 - 2\alpha r/3 + 2\alpha^2 r^2/27) \exp(-\alpha r/3)$

# Appendix E

## Numerical Results

### E.1 $2H\text{-MoS}_2$ convergence

Table E.1: The total energy of  $2H\text{-MoS}_2$  calculated with different  $k$ -mesh in reciprocal lattice using Monkhorst-Pack method.

$k$ -mesh	Energy	
	Total (Hartree)	$\Delta E$ (Hartree)
$1 \times 1 \times 1$	-56.698887359551	—
$2 \times 2 \times 2$	-57.147955647686	-0.44906828813
$4 \times 4 \times 4$	-57.215991393530	-0.06803574584
$6 \times 6 \times 6$	-57.213175105852	-0.00281628767
$8 \times 8 \times 8$	-57.213240241828	-0.00006513597
$18 \times 18 \times 2$	-57.213256580171	-0.00000315276
$20 \times 20 \times 2$	-57.213250601274	0.00000597889
$18 \times 18 \times 3$	-57.213250894849	-0.00000029357
$20 \times 20 \times 3$	-57.213250888212	-0.00000000664

Table E.2: The total energy of 2H-MoS<sub>2</sub> calculated with different kinetic energy cut-off values.

E <sub>cut-off</sub> (Hartree)	Energy	
	Total (Hartree)	ΔE (Hartree)
5	-55.1993441698316	—
10	-56.9179553579825	-1.71861118815
15	-57.0765057942142	-0.15855043623
40	-57.2126945261379	-0.00361028301
45	-57.2131160772200	-0.00042155108
50	-57.2132507918311	-0.00013471461

Table E.3: 2H-MoS<sub>2</sub> stress tensor relaxation

	Residual stress (Hartree/Bohr <sup>-3</sup> )		
	x	y	z
Before relaxation	1.397669035 × 10 <sup>-4</sup>	1.397669035 × 10 <sup>-4</sup>	-2.802830795 × 10 <sup>-4</sup>
After relaxation	-9.218462302 × 10 <sup>-6</sup>	-9.218462302 × 10 <sup>-6</sup>	1.910888615 × 10 <sup>-5</sup>

## E.2 2H-MoS<sub>2</sub> Band Gap Energies

Energy of the highest valence band and the lowest conduction band sampled at certain symmetry points in the Brillouin zone for both bulk and single-layer MoS<sub>2</sub> with different lattice constant is tabulated in this section. These values have been used to produce Figure 3.21 in Chapter 3.

Table E.4: The calculated energy for the highest valence band and lowest conduction band in bulk MoS<sub>2</sub> (*2H*-MoS<sub>2</sub>) at their peaks in the Brillouin zone. Here, *T* is defined as halfway between  $\Gamma$  and *K* symmetry points. All the energy values quoted in the table are in electron-volt (eV).

Lattice constant (Å)	Conduction Band		Valence Band		Direct Gap		Indirect Gap	
	$\Gamma$	<i>K</i>	<i>K</i>	$\Gamma$	$\Gamma \rightarrow K$	$\Gamma \rightarrow K$	$\Gamma \rightarrow T$	Minimum
3.12	1.3189	1.0172	-0.4950	0.0000	1.8139	1.3189	1.0172	1.5121
3.13	1.2681	1.0085	-0.5118	0.0000	1.7799	1.2681	1.0085	1.5203
3.14	1.2183	1.0003	-0.5284	0.0000	1.7467	1.2183	1.0003	1.5287
3.15	1.1695	0.9921	-0.5445	0.0000	1.7140	1.1695	0.9921	1.5366
3.16	1.1222	0.9845	-0.5597	0.0000	1.6819	1.1222	0.9845	1.5442
3.17	1.0757	0.9772	-0.5750	0.0000	1.6506	1.0757	0.9772	1.5521
3.18	1.0305	0.9701	-0.5897	0.0000	1.6202	1.0305	0.9701	1.5598
3.19	0.9861	0.9630	-0.6041	0.0000	1.5902	0.9861	0.9630	1.5671
3.20	0.9431	0.9565	-0.6177	0.0000	1.5608	0.9431	0.9565	1.5742
3.21	0.9010	0.9502	-0.6313	0.0000	1.5323	0.9010	0.9502	1.5815
3.22	0.8599	0.9440	-0.6438	0.0000	1.5037	0.8599	0.9440	1.5878
3.23	0.8199	0.9380	-0.6566	0.0000	1.4765	0.8199	0.9380	1.5946
3.24	0.7810	0.9323	-0.6686	0.0000	1.4496	0.7810	0.9323	1.6008
3.25	0.7431	0.9268	-0.6803	0.0000	1.4234	0.7431	0.9268	1.6071

Table E.5: The calculated energy for the highest valence band and lowest conduction band in single-layer MoS<sub>2</sub> (*1H*-MoS<sub>2</sub>) at their peaks in the Brillouin zone. Here, *T* is defined as halfway between  $\Gamma$  and *K* symmetry points. All the energy values quoted in the table are in electron-volt (eV).

Lattice constant (Å)	Conduction Band		Valence Band		Direct Gap		Indirect Gap	
	$K$	$T$	$K$	$\Gamma$	$K \rightarrow K$	$\Gamma \rightarrow K$	$\Gamma \rightarrow T$	Minimum
3.12	1.9048	1.9160	0.0000	-0.1916	1.9048	2.0964	2.1075	1.9160
3.13	1.8694	1.9198	0.0000	-0.1644	1.8694	2.0338	2.0841	1.9198
3.14	1.8346	1.9233	0.0000	-0.1377	1.8346	1.9723	2.0610	1.9233
3.15	1.8003	1.9263	0.0000	-0.1116	1.8003	1.9119	2.0379	1.9263
3.16	1.7671	1.9293	0.0000	-0.0857	1.7671	1.8528	2.0150	1.9293
3.17	1.7345	1.9320	0.0000	-0.0604	1.7345	1.7949	1.9924	1.9320
3.18	1.7023	1.9345	0.0000	-0.0354	1.7023	1.7377	1.9698	1.9345
3.19	1.6708	1.9366	0.0000	-0.0109	1.6708	1.6817	1.9475	1.9366
3.20	1.6270	1.9252	-0.0133	0.0000	1.6403	1.6270	1.9252	1.9385
3.21	1.5734	1.9032	-0.0367	0.0000	1.6101	1.5734	1.9032	1.9399
3.22	1.5206	1.8811	-0.0601	0.0000	1.5807	1.5206	1.8811	1.9413
3.23	1.4686	1.8591	-0.0830	0.0000	1.5516	1.4686	1.8591	1.9421
3.24	1.4180	1.8373	-0.1053	0.0000	1.5233	1.4180	1.8373	1.9426
3.25	1.3685	1.8155	-0.1271	0.0000	1.4955	1.3685	1.8155	1.9426

Table E.6: Calculated spin, magnetization and ground state energy for various types of zigzag nanoribbon. All the energy values quoted in the table are in Hartree ( $Ha$ ) for better readability. Here,  $\Delta E$  denotes the energy difference between spin polarised and spin un-polarised ground states.

Parameter	Bare edge		2H/S edge		2H/Mo edge	
	FM	AFM	FM	AFM	FM	AFM
$\mu B$	1.11766	0.05688	1.29796	0.01242	1.28977	0.01659
Spin Up	104.55883	104.02844	105.64898	104.99379	105.64489	105.00829
Spin Down	103.44117	103.97156	104.35102	105.00621	104.35511	104.99171
$E_{spin}$	-716.63766	-716.63766	-717.81422	-717.81422	-717.79981	-717.79981
$E_{no-spin}$	-716.63574	-716.63574	-717.81065	-717.81065	-717.79822	-717.79822
$\Delta E$	-0.00193	-0.00193	-0.00357	-0.00357	-0.00159	-0.00159

Parameter	4H		5H		5H	
	FM	AFM	(3H at S edge)	(3H at Mo edge)	(3H at S edge)	(3H at Mo edge)
$\mu B$	1.43321	0.03912	0.58576	0.77322	0.77322	0.00000
Spin Up	106.71660	106.01956	106.79288	106.88661	106.88661	107.00000
Spin Down	105.28340	105.98044	106.20712	106.11339	106.11339	107.00000
$E_{spin}$	-718.99607	-718.99607	-719.58269	-719.58406	-719.58406	-720.17133
$E_{no-spin}$	-718.99235	-718.99235	-719.55536	-719.60324	-719.60324	-720.17133
$\Delta E$	-0.00372	-0.00372	-0.02733	-0.08083	-0.08083	0.00000

# Appendix F

## Supplementary Results

### F.1 2H-MoS<sub>2</sub> and 1H-MoS<sub>2</sub> band structure

In this section, the band structure of bulk MoS<sub>2</sub> (2H-MoS<sub>2</sub>) and single-layer MoS<sub>2</sub> (1H-MoS<sub>2</sub>) calculated using local density approximation (LDA) and generalised gradient approximation (GGA) techniques with and without Projector Augmented Wave (PAW) method are presented for the comparison purposes.

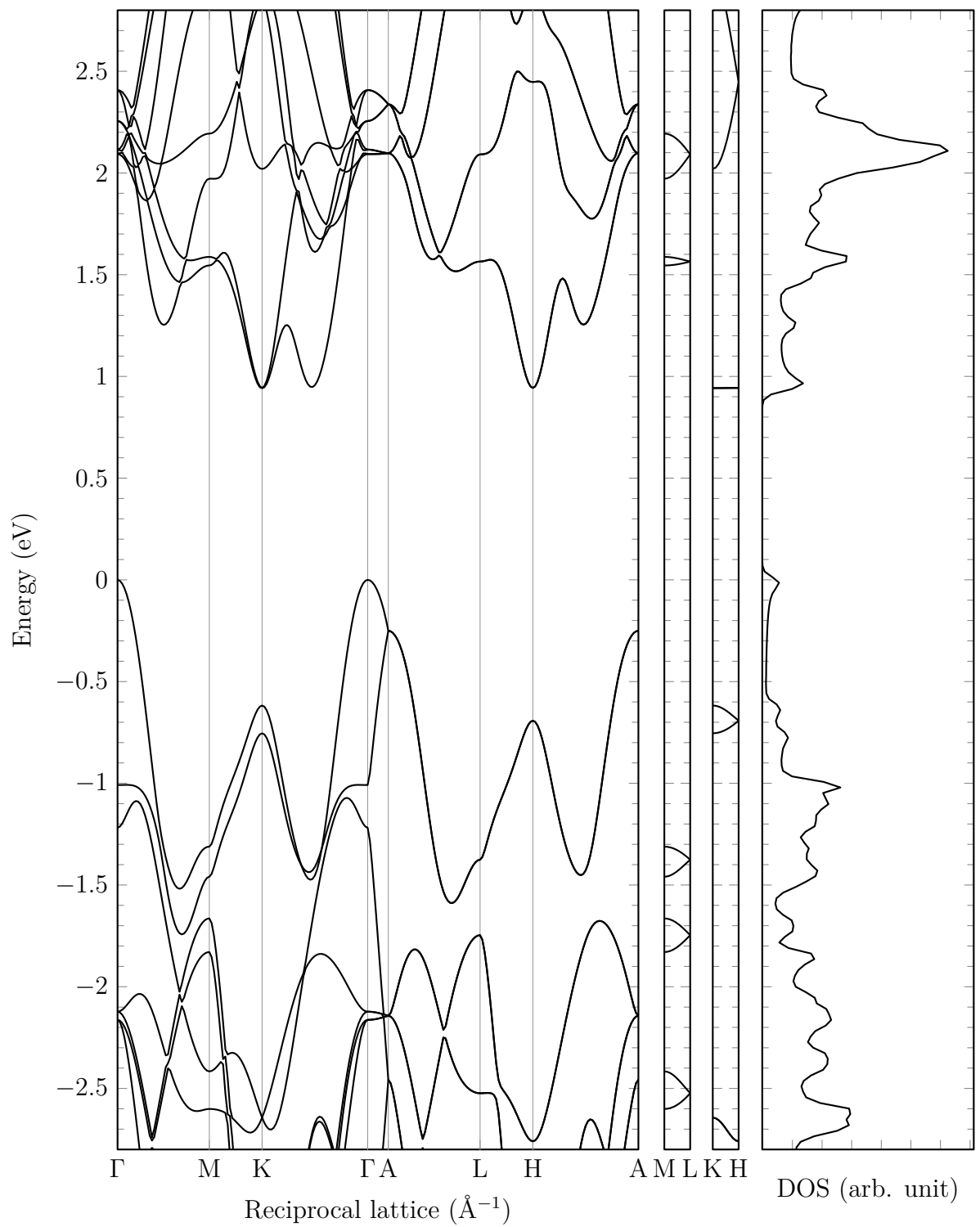


Figure F.1: The calculated band structure of 2H-MoS<sub>2</sub> along the symmetry points of the irreducible wedge of the first Brillouin zone using GGA technique. The second  $\Gamma$  point is located in the next Brillouin zone with the reduced coordinates of (1,0,0). The corresponding density of states (DOS) is on the right with arbitrary unit. The energy axis is set to zero at the Fermi energy.

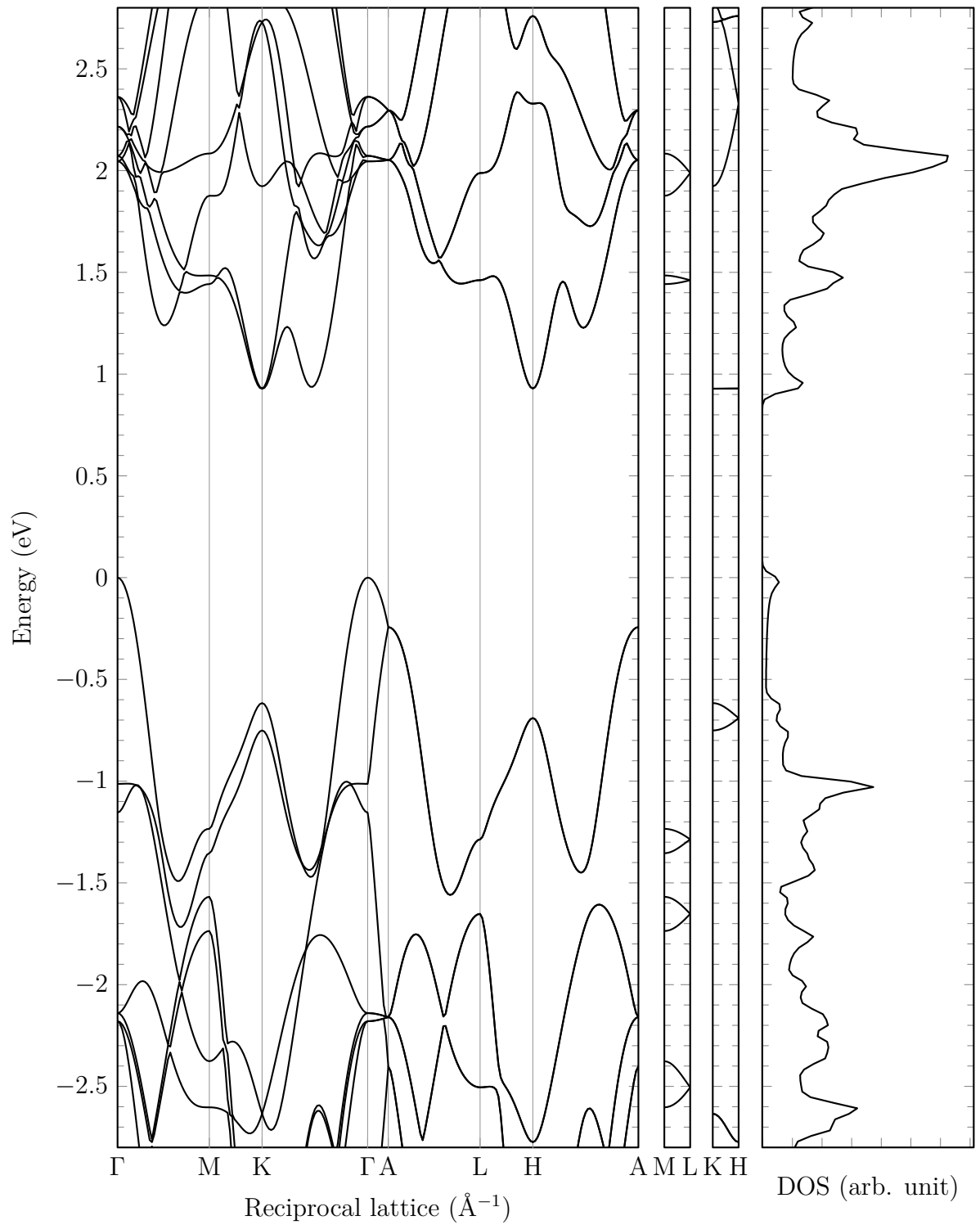


Figure F.2: The calculated band gap of 2H-MoS<sub>2</sub> along the symmetry points of the irreducible wedge of the first Brillouin zone using GGA+PAW technique. The second  $\Gamma$  point is located in the next Brillouin zone with the reduced coordinates of (1,0,0). The corresponding density of states (DOS) is on the right with arbitrary unit. The energy axis is set to zero at the Fermi energy.

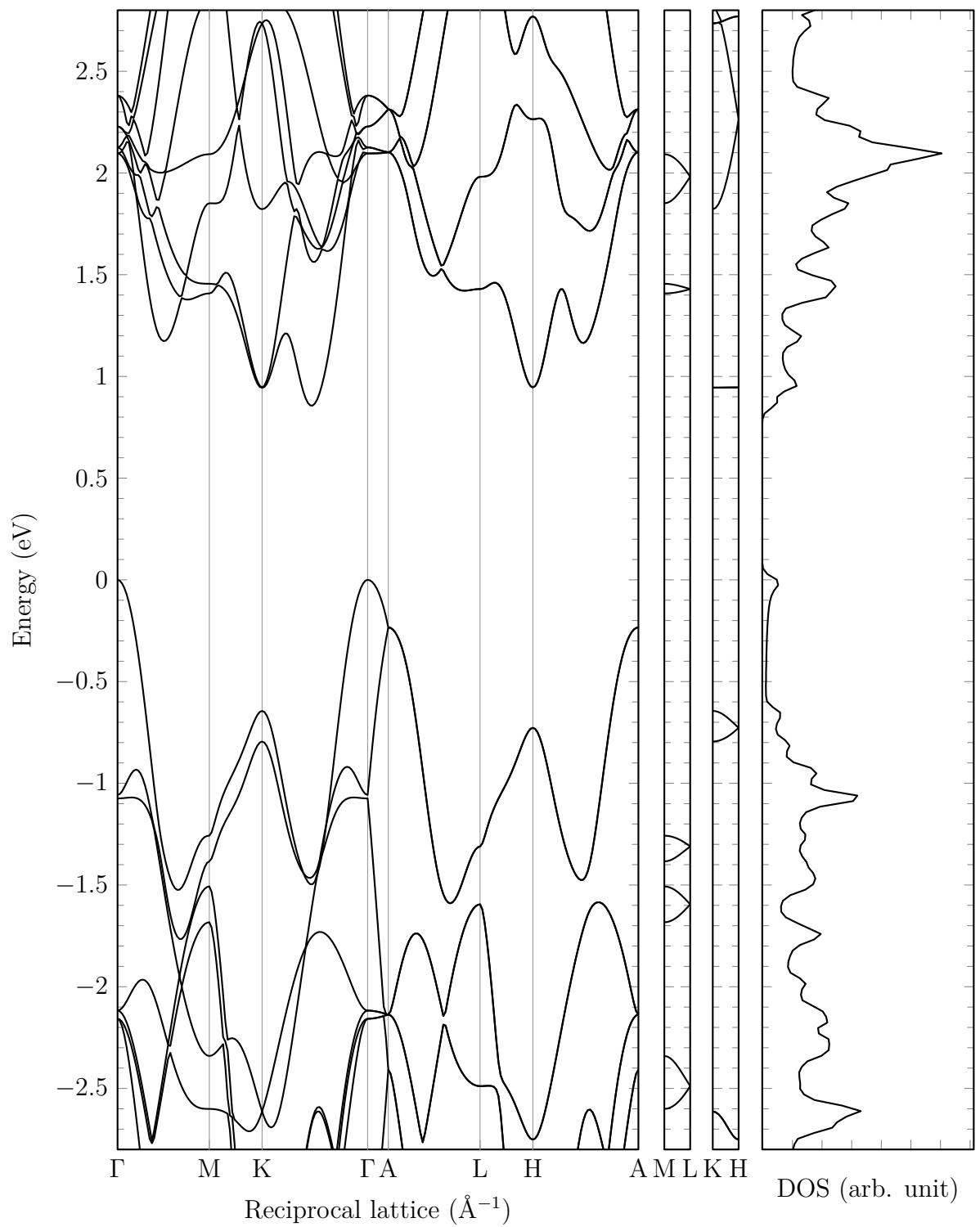


Figure F.3: The calculated band structure of 2H-MoS<sub>2</sub> along the symmetry points of the irreducible wedge of the first Brillouin zone using LDA technique. The second  $\Gamma$  point is located in the next Brillouin zone with the reduced coordinates of (1,0,0). The corresponding density of states (DOS) is on the right with arbitrary unit. The energy axis is set to zero at the Fermi energy.

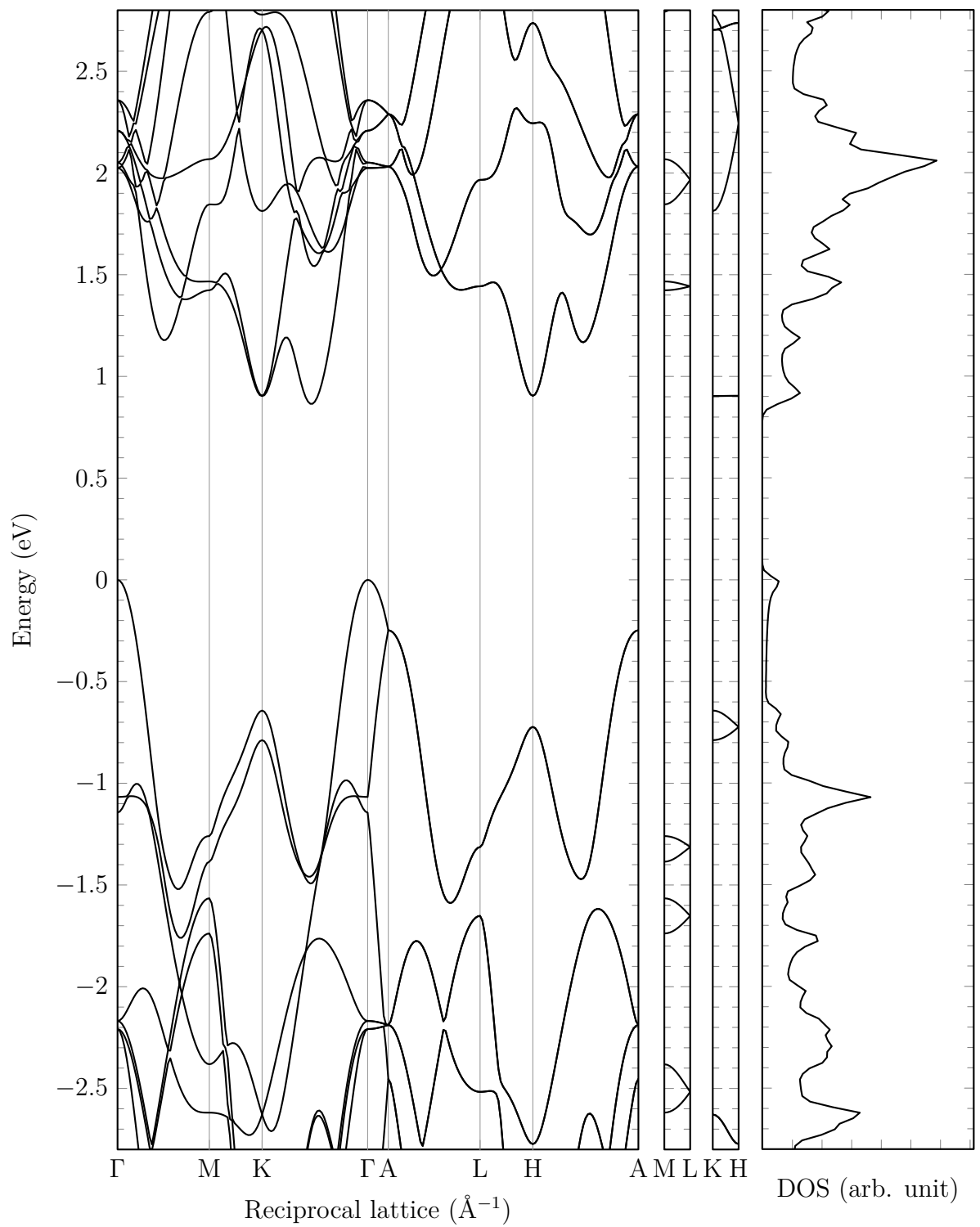


Figure F.4: The calculated band structure of 2H-MoS<sub>2</sub> along the symmetry points of the irreducible wedge of the first Brillouin zone using LDA+PAW technique. The second  $\Gamma$  point is located in the next Brillouin zone with the reduced coordinates of (1,0,0). The corresponding density of states (DOS) is on the right with arbitrary unit. The energy axis is set to zero at the Fermi energy.

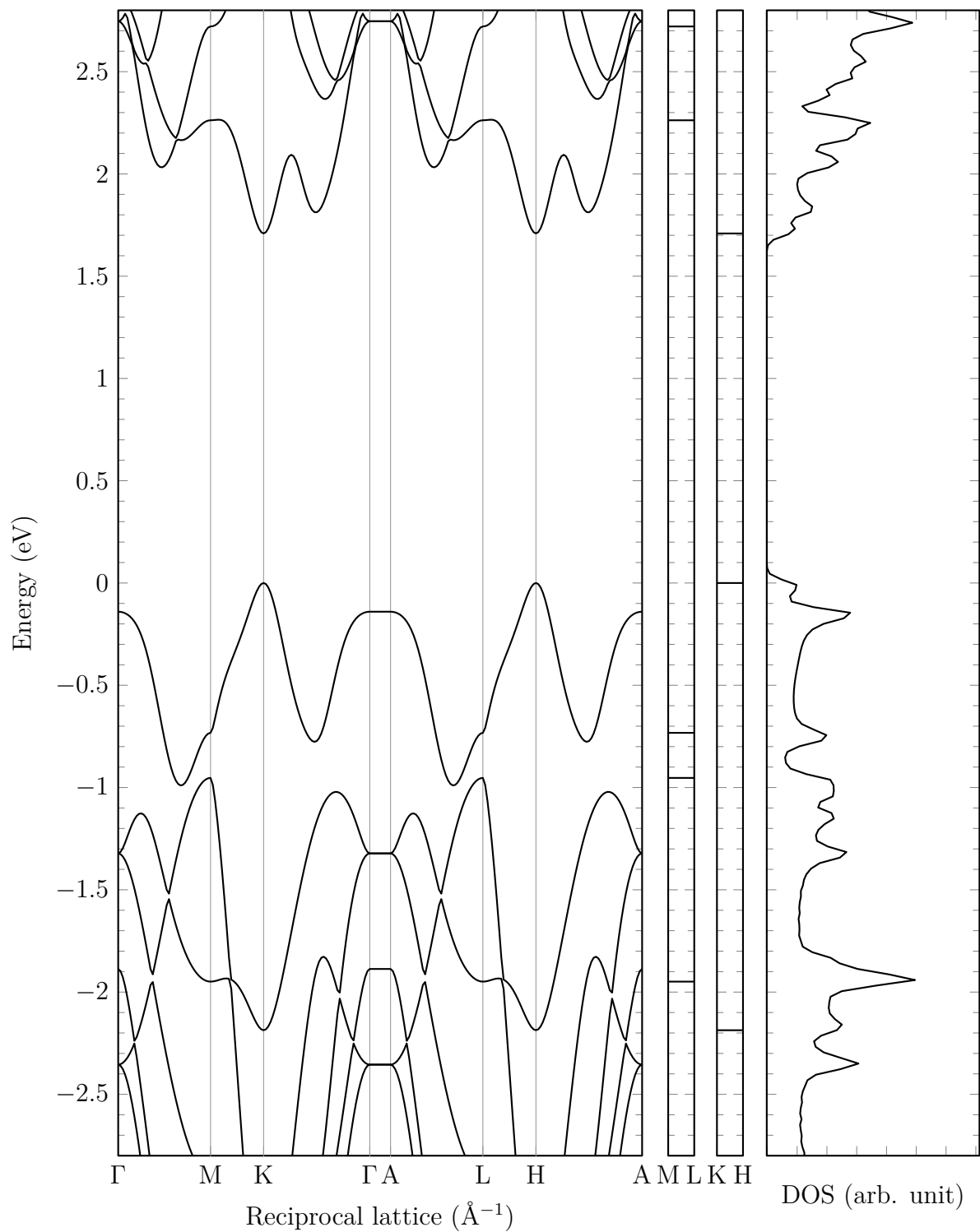


Figure F.5: The calculated band structure of 1H-MoS<sub>2</sub> along the symmetry points of the irreducible wedge of the first Brillouin zone using GGA technique. The second  $\Gamma$  point is located in the next Brillouin zone with the reduced coordinates of (1,0,0). The corresponding density of states (DOS) is on the right with arbitrary unit. The energy axis is set to zero at the Fermi energy.

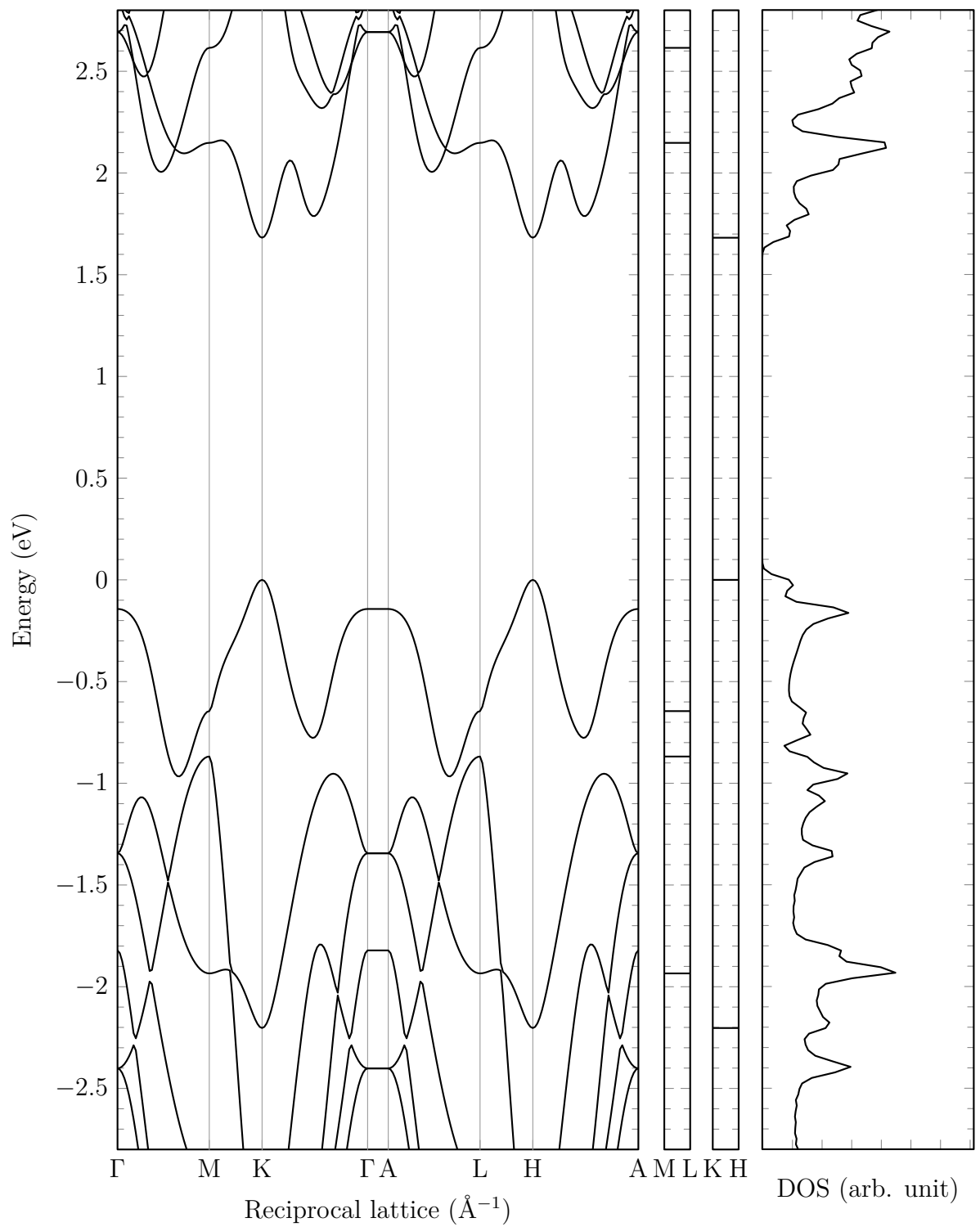


Figure F.6: The calculated band structure of 1H-MoS<sub>2</sub> along the symmetry points of the irreducible wedge of the first Brillouin zone using GGA+PAW technique. The second  $\Gamma$  point is located in the next Brillouin zone with the reduced coordinates of (1,0,0). The corresponding density of states (DOS) is on the right with arbitrary unit. The energy axis is set to zero at the Fermi energy.

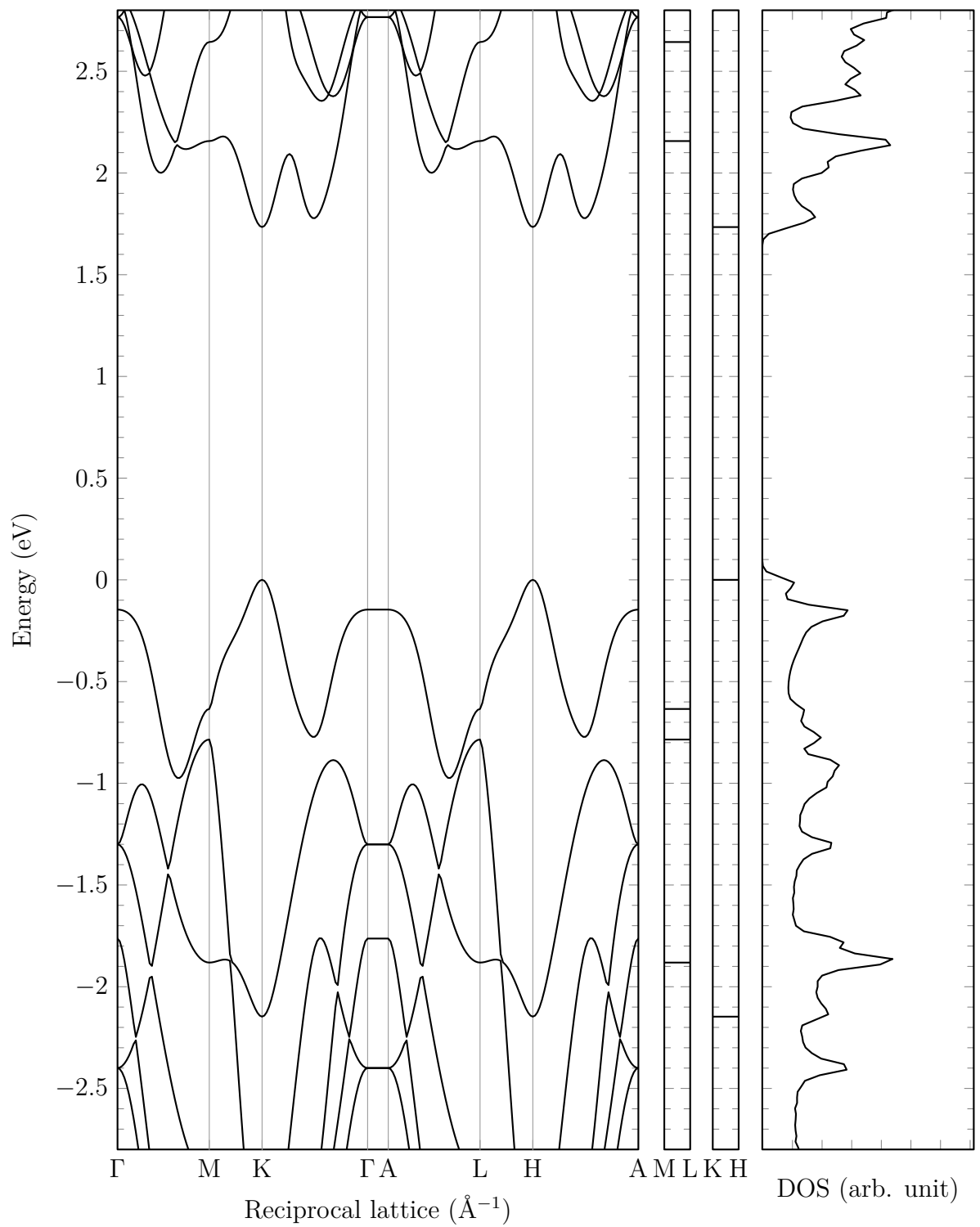


Figure F.7: The calculated band structure of 1H-MoS<sub>2</sub> along the symmetry points of the irreducible wedge of the first Brillouin zone using LDA technique. The second  $\Gamma$  point is located in the next Brillouin zone with the reduced coordinates of (1,0,0). The corresponding density of states (DOS) is on the right with arbitrary unit. The energy axis is set to zero at the Fermi energy.

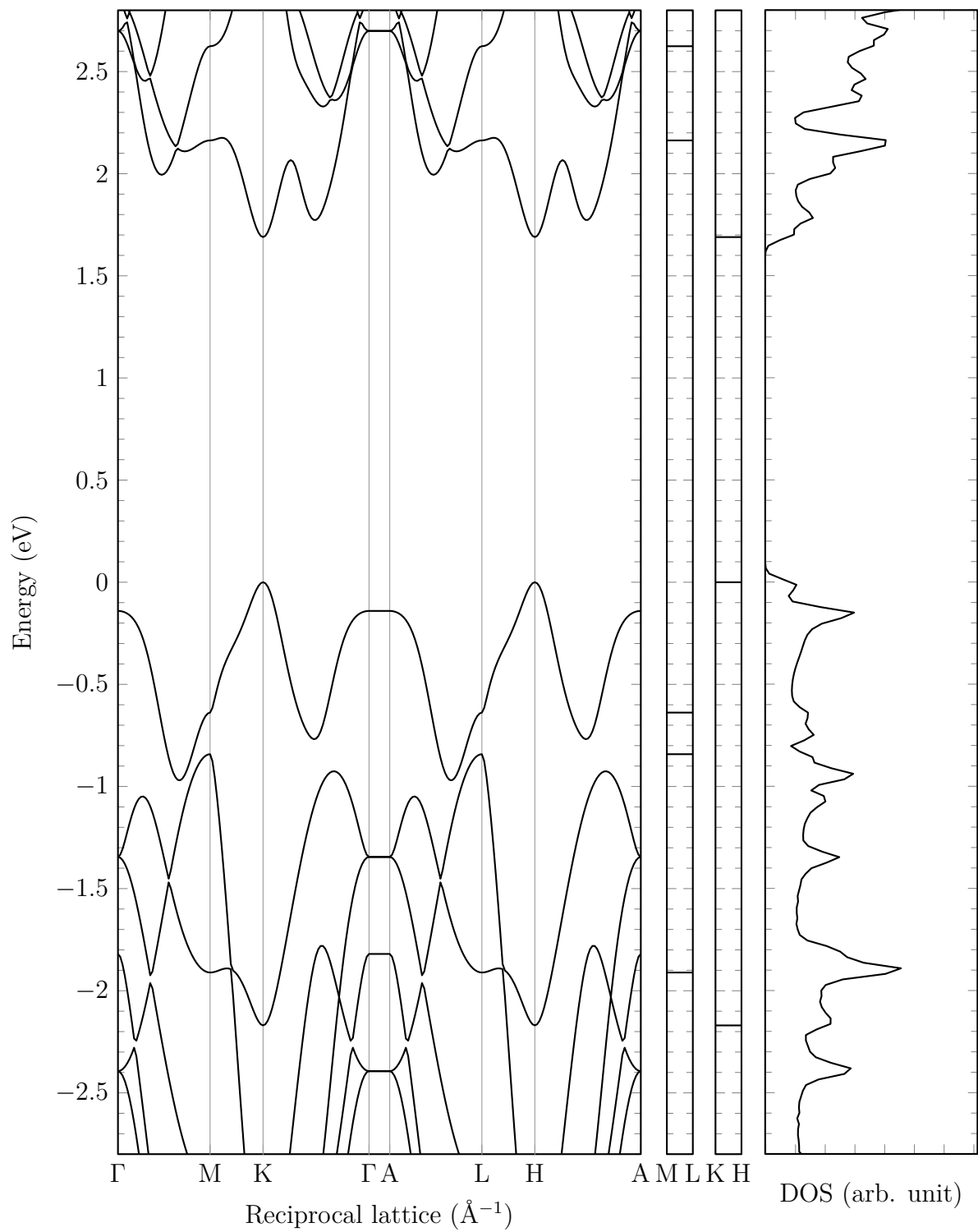


Figure F.8: The calculated band structure of 1H-MoS<sub>2</sub> along the symmetry points of the irreducible wedge of the first Brillouin zone using LDA+PAW technique. The second  $\Gamma$  point is located in the next Brillouin zone with the reduced coordinates of (1,0,0). The corresponding density of states (DOS) is on the right with arbitrary unit. The energy axis is set to zero at the Fermi energy.

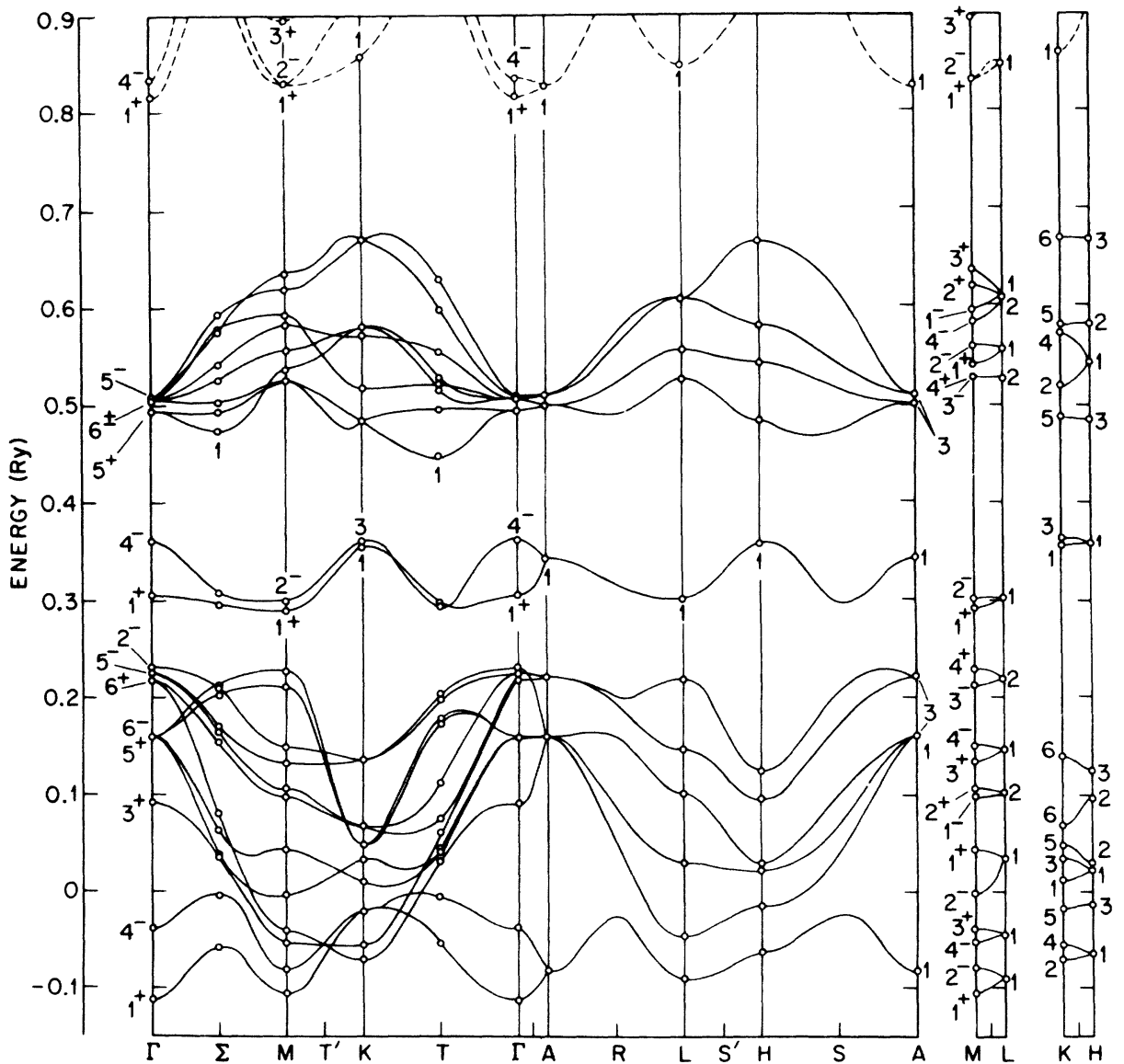


Figure F.9: Band structure of bulk MoS<sub>2</sub> (2H-MoS<sub>2</sub>) calculated using Augmented Plain Waves (APW) with the symmetry properties listed in Table F.1. Figure taken from Band Structure of Transition-Metal-Dichalcogenide Layered Compounds by Mattheiss [263].

Table F.1: Symmetry properties of Bloch sums formed from  $s$ ,  $p$  and  $d$  orbitals at the molybdenum and sulphur sites in  $2H\text{-MoS}_2$  as marked in Figure F.9. Table taken from Band Structure of Transition-Metal-Dichalcogenide Layered Compounds by Mattheiss [263].

$2H\text{-MoS}_2$	$\Gamma$	$M$	$K$	$A$	$L$	$H$
Molybdenum						
$s$	$1^+, 4^-$	$1^+, 2^-$	5	1	1	3
$p_z$	$3^+, 2^-$	$3^+, 4^-$	6	1	1	2
$p_x, p_y$	$5^+, 6^-$	$1^+, 4^+, 2^-, 3^-$	1, 3, 5	3	1, 2	1, 2
$d_{z^2}$	$1^+, 4^-$	$1^+, 2^-$	5	1	1	3
$d_{xy}, d_{x^2-y^2}$	$5^+, 6^-$	$1^+, 4^+, 2^-, 3^-$	1, 3, 5	3	1, 2	1, 2
$d_{xz}, d_{yz}$	$6^+, 5^-$	$2^+, 3^+, 1^-, 4^-$	2, 4, 6	3	1, 2	1, 3
Sulphur						
$s$	$1^+, 3^+, 2^-, 4^-$	$1^+, 3^+, 2^-, 4^-$	5, 6	1, 1	1, 1	2, 3
$p_z$	$1^+, 3^+, 2^-, 4^-$	$1^+, 3^+, 2^-, 4^-$	5, 6	1, 1	1, 1	2, 3
$p_x, p_y$	$5^\pm, 6^\pm$	$1^\pm, 2^\pm, 3^\pm, 4^\pm$	1, 2, 3, 4, 5, 6	3, 3	1, 1, 2, 2	1, 1, 2, 3

## F.2 Atomic Charge and Magnetization of Nanoribbons

In this section atomic charge and magnetization of the individual atoms in various nanoribbon configuration is calculated and presented. The atomic charge is calculated using the Hirshfeld method [290] and the magnetization is calculated by integrating the spin-polarization (or magnetization) density (spin up - spin down difference) on a sphere with the radius of 1.65 Å around each atom. This magnetisation moment only indicates a rough estimation of each atom contribution to the total magnetisation as the bonding length of each atom (e.g. Molybdenum and Hydrogen) are considerably different. The link between atom labels and the position of each atom is illustrated in Figure F.10.

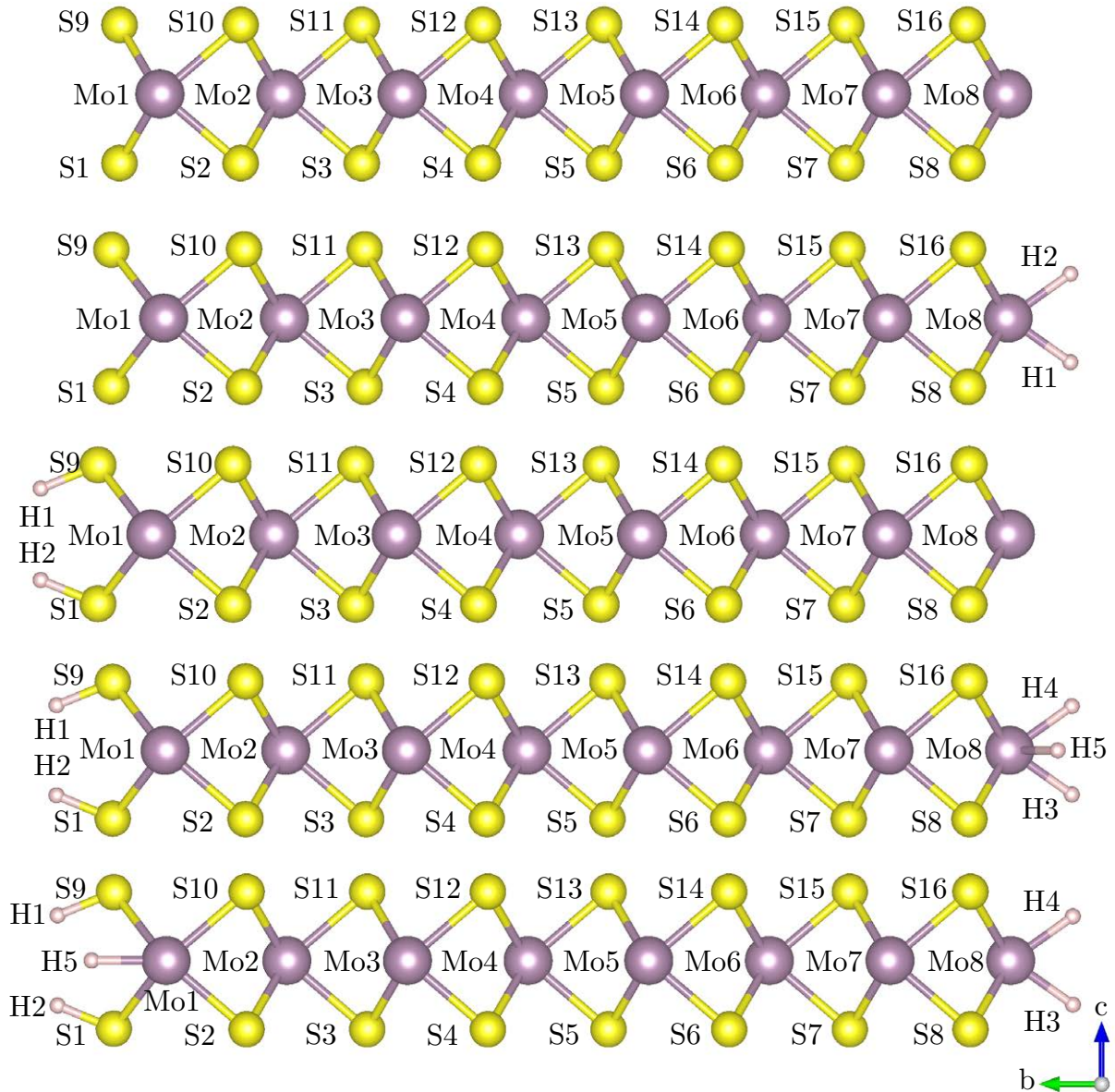


Figure F.10: Position of the atom labels used for tabulating the Hirshfeld charge and magnetic moment of zigzag  $\text{MoS}_2$  nanoribbons ( $\text{Mo}_8\text{S}_{16}$ ). The nanoribbons from top to bottom are bare edge, 2H on the molybdenum edge, 2H on the sulphur edge, 5H type I (2H on S edge and 3H on Mo edge) and 5H type II (3H on S edge and 2H on Mo edge).

Table F.2: Hirshfeld atomic charge and atomic magnetization of zigzag MoS<sub>2</sub> nanoribbon in ferromagnetic state.

Atom	$Z_{ion}$	Hirshfeld Charge	Net Charge	Magnetic Moment
$Mo_1$	14.0000	0.0402	14.0402	-0.0503
$Mo_2$	14.0000	-0.0114	13.9886	0.0060
$Mo_3$	14.0000	-0.0007	13.9993	0.0001
$Mo_4$	14.0000	0.0001	14.0001	-0.0001
$Mo_5$	14.0000	0.0001	14.0001	-0.0000
$Mo_6$	14.0000	0.0042	14.0042	-0.0032
$Mo_7$	14.0000	-0.0215	13.9785	0.0151
$Mo_8$	14.0000	-0.5261	13.4739	0.2533
$S_1$	6.0000	-0.2509	5.7491	0.1752
$S_2$	6.0000	-0.0241	5.9759	0.0169
$S_3$	6.0000	-0.0041	5.9959	0.0028
$S_4$	6.0000	-0.0003	5.9997	0.0002
$S_5$	6.0000	-0.0000	6.0000	0.0000
$S_6$	6.0000	0.0001	6.0001	-0.0000
$S_7$	6.0000	-0.0030	5.9970	0.0008
$S_8$	6.0000	-0.0192	5.9808	0.0007
$S_9$	6.0000	-0.2503	5.7497	0.1742
$S_{10}$	6.0000	-0.0243	5.9757	0.0175
$S_{11}$	6.0000	-0.0042	5.9958	0.0028
$S_{12}$	6.0000	-0.0003	5.9997	0.0002
$S_{13}$	6.0000	-0.0000	6.0000	0.0000
$S_{14}$	6.0000	0.0001	6.0001	-0.0000
$S_{15}$	6.0000	-0.0028	5.9972	0.0005
$S_{16}$	6.0000	-0.0190	5.9810	0.0008

Table F.3: Hirshfeld atomic charge and atomic magnetization of zigzag MoS<sub>2</sub> nanoribbon in anti-ferromagnetic state.

Atom	$Z_{ion}$	Hirshfeld Charge	Net Charge	Magnetic Moment
$Mo_1$	14.0000	-0.0402	13.9597	0.0503
$Mo_2$	14.0000	0.0114	14.0114	-0.0060
$Mo_3$	14.0000	0.0008	14.0008	-0.0002
$Mo_4$	14.0000	-0.0000	14.0000	0.0001
$Mo_5$	14.0000	0.0001	14.0001	0.0000
$Mo_6$	14.0000	0.0042	14.0042	-0.0032
$Mo_7$	14.0000	-0.0216	13.9785	0.0152
$Mo_8$	14.0000	-0.5265	13.4735	0.2535
$S_1$	6.0000	0.2510	6.2510	-0.1752
$S_2$	6.0000	0.0241	6.0241	-0.0169
$S_3$	6.0000	0.0041	6.0041	-0.0028
$S_4$	6.0000	0.0003	6.0003	-0.0002
$S_5$	6.0000	0.0001	6.0001	-0.0001
$S_6$	6.0000	0.0001	6.0001	-0.0001
$S_7$	6.0000	-0.0030	5.9970	0.0008
$S_8$	6.0000	-0.0192	5.9808	0.0006
$S_9$	6.0000	0.2504	6.2504	-0.1743
$S_{10}$	6.0000	0.0243	6.0243	-0.0175
$S_{11}$	6.0000	0.0042	6.0042	-0.0028
$S_{12}$	6.0000	0.0003	6.0003	-0.0002
$S_{13}$	6.0000	0.0001	6.0001	-0.0001
$S_{14}$	6.0000	0.0001	6.0001	-0.0001
$S_{15}$	6.0000	-0.0028	5.9972	0.0005
$S_{16}$	6.0000	-0.0190	5.9810	0.0008

Table F.4: Hirshfeld atomic charge and atomic magnetization of zigzag MoS<sub>2</sub> nanoribbon with 2 hydrogen atoms on the molybdenum edge of the nanoribbon in ferromagnetic state.

Atom	$Z_{ion}$	Hirshfeld Charge	Net Charge	Magnetic Moment
$Mo_1$	14.0000	0.0653	14.0653	-0.0704
$Mo_2$	14.0000	-0.0040	13.9960	0.0018
$Mo_3$	14.0000	-0.0002	13.9998	0.0001
$Mo_4$	14.0000	0.0003	14.0003	-0.0002
$Mo_5$	14.0000	0.0013	14.0013	-0.0010
$Mo_6$	14.0000	-0.0052	13.9948	0.0029
$Mo_7$	14.0000	0.0018	14.0018	-0.0073
$Mo_8$	14.0000	-0.5360	13.4640	0.3876
$S_1$	6.0000	-0.3433	5.6567	0.2363
$S_2$	6.0000	-0.0095	5.9905	0.0056
$S_3$	6.0000	-0.0014	5.9986	0.0009
$S_4$	6.0000	-0.0003	5.9997	0.0002
$S_5$	6.0000	0.0000	6.0000	0.0000
$S_6$	6.0000	-0.0005	5.9995	-0.0000
$S_7$	6.0000	-0.0062	5.9938	0.0039
$S_8$	6.0000	-0.0380	5.9620	0.0055
$S_9$	6.0000	-0.3476	5.6524	0.2374
$S_{10}$	6.0000	-0.0098	5.9902	0.0061
$S_{11}$	6.0000	-0.0014	5.9986	0.0010
$S_{12}$	6.0000	-0.0003	5.9997	0.0002
$S_{13}$	6.0000	0.0000	6.0000	0.0000
$S_{14}$	6.0000	-0.0005	5.9995	-0.0001
$S_{15}$	6.0000	-0.0064	5.9936	0.0041
$S_{16}$	6.0000	-0.0389	5.9611	0.0037
$H_1$	1.0000	-0.0046	0.9954	0.0058
$H_2$	1.0000	-0.0044	0.9956	0.0113

Table F.5: Hirshfeld atomic charge and atomic magnetization of zigzag MoS<sub>2</sub> nanoribbon with 2 hydrogen atoms on the molybdenum edge of the nanoribbon in anti-ferromagnetic state.

Atom	$Z_{ion}$	Hirshfeld Charge	Net Charge	Magnetic Moment
$Mo_1$	14.0000	0.0653	14.0653	-0.0704
$Mo_2$	14.0000	-0.0040	13.9960	0.0018
$Mo_3$	14.0000	-0.0002	13.9998	0.0001
$Mo_4$	14.0000	0.0003	14.0003	-0.0002
$Mo_5$	14.0000	0.0013	14.0013	-0.0010
$Mo_6$	14.0000	-0.0052	13.9948	0.0029
$Mo_7$	14.0000	0.0018	14.0018	-0.0073
$Mo_8$	14.0000	-0.5360	13.4640	0.3876
$S_1$	6.0000	-0.3433	5.6567	0.2363
$S_2$	6.0000	-0.0095	5.9905	0.0056
$S_3$	6.0000	-0.0014	5.9986	0.0009
$S_4$	6.0000	-0.0003	5.9997	0.0002
$S_5$	6.0000	0.0000	6.0000	0.0000
$S_6$	6.0000	-0.0005	5.9995	-0.0000
$S_7$	6.0000	-0.0062	5.9938	0.0039
$S_8$	6.0000	-0.0380	5.9620	0.0055
$S_9$	6.0000	-0.3476	5.6524	0.2374
$S_{10}$	6.0000	-0.0098	5.9902	0.0061
$S_{11}$	6.0000	-0.0014	5.9986	0.0010
$S_{12}$	6.0000	-0.0003	5.9997	0.0002
$S_{13}$	6.0000	0.0000	6.0000	0.0000
$S_{14}$	6.0000	-0.0005	5.9995	-0.0001
$S_{15}$	6.0000	-0.0064	5.9936	0.0041
$S_{16}$	6.0000	-0.0389	5.9611	0.0037
$H_1$	1.0000	-0.0046	0.9954	0.0058
$H_2$	1.0000	-0.0044	0.9956	0.0113

Table F.6: Hirshfeld atomic charge and atomic magnetization of zigzag MoS<sub>2</sub> nanoribbon with 2 hydrogen atoms on the sulphur edge of the nanoribbon in ferromagnetic state.

Atom	$Z_{ion}$	Hirshfeld Charge	Net Charge	Magnetic Moment
$Mo_1$	14.0000	-0.5425	13.4575	0.3901
$Mo_2$	14.0000	-0.0040	13.9960	-0.0002
$Mo_3$	14.0000	-0.0053	13.9947	0.0037
$Mo_4$	14.0000	-0.0007	13.9993	0.0003
$Mo_5$	14.0000	-0.0000	14.0000	0.0001
$Mo_6$	14.0000	0.0039	14.0039	-0.0031
$Mo_7$	14.0000	-0.0224	13.9776	0.0154
$Mo_8$	14.0000	-0.5925	13.4075	0.2847
$S_1$	6.0000	-0.0097	5.9903	-0.0153
$S_2$	6.0000	-0.0240	5.9760	0.0099
$S_3$	6.0000	-0.0005	5.9995	0.0005
$S_4$	6.0000	-0.0001	6.0000	-0.0001
$S_5$	6.0000	0.0001	6.0001	-0.0000
$S_6$	6.0000	-0.0001	5.9999	0.0001
$S_7$	6.0000	-0.0021	5.9979	0.0001
$S_8$	6.0000	-0.0201	5.9799	0.0002
$S_9$	6.0000	-0.0096	5.9904	-0.0153
$S_{10}$	6.0000	-0.0243	5.9757	0.0096
$S_{11}$	6.0000	-0.0005	5.9995	0.0005
$S_{12}$	6.0000	-0.0001	5.9999	-0.0001
$S_{13}$	6.0000	0.0001	6.0001	-0.0000
$S_{14}$	6.0000	-0.0001	5.9999	0.0001
$S_{15}$	6.0000	-0.0019	5.9981	-0.0002
$S_{16}$	6.0000	-0.0200	5.9800	0.0003
$H_1$	1.0000	-0.0107	0.9893	0.0096
$H_2$	1.0000	-0.0107	0.9893	0.0088

Table F.7: Hirshfeld atomic charge and atomic magnetization of zigzag MoS<sub>2</sub> nanoribbon with 2 hydrogen atoms on the sulphur edge of the nanoribbon in anti-ferromagnetic state.

Atom	$Z_{ion}$	Hirshfeld Charge	Net Charge	Magnetic Moment
$Mo_1$	14.0000	-0.5426	13.4574	0.3902
$Mo_2$	14.0000	-0.0040	13.9960	-0.0002
$Mo_3$	14.0000	-0.0054	13.9947	0.0037
$Mo_4$	14.0000	-0.0007	13.9993	0.0004
$Mo_5$	14.0000	-0.0002	13.9998	0.0001
$Mo_6$	14.0000	-0.0039	13.9961	0.0031
$Mo_7$	14.0000	0.0223	14.0223	-0.0154
$Mo_8$	14.0000	0.5927	14.5927	-0.2848
$S_1$	6.0000	-0.0097	5.9903	-0.0153
$S_2$	6.0000	-0.0240	5.9760	0.0100
$S_3$	6.0000	-0.0005	5.9995	0.0005
$S_4$	6.0000	-0.0000	6.0000	-0.0001
$S_5$	6.0000	0.0000	6.0000	-0.0000
$S_6$	6.0000	0.0001	6.0001	-0.0001
$S_7$	6.0000	0.0021	6.0021	-0.0001
$S_8$	6.0000	0.0201	6.0201	-0.0001
$S_9$	6.0000	-0.0096	5.9904	-0.0153
$S_{10}$	6.0000	-0.0243	5.9757	0.0096
$S_{11}$	6.0000	-0.0005	5.9995	0.0005
$S_{12}$	6.0000	-0.0001	6.0000	-0.0001
$S_{13}$	6.0000	0.0000	6.0000	-0.0000
$S_{14}$	6.0000	0.0001	6.0001	-0.0001
$S_{15}$	6.0000	0.0019	6.0019	0.0002
$S_{16}$	6.0000	0.0200	6.0200	-0.0002
$H_1$	1.0000	-0.0107	0.9893	0.0096
$H_2$	1.0000	-0.0107	0.9893	0.0088

Table F.8: Hirshfeld atomic charge and atomic magnetization of zigzag MoS<sub>2</sub> nanoribbon with a total of 4 hydrogen atoms on the edges of the nanoribbon (2 on each side) in ferromagnetic state.

Atom	$Z_{ion}$	Hirshfeld Charge	Net Charge	Magnetic Moment
$Mo_1$	14.0000	-0.5972	13.4028	0.4278
$Mo_2$	14.0000	-0.0168	13.9832	0.0100
$Mo_3$	14.0000	-0.0060	13.9940	0.0041
$Mo_4$	14.0000	-0.0012	13.9988	0.0007
$Mo_5$	14.0000	-0.0003	13.9997	0.0001
$Mo_6$	14.0000	-0.0081	13.9919	0.0048
$Mo_7$	14.0000	-0.0137	13.9863	0.0043
$Mo_8$	14.0000	-0.5695	13.4305	0.4119
$S_1$	6.0000	-0.0116	5.9884	-0.0170
$S_2$	6.0000	-0.0290	5.9710	0.0119
$S_3$	6.0000	-0.0017	5.9983	0.0010
$S_4$	6.0000	-0.0000	6.0000	-0.0002
$S_5$	6.0000	0.0001	6.0001	-0.0001
$S_6$	6.0000	-0.0005	5.9995	-0.0000
$S_7$	6.0000	-0.0072	5.9928	0.0044
$S_8$	6.0000	-0.0389	5.9611	0.0051
$S_9$	6.0000	-0.0115	5.9885	-0.0169
$S_{10}$	6.0000	-0.0293	5.9707	0.0113
$S_{11}$	6.0000	-0.0018	5.9982	0.0010
$S_{12}$	6.0000	-0.0001	6.0000	-0.0002
$S_{13}$	6.0000	0.0001	6.0001	-0.0001
$S_{14}$	6.0000	-0.0005	5.9995	-0.0001
$S_{15}$	6.0000	-0.0073	5.9927	0.0046
$S_{16}$	6.0000	-0.0399	5.9601	0.0034
$H_1$	1.0000	-0.0153	0.9847	0.0135
$H_2$	1.0000	-0.0153	0.9847	0.0126
$H_3$	1.0000	-0.0054	0.9946	0.0070
$H_4$	1.0000	-0.0052	0.9948	0.0130

Table F.9: Hirshfeld atomic charge and atomic magnetization of zigzag MoS<sub>2</sub> nanoribbon with a total of 4 hydrogen atoms on the edges of the nanoribbon (2 on each side) in anti-ferromagnetic state.

Atom	$Z_{ion}$	Hirshfeld Charge	Net Charge	Magnetic Moment
$Mo_1$	14.0000	-0.5972	13.4028	0.4278
$Mo_2$	14.0000	-0.0168	13.9832	0.0100
$Mo_3$	14.0000	-0.0058	13.9942	0.0040
$Mo_4$	14.0000	-0.0002	13.9998	-0.0000
$Mo_5$	14.0000	0.0000	14.0000	0.0001
$Mo_6$	14.0000	0.0080	14.0080	-0.0048
$Mo_7$	14.0000	0.0137	14.0137	-0.0043
$Mo_8$	14.0000	0.5697	14.5697	-0.4120
$S_1$	6.0000	-0.0116	5.9884	-0.0170
$S_2$	6.0000	-0.0290	5.9710	0.0119
$S_3$	6.0000	-0.0017	5.9983	0.0010
$S_4$	6.0000	-0.0000	6.0000	-0.0002
$S_5$	6.0000	-0.0000	6.0000	0.0000
$S_6$	6.0000	0.0005	6.0005	0.0000
$S_7$	6.0000	0.0072	6.0072	-0.0044
$S_8$	6.0000	0.0389	6.0389	-0.0051
$S_9$	6.0000	-0.0115	5.9885	-0.0169
$S_{10}$	6.0000	-0.0293	5.9707	0.0113
$S_{11}$	6.0000	-0.0018	5.9982	0.0010
$S_{12}$	6.0000	-0.0000	6.0000	-0.0001
$S_{13}$	6.0000	-0.0000	6.0000	0.0000
$S_{14}$	6.0000	0.0005	6.0005	0.0001
$S_{15}$	6.0000	0.0073	6.0073	-0.0046
$S_{16}$	6.0000	0.0399	6.0399	-0.0034
$H_1$	1.0000	-0.0153	0.9847	0.0135
$H_2$	1.0000	-0.0153	0.9847	0.0126
$H_3$	1.0000	0.0054	1.0054	-0.0070
$H_4$	1.0000	0.0052	1.0052	-0.0130

Table F.10: Hirshfeld atomic charge and atomic magnetization of zigzag MoS<sub>2</sub> nanoribbon with a total of 5 hydrogen atoms on the edges of the nanoribbon (3 on sulphur side and 2 on molybdenum side) in ferromagnetic state.

Atom	$Z_{ion}$	Hirshfeld Charge	Net Charge	Magnetic Moment
$Mo_1$	14.0000	0.0002	14.0002	-0.0002
$Mo_2$	14.0000	-0.0000	14.0000	0.0000
$Mo_3$	14.0000	-0.0001	13.9999	0.0000
$Mo_4$	14.0000	-0.0003	13.9997	0.0002
$Mo_5$	14.0000	-0.0002	13.9998	0.0001
$Mo_6$	14.0000	-0.0051	13.9949	0.0028
$Mo_7$	14.0000	-0.0161	13.9839	0.0072
$Mo_8$	14.0000	-0.4731	13.5268	0.3398
$S_1$	6.0000	0.0000	6.0000	-0.0000
$S_2$	6.0000	0.0000	6.0000	-0.0000
$S_3$	6.0000	-0.0000	6.0000	0.0000
$S_4$	6.0000	-0.0000	6.0000	-0.0000
$S_5$	6.0000	0.0000	6.0000	-0.0000
$S_6$	6.0000	-0.0003	5.9997	-0.0001
$S_7$	6.0000	-0.0056	5.9944	0.0032
$S_8$	6.0000	-0.0341	5.9659	0.0052
$S_9$	6.0000	0.0000	6.0000	-0.0000
$S_{10}$	6.0000	0.0000	6.0000	-0.0000
$S_{11}$	6.0000	-0.0000	6.0000	0.0000
$S_{12}$	6.0000	0.0000	6.0000	-0.0000
$S_{13}$	6.0000	0.0000	6.0000	-0.0000
$S_{14}$	6.0000	-0.0003	5.9997	-0.0001
$S_{15}$	6.0000	-0.0057	5.9943	0.0034
$S_{16}$	6.0000	-0.0349	5.9651	0.0038
$H_1$	1.0000	0.0000	1.0000	-0.0000
$H_2$	1.0000	0.0000	1.0000	-0.0000
$H_3$	1.0000	-0.0052	0.9948	0.0065
$H_4$	1.0000	-0.0051	0.9949	0.0114
$H_5$	1.0000	0.0000	1.0000	-0.0000

Table F.11: Hirshfeld atomic charge and atomic magnetization of zigzag MoS<sub>2</sub> nanoribbon with a total of 5 hydrogen atoms on the edges of the nanoribbon (2 on sulphur side and 3 on molybdenum side) in ferromagnetic state.

Atom	$Z_{ion}$	Hirshfeld Charge	Net Charge	Magnetic Moment
$Mo_1$	14.0000	-0.6156	13.3844	0.4403
$Mo_2$	14.0000	-0.0228	13.9772	0.0148
$Mo_3$	14.0000	-0.0063	13.9937	0.0042
$Mo_4$	14.0000	-0.0007	13.9993	0.0003
$Mo_5$	14.0000	-0.0002	13.9998	0.0001
$Mo_6$	14.0000	-0.0001	13.9999	0.0001
$Mo_7$	14.0000	-0.0005	13.9994	0.0004
$Mo_8$	14.0000	-0.0002	13.9998	0.0001
$S_1$	6.0000	-0.0124	5.9876	-0.0175
$S_2$	6.0000	-0.0313	5.9687	0.0130
$S_3$	6.0000	-0.0022	5.9978	0.0012
$S_4$	6.0000	-0.0000	6.0000	-0.0002
$S_5$	6.0000	0.0000	6.0000	-0.0000
$S_6$	6.0000	-0.0000	6.0000	0.0000
$S_7$	6.0000	-0.0001	5.9999	0.0000
$S_8$	6.0000	-0.0001	5.9999	0.0000
$S_9$	6.0000	-0.0123	5.9877	-0.0174
$S_{10}$	6.0000	-0.0317	5.9683	0.0122
$S_{11}$	6.0000	-0.0023	5.9977	0.0012
$S_{12}$	6.0000	-0.0000	6.0000	-0.0002
$S_{13}$	6.0000	0.0000	6.0000	-0.0000
$S_{14}$	6.0000	-0.0000	6.0000	0.0000
$S_{15}$	6.0000	-0.0001	5.9999	0.0000
$S_{16}$	6.0000	-0.0001	5.9999	0.0000
$H_1$	1.0000	-0.0171	0.9829	0.0150
$H_2$	1.0000	-0.0171	0.9829	0.0140
$H_3$	1.0000	-0.0000	1.0000	0.0000
$H_4$	1.0000	-0.0000	1.0000	0.0000
$H_5$	1.0000	-0.0000	1.0000	0.0000

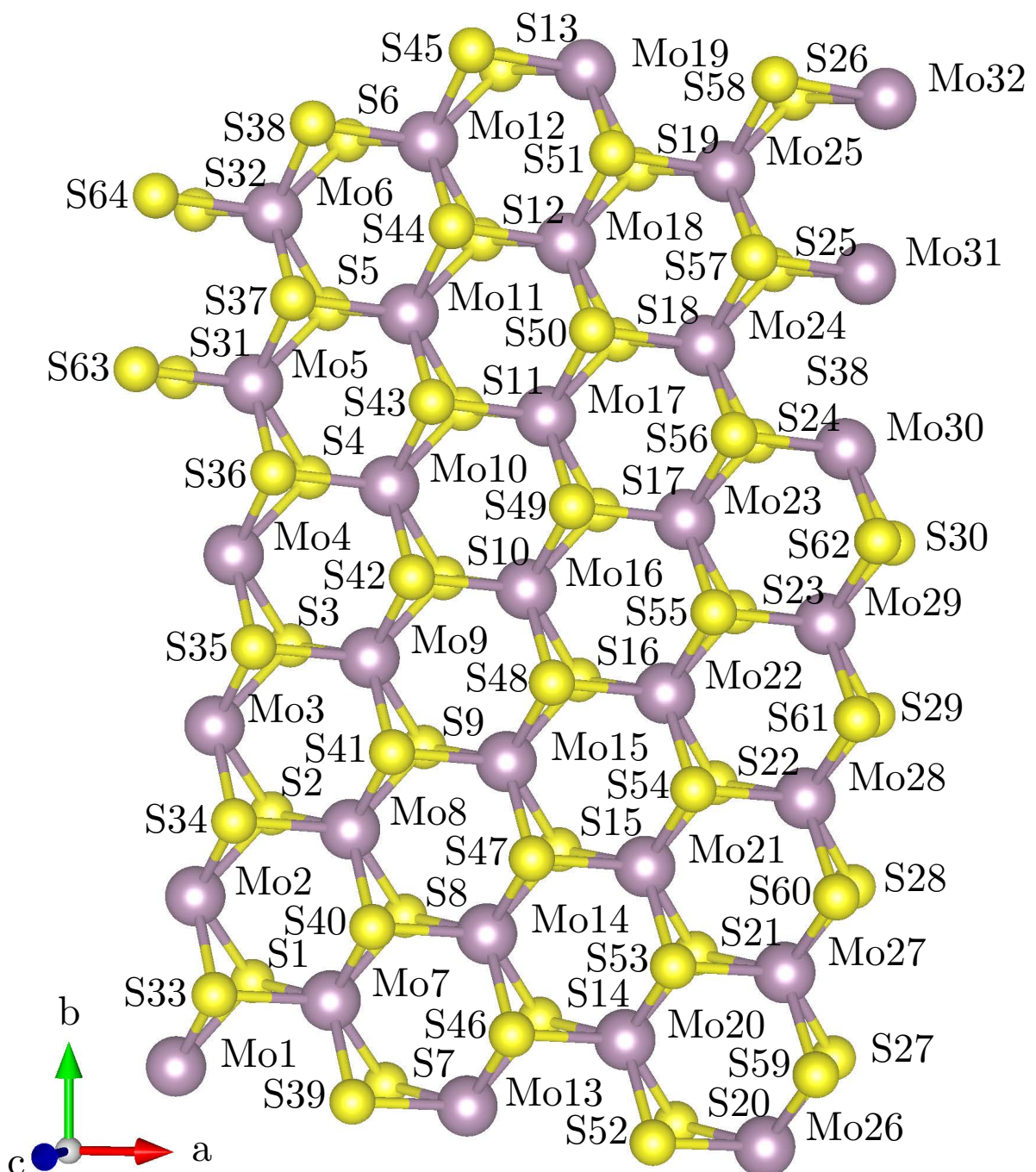


Figure F.11: Position of the atom labels used for tabulating the Hirshfeld charge and magnetic moment of chiral  $\text{MoS}_2$  nanoribbons ( $\text{Mo}_{32}\text{S}_{64}$ ).

Table F.12: Hirshfeld atomic charge and atomic magnetization of chiral MoS<sub>2</sub> nanoribbon (Table 1 of 3: molybdenum atoms).

Atom	$Z_{ion}$	Hirshfeld Charge	Net Charge	Magnetic Moment
$Mo_1$	14.0000	0.2862	14.2862	-0.1315
$Mo_2$	14.0000	0.0056	14.0056	-0.0045
$Mo_3$	14.0000	0.0024	14.0024	-0.0020
$Mo_4$	14.0000	0.0001	14.0001	-0.0001
$Mo_5$	14.0000	-0.0012	13.9988	0.0011
$Mo_6$	14.0000	-0.0557	13.9443	0.0368
$Mo_7$	14.0000	-0.0267	13.9733	0.0232
$Mo_8$	14.0000	0.0011	14.0011	-0.0011
$Mo_9$	14.0000	-0.0000	14.0000	0.0000
$Mo_{10}$	14.0000	-0.0004	13.9996	0.0002
$Mo_{11}$	14.0000	-0.0018	13.9982	0.0012
$Mo_{12}$	14.0000	-0.0544	13.9456	0.0426
$Mo_{13}$	14.0000	-0.1037	13.8963	0.0694
$Mo_{14}$	14.0000	0.0186	14.0186	-0.0159
$Mo_{15}$	14.0000	-0.0011	13.9989	0.0010
$Mo_{16}$	14.0000	0.0001	14.0001	-0.0001
$Mo_{17}$	14.0000	-0.0001	13.9999	0.0001
$Mo_{18}$	14.0000	0.0078	14.0078	-0.0056
$Mo_{19}$	14.0000	-0.1338	13.8662	0.0832
$Mo_{20}$	14.0000	-0.0174	13.9826	0.0105
$Mo_{21}$	14.0000	-0.0056	13.9944	0.0045
$Mo_{22}$	14.0000	0.0002	14.0002	-0.0002
$Mo_{23}$	14.0000	0.0004	14.0004	-0.0003
$Mo_{24}$	14.0000	0.0002	14.0002	-0.0004
$Mo_{25}$	14.0000	-0.0101	13.9899	0.0087
$Mo_{26}$	14.0000	0.5736	14.5736	-0.3344
$Mo_{27}$	14.0000	0.0357	14.0357	-0.0293
$Mo_{28}$	14.0000	-0.0037	13.9963	0.0031
$Mo_{29}$	14.0000	-0.0005	13.9995	0.0004
$Mo_{30}$	14.0000	-0.0014	13.9986	0.0010
$Mo_{31}$	14.0000	0.0100	14.0100	-0.0061
$Mo_{32}$	14.0000	-0.3095	13.6905	0.2029

Table F.13: Hirshfeld atomic charge and atomic magnetization of chiral MoS<sub>2</sub> nanoribbon (Table 2 of 3: lower sulphur atoms).

Atom	$Z_{ion}$	Hirshfeld Charge	Net Charge	Magnetic Moment
$S_1$	6.0000	-0.0000	6.0000	0.0009
$S_2$	6.0000	-0.0002	5.9998	0.0002
$S_3$	6.0000	0.0000	6.0000	0.0000
$S_4$	6.0000	-0.0000	6.0000	-0.0000
$S_5$	6.0000	-0.0016	5.9984	0.0007
$S_6$	6.0000	0.0090	6.0090	-0.0101
$S_7$	6.0000	-0.0070	5.9930	0.0033
$S_8$	6.0000	-0.0015	5.9985	0.0009
$S_9$	6.0000	0.0001	6.0001	-0.0000
$S_{10}$	6.0000	-0.0000	6.0000	0.0000
$S_{11}$	6.0000	0.0001	6.0001	-0.0001
$S_{12}$	6.0000	-0.0017	5.9983	0.0007
$S_{13}$	6.0000	0.0104	6.0104	-0.0104
$S_{14}$	6.0000	-0.0041	5.9959	0.0019
$S_{15}$	6.0000	0.0005	6.0005	-0.0001
$S_{16}$	6.0000	-0.0001	5.9999	0.0000
$S_{17}$	6.0000	0.0001	6.0001	-0.0000
$S_{18}$	6.0000	0.0010	6.0010	-0.0006
$S_{19}$	6.0000	0.0022	6.0022	-0.0027
$S_{20}$	6.0000	-0.0322	5.9678	0.0286
$S_{21}$	6.0000	-0.0014	5.9986	0.0015
$S_{22}$	6.0000	-0.0009	5.9991	0.0006
$S_{23}$	6.0000	-0.0000	6.0000	0.0000
$S_{24}$	6.0000	-0.0000	6.0000	-0.0000
$S_{25}$	6.0000	-0.0005	5.9995	0.0006
$S_{26}$	6.0000	0.0078	6.0078	-0.0105
$S_{27}$	6.0000	0.0029	6.0029	0.0113
$S_{28}$	6.0000	-0.0006	5.9994	0.0016
$S_{29}$	6.0000	0.0003	6.0003	-0.0003
$S_{30}$	6.0000	0.0000	6.0000	-0.0000
$S_{31}$	6.0000	0.0007	6.0007	-0.0002
$S_{32}$	6.0000	-0.0010	5.9990	-0.0035

Table F.14: Hirshfeld atomic charge and atomic magnetization of chiral MoS<sub>2</sub> nanoribbon (Table 3 of 3: upper sulphur atoms).

Atom	$Z_{ion}$	Hirshfeld Charge	Net Charge	Magnetic Moment
$S_{33}$	6.0000	-0.0000	6.0000	0.0008
$S_{34}$	6.0000	-0.0002	5.9998	0.0003
$S_{35}$	6.0000	0.0000	6.0000	0.0000
$S_{36}$	6.0000	-0.0000	6.0000	-0.0000
$S_{37}$	6.0000	-0.0016	5.9984	0.0007
$S_{38}$	6.0000	0.0090	6.0090	-0.0100
$S_{39}$	6.0000	-0.0070	5.9930	0.0031
$S_{40}$	6.0000	-0.0015	5.9985	0.0009
$S_{41}$	6.0000	0.0001	6.0001	-0.0000
$S_{42}$	6.0000	-0.0000	6.0000	0.0000
$S_{43}$	6.0000	0.0001	6.0001	-0.0001
$S_{44}$	6.0000	-0.0017	5.9983	0.0006
$S_{45}$	6.0000	0.0104	6.0104	-0.0104
$S_{46}$	6.0000	-0.0041	5.9959	0.0020
$S_{47}$	6.0000	0.0005	6.0005	-0.0001
$S_{48}$	6.0000	-0.0001	5.9999	0.0000
$S_{49}$	6.0000	0.0001	6.0001	-0.0000
$S_{50}$	6.0000	0.0010	6.0010	-0.0005
$S_{51}$	6.0000	0.0022	6.0022	-0.0025
$S_{52}$	6.0000	-0.0322	5.9678	0.0281
$S_{53}$	6.0000	-0.0014	5.9986	0.0014
$S_{54}$	6.0000	-0.0009	5.9991	0.0006
$S_{55}$	6.0000	-0.0000	6.0000	0.0000
$S_{56}$	6.0000	-0.0000	6.0000	-0.0001
$S_{57}$	6.0000	-0.0005	5.9995	0.0006
$S_{58}$	6.0000	0.0078	6.0078	-0.0107
$S_{59}$	6.0000	0.0029	6.0029	0.0115
$S_{60}$	6.0000	-0.0006	5.9994	0.0016
$S_{61}$	6.0000	0.0003	6.0003	-0.0003
$S_{62}$	6.0000	0.0000	6.0000	-0.0000
$S_{63}$	6.0000	0.0007	6.0007	-0.0001
$S_{64}$	6.0000	-0.0010	5.9990	-0.0033

### F.3 Projected Band Structure and Density of States

In this section the projections of calculated MLWFs on the energy band structure and energy band gap along with the corresponding projected density of states (PDOS) are illustrated.

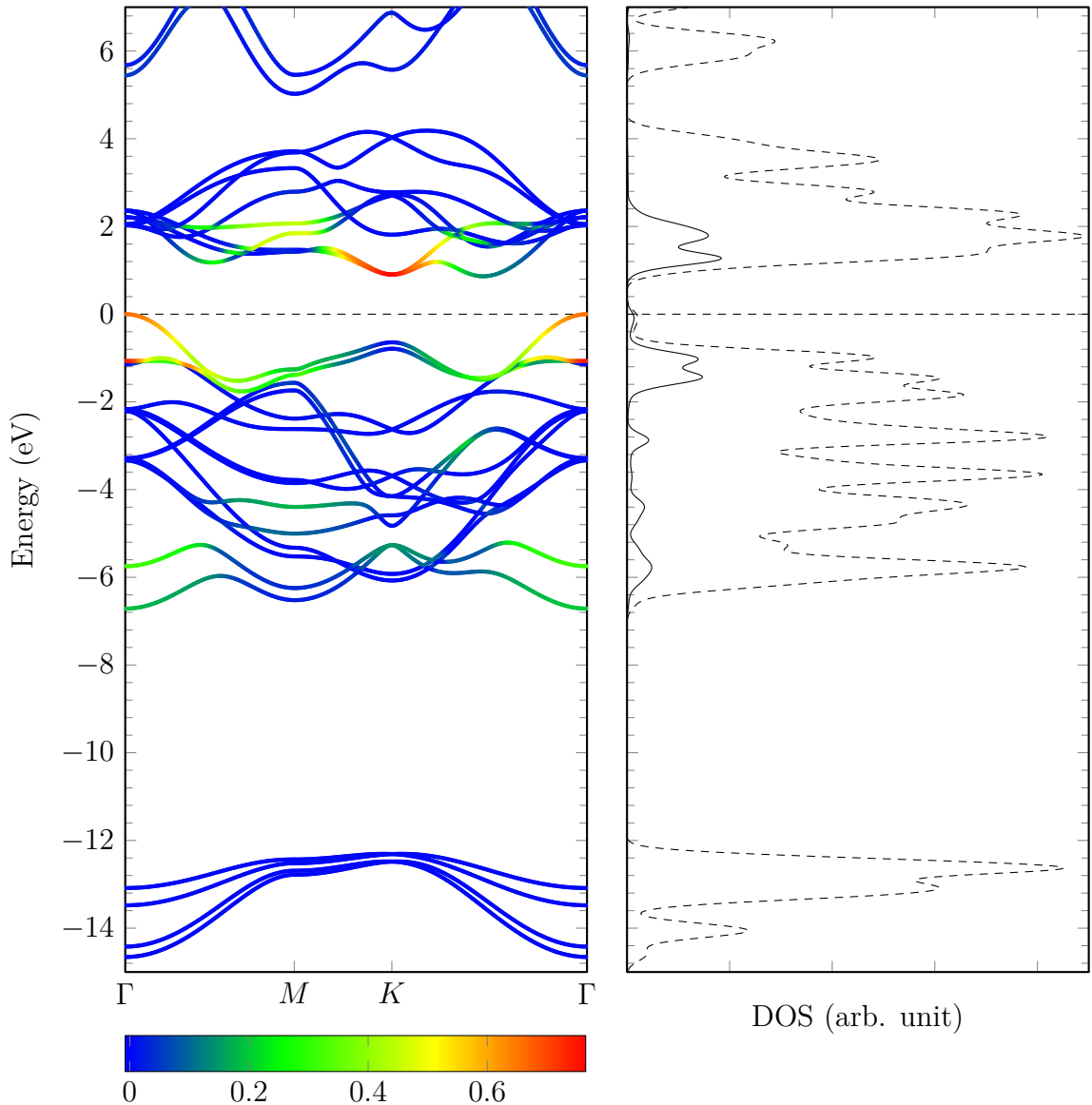


Figure F.12: Projected band structure and density of states (PDOS) calculated using MLWF for bulk MoS<sub>2</sub> ( $2H$ -MoS<sub>2</sub>) showing molybdenum  $4d_{z^2}$  orbital contribution to the energy bands and total DOS.

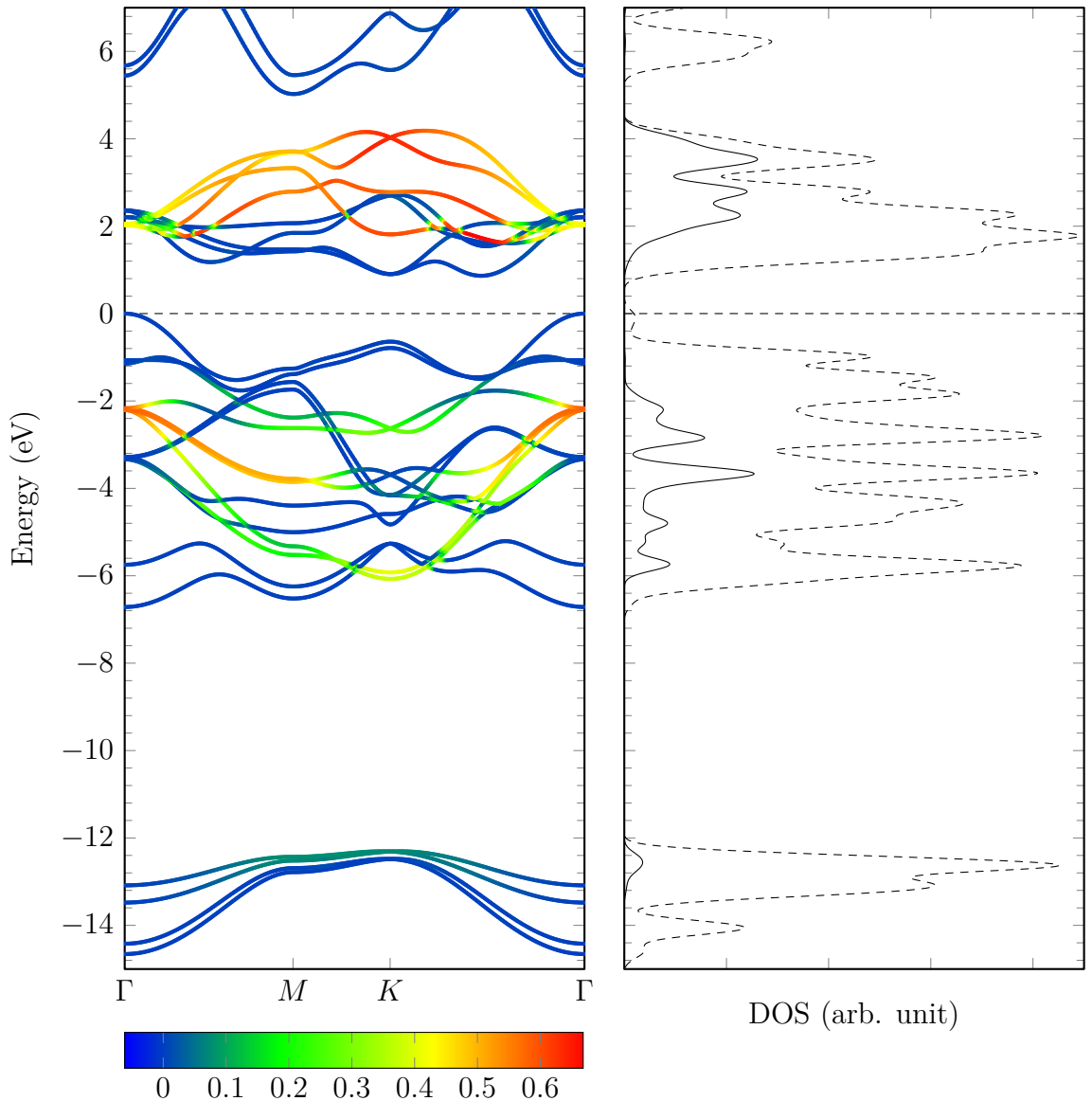


Figure F.13: Projected band structure and density of states (PDOS) calculated using MLWF for bulk MoS<sub>2</sub> ( $2H$ -MoS<sub>2</sub>) showing molybdenum  $4d_{xz}$  and  $4d_{yz}$  orbital contribution to the energy bands and total DOS.

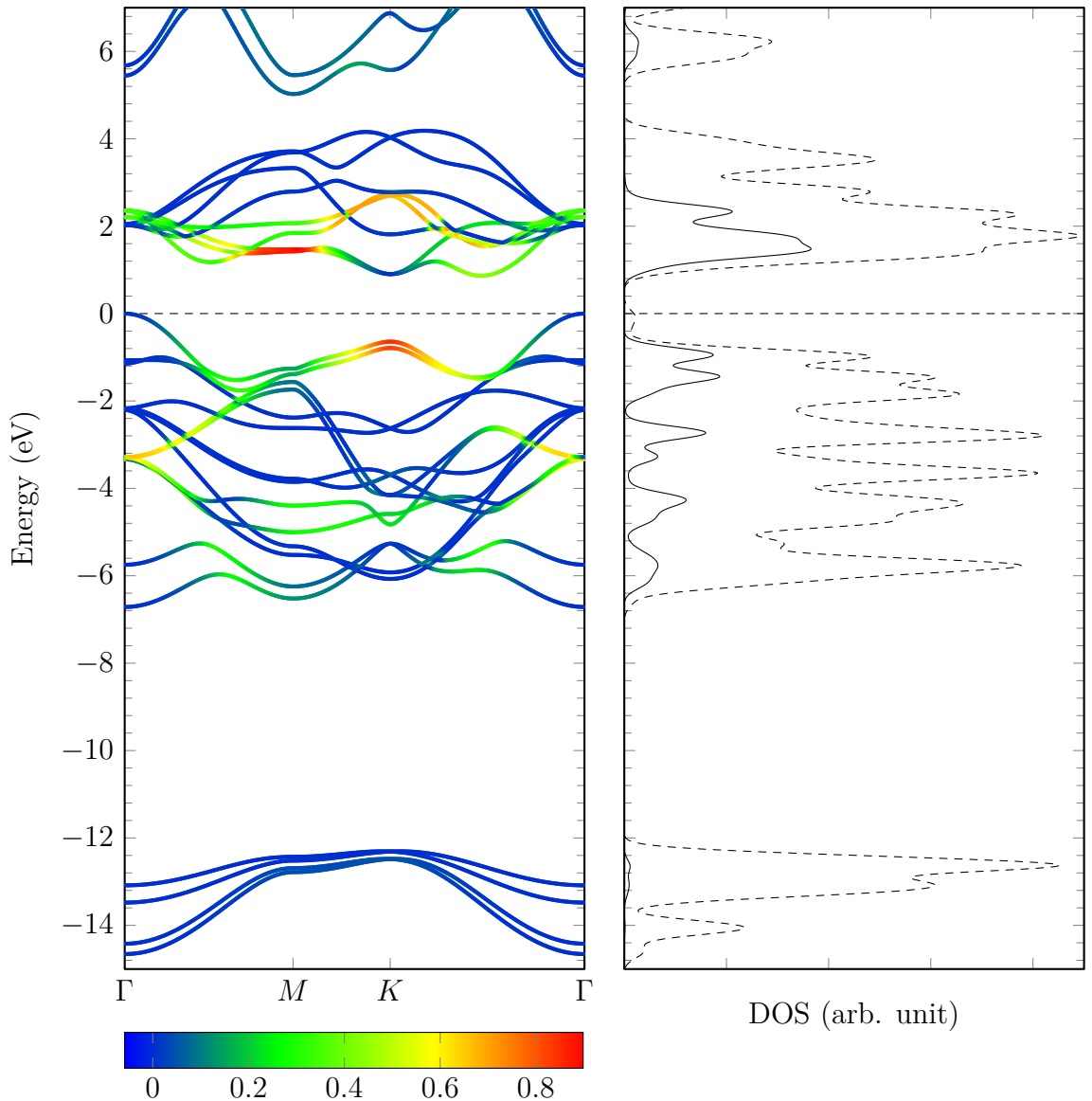


Figure F.14: Projected band structure and density of states (PDOS) calculated using MLWF for bulk MoS<sub>2</sub> (2H-MoS<sub>2</sub>) showing molybdenum 4d<sub>xy</sub> and 4d<sub>x<sup>2</sup>-y<sup>2</sup></sub> orbital contribution to the energy bands and total DOS.

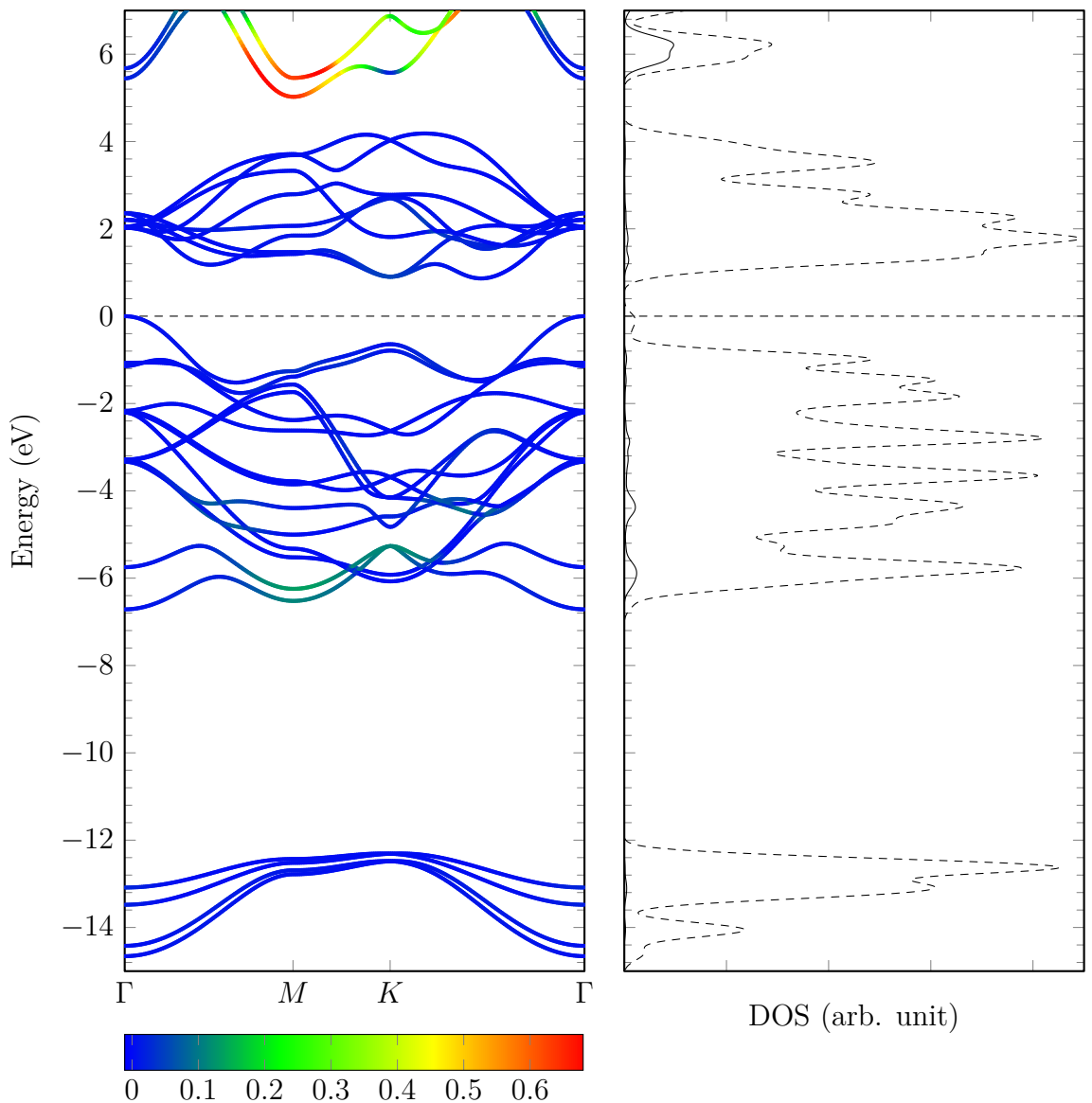


Figure F.15: Projected band structure and density of states (PDOS) calculated using MLWF for bulk MoS<sub>2</sub> ( $2H$ -MoS<sub>2</sub>) showing molybdenum 5s orbital contribution to the energy bands and total DOS.

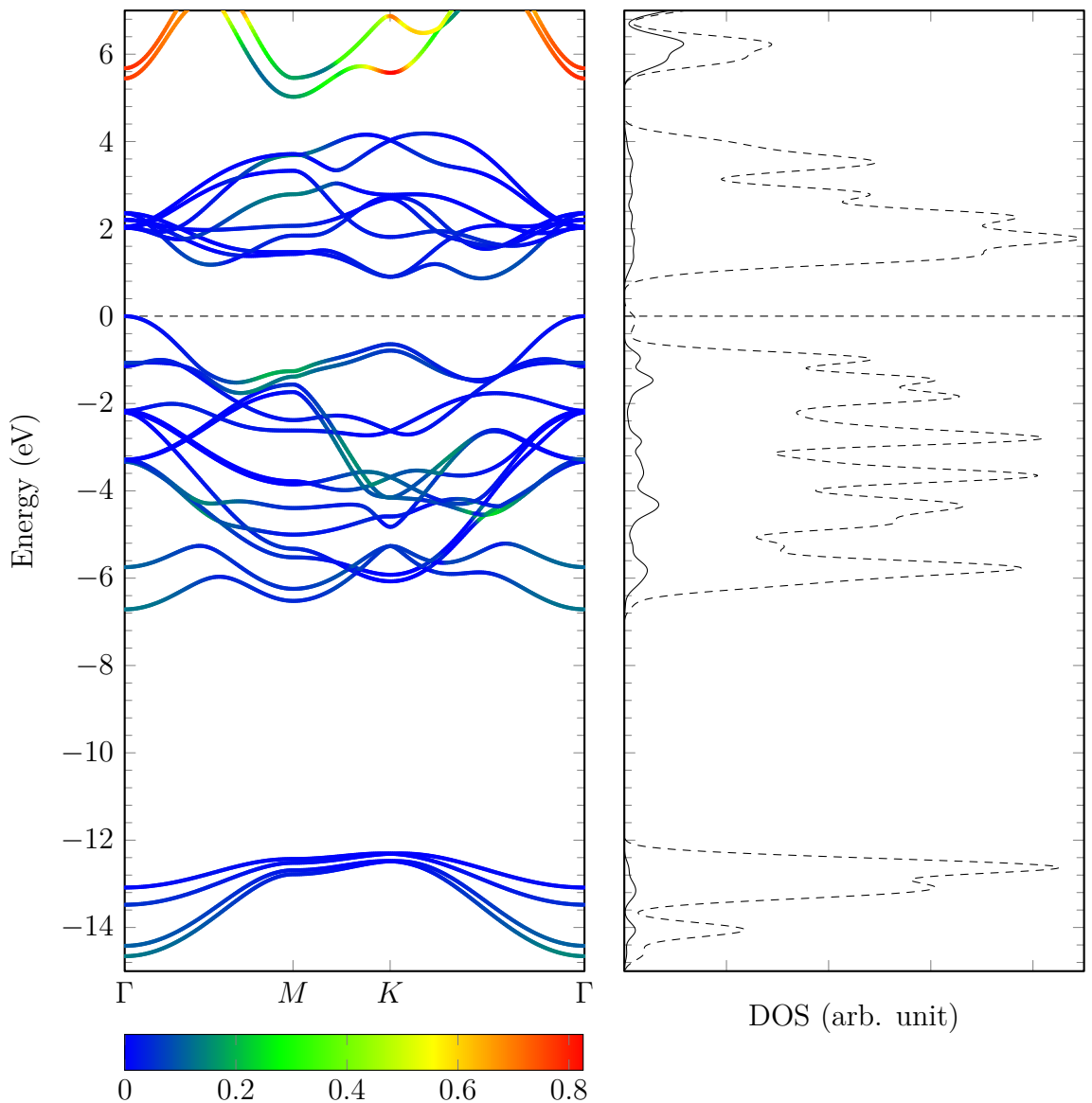


Figure F.16: Projected band structure and density of states (PDOS) calculated using MLWF for bulk MoS<sub>2</sub> ( $2H$ -MoS<sub>2</sub>) showing molybdenum 4p orbital contribution to the energy bands and total DOS.

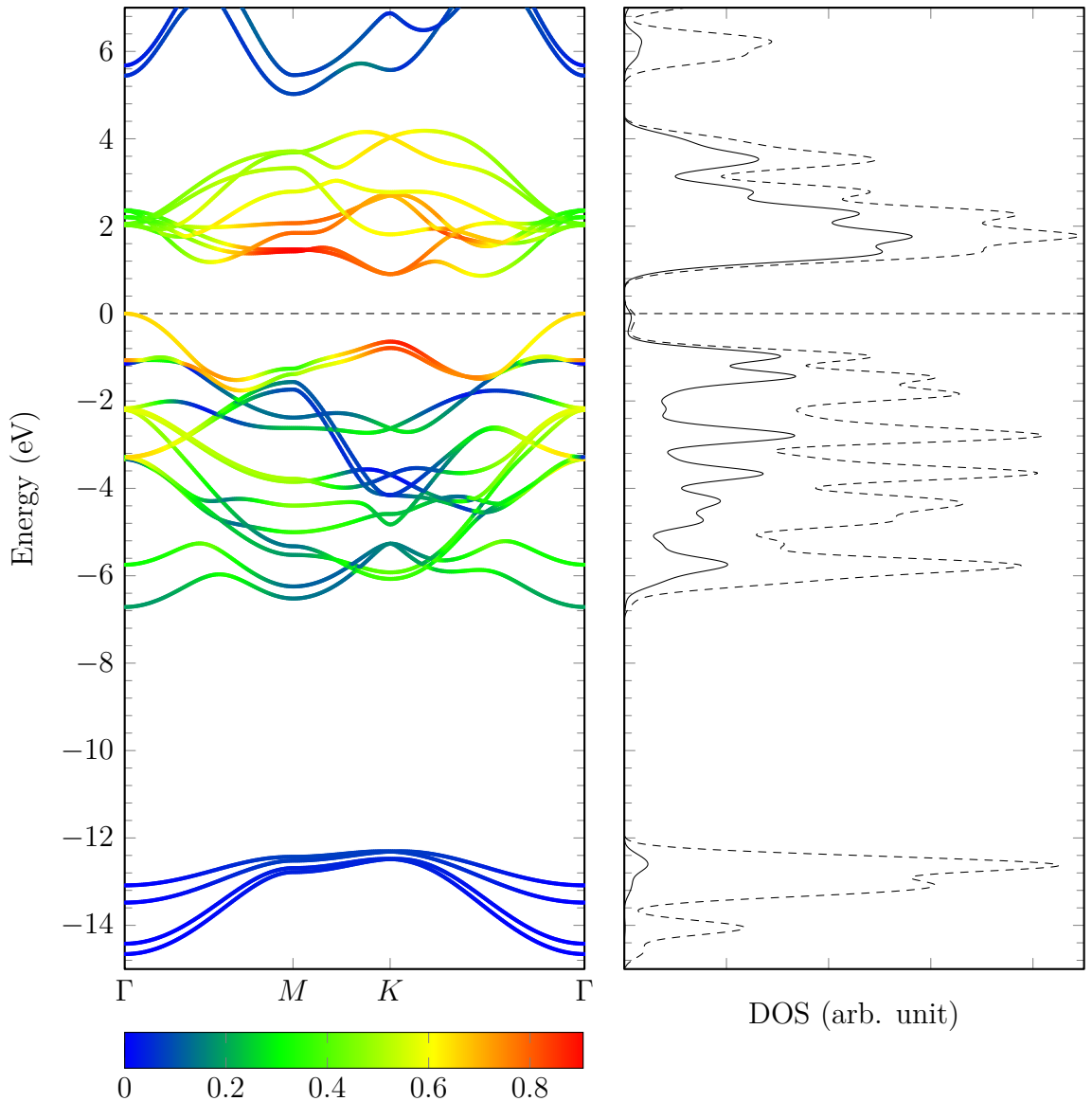


Figure F.17: Projected band structure and density of states (PDOS) calculated using MLWF for bulk MoS<sub>2</sub> ( $2H$ -MoS<sub>2</sub>) showing molybdenum 4d orbital contribution to the energy bands and total DOS.

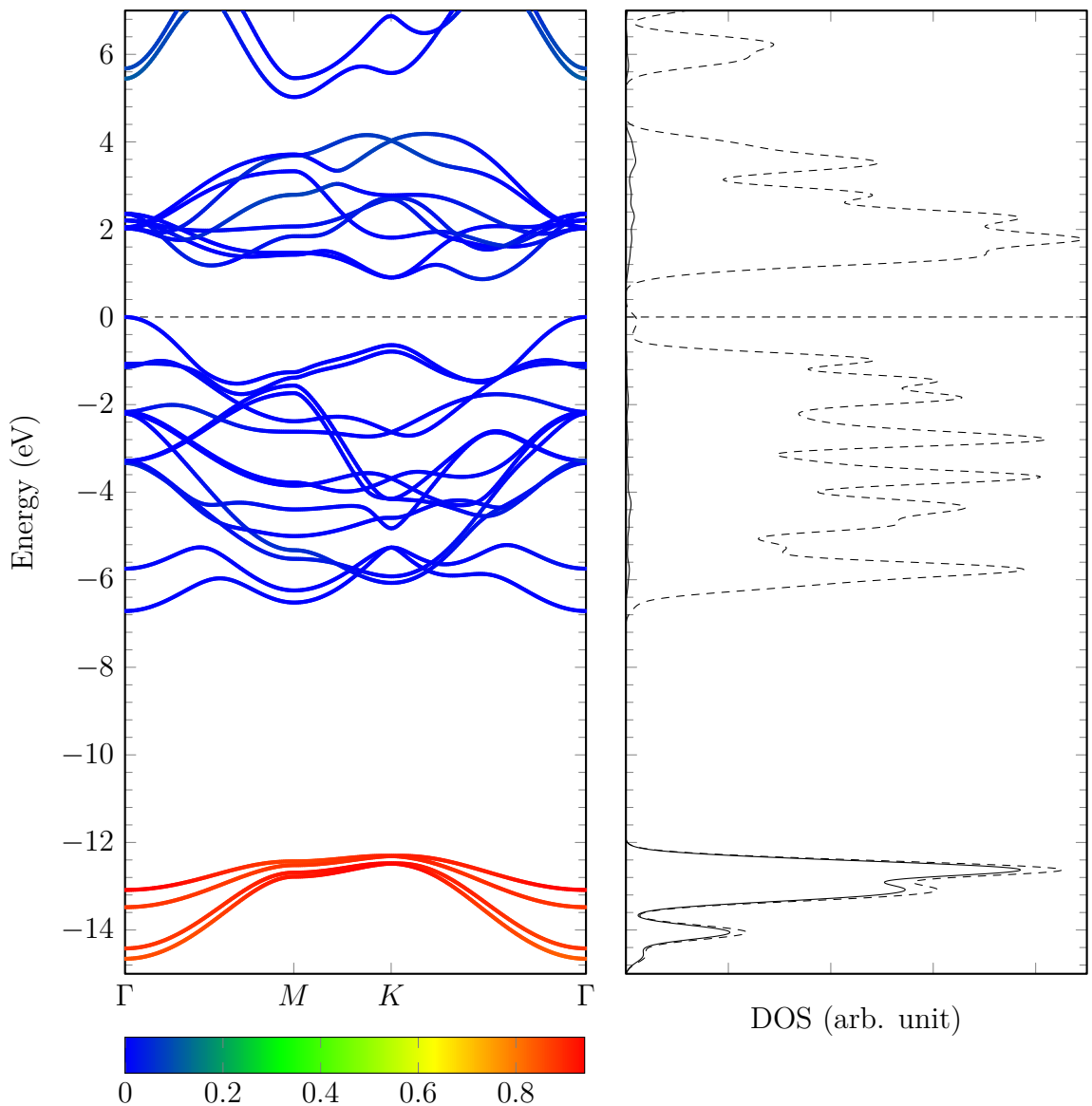


Figure F.18: Projected band structure and density of states (PDOS) calculated using MLWF for bulk MoS<sub>2</sub> (2H-MoS<sub>2</sub>) showing sulphur 3s orbital contribution to the energy bands and total DOS.

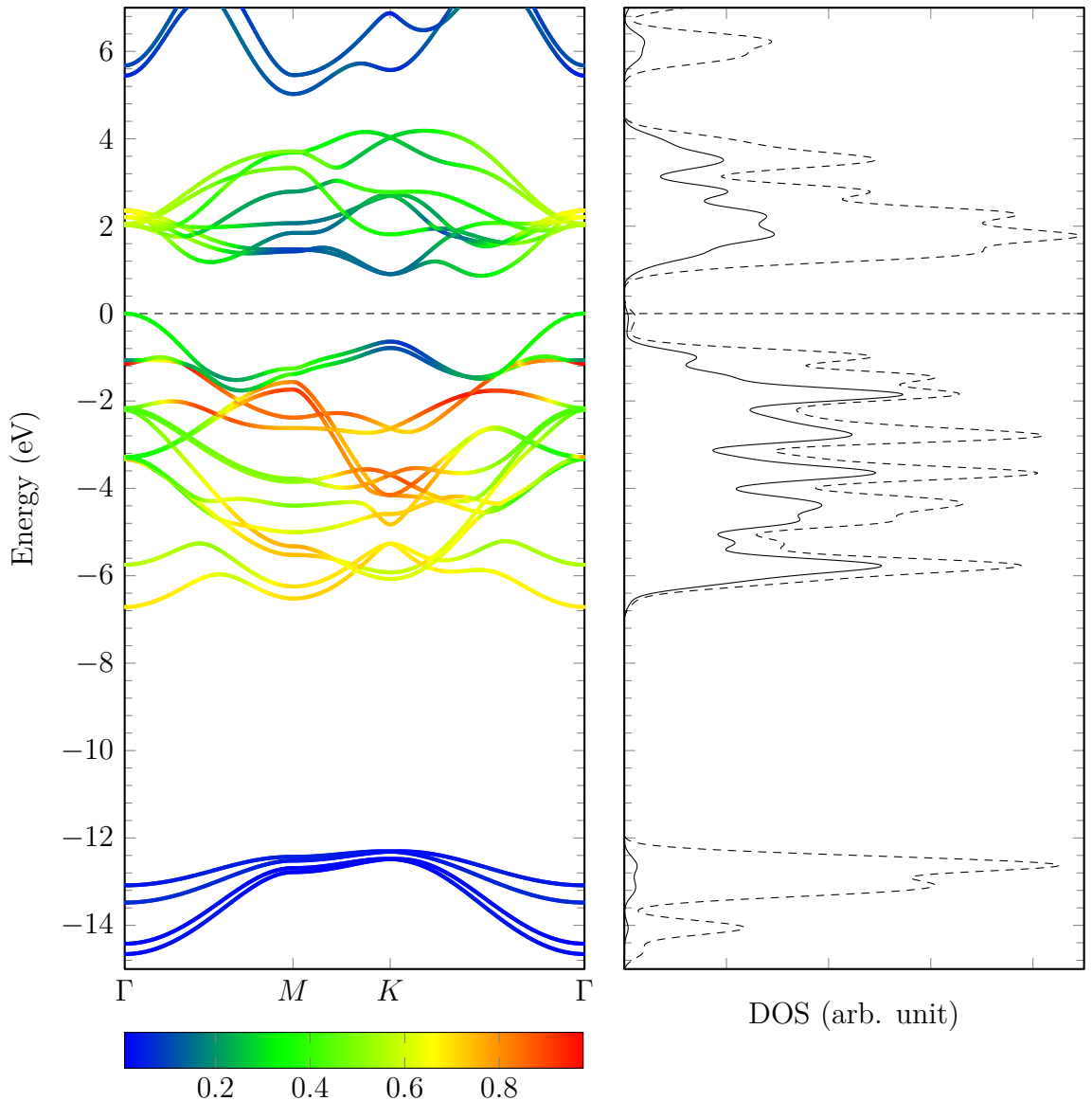


Figure F.19: Projected band structure and density of states (PDOS) calculated using MLWF for bulk  $\text{MoS}_2$  ( $2H\text{-MoS}_2$ ) showing sulphur  $3p$  orbital contribution to the energy bands and total DOS.

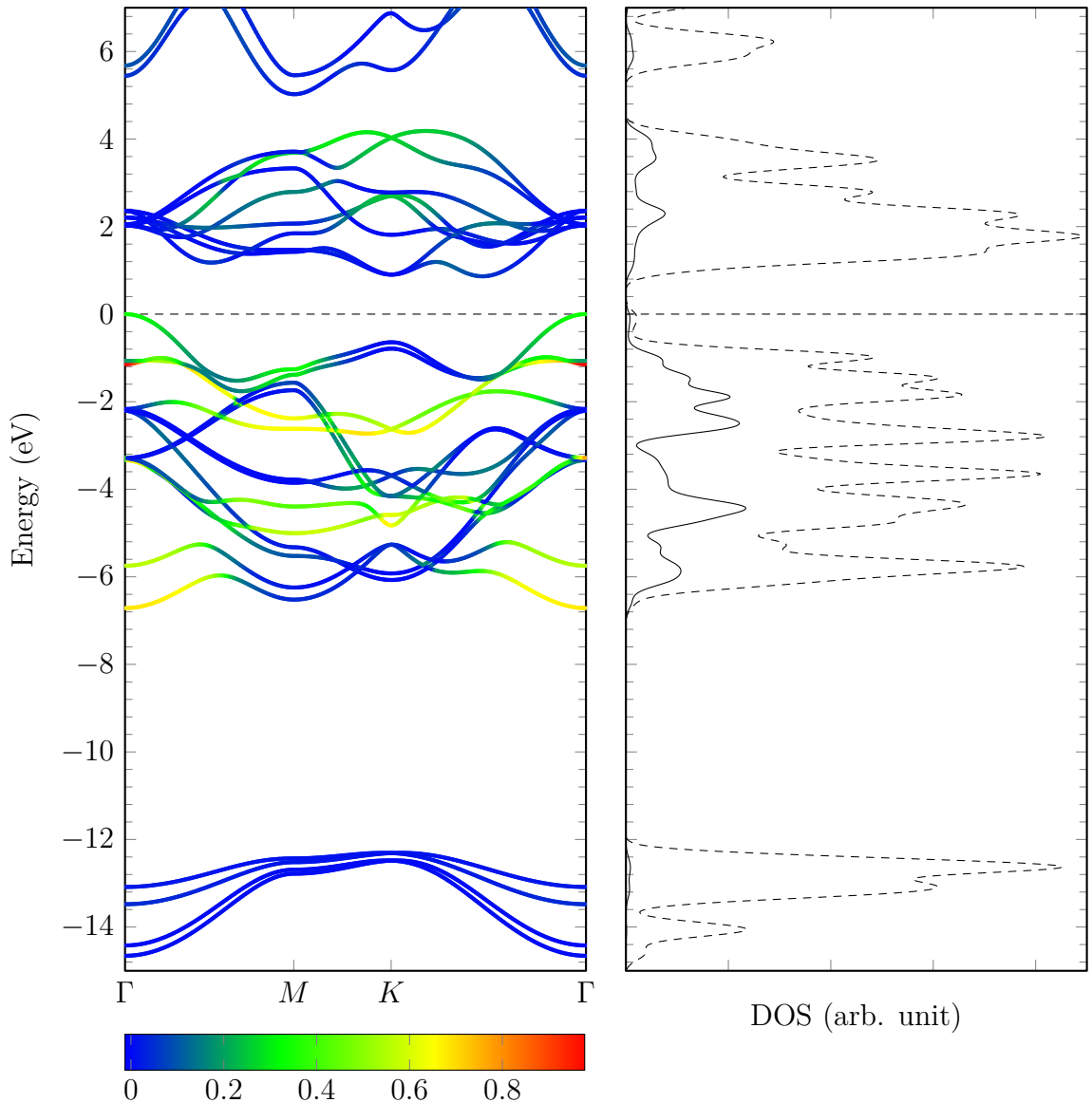


Figure F.20: Projected band structure and density of states (PDOS) calculated using MLWF for bulk MoS<sub>2</sub> (2H-MoS<sub>2</sub>) showing sulphur 3p<sub>z</sub> orbital contribution to the energy bands and total DOS.

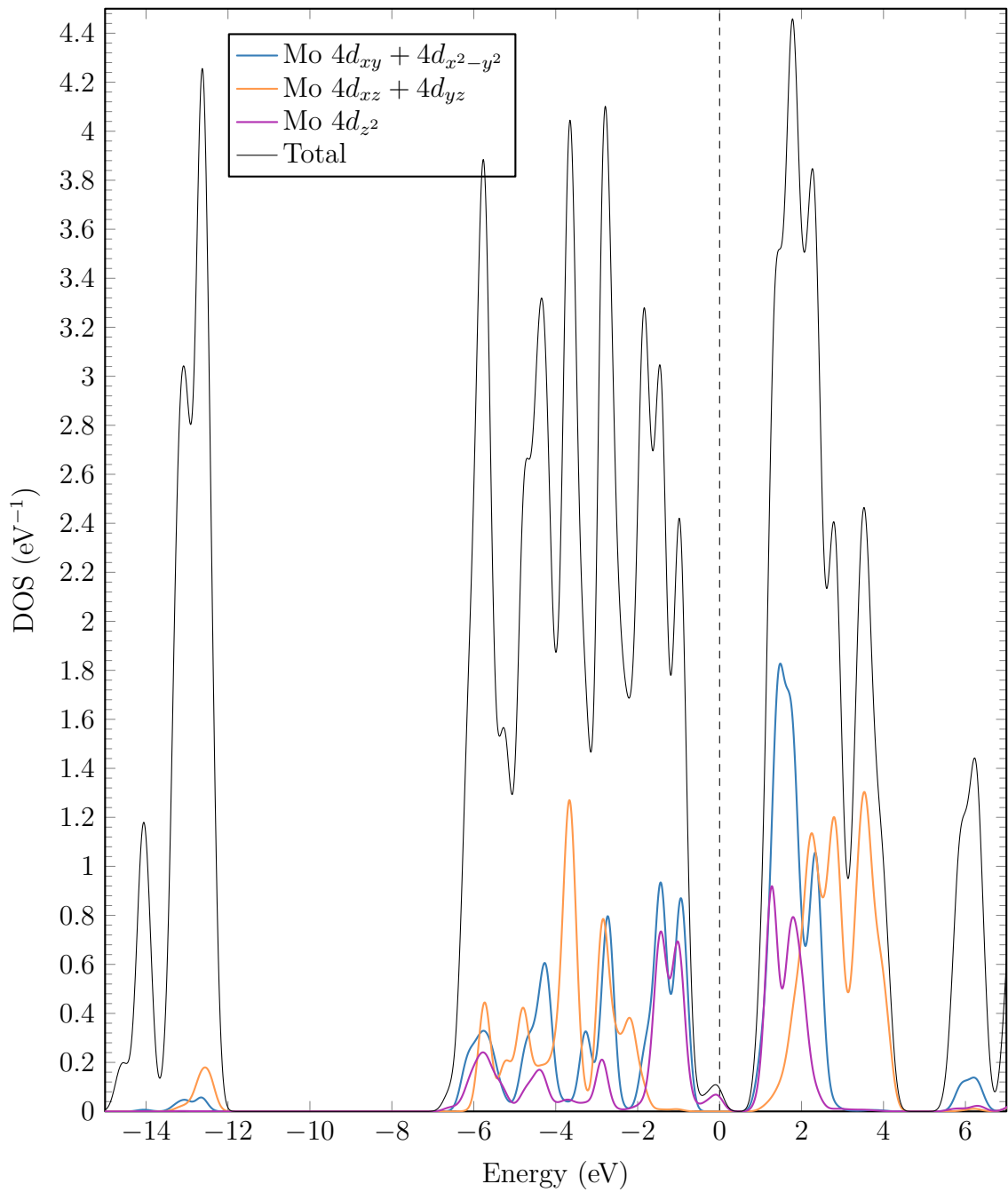


Figure F.21: Projected density of states (PDOS) calculated using MLWF for bulk MoS<sub>2</sub> ( $2H$ -MoS<sub>2</sub>) showing molybdenum individual  $4d$  orbital contribution to the total DOS.

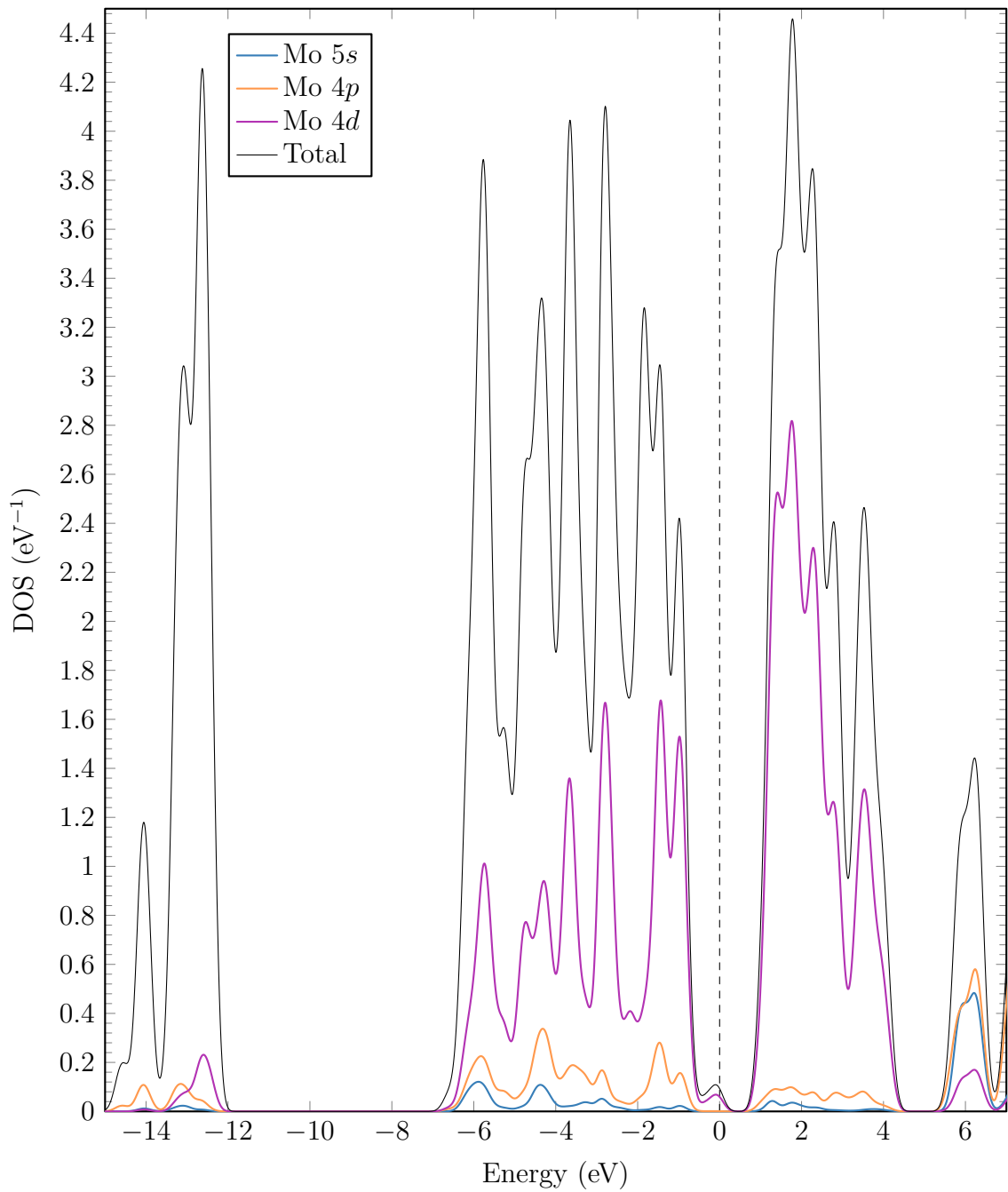


Figure F.22: Projected density of states (PDOS) calculated using MLWF for bulk MoS<sub>2</sub> ( $2H\text{-MoS}_2$ ) showing molybdenum 5s, 4p and 4d orbital contribution to the total DOS.

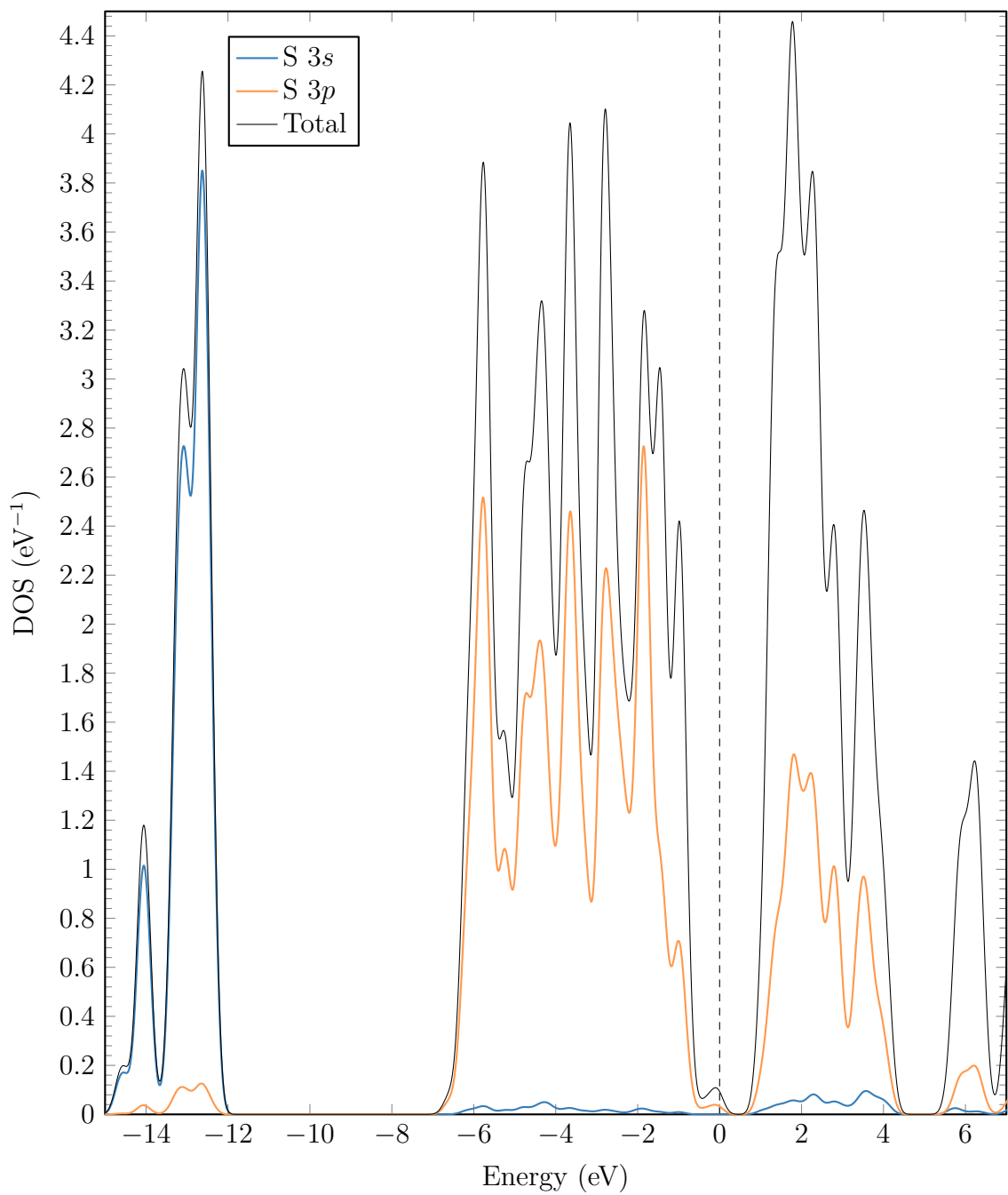


Figure F.23: Projected density of states (PDOS) calculated using MLWF for bulk  $\text{MoS}_2$  ( $2H\text{-MoS}_2$ ) showing sulphur  $3s$  and  $3p$  orbital contribution to the total DOS.

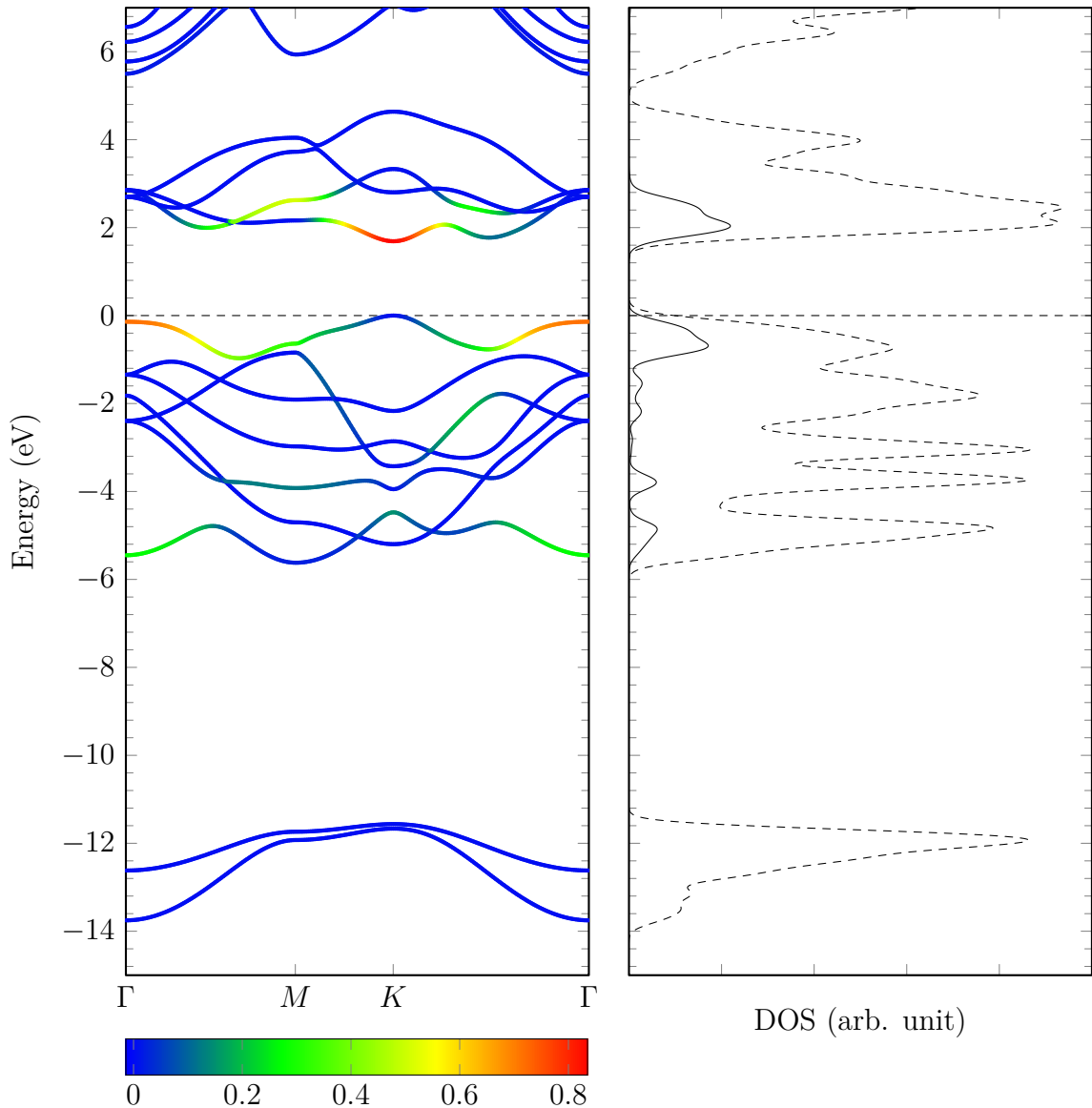


Figure F.24: Projected band structure and density of states (PDOS) calculated using MLWF for single-layer MoS<sub>2</sub> (1H-MoS<sub>2</sub>) showing molybdenum 4d<sub>z2</sub> orbital contribution to the energy bands and total DOS.

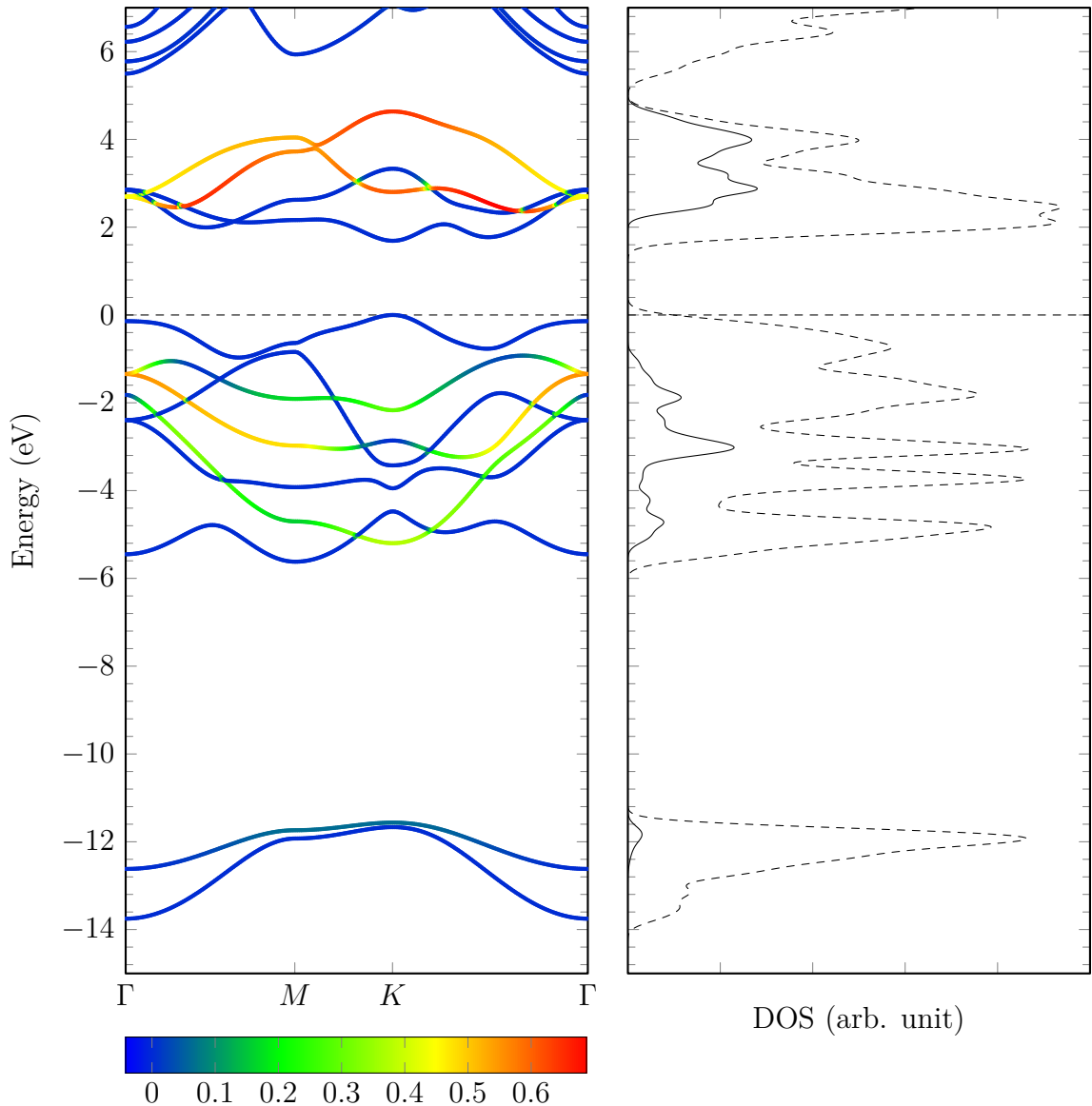


Figure F.25: Projected band structure and density of states (PDOS) calculated using MLWF for single-layer MoS<sub>2</sub> (1H-MoS<sub>2</sub>) showing molybdenum 4d<sub>xz</sub> and 4d<sub>yz</sub> orbital contribution to the energy bands and total DOS.

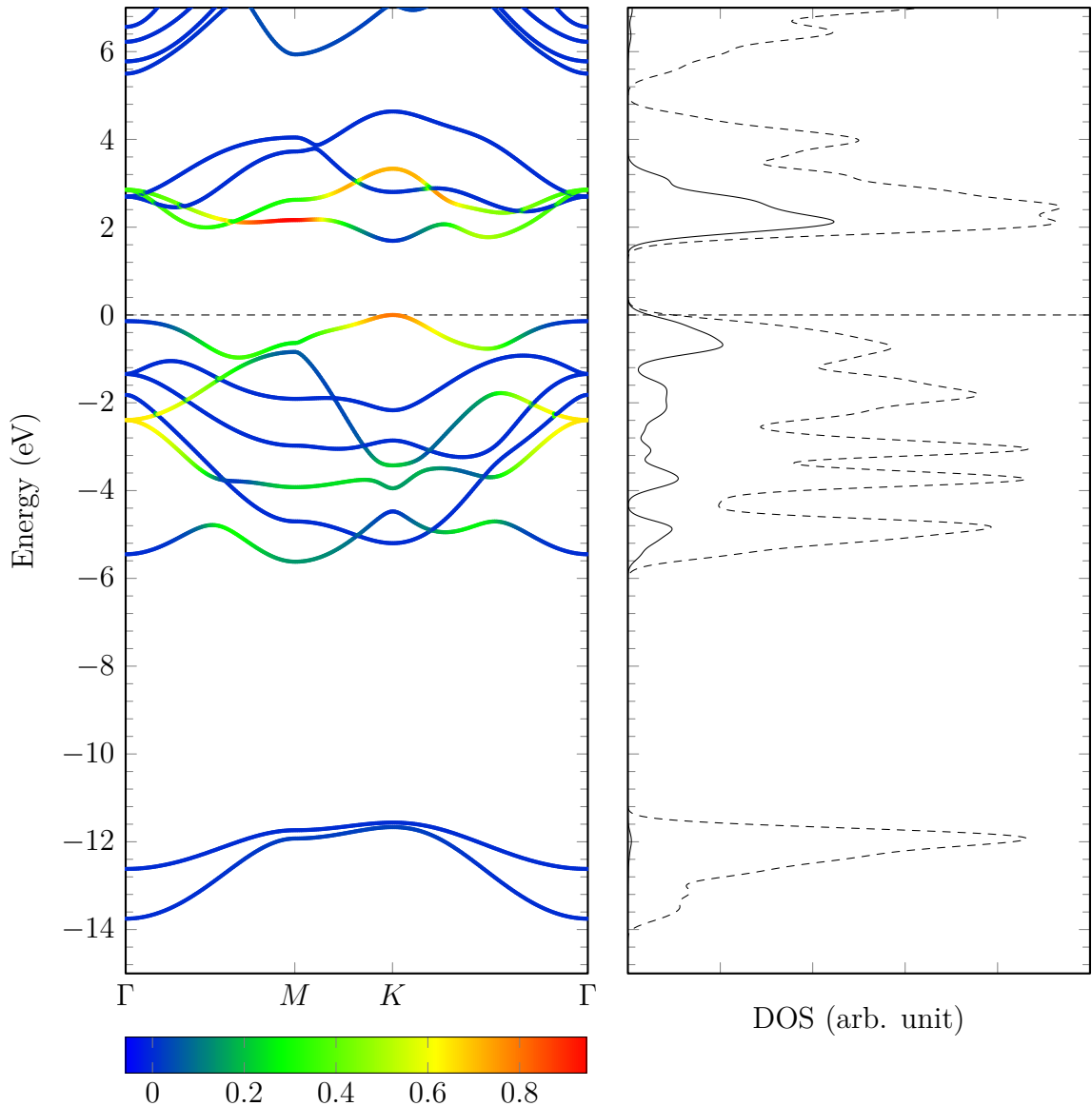


Figure F.26: Projected band structure and density of states (PDOS) calculated using MLWF for single-layer MoS<sub>2</sub> (1H-MoS<sub>2</sub>) showing molybdenum 4*d*<sub>xy</sub> and 4*d*<sub>x<sup>2</sup>-y<sup>2</sup></sub> orbital contribution to the energy bands and total DOS.

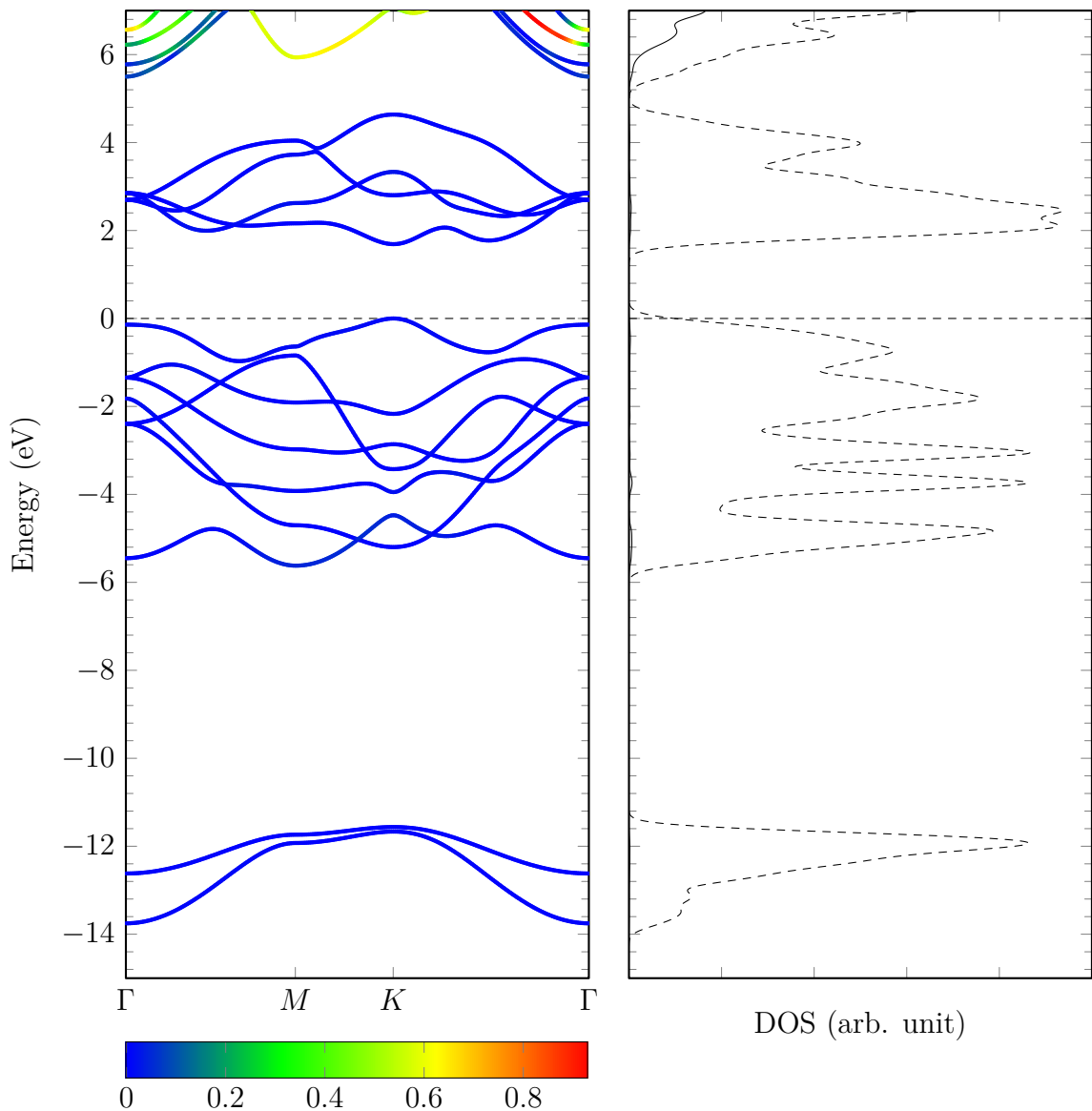


Figure F.27: Projected band structure and density of states (PDOS) calculated using MLWF for single-layer MoS<sub>2</sub> (1H-MoS<sub>2</sub>) showing molybdenum 5s orbital contribution to the energy bands and total DOS.

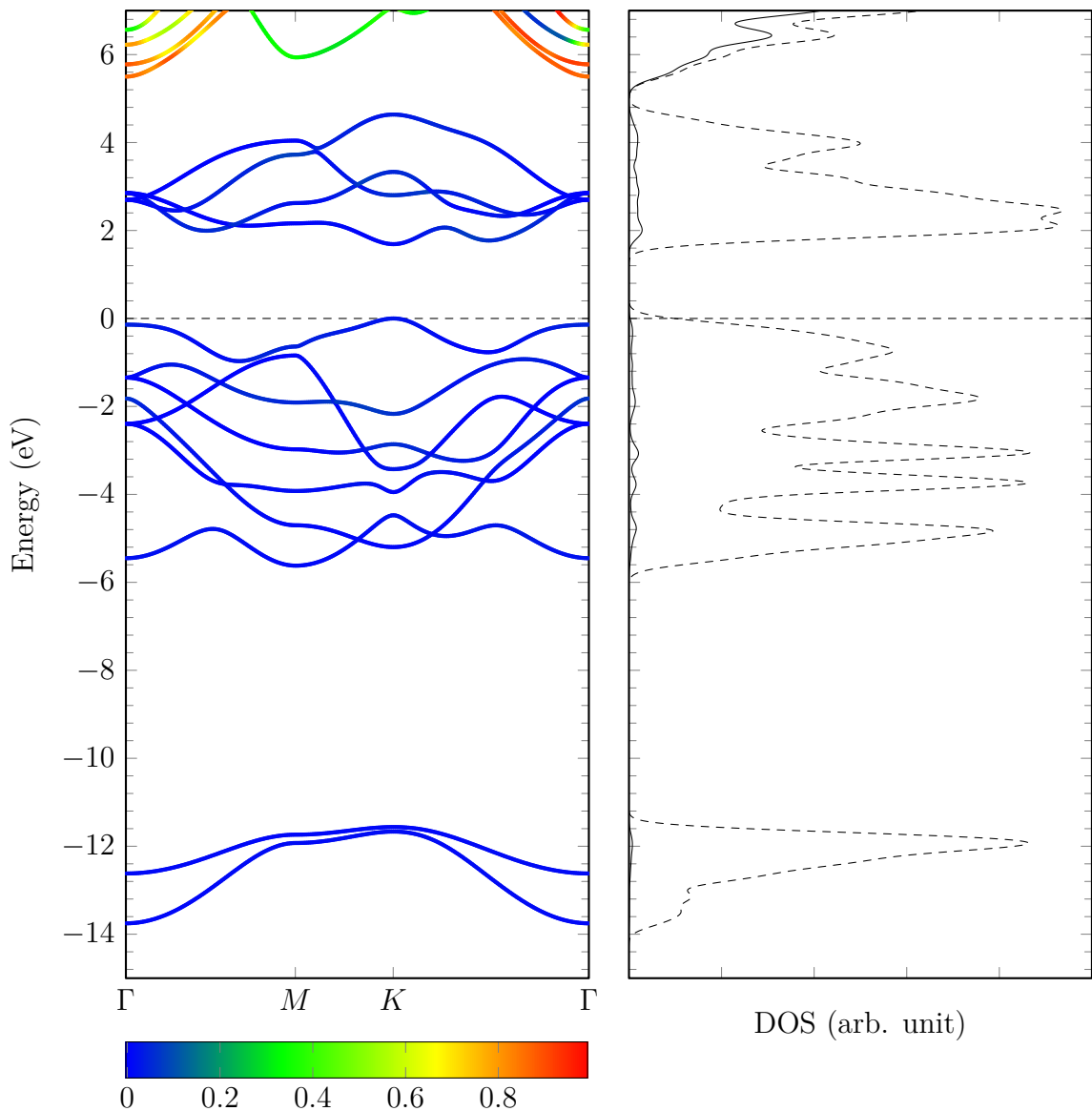


Figure F.28: Projected band structure and density of states (PDOS) calculated using MLWF for single-layer MoS<sub>2</sub> (1H-MoS<sub>2</sub>) showing molybdenum 4p orbital contribution to the energy bands and total DOS.

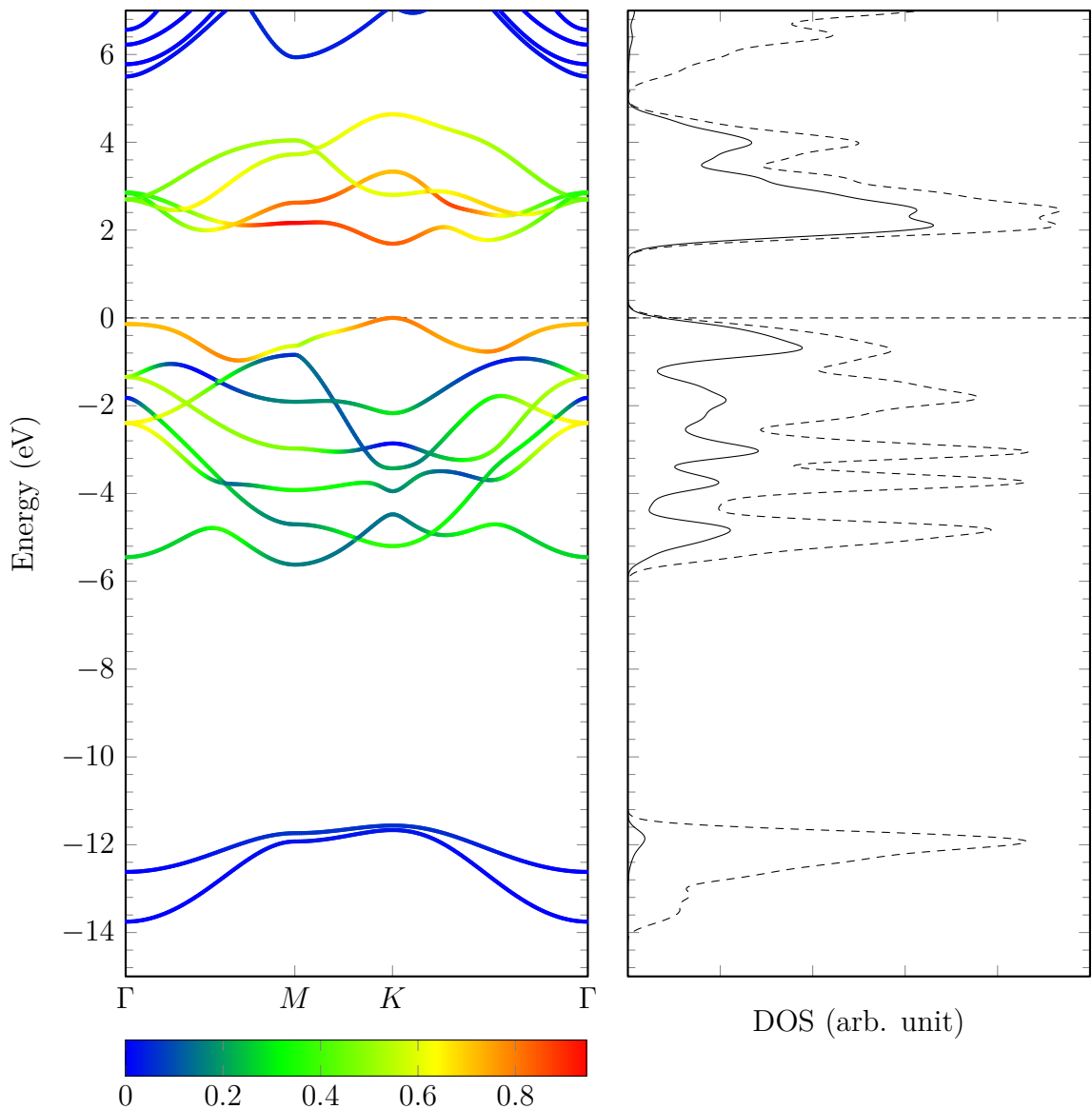


Figure F.29: Projected band structure and density of states (PDOS) calculated using MLWF for single-layer MoS<sub>2</sub> (1H-MoS<sub>2</sub>) showing molybdenum 4d orbital contribution to the energy bands and total DOS.

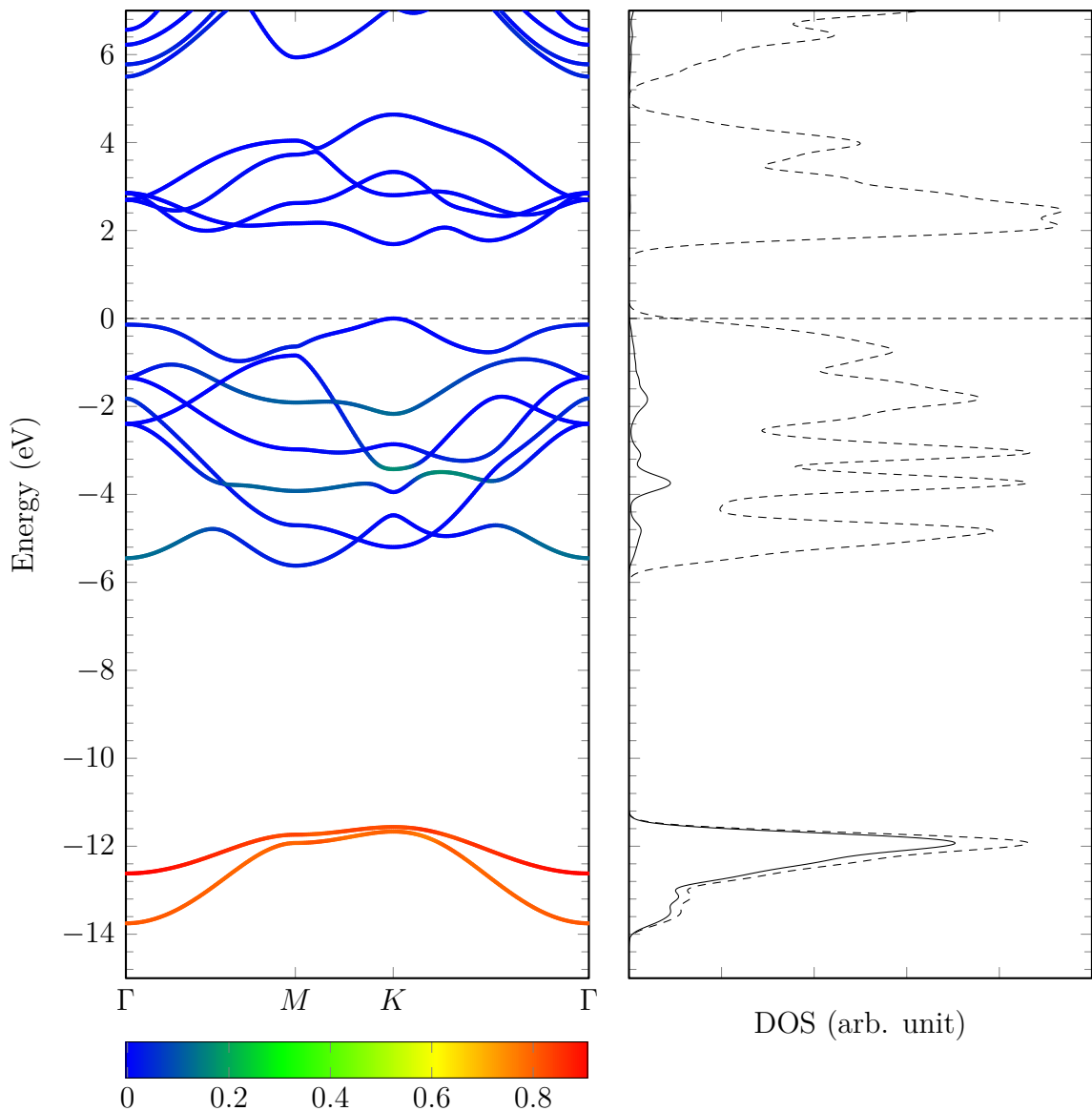


Figure F.30: Projected band structure and density of states (PDOS) calculated using MLWF for single-layer MoS<sub>2</sub> (1H-MoS<sub>2</sub>) showing sulphur 3s orbital contribution to the energy bands and total DOS.

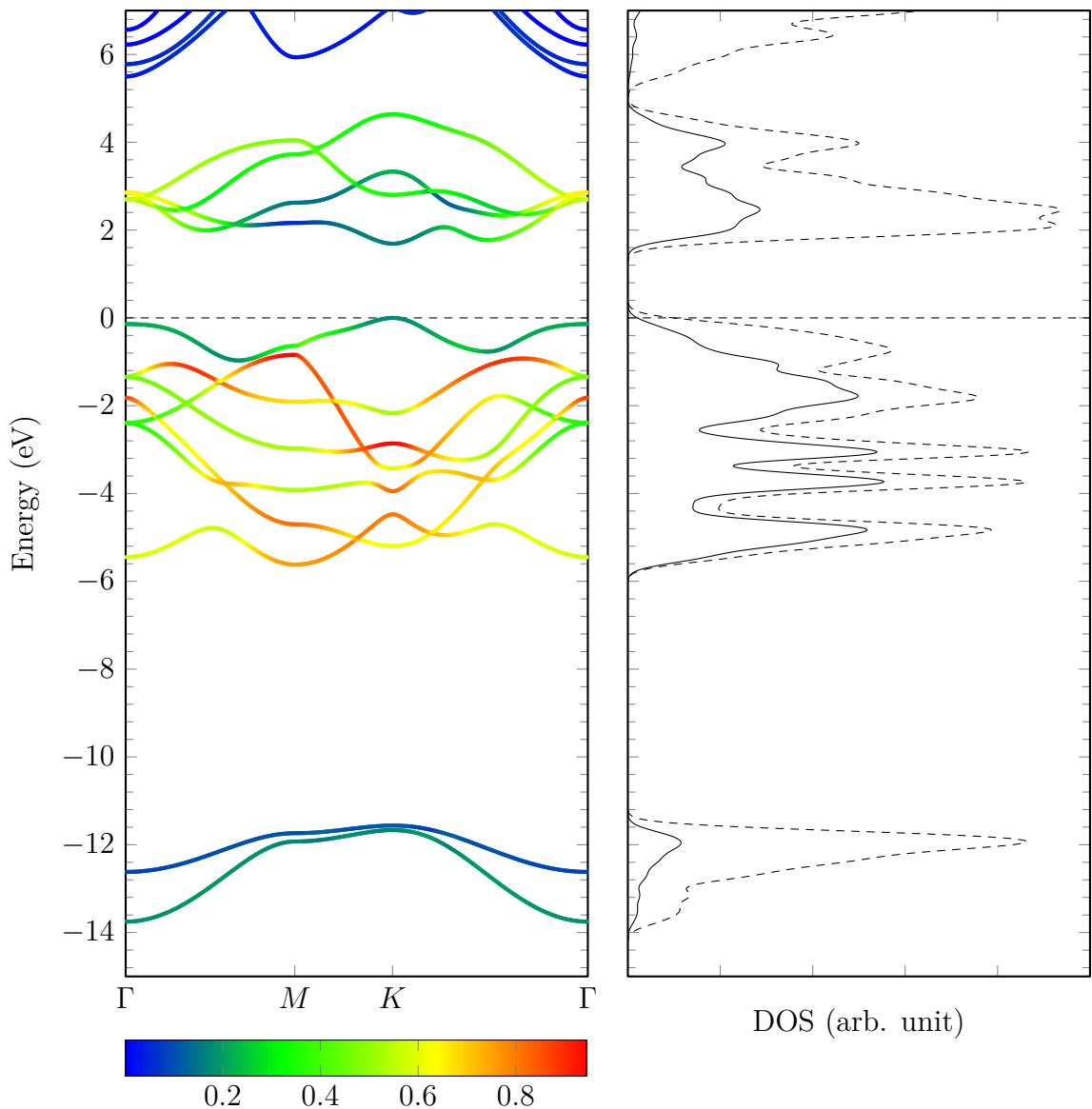


Figure F.31: Projected band structure and density of states (PDOS) calculated using MLWF for single-layer MoS<sub>2</sub> (1H-MoS<sub>2</sub>) showing sulphur 3p orbital contribution to the energy bands and total DOS.

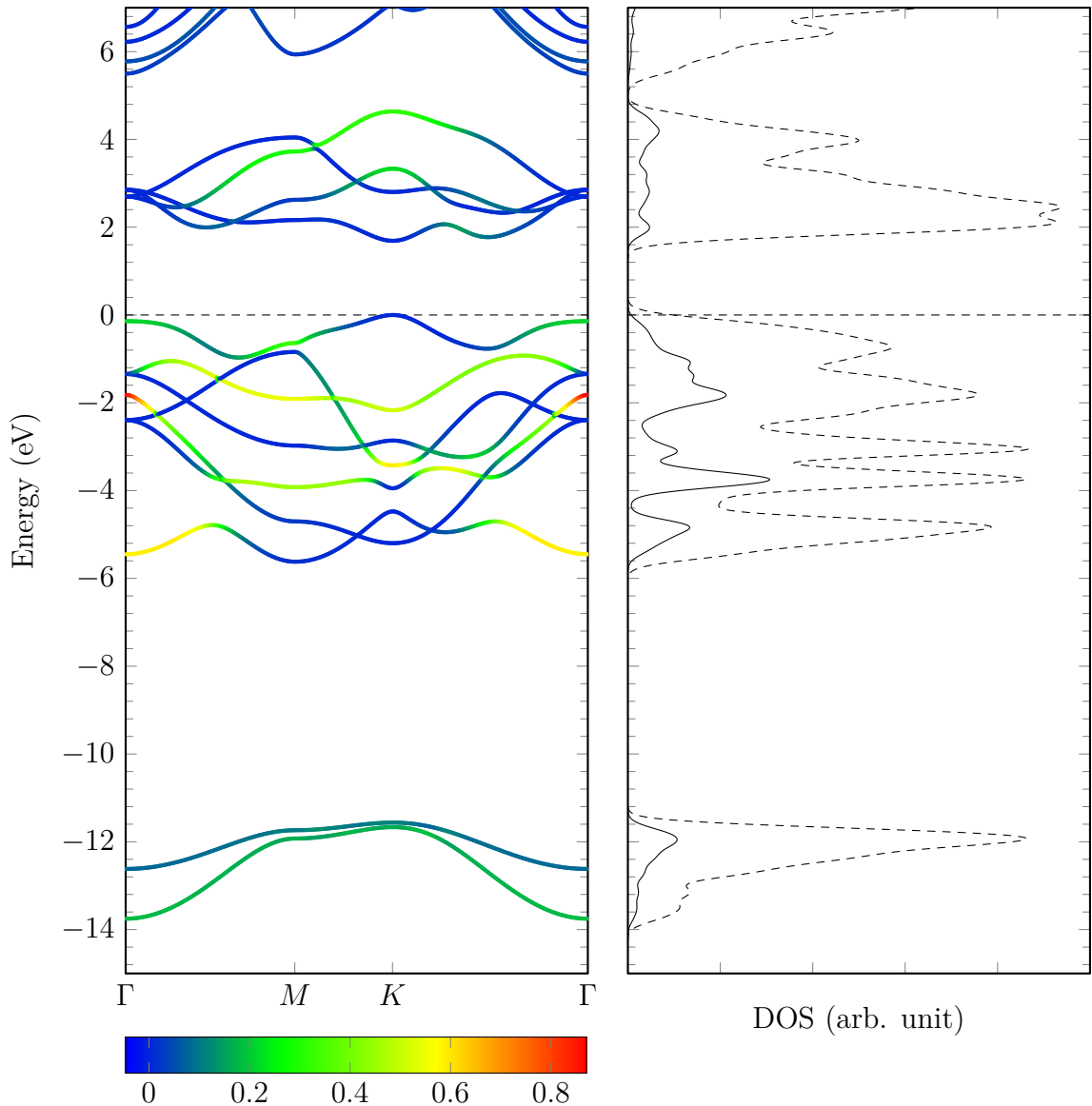


Figure F.32: Projected band structure and density of states (PDOS) calculated using MLWF for single-layer MoS<sub>2</sub> (1H-MoS<sub>2</sub>) showing sulphur 3p<sub>z</sub> orbital contribution to the energy bands and total DOS.

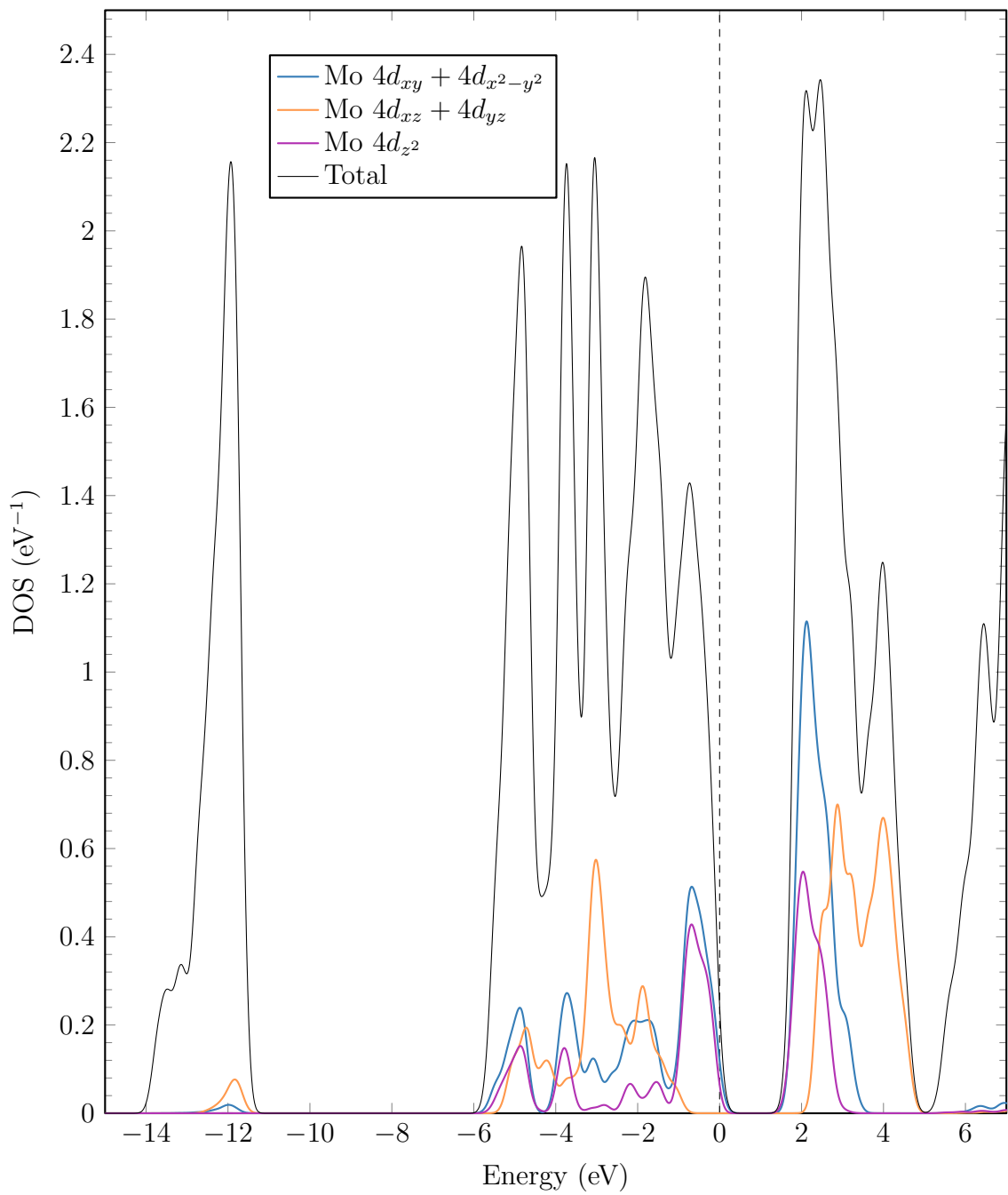


Figure F.33: Projected density of states (PDOS) calculated using MLWF for single-layer MoS<sub>2</sub> (1H-MoS<sub>2</sub>) showing molybdenum individual 4d orbital contribution to the total DOS.

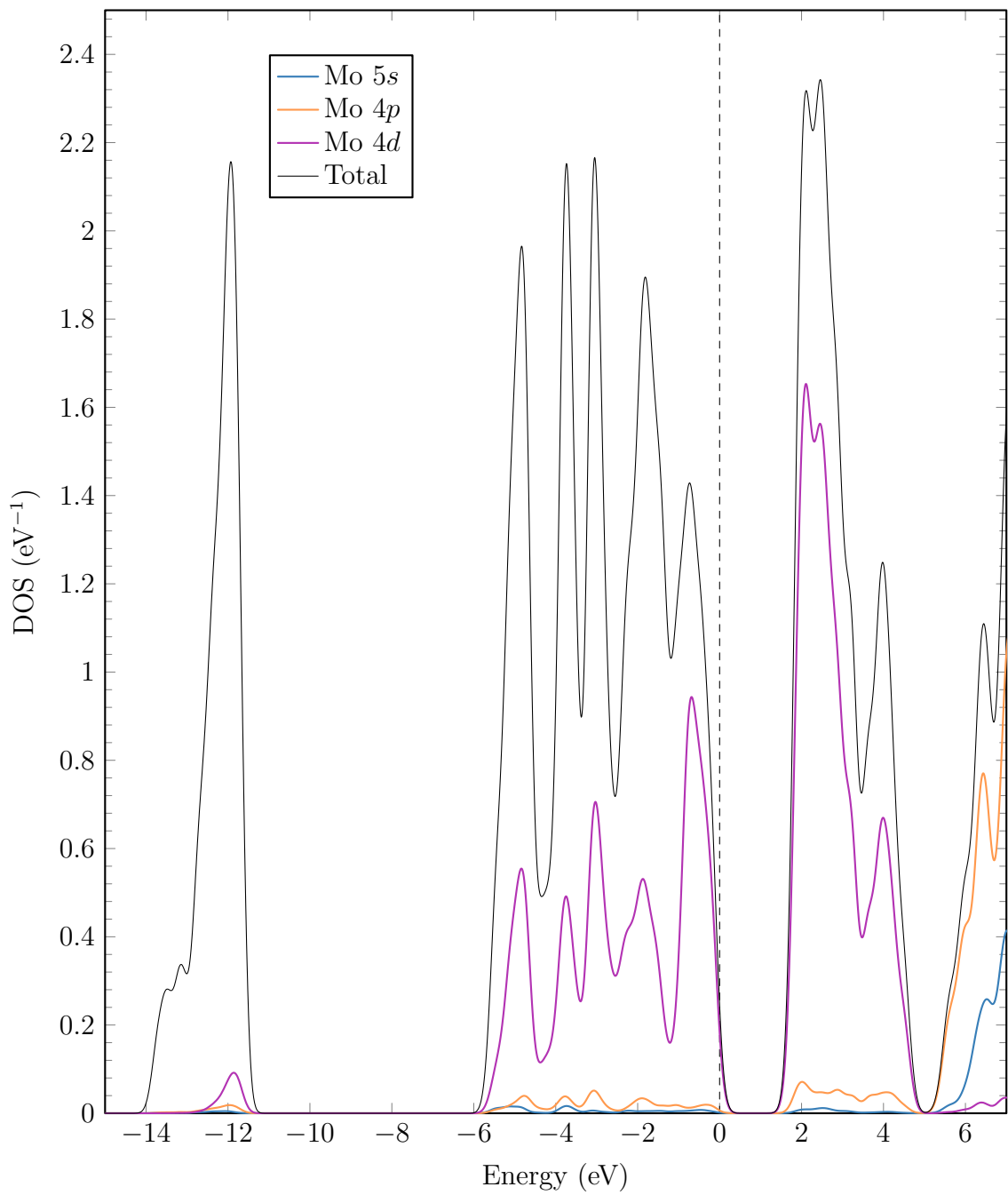


Figure F.34: Projected density of states (PDOS) calculated using MLWF for single-layer  $\text{MoS}_2$  ( $1H\text{-MoS}_2$ ) showing molybdenum  $5s$ ,  $4p$  and  $4d$  orbital contribution to the total DOS.

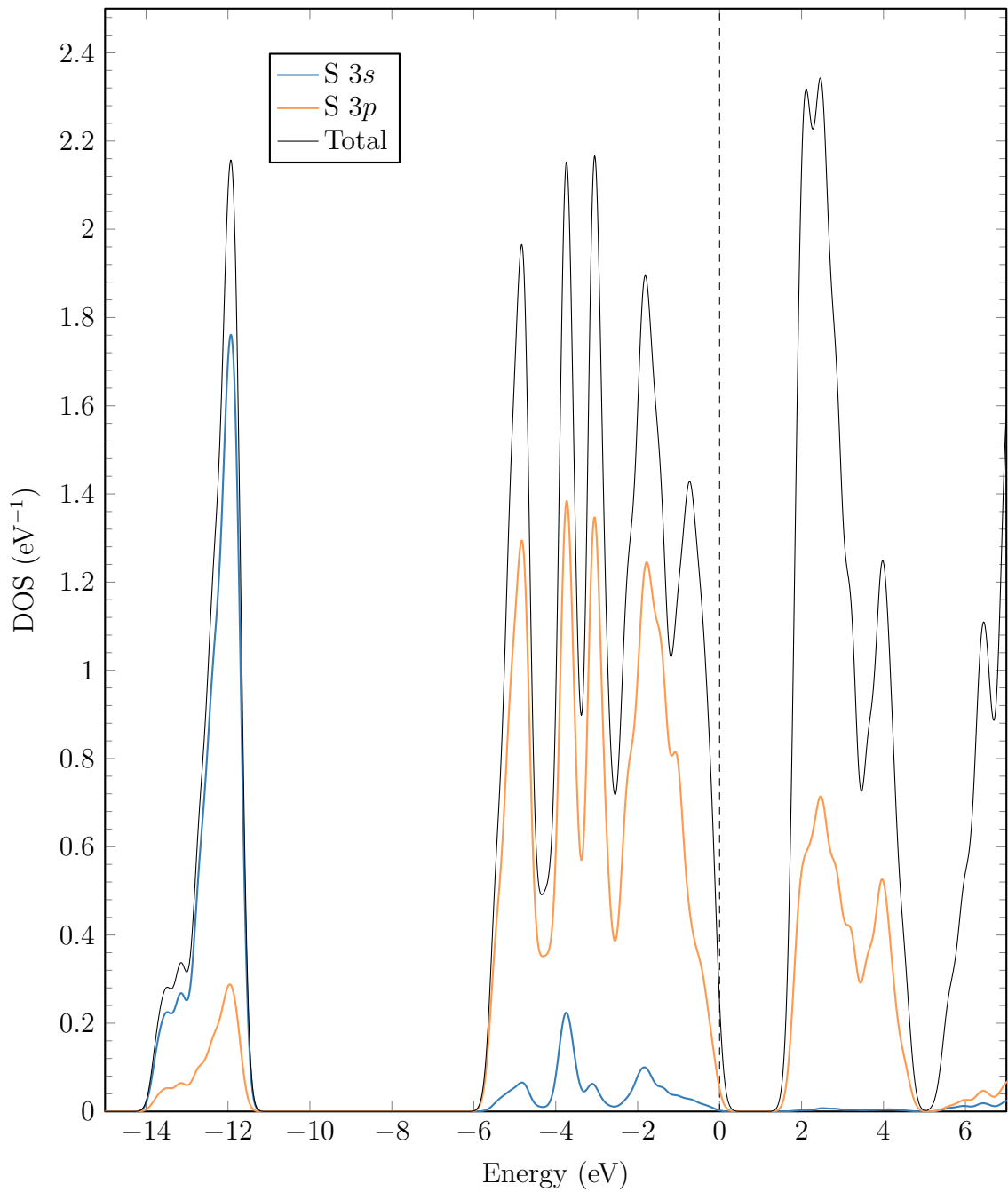


Figure F.35: Projected density of states (PDOS) calculated using MLWF for single-layer MoS<sub>2</sub> (1H-MoS<sub>2</sub>) showing sulphur 3s and 3p orbital contribution to the total DOS.

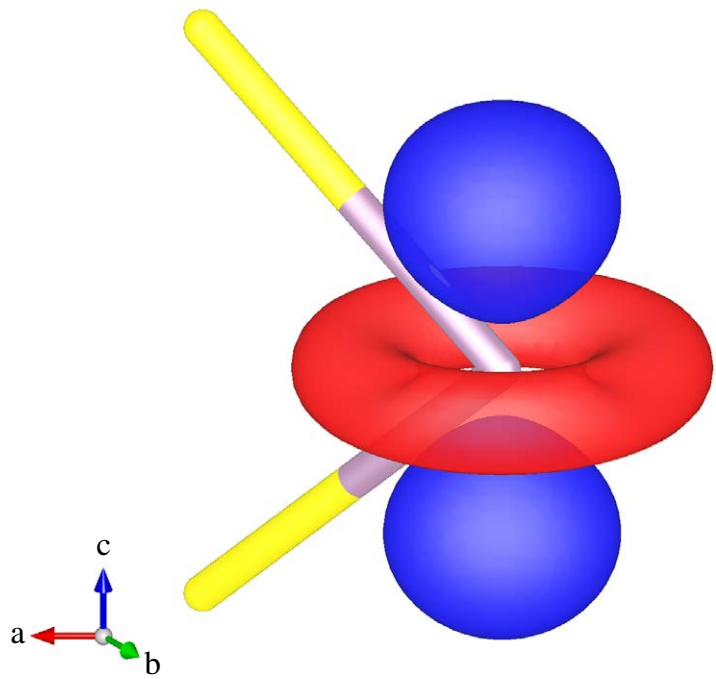
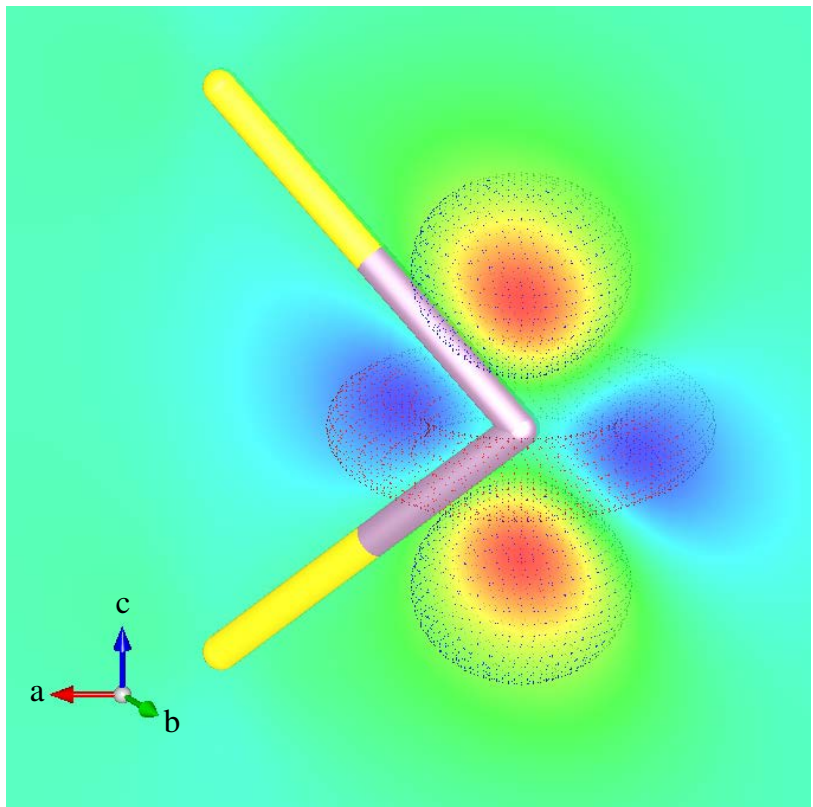


Figure F.36: Molybdenum  $4d_{z^2}$  projected MLWF cross-section along  $(1, 1, 0)$  lattice plane (top) and three-dimensional iso-surface (bottom) for single-layer  $\text{MoS}_2$  (1H- $\text{MoS}_2$ ). The iso-surface is set at a value of 0.3.

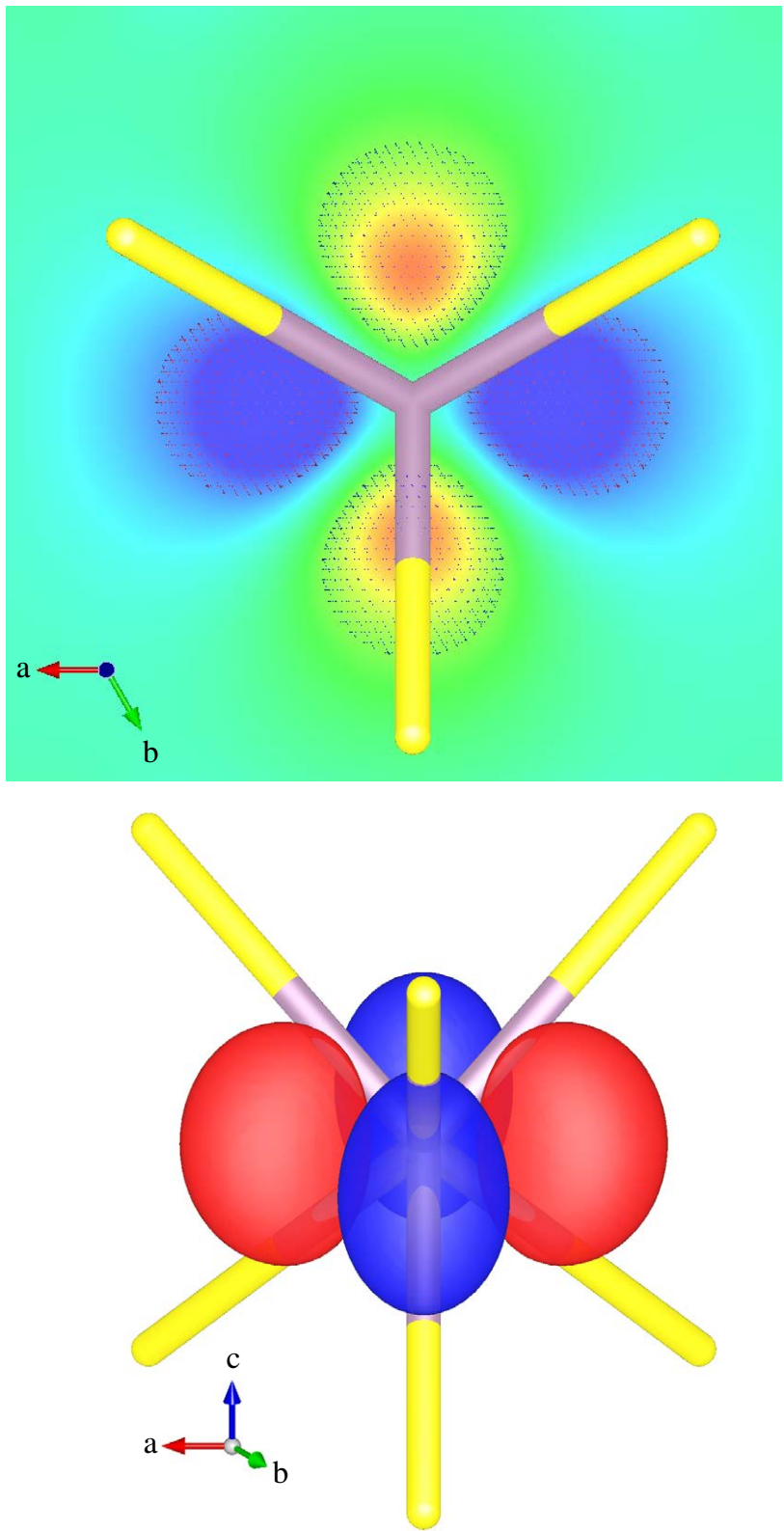


Figure F.37: Molybdenum  $4d_{x^2-y^2}$  projected MLWF cross-section along  $(0, 0, 1)$  lattice plane (top) and three-dimensional iso-surface (bottom) for single-layer MoS<sub>2</sub> (1H-MoS<sub>2</sub>). The iso-surface is set at a value of 0.3.

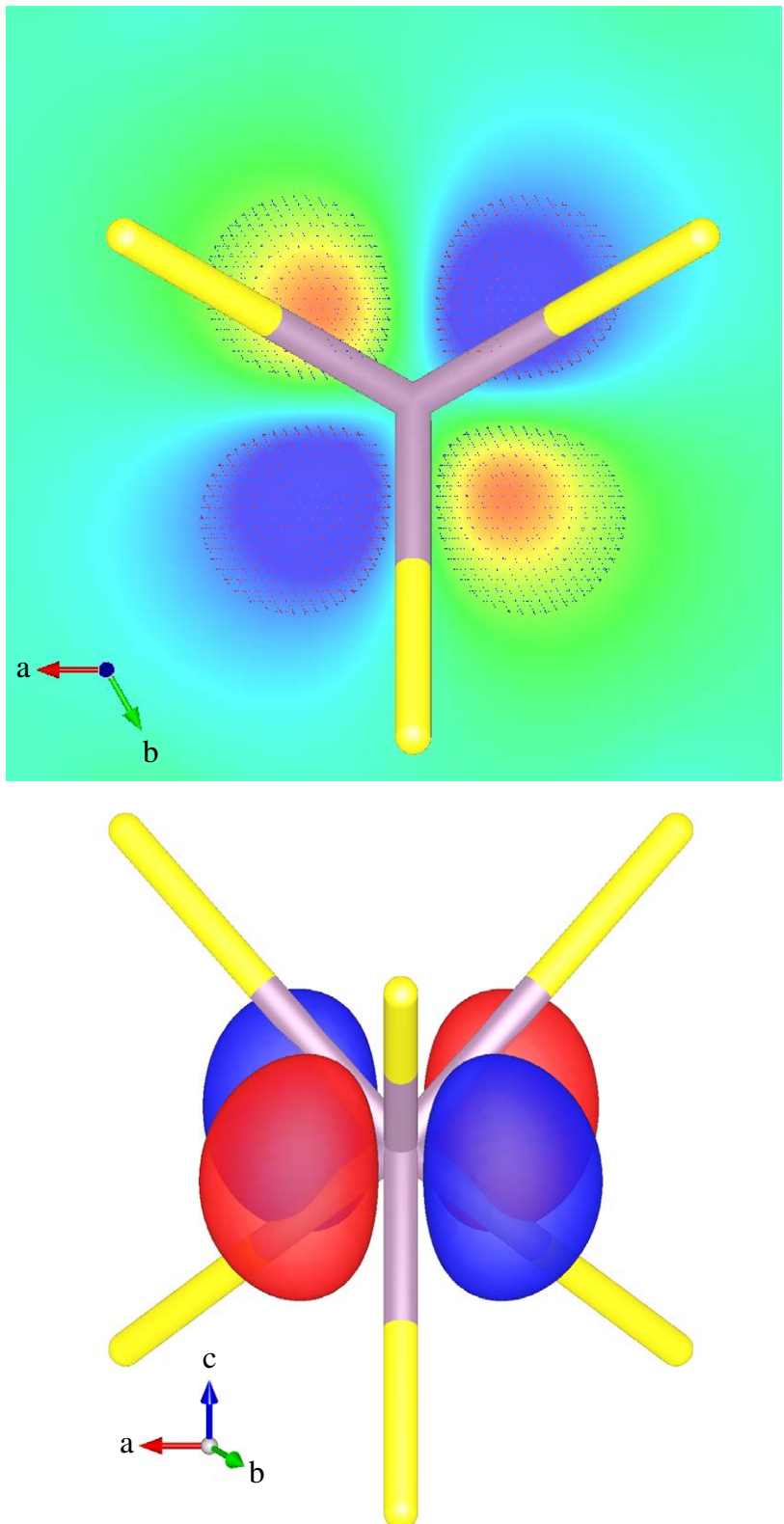


Figure F.38: Molybdenum  $4d_{xy}$  projected MLWF cross-section along  $(0, 0, 1)$  lattice plane (top) and three-dimensional iso-surface (bottom) for single-layer MoS<sub>2</sub> (1H-MoS<sub>2</sub>). The iso-surface is set at a value of 0.3.

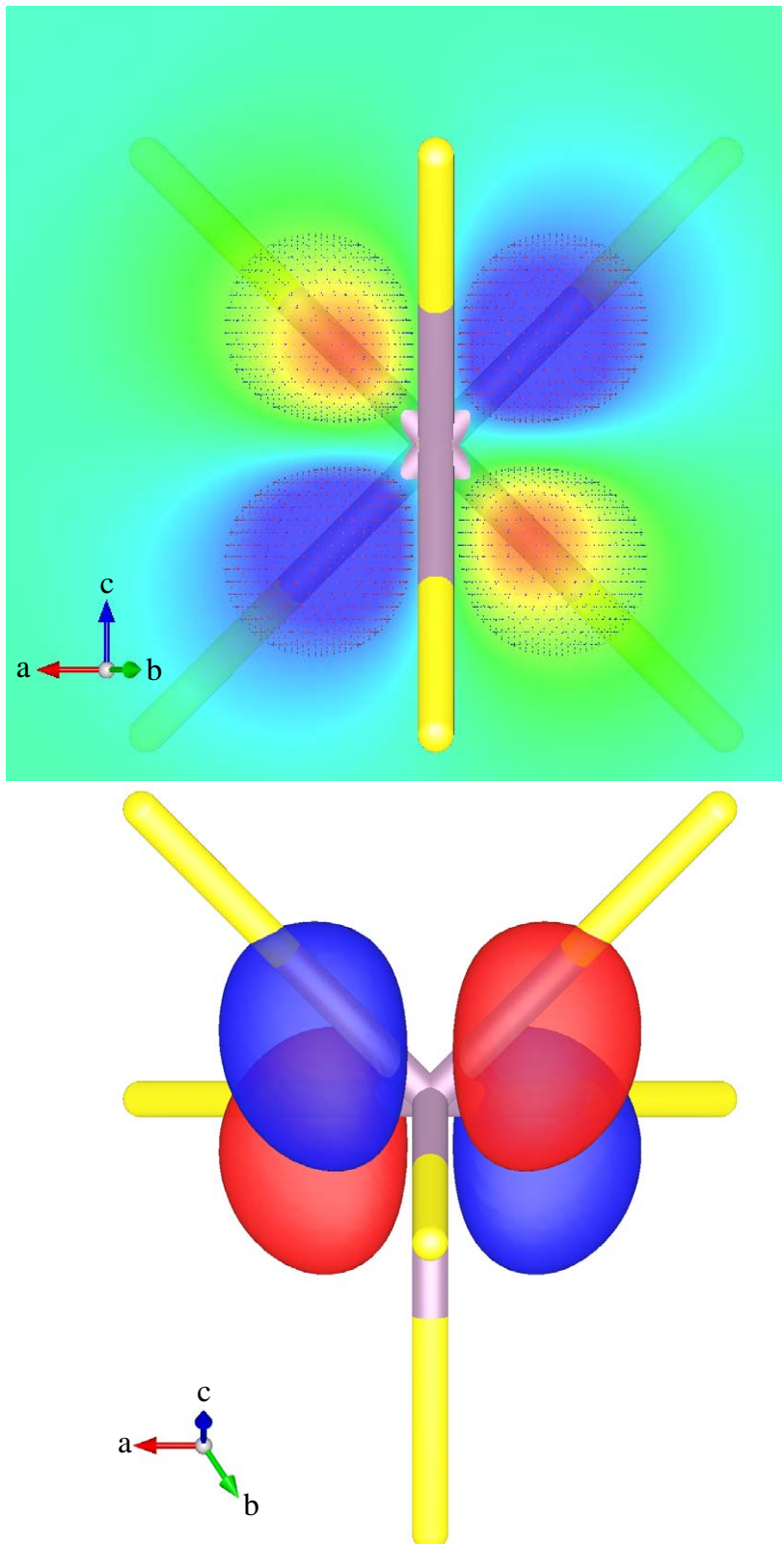


Figure F.39: Molybdenum 4d<sub>xz</sub> projected MLWF cross-section along (0, 1, 0) lattice plane (top) and three-dimensional iso-surface (bottom) for single-layer MoS<sub>2</sub> (1H-MoS<sub>2</sub>). The iso-surface is set at a value of 0.3.

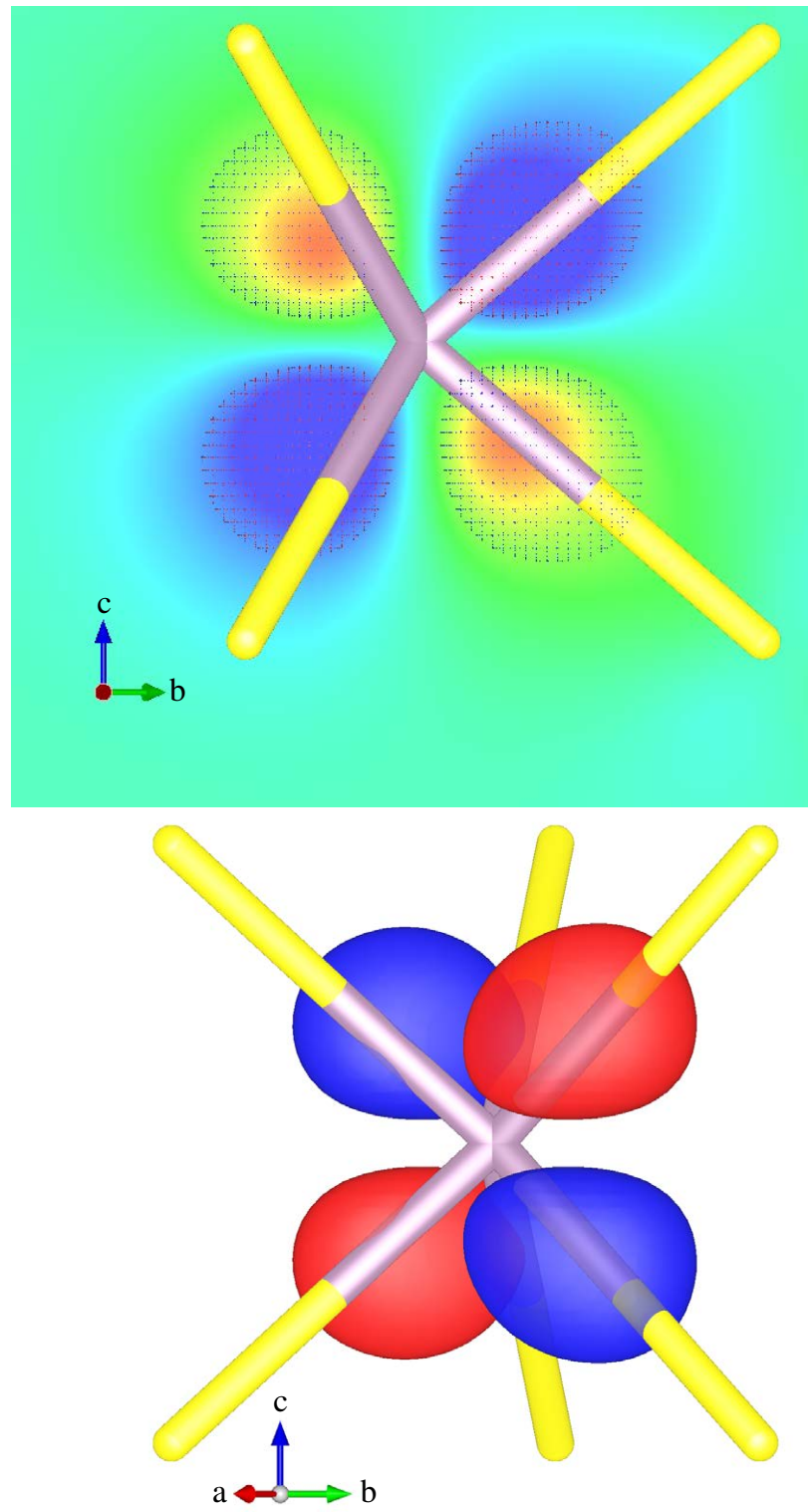


Figure F.40: Molybdenum  $4d_{yz}$  projected MLWF cross-section along  $(1, 1, 0)$  lattice plane (top) and three-dimensional iso-surface (bottom) for single-layer MoS<sub>2</sub> (1H-MoS<sub>2</sub>). The iso-surface is set at a value of 0.3.

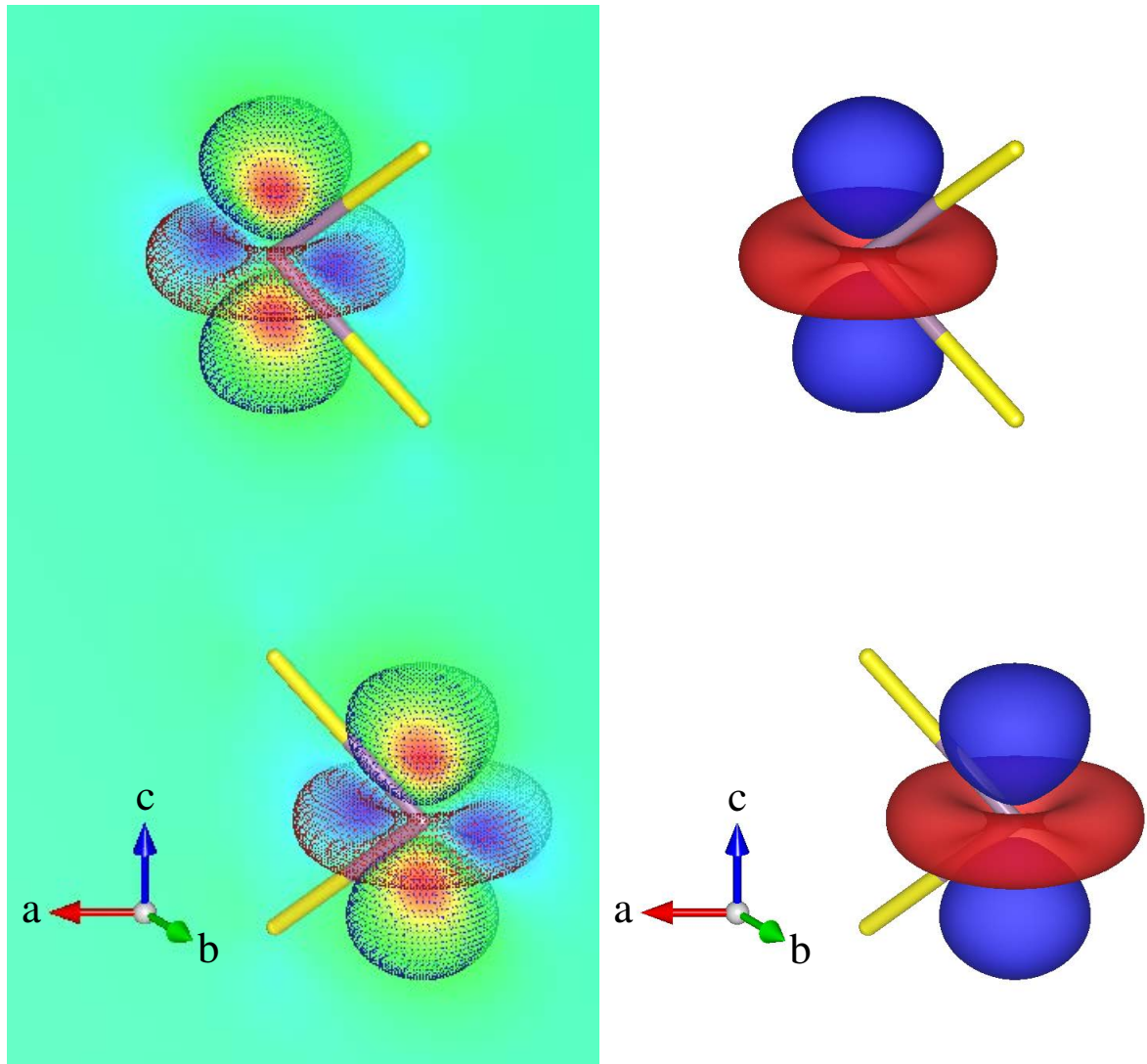


Figure F.41: Molybdenum  $4d_{z^2}$  projected MLWF cross-section along  $(1, 1, 0)$  lattice plane (left) and three-dimensional iso-surface (right) for bulk  $\text{MoS}_2$  ( $2H\text{-MoS}_2$ ). The iso-surface is set at a value of 0.3.

# Appendix G

## Sample ABINIT Script

Listing G.1: SCF and band structure calculation

```
1 # Band Structure - Bulk MoS2 GGA with PAW
2 # Number of datasets
3     ndtset      4
4
5 # MoS2 structure
6             # Lattice Parameters Converged in Model: lp20130313E
7     acell    6.0616327540E+00  6.0616327540E+00  2.3576843054E+01
8     rprim    1.00              0.00              0.00
9             -0.50             0.86602540378   0.00  # sqrt(3)/2
10            0.00             0.00              1.00
11     angdeg   9.00E+01        9.00E+01        1.20E+02
12     spgroup  194
13     natom    6
14     natrd    6
15     xred    3.3333333333E-01  6.6666666667E-01  2.4999999996E-01
16             6.6666666667E-01  3.3333333333E-01  7.5000000004E-01
17             3.3333333333E-01  6.6666666667E-01  6.2472573778E-01
18             6.6666666667E-01  3.3333333333E-01  1.2472573759E-01
19             6.6666666667E-01  3.3333333333E-01  3.7527426222E-01
20             3.3333333333E-01  6.6666666667E-01  8.7527426241E-01
21     ntypat   2
22     typat    2*1  4*2
23
24     znucl    4.20E+01    1.60E+01
25     symmorphi 0 # SYMMORPHic symmetry operations
26     chksymbreak 0
27
28 # enforce calculation of forces at each SCF step
29     optforces 1
30
```

```

31 # Plane wave basis
32     ecut      4.00E+01
33     nstep     2.00E+02
34     pawecutdg 7.00E+01
35
36 # Print Crystallographic structure file for inspection
37     prtcif    1
38
39
40 # kpoint set
41     ngkpt1   2.40E+01    2.40E+01    4.00E+00
42     nshiftk1 2.00
43     shiftk1  0.00        0.00        0.00
44             0.00        0.00        0.50 # half shift in z dir
45     kptopt1  1
46
47 # Self-consistent run to get the density
48     iscf1    7
49     tolvrs1  1.00d-12 # This value is way too large for most
50                           # realistic studies of materials
51                           # Will stop when, twice in a row,
52                           # the difference between two consecutive
53                           # evaluations of total energy
54
55     diemac   6.20
56
57     prtden1  1
58     enunit1  2
59
60
61 # Second dataset: NSCF - Band Structure
62 # NSCF - Band Structure
63     iscf2    -2
64     getden2  1
65     kptopt2  -10
66     nband2   46
67     nshiftk2 1.00           # one k-mesh for hex lattice
68     shiftk2  0.00  0.00  0.00  # no shift in z dir
69
70
71 #          GZ  ZM  MK  KT  TG  GA  AL  LH  HS  SA
72     ndivk2   20  20  23  23  23   9   40  23  23  23
73     # divisions of the 10 segments, delimited by 11 points
74     # actual numbers: 23=23.09, 9=8.91
75     # total k points 20+20+23+23+23+9+40+23+23+23+(1)= 228 kpoint
76     # that means (~4 k-point per processor for 4 nodes)
77
78     kptbounds2 0.00      0.00      0.00      # Gamma point
79             1/4       0.00      0.00      # Sigma point

```

```

80          1/2      0.00      0.00      # M point
81          1/3      1/3       0.00      # K point
82          1/6      1/6       0.00      # T point
83          0.00     0.00      0.00      # Gamma point
84          0.00     0.00      1/2       # A point
85          1/2      0.00      1/2       # L point
86          1/3      1/3       1/2       # H point
87          1/6      1/6       1/2       # S point
88          0.00     0.00      1/2       # A point
89
90
91
92      tolwfr2    1.0d-12
93      enunit2     1           # Will output the eigenenergies in eV
94      nstep2      250
95      prtden2     1
96
97      prtvol2     1
98      prtpot2     1           # PRint the total (kohn-sham) POTential
99      prtkpt2     1           # PRint the K-PointTs sets
100     prtcif2     1
101
102
103
104 # NSCF - Band Structure
105     iscf3      -2
106     getden3     1
107     kptopt3     -1
108     nband3      46
109     nshiftk3    1.00
110     shiftk3     0.00      0.00
111
112 #               ML
113     ndivk3      9
114     # divisions of the 1 segments, delimited by 2 points
115     # actual numbers: 9=8.91
116     # total k points 9+(1)= 10 kpoint
117     # that means (--) k point per processor node for 4 nodes)
118
119     kptbounds3   1/2      0.00      0.00 # M point
120                  1/2      0.00      1/2  # L point
121
122
123     tolwfr3    1.0d-12
124     enunit3     1           # Will output the eigenenergies in eV
125     nstep3      250
126     prtden3     1
127
128     prtvol3     1

```

```

129      prtpot3      1      # PRinT the total (kohn-sham) POTential
130      prtkpt3      1      # PRinT the K-PointTs sets
131      prtcif3      1
132
133
134
135 # NSCF - Band Structure
136      iscf4       -2
137      getden4      1
138      kptopt4      -1
139      nband4       46
140      nshiftk4     1.00
141      shiftk4      0.00      0.00      0.00
142
143
144 #          KH
145      ndivk4       9
146      # divisions of the 1 segments, delimited by 2 points
147      # actual numbers: 9=8.91
148      # total k points 9+(1)= 10 kpoint
149      # that means (--- k point per processor node for 4 nodes)
150
151      kptbounds4   1/3      1/3      0.00 # K point
152                  1/3      1/3      1/2 # H point
153
154
155      tolwfr4      1.0d-12
156      enunit4      1      # Will output the eigenenergies in eV
157      nstep4       250
158      prtden4      1
159
160      prtvol4      1
161      prtpot4      1      # PRinT the total (kohn-sham) POTential
162      prtkpt4      1      # PRinT the K-PointTs sets
163      prtcif4      1

```

# List of References

- [1] Entry. ab initio, adj. & adv. In: Simpson J, Proffitt M, editors. Oxford English Dictionary. vol. 3. Oxford University Press; 1997. p. 3. Accessed: 2015-05-15. Available from: <http://www.oed.com/view/Entry/315>.
- [2] Novoselov KS, Geim AK, Morozov SV, Jiang D, Zhang Y, Dubonos SV, et al. Electric Field Effect in Atomically Thin Carbon Films. *Science*. 2004;306(5696):666–669. Available from: <http://www.sciencemag.org/content/306/5696/666.abstract>.
- [3] Novoselov KS, Geim AK, Morozov SV, Jiang D, Katsnelson MI, Grigorieva IV, et al. Two-dimensional gas of massless Dirac fermions in graphene. *Nature*. 2005;438(7065):197–200. 10.1038/nature04233.
- [4] Geim AK, Novoselov KS. The rise of graphene. *Nat Mater*. 2007;6:183–191. Available from: <http://dx.doi.org/10.1038/nmat1849>.
- [5] Ramakrishna Matte HS, Gomathi A, Manna AK, Late DJ, Datta R, Pati SK, et al. MoS<sub>2</sub> and WS<sub>2</sub> Analogues of Graphene. *Angewandte Chemie International Edition*. 2010;49(24):4059–4062.
- [6] Han MY, Özyilmaz B, Zhang Y, Kim P. Energy Band-Gap Engineering of Graphene Nanoribbons. *Phys Rev Lett*. 2007 May;98:206805. Available from: <http://link.aps.org/doi/10.1103/PhysRevLett.98.206805>.
- [7] Barone V, Hod O, Scuseria GE. Electronic Structure and Stability of Semiconducting Graphene Nanoribbons. *Nano Letters*. 2006;6(12):2748–2754. PMID: 17163699. Available from: <http://dx.doi.org/10.1021/nl0617033>.
- [8] Castro Neto AH, Guinea F, Peres NMR, Novoselov KS, Geim AK. The electronic properties of graphene. *Rev Mod Phys*. 2009 Jan;81:109–162. Available from: <http://link.aps.org/doi/10.1103/RevModPhys.81.109>.
- [9] Das Sarma S, Adam S, Hwang EH, Rossi E. Electronic transport in two-dimensional graphene. *Rev Mod Phys*. 2011 May;83:407–470. Available from: <http://link.aps.org/doi/10.1103/RevModPhys.83.407>.
- [10] Bao Q, Loh KP. Graphene Photonics, Plasmonics, and Broadband Optoelectronic Devices. *ACS Nano*. 2012;6(5):3677–3694. PMID: 22512399. Available from: <http://dx.doi.org/10.1021/nn300989g>.

- [11] Wang H, Maiyalagan T, Wang X. Review on Recent Progress in Nitrogen-Doped Graphene: Synthesis, Characterization, and Its Potential Applications. *ACS Catalysis*. 2012;2(5):781–794. Available from: <http://dx.doi.org/10.1021/cs200652y>.
- [12] Chen JH, Ishigami M, Jang C, Hines DR, Fuhrer MS, Williams ED. Printed Graphene Circuits. *Advanced Materials*. 2007;19(21):3623–3627. Available from: <http://dx.doi.org/10.1002/adma.200701059>.
- [13] Štengl V, Popelková D, Vláčil P. TiO<sub>2</sub>–Graphene Nanocomposite as High Performance Photocatalysts. *The Journal of Physical Chemistry C*. 2011;115(51):25209–25218. Available from: <http://dx.doi.org/10.1021/jp207515z>.
- [14] Bellido EP, Seminario JM. Graphene-Based Vibronic Devices. *The Journal of Physical Chemistry C*. 2012;116(15):8409–8416. Available from: <http://dx.doi.org/10.1021/jp2080429>.
- [15] Eliseeva NS, Kuzubov AA, Ovchinnikov SG, Serzhantova MV, Tomilin FN, Fedorov AS. Theoretical study of the magnetic properties of ordered vacancies in 2D hexagonal structures: Graphene, 2D-SiC, and h-BN. *JETP Letters*. 2012;95(11):555–559. Available from: <http://dx.doi.org/10.1134/S0021364012110045>.
- [16] Chen Q, Hu H, Chen X, Wang J. Tailoring band gap in GaN sheet by chemical modification and electric field: Ab initio calculations. *Applied Physics Letters*. 2011;98(5):053102. Available from: <http://scitation.aip.org/content/aip/journal/apl/98/5/10.1063/1.3549299>.
- [17] Guo H, Zhao Y, Lu N, Kan E, Zeng XC, Wu X, et al. Tunable Magnetism in a Nonmetal-Substituted ZnO Monolayer: A First-Principles Study. *The Journal of Physical Chemistry C*. 2012;116(20):11336–11342. Available from: <http://dx.doi.org/10.1021/jp2125069>.
- [18] Tang Q, Cui Y, Li Y, Zhou Z, Chen Z. How Do Surface and Edge Effects Alter the Electronic Properties of GaN Nanoribbons? *The Journal of Physical Chemistry C*. 2011;115(5):1724–1731. Available from: <http://dx.doi.org/10.1021/jp109829c>.
- [19] Tang Q, Li F, Zhou Z, Chen Z. Versatile Electronic and Magnetic Properties of Corrugated V<sub>2</sub>O<sub>5</sub> Two-Dimensional Crystal and Its Derived One-Dimensional Nanoribbons: A Computational Exploration. *The Journal of Physical Chemistry C*. 2011;115(24):11983–11990. Available from: <http://dx.doi.org/10.1021/jp204174p>.
- [20] Stock N, Biswas S. Synthesis of Metal-Organic Frameworks (MOFs): Routes to Various MOF Topologies, Morphologies, and Composites. *Chemical Reviews*. 2012;112(2):933–969. PMID: 22098087. Available from: <http://dx.doi.org/10.1021/cr200304e>.
- [21] Zhou J, Sun Q. Magnetism of Phthalocyanine-Based Organometallic Single Porous Sheet. *Journal of the American Chemical Society*. 2011;133(38):15113–15119. PMID: 21838296. Available from: <http://dx.doi.org/10.1021/ja204990j>.

- [22] Wang L, Takada K, Kajiyama A, Onoda M, Michiue Y, Zhang L, et al. Synthesis of a Li-Mn-oxide with Disordered Layer Stacking through Flocculation of Exfoliated MnO<sub>2</sub> Nanosheets, and Its Electrochemical Properties. *Chemistry of Materials*. 2003;15(23):4508–4514. Available from: <http://dx.doi.org/10.1021/cm0217809>.
- [23] Wang QH, Kalantar-Zadeh K, Kis A, Coleman JN, Strano MS. Electronics and optoelectronics of two-dimensional transition metal dichalcogenides. *Nature nanotechnology*. 2012;7(11):699–712.
- [24] Radisavljevic B, Radenovic A, Brivio J, Giacometti V, Kis A. Single-layer MoS<sub>2</sub> transistors. *Nat Nano*. 2011;6(3):147–150. 10.1038/nnano.2010.279.
- [25] Novoselov KS, Jiang D, Schedin F, Booth TJ, Khotkevich VV, Morozov SV, et al. Two-dimensional atomic crystals. *Proceedings of the National Academy of Sciences of the United States of America*. 2005;102(30):10451–10453. Available from: <http://www.pnas.org/content/102/30/10451.abstract>.
- [26] Rode DL. Electron Transport in InSb, InAs, and InP. *Phys Rev B*. 1971 May;3:3287–3299. Available from: <http://link.aps.org/doi/10.1103/PhysRevB.3.3287>.
- [27] of Maryland U. Electrons Can Travel Over 100 Times Faster In Graphene Than In Silicon, Physicists Show. *ScienceDaily*; 2008. Accessed: 2015-05-15. Online. Available from: <http://www.sciencedaily.com/releases/2008/03/080324094514.htm>.
- [28] Dominko R, Arčon D, Mrzel A, Zorko A, Cevc P, Venturini P, et al. Dichalcogenide Nanotube Electrodes for Li-Ion Batteries. *Advanced Materials*. 2002;14(21):1531–1534. Available from: [http://dx.doi.org/10.1002/1521-4095\(20021104\)14:21<1531::AID-ADMA1531>3.0.CO;2-P](http://dx.doi.org/10.1002/1521-4095(20021104)14:21<1531::AID-ADMA1531>3.0.CO;2-P).
- [29] Ionescu A, Allouche A, Aycard JP, Rajzmann M, Gall RL. Study of  $\gamma$ -Alumina-Supported Hydrotreating Catalyst: I. Adsorption of Bare MoS<sub>2</sub> Sheets on  $\gamma$ -Alumina Surfaces. *The Journal of Physical Chemistry B*. 2003;107(33):8490–8497. Available from: <http://dx.doi.org/10.1021/jp0343382>.
- [30] Hinnemann B, Moses PG, Bonde J, Jørgensen KP, Nielsen JH, Horch S, et al. Biomimetic Hydrogen Evolution: MoS<sub>2</sub> Nanoparticles as Catalyst for Hydrogen Evolution. *Journal of the American Chemical Society*. 2005;127(15):5308–5309. PMID: 15826154. Available from: <http://dx.doi.org/10.1021/ja0504690>.
- [31] Voevodin AA, Zabinski JS. Laser surface texturing for adaptive solid lubrication. *Wear*. 2006;261(11–12):1285–1292. Available from: <http://www.sciencedirect.com/science/article/pii/S0043164806001335>.
- [32] Hamilton MA, Alvarez LA, Mauntler NA, Argibay N, Colbert R, Burris DL, et al. A possible link between macroscopic wear and temperature dependent friction behaviors of MoS<sub>2</sub> coatings. *Tribology Letters*. 2008;32(2):91–98.

- [33] Frame FA, Osterloh FE. CdSe-MoS<sub>2</sub>: A Quantum Size-Confining Photocatalyst for Hydrogen Evolution from Water under Visible Light. *The Journal of Physical Chemistry C*. 2010;114(23):10628–10633. Available from: <http://dx.doi.org/10.1021/jp101308e>.
- [34] Min S, Lu G. Sites for High Efficient Photocatalytic Hydrogen Evolution on a Limited-Layered MoS<sub>2</sub> Cocatalyst Confined on Graphene Sheets-The Role of Graphene. *The Journal of Physical Chemistry C*. 2012;116(48):25415–25424. Available from: <http://dx.doi.org/10.1021/jp3093786>.
- [35] Splendiani A, Sun L, Zhang Y, Li T, Kim J, Chim CY, et al. Emerging Photoluminescence in Monolayer MoS<sub>2</sub>. *Nano Letters*. 2010;10(4):1271–1275. Doi: 10.1021/nl903868w.
- [36] 2D Semiconductors. Molybdenum Disulfide (MoS<sub>2</sub>). 2D Semiconductors; 2015. Copyright: Copyright 2003, 2d Semiconductors ALL RIGHTS RESERVED. Accessed: 2015-10-10. Online. Available from: <http://www.2dsemiconductors.com/2d-semiconductors/mos2>.
- [37] Moller P, Kramer B. Electric Fish. *BioScience*. 1991 Dec;41(11):794–796. Available from: <http://dx.doi.org/10.2307/1311732>.
- [38] Rutherford E. The Scattering of  $\alpha$  and  $\beta$  Particles by Matter and the Structure of the Atom. *Philosophical Magazine, Series 6*. 1911 May;21:669–688.
- [39] Bohr N. On the Constitution of Atoms and Molecules, Part I. *Philosophical Magazine, Series 6*. 1913;26:1–25.
- [40] Unknown author. Solvay Conference 1933. fm web site; 2011. Copyright: This image is in the “public domain” because its copyright has expired and its author is anonymous. Accessed: 2015-02-15. Available from: <http://fmwebsite.altervista.org/pages/solvay.htm>.
- [41] Hoddeson L, Braun E, Teichmann J, Weart S. Out of the crystal maze : chapters from the history of solid state physics. New York, Oxford: Oxford University Press; 1992.
- [42] Brillouin LN. Les électrons dans les métaux et le classement des ondes de de Broglie correspondantes. *Comptes Rendus Hebdomadaires des Séances de l'Académie des Sciences*. 1930;191:292–294.
- [43] Wilson AH. The Theory of Electronic Semi-Conductors. *Proceedings of the Royal Society of London A: Mathematical, Physical and Engineering Sciences*. 1931;133(822):458–491.
- [44] Hartree DR. The Wave Mechanics of an Atom with a Non-Coulomb Central Field. Part II. Some Results and Discussion. *Mathematical Proceedings of the Cambridge Philosophical Society*. 1928 1;24:111–132. Available from: [http://journals.cambridge.org/article\\_S0305004100011920](http://journals.cambridge.org/article_S0305004100011920).

- [45] Martin RM. Electronic structure : basic theory and practical methods. Cambridge University Press; 2004.
- [46] Drake GWF, editor. Springer handbook of atomic, molecular, and optical physics. Rev. ed. New York: Springer; 2006. Previous ed.: 1996.
- [47] Parr RG, Yang W. Density-Functional Theory of Atoms and Molecules. International Series of Monographs on Chemistry. Oxford University Press, USA; 1989.
- [48] Dreizler RM, Gross EKU. Density functional theory : an approach to the quantum many-body problem. Berlin ; New York: Springer-Verlag; c1990.
- [49] de Broglie L. The reinterpretation of wave mechanics. Foundations of Physics. 1970;1(1):5–15. Available from: <http://dx.doi.org/10.1007/BF00708650>.
- [50] Schrödinger E. An Undulatory Theory of the Mechanics of Atoms and Molecules. Phys Rev. 1926 Dec;28:1049–1070. Available from: <http://link.aps.org/doi/10.1103/PhysRev.28.1049>.
- [51] Born M, Oppenheimer JR. Zur Quantentheorie der Moleküle. Annalen der Physik. 1927;389:457–484.
- [52] Pauli W. Zur Quantenmechanik des magnetischen Elektrons. Zeitschrift für Physik. 1927;43(9):601–623. Available from: <http://dx.doi.org/10.1007/BF01397326>.
- [53] Cohen-Tannoudji C, Diu B, Laloe F. Quantum Mechanics. vol. 1. Wiley; 1977.
- [54] Jacob CR, Reiher M. Spin in density-functional theory. International Journal of Quantum Chemistry. 2012;112(23):3661–3684. Available from: <http://dx.doi.org/10.1002/qua.24309>.
- [55] McWeeny R, of Brooklyn PI. Spins in chemistry. Current chemical concepts. Academic Press; 1970. Reprinted in 2004. Available from: <https://books.google.co.in/books?id=bgyGAAAAIAAJ>.
- [56] Reiher M, Wolf A. Relativistic Quantum Chemistry: The Fundamental Theory of Molecular Science. Wiley; 2009. Available from: <http://onlinelibrary.wiley.com/book/10.1002/9783527627486>.
- [57] Szabo A, Ostlund NS. Modern quantum chemistry: introduction to advanced electronic structure theory. McGraw-Hill; 1989. Reprinted in 1996.
- [58] Thomas LH. The calculation of atomic fields. Mathematical Proceedings of the Cambridge Philosophical Society. 1927 1;23:542–548. Available from: [http://journals.cambridge.org/article\\_S0305004100011683](http://journals.cambridge.org/article_S0305004100011683).
- [59] Fermi E. Un Metodo Statistico per la Determinazione di alcune Proprietà dell'Atomo. Rend Accad Naz Lincei. 1927;6:602–607.
- [60] Arfken GB, Weber HJ, Harris F. Mathematical methods for physicists. 7th ed. Oxford: Academic; 2012. Previous ed.: Amsterdam; London: Elsevier Academic, 2005. Includes bibliographical references and index.

- [61] Dirac PAM. Note on Exchange Phenomena in the Thomas Atom. Mathematical Proceedings of the Cambridge Philosophical Society. 1930;7:26:376–385. Available from: [http://journals.cambridge.org/article\\_S0305004100016108](http://journals.cambridge.org/article_S0305004100016108).
- [62] Iadonisi G, Chiofalo ML, Cantele G. Introduction to solid state physics and of crystalline nanostructures. UNITEXT for physics. Milan: Springer; c2014. Includes bibliographical references and index.
- [63] Hohenberg P, Kohn W. Inhomogeneous Electron Gas. Phys Rev. 1964 Nov;136:B864–B871. Available from: <http://link.aps.org/doi/10.1103/PhysRev.136.B864>.
- [64] Levy M. Universal variational functionals of electron densities, first-order density matrices, and natural spin-orbitals and solution of the v-representability problem. Proceedings of the National Academy of Sciences. 1979;76(12):6062–6065.
- [65] Dirac PAM. A new notation for quantum mechanics. Mathematical Proceedings of the Cambridge Philosophical Society. 1939;7:35:416–418. Available from: [http://journals.cambridge.org/article\\_S0305004100021162](http://journals.cambridge.org/article_S0305004100021162).
- [66] Lieb EH. Density functionals for Coulomb systems. International Journal of Quantum Chemistry. 1983;24(3):243–277. Available from: <http://dx.doi.org/10.1002/qua.560240302>.
- [67] Entry. ansatz, n. In: Simpson J, Proffitt M, editors. Oxford English Dictionary Additions Series. vol. 3. Oxford University Press; 1997. p. 56. Accessed: 2015-05-15. Available from: <http://www.oed.com/view/Entry/240569>.
- [68] Kohn W, Sham LJ. Self-Consistent Equations Including Exchange and Correlation Effects. Phys Rev. 1965 Nov;140:A1133–A1138. Available from: <http://link.aps.org/doi/10.1103/PhysRev.140.A1133>.
- [69] Janak JF. Proof that  $\frac{\partial E}{\partial n_i} = \epsilon$  in density-functional theory. Phys Rev B. 1978 Dec;18:7165–7168. Available from: <http://link.aps.org/doi/10.1103/PhysRevB.18.7165>.
- [70] Engel E, Dreizler RM. Density Functional Theory: An Advanced Course. Springer-Verlag Berlin Heidelberg; 2011. Available from: <http://www.springer.com/gb/book/9783642140891>.
- [71] Schipper PRT, Gritsenko OV, Baerends EJ. One - determinantal pure state versus ensemble Kohn-Sham solutions in the case of strong electron correlation: CH2 and C2. Theoretical Chemistry Accounts. 1998;99(5):329–343. Available from: <http://dx.doi.org/10.1007/s002140050343>.
- [72] Güttinger P. Das Verhalten von Atomen im magnetischen Drehfeld. Zeitschrift für Physik. 1932;73(3):169–184. Available from: <http://dx.doi.org/10.1007/BF01351211>.
- [73] Pauli W. Die allgemeinen Prinzipien der Wellenmechanik. In: Handbuch der Physik. 2nd ed. Berlin: Springer-Verlag Berlin Heidelberg; 1933. p. 83–272.

- [74] Hellmann H. Einführung in die Quantenchemie. Franz Deuticke; 1937.
- [75] Feynman RP. Forces in Molecules. *Phys Rev*. 1939 Aug;56:340–343. Available from: <https://link.aps.org/doi/10.1103/PhysRev.56.340>.
- [76] Sorbello RS, Dasgupta BB. Force on an atom in an electrostatic field: Feynman-Hellmann theorem and oscillator strengths. *Phys Rev B*. 1980 Mar;21:2196–2200. Available from: <https://link.aps.org/doi/10.1103/PhysRevB.21.2196>.
- [77] Perdew JP, Schmidt K. Jacob's ladder of density functional approximations for the exchange-correlation energy. *AIP Conference Proceedings*. 2001;577(1):1–20. Available from: <http://scitation.aip.org/content/aip/proceeding/aipcp/10.1063/1.1390175>.
- [78] Perdew JP, Burke K, Ernzerhof M. Generalized Gradient Approximation Made Simple. *Physical Review Letters*. 1996/10/28;77(18):3865–. Erratum [314].
- [79] Fock V. Näherungsmethode zur Lösung des quantenmechanischen Mehrkörperproblems. *Zeitschrift für Physik*. 1930;61(1-2):126–148. Available from: <http://dx.doi.org/10.1007/BF01340294>.
- [80] Slater JC. A Simplification of the Hartree-Fock Method. *Phys Rev*. 1951 Feb;81:385–390. Available from: <http://link.aps.org/doi/10.1103/PhysRev.81.385>.
- [81] Kleinman L. Relationship between Slater and Kohn-Sham exchange potentials. *Phys Rev B*. 1994 May;49:14197–14201. Available from: <http://link.aps.org/doi/10.1103/PhysRevB.49.14197>.
- [82] Becke AD. Density-functional thermochemistry. III. The role of exact exchange. *The Journal of Chemical Physics*. 1993;98(7):5648–5652. Available from: <http://scitation.aip.org/content/aip/journal/jcp/98/7/10.1063/1.464913>.
- [83] Lee C, Yang W, Parr RG. Development of the Colle-Salvetti correlation-energy formula into a functional of the electron density. *Phys Rev B*. 1988 Jan;37:785–789. Available from: <http://link.aps.org/doi/10.1103/PhysRevB.37.785>.
- [84] Vosko SH, Wilk L, Nusair M. Accurate spin-dependent electron liquid correlation energies for local spin density calculations: a critical analysis. *Canadian Journal of Physics*. 1980;58(8):1200–1211. Available from: <http://dx.doi.org/10.1139/p80-159>.
- [85] Stephens PJ, Devlin FJ, Chabalowski CF, Frisch MJ. Ab Initio Calculation of Vibrational Absorption and Circular Dichroism Spectra Using Density Functional Force Fields. *The Journal of Physical Chemistry*. 1994;98(45):11623–11627. Available from: <http://dx.doi.org/10.1021/j100096a001>.
- [86] Sólyom J. Fundamentals of the Physics of Solids: Volume 3 - Normal, Broken-Symmetry, and Correlated Systems. *Theoretical Solid State Physics: Interaction Among Electrons*. Springer Berlin Heidelberg; 2010. Available from: <https://books.google.co.uk/books?id=rL5eGGiY1WUC>.

- [87] Slater JC. Comparison of TFD and  $X\alpha$  methods for molecules and solids. International Journal of Quantum Chemistry. 1975;9(S9):7–21. Available from: <http://dx.doi.org/10.1002/qua.560090805>.
- [88] Gell-Mann M, Brueckner KA. Correlation Energy of an Electron Gas at High Density. Phys Rev. 1957 Apr;106:364–368. Available from: <http://link.aps.org/doi/10.1103/PhysRev.106.364>.
- [89] Wigner E. On the Interaction of Electrons in Metals. Phys Rev. 1934 Dec;46:1002–1011. Available from: <http://link.aps.org/doi/10.1103/PhysRev.46.1002>.
- [90] Macke W. Über die Wechselwirkungen im Fermi-Gas. Polarisationserscheinungen, Correlationsenergie, Elektronenkondensation. Zeitschrift für Naturforschung A. 1950;5a:192–208. Available from: [http://zfn.mpdl.mpg.de/data/Reihe\\_A/5/ZNA-1950-5a-0192.pdf](http://zfn.mpdl.mpg.de/data/Reihe_A/5/ZNA-1950-5a-0192.pdf).
- [91] Pines D. A Collective Description of Electron Interactions: IV. Electron Interaction in Metals. Phys Rev. 1953 Nov;92:626–636. Available from: <http://link.aps.org/doi/10.1103/PhysRev.92.626>.
- [92] Kreyszig E, Kreyszig H, Norminton EJEJ. Advanced engineering mathematics. 10th ed. Hoboken, N.J.: Wiley; 2011.
- [93] Perdew JP, Zunger A. Self-interaction correction to density-functional approximations for many-electron systems. Phys Rev B. 1981 May;23:5048–5079. Available from: <http://link.aps.org/doi/10.1103/PhysRevB.23.5048>.
- [94] Perdew JP, Wang Y. Accurate and simple analytic representation of the electron-gas correlation energy. Phys Rev B. 1992 Jun;45:13244–13249. Available from: <http://link.aps.org/doi/10.1103/PhysRevB.45.13244>.
- [95] Kent PRC. Techniques and Applications of Quantum Monte Carlo. University of Cambridge; 1999. Available from: <https://books.google.co.uk/books?id=jMjDrQEACAAJ>.
- [96] Herman F, Van Dyke JP, Ortenburger IB. Improved Statistical Exchange Approximation for Inhomogeneous Many-Electron Systems. Phys Rev Lett. 1969 Apr;22:807–811. Available from: <http://link.aps.org/doi/10.1103/PhysRevLett.22.807>.
- [97] Perdew JP. Accurate Density Functional for the Energy: Real-Space Cutoff of the Gradient Expansion for the Exchange Hole. Phys Rev Lett. 1985 Oct;55:1665–1668. Erratum [315]. Available from: <http://link.aps.org/doi/10.1103/PhysRevLett.55.1665>.
- [98] Perdew JP, Yue W. Accurate and simple density functional for the electronic exchange energy: Generalized gradient approximation. Phys Rev B. 1986 Jun;33:8800–8802. Erratum [316]. Available from: <http://link.aps.org/doi/10.1103/PhysRevB.33.8800>.

- [99] Becke AD. Density-functional exchange-energy approximation with correct asymptotic behavior. *Phys Rev A*. 1988 Sep;38:3098–3100. Available from: <http://link.aps.org/doi/10.1103/PhysRevA.38.3098>.
- [100] Herman F, Ortenburger IB, Van Dyke JP. A method for improving the physical realism of first-principles band structure calculations. *International Journal of Quantum Chemistry*. 1969;4(S3B):827–846. Available from: <http://dx.doi.org/10.1002/qua.560040746>.
- [101] Xu X, Goddard WA. The X3LYP extended density functional for accurate descriptions of nonbond interactions, spin states, and thermochemical properties. *Proceedings of the National Academy of Sciences of the United States of America*. 2004;101(9):2673–2677. Available from: <http://www.pnas.org/content/101/9/2673.abstract>.
- [102] Wang Y, Perdew JP. Correlation hole of the spin-polarized electron gas, with exact small-wave-vector and high-density scaling. *Phys Rev B*. 1991 Dec;44:13298–13307. Available from: <http://link.aps.org/doi/10.1103/PhysRevB.44.13298>.
- [103] Burke K, Perdew J, Wang Y. Derivation of a Generalized Gradient Approximation: The PW91 Density Functional. In: Dobson J, Vignale G, Das M, editors. *Electronic Density Functional Theory*. Springer US; 1998. p. 81–111. Available from: [http://dx.doi.org/10.1007/978-1-4899-0316-7\\_7](http://dx.doi.org/10.1007/978-1-4899-0316-7_7).
- [104] Perdew JP, Chevary JA, Vosko SH, Jackson KA, Pederson MR, Singh DJ, et al. Atoms, molecules, solids, and surfaces: Applications of the generalized gradient approximation for exchange and correlation. *Phys Rev B*. 1992 Sep;46:6671–6687. Available from: <http://link.aps.org/doi/10.1103/PhysRevB.46.6671>.
- [105] Xu X, Zhang Q, Muller RP, Goddard WA. An extended hybrid density functional (X3LYP) with improved descriptions of nonbond interactions and thermodynamic properties of molecular systems. *The Journal of Chemical Physics*. 2005;122(1):–. Available from: <http://scitation.aip.org/content/aip/journal/jcp/122/1/10.1063/1.1812257>.
- [106] Zhang I, Xu X. An Overview of Modern Density Functional Theory. In: *A New-Generation Density Functional*. SpringerBriefs in Molecular Science. Springer Berlin Heidelberg; 2014. p. 1–24. Available from: [http://dx.doi.org/10.1007/978-3-642-40421-4\\_1](http://dx.doi.org/10.1007/978-3-642-40421-4_1).
- [107] Perdew JP, Burke K, Ernzerhof M. Perdew, Burke, and Ernzerhof Reply:. *Physical Review Letters*. 1998/1/26;80(4):891–.
- [108] Lieb EH, Oxford S. Improved lower bound on the indirect Coulomb energy. *International Journal of Quantum Chemistry*. 1981;19(3):427–439. Available from: <http://dx.doi.org/10.1002/qua.560190306>.
- [109] Fiolhais CC, Nogueira FF, Marques MM. A primer in density functional theory. *Lecture notes in physics*. Berlin ; New York: Springer; c2003. In: 997823294401631. Available from: <http://www.springer.com/gb/>.

- [110] Zhang IY, Xu X. A New-Generation Density Functional: Towards Chemical Accuracy for Chemistry of Main Group Elements. SpringerBriefs in Molecular Science. Springer Berlin Heidelberg; 2013. Available from: <https://books.google.co.uk/books?id=1P28BAAAQBAJ>.
- [111] Pickett WE. Pseudopotential methods in condensed matter applications. Computer Physics Reports. 1989;9(3):115 – 197. Available from: <http://www.sciencedirect.com/science/article/pii/0167797789900026>.
- [112] Phillips JC, Kleinman L. New Method for Calculating Wave Functions in Crystals and Molecules. Phys Rev. 1959 Oct;116:287–294. Available from: <http://link.aps.org/doi/10.1103/PhysRev.116.287>.
- [113] Herring C. A New Method for Calculating Wave Functions in Crystals. Phys Rev. 1940 Jun;57:1169–1177. Available from: <http://link.aps.org/doi/10.1103/PhysRev.57.1169>.
- [114] Mohraz M, Lohr LL. A comparison of orthogonalized plane wave and augmented plane wave methods for calculating photodetachment cross-sections. International Journal of Quantum Chemistry. 1976;10(5):811–835. Available from: <http://dx.doi.org/10.1002/qua.560100512>.
- [115] Rostgaard C. The Projector Augmented-wave Method. ArXiv e-prints. 2009 Oct;.
- [116] Blöchl PE. Projector augmented-wave method. Phys Rev B. 1994 Dec;50:17953–17979. Available from: <https://link.aps.org/doi/10.1103/PhysRevB.50.17953>.
- [117] Holzwarth NAW, Tackett AR, Matthews GE. A Projector Augmented Wave (PAW) code for electronic structure calculations, Part I: atompaw for generating atom-centered functions. Computer Physics Communications. 2001;135(3):329–347.
- [118] Almbladh CO, von Barth U. Exact results for the charge and spin densities, exchange-correlation potentials, and density-functional eigenvalues. Phys Rev B. 1985 Mar;31:3231–3244. Available from: <http://link.aps.org/doi/10.1103/PhysRevB.31.3231>.
- [119] Hybertsen MS, Louie SG. Theory and Calculation of Quasiparticle Energies and Band Gaps. Comments Cond Mat Phys. 1987;13:223–247. Available from: [http://civet.berkeley.edu/hybertsen\\_louie\\_comments\\_on\\_cond\\_mat.pdf](http://civet.berkeley.edu/hybertsen_louie_comments_on_cond_mat.pdf).
- [120] Landau LD. The Theory of a Fermi Liquid. J Exptl Theoret Phys (USSR). 1956 Dec;30(6):1058–1064. JETP, Vol. 3, No. 6, p. 920 (December 1956). Available from: [http://www.jetp.ac.ru/cgi-bin/dn/e\\_003\\_06\\_0920.pdf](http://www.jetp.ac.ru/cgi-bin/dn/e_003_06_0920.pdf).
- [121] Landau LD. Oscillations in a Fermi Liquid. J Exptl Theoret Phys (USSR). 1957 Jan;32(1):59–66. JETP, Vol. 5, No. 1, p. 101 (July 1957). Available from: [http://www.jetp.ac.ru/cgi-bin/dn/e\\_005\\_01\\_0101.pdf](http://www.jetp.ac.ru/cgi-bin/dn/e_005_01_0101.pdf).

- [122] Galitskii VM, Migdal AB. Application of quantum field theory methods to the many body problem. *J Exptl Theoret Phys (USSR)*. 1958 Jan;34(1):139–150. JETP, Vol. 7, No. 1, p. 96 (July 1958). Available from: [http://www.jetp.ac.ru/cgi-bin/dn/e\\_007\\_01\\_0096.pdf](http://www.jetp.ac.ru/cgi-bin/dn/e_007_01_0096.pdf).
- [123] Galitskii VM. The energy spectrum of a non-ideal Fermi gas. *J Exptl Theoret Phys (USSR)*. 1958 Jan;34(1):151–162. JETP, Vol. 7, No. 1, p. 104 (July 1958). Available from: [http://www.jetp.ac.ru/cgi-bin/dn/e\\_007\\_01\\_0104.pdf](http://www.jetp.ac.ru/cgi-bin/dn/e_007_01_0104.pdf).
- [124] Hybertsen MS, Louie SG. First-Principles Theory of Quasiparticles: Calculation of Band Gaps in Semiconductors and Insulators. *Phys Rev Lett*. 1985 Sep;55:1418–1421. Available from: <http://link.aps.org/doi/10.1103/PhysRevLett.55.1418>.
- [125] Godby RW, Schlüter M, Sham LJ. Quasiparticle energies in GaAs and AlAs. *Phys Rev B*. 1987 Mar;35:4170–4171. Available from: <http://link.aps.org/doi/10.1103/PhysRevB.35.4170>.
- [126] Bimberg D, Blachnik R, Cardona M, Dean PJ, Grave T, Harbeke G, et al. Zahlenwerte und Funktionen aus Naturwissenschaften und Technik. In: Madelung O, editor. Landolt-Börnstein. vol. III. Springer-Verlag Berlin Heidelberg; 1982. Subvol. 17a. see also ref. [119]. Available from: <http://www.springer.com/gb/book/9783540106104>.
- [127] Quinn JJ, Ferrell RA. Electron Self-Energy Approach to Correlation in a Degenerate Electron Gas. *Phys Rev*. 1958 Nov;112:812–827. Available from: <http://link.aps.org/doi/10.1103/PhysRev.112.812>.
- [128] DuBois DF. Electron interactions: Part I. Field theory of a degenerate electron gas. *Annals of Physics*. 1959;7(2):174–237. Available from: <http://www.sciencedirect.com/science/article/pii/0003491659900168>.
- [129] DuBois DF. Electron interactions: Part II. Properties of a dense electron gas. *Annals of Physics*. 1959;8(1):24–77. Available from: <http://www.sciencedirect.com/science/article/pii/0003491659900624>.
- [130] Hedin L. New Method for Calculating the One-Particle Green's Function with Application to the Electron-Gas Problem. *Phys Rev*. 1965 Aug;139:A796–A823. Available from: <http://link.aps.org/doi/10.1103/PhysRev.139.A796>.
- [131] Rice TM. The effects of electron-electron interaction on the properties of metals. *Annals of Physics*. 1965;31(1):100–129. Available from: <http://www.sciencedirect.com/science/article/pii/0003491665902344>.
- [132] Lundqvist BI. Single-particle spectrum of the degenerate electron gas. *Physik der kondensierten Materie*. 1967;6(3):193–205. Available from: <http://dx.doi.org/10.1007/BF02422716>.
- [133] Lundqvist BI. Single-particle spectrum of the degenerate electron gas. *Physik der kondensierten Materie*. 1967;6(3):206–217. Available from: <http://dx.doi.org/10.1007/BF02422717>.

- [134] Lundqvist BI. Single-particle spectrum of the degenerate electron gas. *Physik der kondensierten Materie*. 1968;7(2):117–123. Available from: <http://dx.doi.org/10.1007/BF02422898>.
- [135] Hybertsen MS, Louie SG. Electron correlation and the band gap in ionic crystals. *Phys Rev B*. 1985 Nov;32:7005–7008. Available from: <http://link.aps.org/doi/10.1103/PhysRevB.32.7005>.
- [136] Hybertsen MS, Louie SG. Electron correlation in semiconductors and insulators: Band gaps and quasiparticle energies. *Phys Rev B*. 1986 Oct;34:5390–5413. Available from: <http://link.aps.org/doi/10.1103/PhysRevB.34.5390>.
- [137] Godby RW, Schlüter M, Sham LJ. Accurate Exchange-Correlation Potential for Silicon and Its Discontinuity on Addition of an Electron. *Phys Rev Lett*. 1986 Jun;56:2415–2418. Available from: <http://link.aps.org/doi/10.1103/PhysRevLett.56.2415>.
- [138] Godby RW, Schlüter M, Sham LJ. Trends in self-energy operators and their corresponding exchange-correlation potentials. *Phys Rev B*. 1987 Oct;36:6497–6500. Available from: <http://link.aps.org/doi/10.1103/PhysRevB.36.6497>.
- [139] Godby RW, Schlüter M, Sham LJ. Self-energy operators and exchange-correlation potentials in semiconductors. *Phys Rev B*. 1988 Jun;37:10159–10175. Available from: <http://link.aps.org/doi/10.1103/PhysRevB.37.10159>.
- [140] Aryasetiawan F, Gunnarsson O. The GW method. *Reports on Progress in Physics*. 1998 mar;61:237–312. Provided by the SAO/NASA Astrophysics Data System. Available from: <http://adsabs.harvard.edu/abs/1998RPPh...61..237A>.
- [141] Mahan GD, Sernelius BE. Electron-electron interactions and the bandwidth of metals. *Phys Rev Lett*. 1989 Jun;62:2718–2720. Available from: <http://link.aps.org/doi/10.1103/PhysRevLett.62.2718>.
- [142] Frota HO, Mahan GD. Band tails and bandwidth in simple metals. *Phys Rev B*. 1992 Mar;45:6243–6246. Available from: <http://link.aps.org/doi/10.1103/PhysRevB.45.6243>.
- [143] Peskin ME, Schroeder DV. An Introduction To Quantum Field Theory. Addison-Wesley Publishing Company; 1995.
- [144] March NH. Electron Correlation in Molecules and Condensed Phases. 1st ed. Physics of Solids and Liquids. Springer US; 1996. Available from: <http://www.springer.com/gp/book/9780306448447>.
- [145] Abrikosov AA, Gor'kov LP, Dzyaloshinskii IY. Quantum field theoretical methods in statistical physics. International series of monographs in natural philosophy. Pergamon Press; 1965. Available from: <https://books.google.co.uk/books?id=J6rvAAAAMAAJ>.
- [146] Mahan GD. Many-Particle Physics. Physics of Solids and Liquids. Springer; 2000. Available from: <https://books.google.co.uk/books?id=xzSgZ4-yyMEC>.

- [147] Rieger MM, Steinbeck L, White ID, Rojas HN, Godby RW. The {GW} space-time method for the self-energy of large systems. Computer Physics Communications. 1999;117(3):211–228. Available from: <http://www.sciencedirect.com/science/article/pii/S001046559800174X>.
- [148] Valentin CD, Botti S, Cococcioni M, editors. First Principles Approaches to Spectroscopic Properties of Complex Materials. vol. 347 of Topics in Current Chemistry. Springer; 2014. Available from: <http://link.springer.com/book/10.1007/978-3-642-55068-3>.
- [149] Bohm D, Pines D. A Collective Description of Electron Interactions. I. Magnetic Interactions. Phys Rev. 1951 Jun;82:625–634. Available from: <http://link.aps.org/doi/10.1103/PhysRev.82.625>.
- [150] Pines D, Bohm D. A Collective Description of Electron Interactions: II. Collective vs Individual Particle Aspects of the Interactions. Phys Rev. 1952 Jan;85:338–353. Available from: <http://link.aps.org/doi/10.1103/PhysRev.85.338>.
- [151] Bohm D, Pines D. A Collective Description of Electron Interactions: III. Coulomb Interactions in a Degenerate Electron Gas. Phys Rev. 1953 Nov;92:609–625. Available from: <http://link.aps.org/doi/10.1103/PhysRev.92.609>.
- [152] Dyson FJ. The  $S$  Matrix in Quantum Electrodynamics. Phys Rev. 1949 Jun;75:1736–1755. Available from: <http://link.aps.org/doi/10.1103/PhysRev.75.1736>.
- [153] Schwinger J. On the Green's Functions of Quantized Fields. I. Proceedings of the National Academy of Science. 1951 jul;37:452–455.
- [154] Dickhoff WH, Van Neck D. Many-body Theory Exposed!: Propagator Description of Quantum Mechanics in Many-body Systems. World Scientific; 2008. Available from: <https://books.google.co.uk/books?id=XcnRa57zEPEC>.
- [155] Marzari N, Mostofi AA, Yates JR, Souza I, Vanderbilt D. Maximally localized Wannier functions: Theory and applications. Rev Mod Phys. 2012 Oct;84:1419–1475. Available from: <http://link.aps.org/doi/10.1103/RevModPhys.84.1419>.
- [156] Kittel C. Introduction to solid state physics. 7th ed. New York ; Chichester: Wiley; 1996. GB9663760 bnb2431Charles Kittel.ill. ; 25cm.Previous ed.: 1986.Includes index.Tables on lining papers.
- [157] Wannier GH. The Structure of Electronic Excitation Levels in Insulating Crystals. Phys Rev. 1937 Aug;52:191–197. Available from: <http://link.aps.org/doi/10.1103/PhysRev.52.191>.
- [158] Wannier GH. Dynamics of Band Electrons in Electric and Magnetic Fields. Rev Mod Phys. 1962 Oct;34:645–655. Available from: <http://link.aps.org/doi/10.1103/RevModPhys.34.645>.

- [159] Kohn W. Analytic Properties of Bloch Waves and Wannier Functions. *Phys Rev.* 1959 Aug;115:809–821. Available from: <http://link.aps.org/doi/10.1103/PhysRev.115.809>.
- [160] Boys SF. Construction of Some Molecular Orbitals to Be Approximately Invariant for Changes from One Molecule to Another. *Rev Mod Phys.* 1960 Apr;32:296–299. Available from: <http://link.aps.org/doi/10.1103/RevModPhys.32.296>.
- [161] Boys SF. Localized Orbitals and Localized Adjustment Functions. In: Löwdin PO, editor. *Quantum Theory of Atoms, Molecules, and the Solid State: a tribute to John C. Slater*. Academic Press, New York; 1966. p. 253.
- [162] Foster JM, Boys SF. Canonical Configurational Interaction Procedure. *Rev Mod Phys.* 1960 Apr;32:300–302. Available from: <http://link.aps.org/doi/10.1103/RevModPhys.32.300>.
- [163] Foster JM, Boys SF. A Quantum Variational Calculation for HCHO. *Rev Mod Phys.* 1960 Apr;32:303–304. Available from: <http://link.aps.org/doi/10.1103/RevModPhys.32.303>.
- [164] Edmiston C, Ruedenberg K. Localized Atomic and Molecular Orbitals. *Rev Mod Phys.* 1963 Jul;35:457–464. Available from: <http://link.aps.org/doi/10.1103/RevModPhys.35.457>.
- [165] Marzari N, Vanderbilt D. Maximally localized generalized Wannier functions for composite energy bands. *Phys Rev B.* 1997 Nov;56:12847–12865. Available from: <http://link.aps.org/doi/10.1103/PhysRevB.56.12847>.
- [166] Blount EI. Formalisms of Band Theory. In: Seitz F, Turnbull D, editors. *Solid State Physics, Advances in Research and Applications*. vol. 13 of *Solid State Physics*. Academic Press; 1962. p. 305 – 373. Available from: <http://www.sciencedirect.com/science/article/pii/S0081194708604592>.
- [167] Souza I, Marzari N, Vanderbilt D. Maximally localized Wannier functions for entangled energy bands. *Phys Rev B.* 2001 Dec;65:035109. Available from: <http://link.aps.org/doi/10.1103/PhysRevB.65.035109>.
- [168] Podberezskaya NV, Magarill SA, Pervukhina NV, Borisov SV. Crystal Chemistry of Dichalcogenides MX<sub>2</sub>. *Journal of Structural Chemistry.* 2001/7/1;42(4):654–681.
- [169] Wilson JA, Yoffe AD. The transition metal dichalcogenides discussion and interpretation of the observed optical, electrical and structural properties. *Advances in Physics.* 1969;18(73):193–335.
- [170] Mak KF, Lee C, Hone J, Shan J, Heinz TF. Atomically Thin MoS<sub>2</sub>: A New Direct-Gap Semiconductor. *Physical Review Letters.* 2010/9/24;105(13):136805–.
- [171] Alexiev V, Prins R, Weber T. *Ab initio* study of MoS<sub>2</sub> and Li adsorbed on the (10̄10) face of MoS<sub>2</sub>. *Phys Chem Chem Phys.* 2000;2:1815–1827. Available from: <http://dx.doi.org/10.1039/A909293E>.

- [172] Schönfeld B, Huang JJ, Moss SC. Anisotropic mean-square displacements (MSD) in single-crystals of 2H- and 3R-MoS<sub>2</sub>. *Acta Crystallographica Section B*. 1983 Aug;39(4):404–407. doi:10.1107/S0108768183002645. Available from: <http://dx.doi.org/10.1107/S0108768183002645>.
- [173] Hahn T, editor. International Tables for Crystallography. vol. A. Space-group symmetry. 5th ed. Wiley; 2005.
- [174] Benavente E, Ana MAS, Mendizábal F, González G. Intercalation chemistry of molybdenum disulfide. *Coordination Chemistry Reviews*. 2002;224(1-2):87 – 109. Available from: <http://www.sciencedirect.com/science/article/pii/S0010854501003927>.
- [175] Dungey KE, Curtis MD, Penner-Hahn JE. Structural Characterization and Thermal Stability of MoS<sub>2</sub> Intercalation Compounds. *Chemistry of Materials*. 1998;10(8):2152–2161. Available from: <http://dx.doi.org/10.1021/cm980034u>.
- [176] Calandra M. Chemically exfoliated single-layer MoS<sub>2</sub>: Stability, lattice dynamics, and catalytic adsorption from first principles. *Phys Rev B*. 2013 Dec;88:245428. Available from: <http://link.aps.org/doi/10.1103/PhysRevB.88.245428>.
- [177] Frondel JW, Wickman FE. Molybdenite polytypes in theory and occurrence. II. Some naturally-occurring polytypes of molybdenite. *AmMineral*. 1970;55:1857–1875.
- [178] Miller WH. A Treatise on Crystallography. For J. & J. J. Deighton; 1839. Available from: <http://books.google.co.uk/books?id=MDcAAAAQAAJ>.
- [179] Raghavan V. Materials Science and Engineering: A First Course. vol. 5. Prentice-Hall; 2006/7.
- [180] Momma K. Visualisation for Electronic and STructural Analysis (VESTA). JP-Minerals; 2015. Accessed: 2015-05-25. Online. Available from: <http://jp-minerals.org/vesta/en/>.
- [181] Sólyom J, Piróth A. Fundamentals of the physics of solids. Volume I, Structure and dynamics. vol. 1. Springer; 2007.
- [182] Ewald PP, Hermann C. Strukturbericht, 1913-1928. *Zeitschrift für Kristallographie, Kristallgeometrie, Kristallphysik, Kristallchemie*. Akademische Verlagsgesellschaft; 1931. Available from: <https://books.google.co.uk/books?id=Na2mQAAACAAJ>.
- [183] Wyckoff RWG. Crystal Structures. No. 1 in Crystal Structures. Wiley; 1963. Available from: <https://books.google.co.uk/books?id=40uGpwAACAAJ>.
- [184] Hulliger F. Structural Chemistry of Layer-Type Phases. In: Lévy F, editor. Physics and Chemistry of Materials with Layered Structures. 5. Springer Netherlands; 1976. p. 237. Available from: <http://dx.doi.org/10.1007/978-94-010-1146-4>.

- [185] Ernst T. Zahlenwerte und Funktionen, Kristalle. In: Bartels J, Börnstein R, Landolt H, editors. Landolt-Börnstein. vol. Bd. 1, Teil 4. Springer-Verlag Berlin Heidelberg; 1955. p. 34. See also ref. [168].
- [186] Villars P, Cenzual K, Daams J, Gladyshevskii R, Shcherban O, Dubenskyy V, et al. 19. In: Villars P, Cenzual K, editors. MoS<sub>2</sub>. vol. 43A3 of Landolt-Börnstein - Group III Condensed Matter. Springer Berlin Heidelberg; 2006. p. 1–1.
- [187] Setyawan W, Curtarolo S. High-throughput electronic band structure calculations: Challenges and tools. Computational Materials Science. 2010/8;49(2):299–312.
- [188] Liu D, Chen X, Li D, Wang F, Luo X, Yang B. Simulation of MoS<sub>2</sub> crystal structure and the experimental study of thermal decomposition. Journal of Molecular Structure. 2010;980(1–3):66 – 71. Available from: <http://www.sciencedirect.com/science/article/pii/S0022286010005478>.
- [189] M-K-Impex-Canada. Lower-Friction, editor. Comparison between Molybdenum Disulfide (MoS<sub>2</sub>) & Tungsten Disulfide (WS<sub>2</sub>). M K Impex Canada; 2011. Accessed: 2011-05-25. <http://www.lowerfriction.com/pdf/8.pdf>.
- [190] Tsigdinos GA. Inorganic sulfur compounds of molybdenum and tungsten. In: Tsigdinos GA, Moh GH, editors. Aspects of Molybdenum and Related Chemistry. vol. 76. Springer-Verlag Berlin Heidelberg; 1978. p. 65–105.
- [191] Song I, Park C, Choi HC. Synthesis and properties of molybdenum disulphide: from bulk to atomic layers. RSC Adv. 2015;5:7495–7514. Available from: <http://dx.doi.org/10.1039/C4RA11852A>.
- [192] Savage RH. Graphite Lubrication. Journal of Applied Physics. 1948;19(1):1–10. Available from: <http://scitation.aip.org/content/aip/journal/jap/19/1/10.1063/1.1697867>.
- [193] Bryant PJ, Gutshall PL, Taylor LH. A study of mechanisms of graphite friction and wear. Wear. 1964;7(1):118 – 126. Available from: <http://www.sciencedirect.com/science/article/pii/0043164864900833>.
- [194] Moore DF. Principles and applications of tribology. vol. 14 of International series in materials science and technology. 1st ed. Oxford: Pergamon; 1975.
- [195] Dickinson RG, Pauling L. The crystal structure of molybdenite. Journal of the American Chemical Society. 1923;45(6):1466–1471. Available from: <http://dx.doi.org/10.1021/ja01659a020>.
- [196] Winer WO. Molybdenum disulfide as a lubricant: A review of the fundamental knowledge. Wear. 1967;10(6):422 – 452. Available from: <http://www.sciencedirect.com/science/article/pii/0043164867901871>.
- [197] Holinski R, Gänshimer J. A study of the lubricating mechanism of molybdenum disulfide. Wear. 1972;19(3):329 – 342. Available from: <http://www.sciencedirect.com/science/article/pii/004316487290124X>.

- [198] Savan A, Pflüger E, Voumard P, Schröer A, Simmonds M. Modern solid lubrication: Recent developments and applications of MoS<sub>2</sub>. *Lubrication Science*. 2000;12(2):185–203. Available from: <http://dx.doi.org/10.1002/ls.3010120206>.
- [199] Du G, Guo Z, Wang S, Zeng R, Chen Z, Liu H. Superior stability and high capacity of restacked molybdenum disulfide as anode material for lithium ion batteries. *Chemical Communications*. 2010;46(7):1106–1108.
- [200] Ataca C, Sahin E, Aktürk E, Ciraci S. Mechanical and Electronic Properties of MoS<sub>2</sub> Nanoribbons and Their Defects. *The Journal of Physical Chemistry C*. 2011/2/20;115(10):3934–3941. Doi: 10.1021/jp1115146.
- [201] Botello-Méndez R A, López-Urías F, Terrones M, Terrones H. Metallic and ferromagnetic edges in molybdenum disulfide nanoribbons. *Nanotechnology*. 2009;20(32):325703–.
- [202] Suzuki R, Sakano M, Zhang Y, Akashi R, Morikawa D, Harasawa A, et al. Valley-dependent spin polarization in bulk MoS<sub>2</sub> with broken inversion symmetry. *Nature nanotechnology*. 2014;9(8):611–617.
- [203] Hooley JG. Elements. In: Lieth R, editor. Preparation and crystal growth of materials with layered structures. Springer; 1977. p. 1–33.
- [204] Koehler W, inventor; William Koehler, assignee. Antifriction And Antiabrasive Metal. US 1714564 A; 1929. Available from: [https://www.lens.org/lens/patent/US\\_1714564\\_A](https://www.lens.org/lens/patent/US_1714564_A).
- [205] Stubbles JR, Richardson FD. Equilibria in the system molybdenum + sulphur + hydrogen. *Trans Faraday Soc*. 1960;56:1460–1466. Available from: <http://dx.doi.org/10.1039/TF9605601460>.
- [206] Prasad TP, Diemann E, Müller A. Thermal decomposition of (NH<sub>4</sub>)<sub>2</sub>MoO<sub>2</sub>S<sub>2</sub>, (NH<sub>4</sub>)<sub>2</sub>MoS<sub>4</sub>, (NH<sub>4</sub>)<sub>2</sub>WO<sub>2</sub>S<sub>2</sub> and (NH<sub>4</sub>)<sub>2</sub>WS<sub>4</sub>. *Journal of Inorganic and Nuclear Chemistry*. 1973;35(6):1895 – 1904. Available from: <http://www.sciencedirect.com/science/article/pii/0022190273801241>.
- [207] Bell RE, Herfert RE. Preparation and Characterization of a New Crystalline Form of Molybdenum Disulfide. *Journal of the American Chemical Society*. 1957;79(13):3351–3354. Available from: <http://dx.doi.org/10.1021/ja01570a012>.
- [208] Silverman MS. Ultrahigh pressure-high temperature synthesis of rhombohedral dichalcogenides of molybdenum and tungsten. *Inorganic Chemistry*. 1967;6(5):1063–1064. Available from: <http://dx.doi.org/10.1021/ic50051a047>.
- [209] Wildervanck JC, Jellinek F. Preparation and Crystallinity of Molybdenum and Tungsten Sulfides. *Zeitschrift für anorganische und allgemeine Chemie*. 1964;328(5-6):309–318. Available from: <http://dx.doi.org/10.1002/zaac.19643280514>.

- [210] Li Q, Newberg JT, Walter EC, Hemminger JC, Penner RM. Polycrystalline Molybdenum Disulfide (2H-MoS<sub>2</sub>) Nano- and Microribbons by Electrochemical/Chemical Synthesis. *Nano Letters*. 2004;4(2):277–281.
- [211] Kresse G, Hafner J. *Ab initio* molecular dynamics for liquid metals. *Phys Rev B*. 1993 Jan;47:558–561. Available from: <http://link.aps.org/doi/10.1103/PhysRevB.47.558>.
- [212] Kresse G, Hafner J. *Ab initio* molecular-dynamics simulation of the liquid-metal–amorphous-semiconductor transition in germanium. *Phys Rev B*. 1994 May;49:14251–14269. Available from: <http://link.aps.org/doi/10.1103/PhysRevB.49.14251>.
- [213] Kresse G, Furthmüller J. Efficiency of ab-initio total energy calculations for metals and semiconductors using a plane-wave basis set. *Computational Materials Science*. 1996;6(1):15 – 50. Available from: <http://www.sciencedirect.com/science/article/pii/0927025696000080>.
- [214] Kresse G, Furthmüller J. Efficient iterative schemes for *ab initio* total-energy calculations using a plane-wave basis set. *Phys Rev B*. 1996 Oct;54:11169–11186. Available from: <http://link.aps.org/doi/10.1103/PhysRevB.54.11169>.
- [215] Soler JM, Artacho E, Gale JD, García A, Junquera J, Ordejón P, et al. The SIESTA method for ab initio order- N materials simulation. *Journal of Physics: Condensed Matter*. 2002;14(11):2745. Available from: <http://stacks.iop.org/0953-8984/14/i=11/a=302>.
- [216] Wavefunction INC. Spartan software. Wavefunction Inc.; 2015. Accessed: 2015-05-25. Online. Available from: <http://wavefun.com/products/spartan.html>.
- [217] Giannozzi P, Baroni S, Bonini N, Calandra M, Car R, Cavazzoni C, et al. QUANTUM ESPRESSO: a modular and open-source software project for quantum simulations of materials. *Journal of Physics: Condensed Matter*. 2009;21(39):395502. Available from: <http://stacks.iop.org/0953-8984/21/i=39/a=395502>.
- [218] Clark SJ, Segall MD, Pickard CJ, Hasnip PJ, Probert MJ, Refson K, et al. First principles methods using CASTEP. *Zeitschrift für Kristallographie – Crystalline Materials*. 2005;220(5/6):567–570. Available from: <https://doi.org/10.1524/zkri.220.5.567.65075>.
- [219] Young DC. Appendix A: Software Packages. In: *Computational Chemistry: A Practical Guide for Applying Techniques to Real World Problems*. John Wiley & Sons, Inc.; 2002. p. 322–359. Available from: <http://dx.doi.org/10.1002/0471220655.app1>.
- [220] Gonze X, Beuken JM, Caracas R, Detraux F, Fuchs M, Rignanese GM, et al. First-principles computation of material properties: the {ABINIT} software project. *Computational Materials Science*. 2002;25(3):478 – 492. Available from: <http://www.sciencedirect.com/science/article/pii/S0927025602003257>.

- [221] Gonze X, Rignanese G, Verstraete M, Betiken J, Pouillon Y, Caracas R, et al. A brief introduction to the ABINIT software package. *Zeitschrift für Kristallographie(Special issue on Computational Crystallography)*. 2005;220:558–562.
- [222] Gonze X, Amadon B, Anglade PM, Beuken JM, Bottin F, Boulanger P, et al. ABINIT: First-principles approach to material and nanosystem properties. *Computer Physics Communications*. 2009/12;180(12):2582–2615. Available from: <http://www.sciencedirect.com/science/article/pii/S0010465509002276>.
- [223] Torrent M, Jollet F, Bottin F, Zérah G, Gonze X. Implementation of the projector augmented-wave method in the {ABINIT} code: Application to the study of iron under pressure. *Computational Materials Science*. 2008;42(2):337 – 351. Available from: <http://www.sciencedirect.com/science/article/pii/S0927025607002108>.
- [224] Lejaeghere K, Bihlmayer G, Björkman T, Blaha P, Blügel S, Blum V, et al. Reproducibility in density functional theory calculations of solids. *Science*. 2016;351(6280). Available from: <http://science.sciencemag.org/content/351/6280/aad3000>.
- [225] Mortensen JJ, Hansen LB, Jacobsen KW. Real-space grid implementation of the projector augmented wave method. *Phys Rev B*. 2005 Jan;71:035109. Available from: <https://link.aps.org/doi/10.1103/PhysRevB.71.035109>.
- [226] Enkovaara Je, Rostgaard C, Mortensen JJ, Chen J, Dułak M, Ferrighi L, et al. Electronic structure calculations with GPAW: a real-space implementation of the projector augmented-wave method. *Journal of Physics: Condensed Matter*. 2010;22(25):253202.
- [227] Payne MC, Teter MP, Allan DC, Arias TA, Joannopoulos JD. Iterative minimization techniques for *ab initio* total-energy calculations: molecular dynamics and conjugate gradients. *Rev Mod Phys*. 1992 Oct;64:1045–1097. Available from: <http://link.aps.org/doi/10.1103/RevModPhys.64.1045>.
- [228] Gonze X. First-principles responses of solids to atomic displacements and homogeneous electric fields: Implementation of a conjugate-gradient algorithm. *Phys Rev B*. 1997 Apr;55:10337–10354. Available from: <http://link.aps.org/doi/10.1103/PhysRevB.55.10337>.
- [229] Gonze X, Lee C. Dynamical matrices, Born effective charges, dielectric permittivity tensors, and interatomic force constants from density-functional perturbation theory. *Phys Rev B*. 1997 Apr;55:10355–10368. Available from: <http://link.aps.org/doi/10.1103/PhysRevB.55.10355>.
- [230] Hamann DR, Wu X, Rabe KM, Vanderbilt D. Metric tensor formulation of strain in density-functional perturbation theory. *Phys Rev B*. 2005 Jan;71:035117. Available from: <http://link.aps.org/doi/10.1103/PhysRevB.71.035117>.
- [231] Fuchs M, Scheffler M. Ab initio pseudopotentials for electronic structure calculations of poly-atomic systems using density-functional theory. *Computer Physics Communications*. 1999/6/1;119(1):67–98. Available from: <http://www.sciencedirect.com/science/article/pii/S001046559800201X>.

- [232] Veithen M, Gonze X, Ghosez P. Nonlinear optical susceptibilities, Raman efficiencies, and electro-optic tensors from first-principles density functional perturbation theory. *Phys Rev B*. 2005 Mar;71:125107. Available from: <http://link.aps.org/doi/10.1103/PhysRevB.71.125107>.
- [233] Lee C, Gonze X. *Ab initio* calculation of the thermodynamic properties and atomic temperature factors of SiO<sub>2</sub>  $\alpha$ -quartz and stishovite. *Phys Rev B*. 1995 Apr;51:8610–8613. Available from: <http://link.aps.org/doi/10.1103/PhysRevB.51.8610>.
- [234] Bruneval F, Vast N, Reining L. Effect of self-consistency on quasiparticles in solids. *Phys Rev B*. 2006 Jul;74:045102. Available from: <http://link.aps.org/doi/10.1103/PhysRevB.74.045102>.
- [235] Bruneval F, Gonze X. Accurate *GW* self-energies in a plane-wave basis using only a few empty states: Towards large systems. *Phys Rev B*. 2008 Aug;78:085125. Available from: <http://link.aps.org/doi/10.1103/PhysRevB.78.085125>.
- [236] Bottin F, Leroux S, Knyazev A, Zérah G. Large-scale ab initio calculations based on three levels of parallelization. *Computational Materials Science*. 2008;42(2):329 – 336. Available from: <http://www.sciencedirect.com/science/article/pii/S0927025607002091>.
- [237] Amadon B, Jollet F, Torrent M.  $\gamma$  and  $\beta$  cerium: LDA + U calculations of ground-state parameters. *Phys Rev B*. 2008 Apr;77:155104. Available from: <http://link.aps.org/doi/10.1103/PhysRevB.77.155104>.
- [238] Anglade PM, Gonze X. Preconditioning of self-consistent-field cycles in density-functional theory: The extrapolar method. *Phys Rev B*. 2008 Jul;78:045126. Available from: <http://link.aps.org/doi/10.1103/PhysRevB.78.045126>.
- [239] Caliste D, Pouillon Y, Verstraete MJ, Olevano V, Gonze X. Sharing electronic structure and crystallographic data with ETSF\_IO. *Computer Physics Communications*. 2008;179(10):748 – 758. Available from: <http://www.sciencedirect.com/science/article/pii/S0010465508001963>.
- [240] Goedecker S. Fast Radix 2, 3, 4, and 5 Kernels for Fast Fourier Transformations on Computers with Overlapping Multiply–Add Instructions. *SIAM Journal on Scientific Computing*. 1997;18(6):1605–1611. Available from: <http://dx.doi.org/10.1137/S1064827595281940>.
- [241] Gonze X. Towards a potential-based conjugate gradient algorithm for order-  $N$  self-consistent total energy calculations. *Phys Rev B*. 1996 Aug;54:4383–4386. Available from: <http://link.aps.org/doi/10.1103/PhysRevB.54.4383>.
- [242] Troullier N, Martins JL. Efficient pseudopotentials for plane-wave calculations. *Phys Rev B*. 1991 Jan;43:1993–2006. Available from: <http://link.aps.org/doi/10.1103/PhysRevB.43.1993>.
- [243] Gonze X, Stumpf R, Scheffler M. Analysis of separable potentials. *Phys Rev B*. 1991 Oct;44:8503–8513. Available from: <http://link.aps.org/doi/10.1103/PhysRevB.44.8503>.

- [244] Hartwigsen C, Goedecker S, Hutter J. Relativistic separable dual-space Gaussian pseudopotentials from H to Rn. *Phys Rev B*. 1998 Aug;58:3641–3662. Available from: <http://link.aps.org/doi/10.1103/PhysRevB.58.3641>.
- [245] Hamann DR. Optimized norm-conserving Vanderbilt pseudopotentials. *Phys Rev B*. 2013 Aug;88:085117. Available from: <https://link.aps.org/doi/10.1103/PhysRevB.88.085117>.
- [246] Dellaripa N, Harris D, Xu X, Holzwarth NAW. Periodic Table of the Elements for PAW Functions. Dept. of Physics, Wake Forest University; 2009. Accessed: 2011-06-25. Online. Available from: <http://users.wfu.edu/natalie/papers/pwpaw/periodictable/periodictable.html>.
- [247] Murnaghan FD. The Compressibility of Media under Extreme Pressures. *Proceedings of the National Academy of Sciences*. 1944;30(9):244–247.
- [248] Morse PM. Diatomic Molecules According to the Wave Mechanics. II. Vibrational Levels. *Physical Review*. 1929;34(1):57–64. PR.
- [249] Lee YS, Nardelli MB, Marzari N. Band Structure and Quantum Conductance of Nanostructures from Maximally Localized Wannier Functions: The Case of Functionalized Carbon Nanotubes. *Phys Rev Lett*. 2005 Aug;95:076804. Available from: <http://link.aps.org/doi/10.1103/PhysRevLett.95.076804>.
- [250] Mostofi AA, Yates JR, Lee YS, Souza I, Vanderbilt D, Marzari N. wannier90: A tool for obtaining maximally-localised Wannier functions. *Computer Physics Communications*. 2008;178(9):685–699.
- [251] Quinion M. Garbage in, garbage out. World Wide Words; 2005. Accessed: 2015-05-17. Online. Available from: <http://www.worldwidewords.org/qa/qa-gar1.htm>.
- [252] Monkhorst HJ, Pack JD. Special points for Brillouin-zone integrations. *Physical Review B*. 1976;13(12):5188–5192. PRB.
- [253] Goedecker S, Teter M, Hutter J. Separable dual-space Gaussian pseudopotentials. *Physical Review B*. 1996;54(3):1703–1710. PRB.
- [254] Nocedal J, Wright SJ. Numerical optimization. 2nd ed. Springer series in operations research. New York: Springer; c2006.
- [255] Schlegel HB. Optimization of equilibrium geometries and transition structures. *Journal of Computational Chemistry*. 1982;3(2):214–218.
- [256] Allen P, Tildesley DJ. Computer simulation of liquids. Oxford science publications. Clarendon Press; 1987. Available from: <http://books.google.co.uk/books?id=ibURAQAAIAAJ>.
- [257] Cho JH, Scheffler M. Ab *initio* pseudopotential study of Fe, Co, and Ni employing the spin-polarized LAPW approach. *Phys Rev B*. 1996 Apr;53:10685–10689. Available from: <https://link.aps.org/doi/10.1103/PhysRevB.53.10685>.

- [258] Böker T, Severin R, Müller A, Janowitz C, Manzke R, VoßD, et al. Band structure of MoS<sub>2</sub>, MoSe<sub>2</sub>, and alpha -MoTe<sub>2</sub>: Angle-resolved photoelectron spectroscopy and ab initio calculations. *Physical Review B*. 2001/11/15;64(23):235305–.
- [259] Kadantsev ES, Hawrylak P. Electronic structure of a single MoS<sub>2</sub> monolayer. *Solid State Communications*. 2012;152(10):909 – 913. Available from: <http://www.sciencedirect.com/science/article/pii/S0038109812000889>.
- [260] Joensen P, Crozier ED, Alberding N, Frindt RF. A study of single-layer and restacked MoS<sub>2</sub> by X-ray diffraction and X-ray absorption spectroscopy. *Journal of Physics C: Solid State Physics*. 1987;20(26):4043. Available from: <http://stacks.iop.org/0022-3719/20/i=26/a=009>.
- [261] Heda NL, Dashora A, Marwal A, Sharma Y, Srivastava SK, Ahmed G, et al. Electronic properties and Compton profiles of molybdenum dichalcogenides. *Journal of Physics and Chemistry of Solids*. 2010;71(3):187–193.
- [262] Ataca C, Ciraci S. Functionalization of Single-Layer MoS<sub>2</sub> Honeycomb Structures. *The Journal of Physical Chemistry C*. 2011/6/1;115(27):13303–13311. Doi: 10.1021/jp2000442.
- [263] Mattheiss LF. Band Structures of Transition-Metal-Dichalcogenide Layer Compounds. *Physical Review B*. 1973;8(8):3719–3740. PRB.
- [264] Heyd J, Scuseria GE, Ernzerhof M. Hybrid functionals based on a screened Coulomb potential. *The Journal of Chemical Physics*. 2003;118(18):8207–8215.
- [265] Kam KK, Parkinson BA. Detailed photocurrent spectroscopy of the semiconducting group VIB transition metal dichalcogenides. *The Journal of Physical Chemistry*. 1982;86(4):463–467.
- [266] Faleev SV, van Schilfgaarde M, Kotani T. All-Electron Self-Consistent GW Approximation: Application to Si, MnO, and NiO. *Physical Review Letters*. 2004;93(12):126406. PRL.
- [267] Godby RW, Needs RJ. Metal-insulator transition in Kohn-Sham theory and quasi-particle theory. *Physical Review Letters*. 1989;62(10):1169–1172. PRL.
- [268] Disko MM, Treacy MMJ, Rice SB, Chianelli RR, Gland JA, Halbert TR, et al. Spatially resolved electron energy-loss spectroscopy of MoS<sub>2</sub> platelets. *Ultramicroscopy*. 1987;23(3–4):313–319.
- [269] Becke AD. A new mixing of Hartree–Fock and local density-functional theories. *The Journal of Chemical Physics*. 1993;98(2):1372–1377.
- [270] Fleischauer PD, Lince JR, Bertrand PA, Bauer R. Electronic structure and lubrication properties of molybdenum disulfide: a qualitative molecular orbital approach. *Langmuir*. 1989;5(4):1009–1015. Available from: <http://dx.doi.org/10.1021/la00088a022>.

- [271] Lebègue S, Eriksson O. Electronic structure of two-dimensional crystals from ab initio theory. *Physical Review B*. 2009;79(11):115409. PRB.
- [272] Yue Q, Kang J, Shao Z, Zhang X, Chang S, Wang G, et al. Mechanical and electronic properties of monolayer MoS<sub>2</sub> under elastic strain. *Physics Letters A*. 2012;376(12-13):1166–1170.
- [273] Li T. Ideal strength and phonon instability in single-layer MoS<sub>2</sub>. *Phys Rev B*. 2012 Jun;85:235407. Available from: <https://link.aps.org/doi/10.1103/PhysRevB.85.235407>.
- [274] Scalise E, Houssa M, Pourtois G, Afanas'ev V, Stesmans A. Strain-induced semiconductor to metal transition in the two-dimensional honeycomb structure of MoS<sub>2</sub>. *Nano Research*. 2012;5(1):43–48. Available from: <http://dx.doi.org/10.1007/s12274-011-0183-0>.
- [275] Kumar A, Ahluwalia PK. A first principle Comparative study of electronic and optical properties of 1H – MoS<sub>2</sub> and 2H – MoS<sub>2</sub>. *Materials Chemistry and Physics*. 2012;135(2-3):755–761. Available from: <http://www.sciencedirect.com/science/article/pii/S0254058412005159>.
- [276] Ataca C, Topsakal M, Aktürk E, Ciraci S. A Comparative Study of Lattice Dynamics of Three- and Two-Dimensional MoS<sub>2</sub>. *The Journal of Physical Chemistry C*. 2011;115(33):16354–16361.
- [277] Grimme S. Semiempirical GGA-type density functional constructed with a long-range dispersion correction. *Journal of Computational Chemistry*. 2006;27(15):1787–1799. Available from: <http://dx.doi.org/10.1002/jcc.20495>.
- [278] Dion M, Rydberg H, Schröder E, Langreth DC, Lundqvist BI. Van der Waals Density Functional for General Geometries. *Phys Rev Lett*. 2004 Jun;92:246401. Available from: <https://link.aps.org/doi/10.1103/PhysRevLett.92.246401>.
- [279] Song YL, Zhang Y, Zhang JM, Lu DB. Effects of the edge shape and the width on the structural and electronic properties of silicene nanoribbons. *Applied Surface Science*. 2010;256(21):6313 – 6317. Available from: <http://www.sciencedirect.com/science/article/pii/S0169433210005052>.
- [280] Li H, Dai J, Li J, Zhang S, Zhou J, Zhang L, et al. Electronic Structures and Magnetic Properties of GaN Sheets and Nanoribbons. *The Journal of Physical Chemistry C*. 2010;114(26):11390–11394. Available from: <http://dx.doi.org/10.1021/jp1024558>.
- [281] Pan L, Liu HJ, Tan XJ, Lv HY, Shi J, Tang XF, et al. Thermoelectric properties of armchair and zigzag silicene nanoribbons. *Phys Chem Chem Phys*. 2012;14:13588–13593. Available from: <http://dx.doi.org/10.1039/C2CP42645E>.
- [282] Kang J, Wu F, Li J. Symmetry-dependent transport properties and magnetoresistance in zigzag silicene nanoribbons. *Applied Physics Letters*. 2012;100(23). Available from: <http://scitation.aip.org/content/aip/journal/apl/100/23/10.1063/1.4726276>.

- [283] Chai GL, Lin CS, Cheng WD. Structure dependent electronic and magnetic properties of graphitic GaN-ZnO nanoribbons. *J Mater Chem*. 2012;22:7708–7711. Available from: <http://dx.doi.org/10.1039/C2JM30441D>.
- [284] Lin Y, Connell JW. Advances in 2D boron nitride nanostructures: nanosheets, nanoribbons, nanomeshes, and hybrids with graphene. *Nanoscale*. 2012;4:6908–6939. Available from: <http://dx.doi.org/10.1039/C2NR32201C>.
- [285] Shi H, Pan H, Zhang YW, Yakobson BI. Quasiparticle band structures and optical properties of strained monolayer MoS<sub>2</sub> and WS<sub>2</sub>. *Phys Rev B*. 2013 Apr;87:155304. Available from: <http://link.aps.org/doi/10.1103/PhysRevB.87.155304>.
- [286] Pan H, Zhang YW. Edge-dependent structural, electronic and magnetic properties of MoS<sub>2</sub> nanoribbons. *J Mater Chem*. 2012;22:7280–7290. Available from: <http://dx.doi.org/10.1039/C2JM15906F>.
- [287] Li Y, Zhou Z, Zhang S, Chen Z. MoS<sub>2</sub> Nanoribbons: High Stability and Unusual Electronic and Magnetic Properties. *Journal of the American Chemical Society*. 2008;130(49):16739–16744. PMID: 19007118. Available from: <http://dx.doi.org/10.1021/ja805545x>.
- [288] Wang R, Zhou X, Xu X, Hu J, Pan J. The indirect-direct band gap tuning in armchair MoS<sub>2</sub> nanoribbon by edge passivation. *Journal of Physics D: Applied Physics*. 2017;50(9):095102. Available from: <http://stacks.iop.org/0022-3727/50/i=9/a=095102>.
- [289] Hong J, Hu Z, Probert M, Li K, Lv D, Yang X, et al. Exploring atomic defects in molybdenum disulphide monolayers. *Nature communications*. 2015;6. Available from: <http://dx.doi.org/10.1038/ncomms7293>.
- [290] Hirshfeld FL. Bonded-atom fragments for describing molecular charge densities. *Theoretica chimica acta*. 1977;44(2):129–138. Available from: <http://dx.doi.org/10.1007/BF00549096>.
- [291] Cui P, Choi JH, Chen W, Zeng J, Shih CK, Li Z, et al. Contrasting Structural Reconstructions, Electronic Properties, and Magnetic Orderings along Different Edges of Zigzag Transition Metal Dichalcogenide Nanoribbons. *Nano Letters*. 2017;17(2):1097–1101. PMID: 28029259. Available from: <http://dx.doi.org/10.1021/acs.nanolett.6b04638>.
- [292] Hanoka JI, Seager CH, Sharp DJ, Panitz JKG. Hydrogen passivation of defects in silicon ribbon grown by the edge-defined film-fed growth process. *Applied Physics Letters*. 1983;42(7):618–620. Available from: <http://scitation.aip.org/content/aip/journal/apl/42/7/10.1063/1.94022>.
- [293] Chen Q, Zhu L, Wang J. Edge-passivation induced half-metallicity of zigzag zinc oxide nanoribbons. *Applied Physics Letters*. 2009;95(13). Available from: <http://scitation.aip.org/content/aip/journal/apl/95/13/10.1063/1.3238561>.

- [294] Lu YH, Wu RQ, Shen L, Yang M, Sha ZD, Cai YQ, et al. Effects of edge passivation by hydrogen on electronic structure of armchair graphene nanoribbon and band gap engineering. *Applied Physics Letters*. 2009;94(12). Available from: <http://scitation.aip.org/content/aip/journal/apl/94/12/10.1063/1.3103551>.
- [295] Erdogan E, Popov I, Enyashin A, Seifert G. Transport properties of MoS<sub>2</sub> nanoribbons: edge priority. *The European Physical Journal B*. 2012;85(1):1–4. Available from: <http://link.springer.com/article/10.1140/epjb/e2011-20456-7>.
- [296] Spirko JA, Neiman ML, Oelker AM, Klier K. Electronic structure and reactivity of defect MoS<sub>2</sub> II. Bonding and activation of hydrogen on surface defect sites and clusters. *Surface Science*. 2004;572(2–3):191 – 205. Available from: <http://www.sciencedirect.com/science/article/pii/S0039602804010908>.
- [297] Cordero B, Gomez V, Platero-Prats AE, Reves M, Echeverria J, Cremades E, et al. Covalent radii revisited. *Dalton Trans*. 2008;p. 2832–2838. Available from: <http://dx.doi.org/10.1039/B801115J>.
- [298] Ouyang F, Yang Z, Ni X, Wu N, Chen Y, Xiong X. Hydrogenation-induced edge magnetization in armchair MoS<sub>2</sub> nanoribbon and electric field effects. *Applied Physics Letters*. 2014;104(7). Available from: <http://scitation.aip.org/content/aip/journal/apl/104/7/10.1063/1.4865902>.
- [299] Kou L, Tang C, Zhang Y, Heine T, Chen C, Frauenheim T. Tuning Magnetism and Electronic Phase Transitions by Strain and Electric Field in Zigzag MoS<sub>2</sub> Nanoribbons. *The Journal of Physical Chemistry Letters*. 2012;3(20):2934–2941. PMID: 26292229. Available from: <http://dx.doi.org/10.1021/jz301339e>.
- [300] Sagynbaeva M, Panigrahi P, Yunguo L, Ramzan M, Ahuja R. Tweaking the magnetism of MoS<sub>2</sub> nanoribbon with hydrogen and carbon passivation. *Nanotechnology*. 2014;25(16):165703. Available from: <http://stacks.iop.org/0957-4484/25/i=16/a=165703>.
- [301] Cristol S, Paul JF, Payen E, Bougeard D, Clémendot S, Hutschka F. Theoretical Study of the MoS<sub>2</sub> (100) Surface: A Chemical Potential Analysis of Sulfur and Hydrogen Coverage. *The Journal of Physical Chemistry B*. 2000;104(47):11220–11229. Available from: <http://dx.doi.org/10.1021/jp0023819>.
- [302] Cristol S, Paul JF, Payen E, Bougeard D, Clémendot S, Hutschka F. Theoretical Study of the MoS<sub>2</sub> (100) Surface: A Chemical Potential Analysis of Sulfur and Hydrogen Coverage. 2. Effect of the Total Pressure on Surface Stability. *The Journal of Physical Chemistry B*. 2002;106(22):5659–5667. Available from: <http://pubs.acs.org/doi/abs/10.1021/jp0134603>.
- [303] Lucking MC, Bang J, Terrones H, Sun YY, Zhang S. Multivalency-Induced Band Gap Opening at MoS<sub>2</sub> Edges. *Chemistry of Materials*. 2015;27(9):3326–3331. Available from: <http://dx.doi.org/10.1021/acs.chemmater.5b00398>.

- [304] Wang R, Sun H, Ma B, Hu J, Pan J. Edge passivation induced single-edge ferromagnetism of zigzag MoS<sub>2</sub> nanoribbons. Physics Letters A. 2017;381(4):301 – 306. Available from: <http://www.sciencedirect.com/science/article/pii/S0375960116313251>.
- [305] Yazyev OV, Capaz RB, Louie SG. Theory of magnetic edge states in chiral graphene nanoribbons. Phys Rev B. 2011 Sep;84:115406. Available from: <http://link.aps.org/doi/10.1103/PhysRevB.84.115406>.
- [306] Momma K, Izumi F. VESTA: a Three-Dimensional Visualization System for Electronic and Structural Analysis. JP-Minerals; 2014. Accessed: 2015-05-25. Online. Available from: [http://www.geocities.jp/kmo\\_mma/crystal/download/VESTA\\_Manual.pdf](http://www.geocities.jp/kmo_mma/crystal/download/VESTA_Manual.pdf).
- [307] Xiao J, Long M, Li M, Li X, Xu H, Chan K. Carrier mobility of MoS<sub>2</sub> nanoribbons with edge chemical modification. Phys Chem Chem Phys. 2015;17:6865–6873. Available from: <http://dx.doi.org/10.1039/C4CP05199H>.
- [308] Ridolfi E, Lima LRF, Mucciolo ER, Lewenkopf CH. Electronic transport in disordered MoS<sub>2</sub> nanoribbons. Phys Rev B. 2017 Jan;95:035430. Available from: <https://link.aps.org/doi/10.1103/PhysRevB.95.035430>.
- [309] Wang Y, Qi L, Shen L, Wu Y. Surface defect passivation of MoS<sub>2</sub> by sulfur, selenium, and tellurium. Journal of Applied Physics. 2016;119(15):154301. Available from: <http://dx.doi.org/10.1063/1.4946840>.
- [310] Koós AA, Vancsó P, Magda GZ, Osváth Z, Kertész K, Dobrik G, et al. STM study of the MoS<sub>2</sub> flakes grown on graphite: A model system for atomically clean 2D heterostructure interfaces. Carbon. 2016;105:408–415. Available from: <http://www.sciencedirect.com/science/article/pii/S0008622316303402>.
- [311] Dolui K, Pemmaraju CD, Sanvito S. Electric Field Effects on Armchair MoS<sub>2</sub> Nanoribbons. ACS Nano. 2012;6(6):4823–4834. PMID: 22546015. Available from: <http://dx.doi.org/10.1021/nn301505x>.
- [312] Bollinger MV, Lauritsen JV, Jacobsen KW, Nørskov JK, Helveg S, Besenbacher F. One-Dimensional Metallic Edge States in MoS<sub>2</sub>. Phys Rev Lett. 2001 Oct;87:196803. Available from: <https://link.aps.org/doi/10.1103/PhysRevLett.87.196803>.
- [313] Beiser A. Concepts of modern physics. 2nd ed. McGraw-Hill series in fundamentals of physics. McGraw-Hill Book Company; 1973.
- [314] Perdew JP, Burke K, Ernzerhof M. Generalized Gradient Approximation Made Simple [Phys. Rev. Lett. 77, 3865 (1996)]. Phys Rev Lett. 1997 Feb;78:1396–1396. Available from: <http://link.aps.org/doi/10.1103/PhysRevLett.78.1396>.
- [315] Perdew JP. Accurate Density Functional for the Energy: Real-Space Cutoff of the Gradient Expansion for the Exchange Hole. Phys Rev Lett. 1985 Nov;55:2370–2370. Available from: <http://link.aps.org/doi/10.1103/PhysRevLett.55.2370.2>.

- [316] Perdew JP, Yue W. Erratum: Accurate and simple density functional for the electronic exchange energy: Generalized gradient approximation. *Phys Rev B*. 1989 Aug;40:3399–3399. Available from: <http://link.aps.org/doi/10.1103/PhysRevB.40.3399>.



This Thesis is Printed on a 100% Recycled Paper in Birmingham, UK (May 2017)